Materials for high energy Li-ion and post Li-ion batteries

(Article begins on next page)

08 November 2022

Doctoral Dissertation
Doctoral Program in Material Science and Technology (33th Cycle)

Materials for high energy Li-ion and post Li-ion batteries

Daniele Versaci
* * * * * *
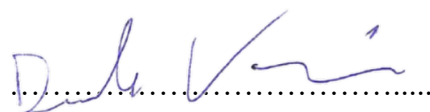
Supervisors
Prof. S. Bodoardo
Prof. C. Francia

Doctoral Examination Committee:
Prof. Diana Golodnisky, Referee, University of Tel Aviv
Prof. Catia Arbizzani, Referee, University of Bologna
Prof. Arnaldo Visintin, Referee, University of La Plata
Prof. Barbara Onida, Referee, Politecnico of Torino
Prof. Marco Sangermano, Referee, Politecnico of Torino

Politecnico di Torino
March 5, 2021

I hereby declare that, the contents and organisation of this dissertation constitute my own original work and does not compromise in any way the rights of third parties, including those relating to the security of personal data.

....

Daniele Versaci

Turin, March 5, 2021

Summary

Lithium-ion batteries (LIBs) are well established energy storage devices for electronic, transportation and renewable-energy applications.

Nevertheless, to meet the ever-increasing energy storage demand for electrical mobility and smart grid, future batteries have to guarantee higher energy density and, at the same time, sustainable and cheaper solutions.

In this frame anode and cathode materials with higher specific capacity are required.

Beyond traditional Li-ion cathode materials, one of the most promising material for high energy application is sulphur. In fact, lithium-sulphur (Li-S) technology presents high theoretical energy density (about 2600 Wh kg^{-1}) and low-cost (because sulphur is relatively inexpensive and non-toxic). Nowadays, lithium-sulphur battery, are still not fully commercialized because, during the electrochemical reaction, sulphur is reduced producing lithium polysulfides (LiPSs), which can migrate to the anode side giving some parasitic reaction and, consequently, fast capacity fading and battery degradation.

Many strategies have been proposed to prevent the polysulfide shuttle phenomenon. In the present dissertation, the use of a thin and selective interlayer, directly coated on the sulphur cathode surface, is presented as effective strategy to limit the fast capacity fading of the battery.

According to preliminary DFT calculations carbon nitride (C_3N_4) was selected and investigated as lithium polysulfides trapping agent. In particular, carbon nitrides with different morphologies and surface functionalities (obtained from different precursors and at different temperatures) were thoroughly investigated for the first time in order to correlate these properties with the electrochemical performances of the electrodes.

From the anode side, one of the most interesting material, able to guarantee higher specific capacity to the system, is tin oxide. Tin-based materials, especially tin oxide, have been widely investigated as potential graphite substitute anodes for Li-ion batteries. In comparison to graphite, SnO_2 anodes shows higher theoretical capacity of 1494 mAh g^{-1} vs. 375 mAh g^{-1}. Furthermore, SnO_2 is also easy to obtain, inexpensive and environmentally friendly. Unfortunately, during the lithiation process (*i.e.* conversion and alloying reaction) tin oxide suffers from a drastic volumetric expansion that induces surface cracking accompanied by an electrical contact loss with the current collector and subsequent capacity fading.

In this dissertation two possible strategies to synthesized tin oxide-based compounds were investigated.

Firstly, a wet impregnation synthesis was adopted to finely disperse tin oxide nanoparticles on a commercial carbon black matrix.

In the second case, tin oxide was synthetized by a solid-state process, directly mixing the precursors with g-C_3N_4, in order to increase the specific surface area of the compound, able to limit the huge volumetric expansion, during cycling.

Both the compounds were characterized by multi-technique approach in order to individuate the electrochemical performances in relation to the crystal structure, particle size, morphology, surface area and pore size distribution of the material.

Acknowledgment

The completion of this dissertation would not have been possible without the help and support of many different people.

First, I would like to express my gratitude to my supervisors Silvia Bodoardo and Carlotta Francia for the continuous support during my years at Politecnico di Torino and for providing me the opportunity to conduct my research autonomously. Without the discussions, in front of a whiteboard, fully covered after few minutes, part of my PhD work would not have been possible!

I would like to thank Julia Amici, who supported me from my first day in the "lab". Thank you because we spent together many funny moments but, in particular, because you sustained me also during bad moments.

I would like to thank Prof. Arnaldo Visintin (INIFTA), PhD. Melina Cozzarin (YTEC) and Prof. Ezequiel Leiva (FAMAF) who welcomed me in Argentina, making me feel at home. I will never forget your help and the constructive discussions with you.

Thanks to Prof. Nerino Penazzi for fruitful electrochemical discussions and for all the nice anecdotes.

I would like to thank all my colleagues. Together we spent a lot of nice moments in the lab, and each of you helped me to complete my work. So, thanks to: Alberto, Svetla, Juqin, Pietro, Claudia, Riccardo, Roberto, Simone, Mojtaba and Usman.

A special thanks go to Andrea and Davide (the *"G(I)TT team"*), because the discussion with you are never ordinary and because you helped me a lot in my work. You are more than colleagues for me, you are friends!

I would also like to thank Aneta Dumitrescu, for her helpfulness showed during these years. I learned a lot from you!

Another special thanks go to my first mentors: Marco and Fabrizio who taught me the basics to do this job to the best of my ability.

Thank also to Fernando, Veronica and Erika. I hope to work again with you in the future.

I am also grateful to many people whom I had the opportunity to meet during these years. The complete list of you will take too many pages!

Last but not least, I would like to thank my parents who has provided me unconditional love and support. You always believed in me, and softly encourage me in the bad moments. This work could not be possible without these pillars.

A special thanks also to my friends: Davis, Elisa, Alessandro, Stefano, Fabio, Sara, Simone, Gabriele, Emanuele, Matteo, Veronica, Klizia. We spent more than half of our life together, with nice dinners, barbecues, drinks, travels, discussions. I think, your contribution to this work cannot be denied!

*To my parents,
for their love and
support.*

*"I have learned more from my mistakes than
from my successes"*

Sir Humphry Davy

1 Contents

List of Tables

List of Figures

Chapter 1

Introduction

1.1 State of the art

Since the first Industrial Revolution in 1750 human activities have contributed substantially to climate change by adding CO_2 and other heat-trapping gases to the atmosphere.

Greenhouse gas (GHG) emissions are still growing and, considering the last IPCC report, global warming is likely to reach 1.5 °C between 2030 and 2052[1]. In particular, the transport sector is responsible for 27 % of total energy-related CO_2 emissions, and 72 % of transport emissions come from road vehicles, this is intimately connected to the domination of this sector by internal combustion engines (ICEs) in which oil is the main fuel source [1].

Taking into account the increasing consequences of global warming, in December 2015, 195 countries signed the Paris Agreement (PA) with the aim to limit global warming to "well below 2 °C above pre-industrial levels" and to make efforts to "limit the temperature rise to 1.5 °C above pre-industrial levels"[2].

The European Union is currently making several changes to the organization of the energy market and setting new targets for deregulation and fighting climate change. According to *Paris declaration on electro mobility and climate change* it seems clear that the development of an integrated electro-mobility, encompassing various transport modes, coupled with the low-carbon production of electricity and hydrogen, is fundamental to achieve the fixed limits[3].

In this frame the drastic permeation of hybrid and full electric vehicles in the market and their competitiveness with ICEs systems is the most promising option for a cleaner mobility. At the same time, efficient storage systems are required for

---

[1] Available online: https://www.ipcc.ch/sr15/
[2] COP21. Available online: http://www.cop21paris.org/about/cop21/
[3] Available online: https://unfccc.int/news/the-paris-declaration-on-electro-mobility-and-climate change-and-call-to-action

the growing demand of energy from intermittent renewable sources (wind, solar, etc), insuring the energy demands of the ever-increasing global population [2].

The energy storage market has shown steady growth in the last decades, as consequence to the great expansion of consumer electronics (laptops, smartphones and tablets) and, more recently, as a response to the increase in energy needs and its accumulation. In particular, the past 30 years have shown rapid growth in the diffusion and use of new battery technologies with increased energy density.

Nowadays the automotive market leads a further expansion of batteries, with the growing interest in plug-in hybrid electric vehicles (PHEV) and electric vehicles (EV). The electric automotive market is still in its introduction stage, however many studies, ensure that this market will probably increase by a factor higher than 50 in the near future [3].

During the last years a big effort was done by manufacturers to significantly extend the driving range of electric vehicles and within the next decade improvements regarding energy density and safety can be expected [3].

Anyway, carmakers and governments are asking for fast battery improvements in terms of energy, combined with safety, low cost, high cycle life and good rate capability in order to fulfil the needs of greenhouse gas reductions through implementation of electric vehicles [4].

In the near future the two key-topics in which more significant achievement can be expected are: energy density and safety.

The energy density can be simply represented as integral of the capacity multiplied with the voltage. So, to increase the energy, and consequently the performance of a battery, two main approaches are possible: the first possibility is to increase the voltage of the cell, using high voltage electrode materials while, the second possibility, is to increase the energy, using materials with high specific capacity, or using different electrochemical technologies, called post Li-Ion technologies, like Lithium-sulphur or Lithium-air (Figure 1.0.1) [5][6].
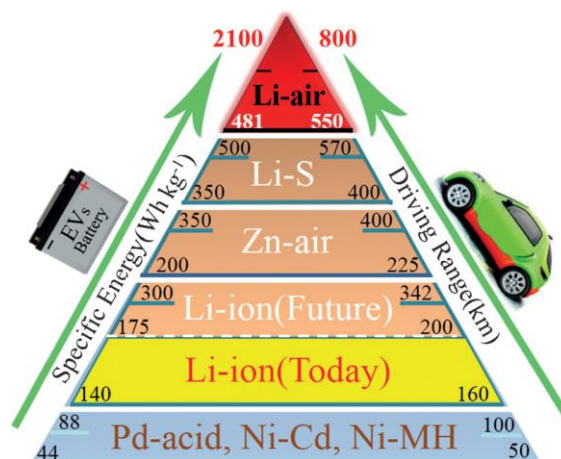
Figure 1.0.1: comparison of different battery systems according to their energy densities (Wh kg^{-1}) and EV driving force (km) [6] .

It seems clear that a huge volume of research in Li-ion batteries has to be done in electrode materials. Electrodes with higher rate capability, higher charge capacity, and sufficient higher or lower voltage can improve the energy and power densities of Li batteries making them smaller and cheaper [7]. Therefore, with a continuous progress on materials, lithium ion and post-lithium ion batteries will continue to improve in all of their properties.

1.2 Goal of dissertation

According to the considerations done in the previous paragraph, in my PhD work I focused my attention on high capacity anode and cathode materials which can improve the energy density of lithium battery systems.

In chapter 2, a general introduction to Li-ion battery technology along with its working principles and fundamentals parameters is provided. A brief summary of most common materials and components employed in Li-ion cells is also given, with particular attention to advantages and drawbacks for each material.

The third chapter is focused on Lithium-sulphur battery. A general introduction to the Li-S chemistry is given in the first part of the chapter, followed by a general overview on sulphur cathode preparation and an overview on the most common materials and strategies adopted to avoid shuttle phenomenon.

Chapter 4 is focused on carbon nitride and, in particular, on synthesis strategies and structural, chemical and morphological characteristics of g-C_3N_4.

In the second paragraph of the chapter, a general overview is given about carbon nitride applications in Li-S systems. In the last paragraph all the different strategies adopted, in the last 5 years, to insert and study carbon nitride as effective lithium polysulfides trapping agent are reported.

Chapter 5 reports the investigation of a carbon nitride-based double-layer approach, as an effective way to limit the shuttle effect and increase the electrochemical performances of a Li-S cell. The synthesis of different carbon nitrides from different precursors and at different temperatures is investigated and correlated to the corresponding electrochemical performances of Li-S cell.

Starting from chapter 6 the attention was moved to high capacity anode material, in particular on tin oxide. In this chapter a brief introduction to state of the art of this material is reported.

In chapter 7 and 8 the synthesis and the electrochemical performances of two tin oxide-based anode compound: SnO_2@C45 and SnO_2@C_3N_4 are reported and investigated.

A final conclusions and perspectives are proposed at the end of this manuscript, as a summary of a complete work.

Chapter 2

2 Li-ion battery (LIB)

2.1 Battery nowadays

Batteries are the most common type of energy storage devices. More precisely, it is possible to define a battery as an electrochemical storage device in which energy is stored in chemical bonds [8].

Typically, chemical energy can be converted to other forms of energy, for example, in mechanical energy using a combustion process, by an engine, or to heat (and then to electricity) by nuclear fission in nuclear power plants. In this frame electrochemical devices are unique because they convert chemical energy directly to electrical energy without involving the transfer of heat, so Carnot limitations are avoided and consequently the process can be highly efficient.

Electrochemical power sources are usually identified as primary (not rechargeable) or secondary (rechargeable), depending on their capability of being electrically recharged.

A primary battery is a galvanic cell that simply converts chemical energy into work. While a secondary battery is rechargeable because electrical work is converted back into chemical energy upon charging [9]. Examples of rechargeable battery include lead acid, nickel-cadmium, nickel-metal-hydride, lithium-ion, sodium-sulphur, metal-air and flow batteries.

Batteries are classified by chemistry, and the most common are: lithium-, lead-, and nickel-based systems.

The lithium-ion family receives the most attention and is gradually replacing the lead and nickel-based predecessors which dominated the battery world until the 1990s. Lithium-ion (Li-ion) batteries are now widely implemented as power or energy source for portable electronics and are increasingly promoted as a greener energy solution to liberate society from the dependency of fossil fuel.

The comparison of the different battery technologies in terms of volumetric and gravimetric energy density is shown in the Ragone plot [10] in Figure 2.1.
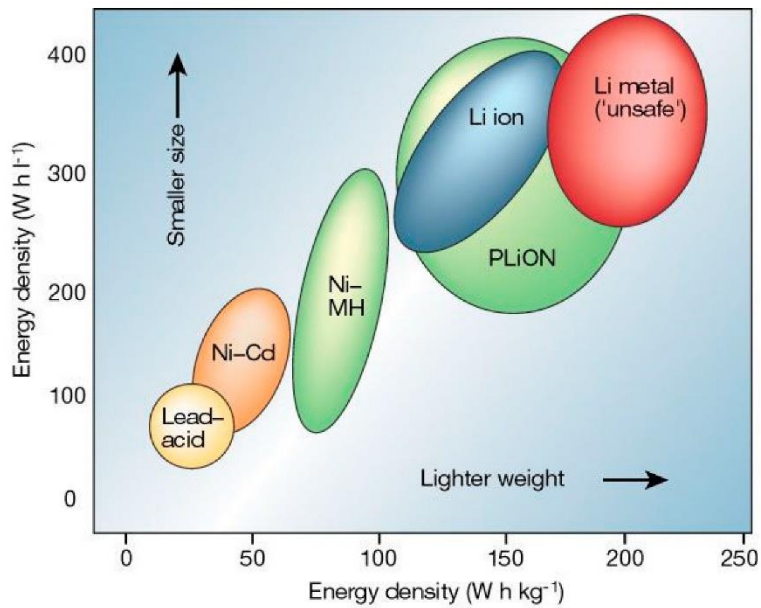
Figure 2.1: Ragone plot of several of the battery technologies [10].

The Ragone plot clearly shows that Li-ion batteries have higher energy density (> 200 Wh kg^{-1}) in comparison to other systems. Moreover, they are also characterized by low self-discharge rate (2 % to 8 % per month), long cycle life (greater than 1000 cycles) and a broad temperature range of operation (-20 °C to 60 °C).

In the last three decades LIBs have seen a great improvement in energy density from ~200 Wh kg^{-1} to values higher than 400 Wh kg^{-1}, which were mostly achieved by new type of materials and better cell engineering [11]. The next big goal will be the development of adequate LIB, with higher energy density for electric vehicles (EV) and for stationary application [12].

As mentioned in the previous chapter the improvement of current lithium ion batteries performances inevitably passes through an implementation and an engineering of new materials. So, the current chapter will be focused on materials used in Li-ion batteries.

2.2   Battery parameters

Several factors or parameters characterize a cell, from the performance, economic or environmental point of view. These parameters depend on the intrinsic characteristics of the materials involved, on the chemical reactions, on the transport phenomena and on the diffusion kinetics of the chemical species.

The most important battery parameters definitions are given below.

I. Open-Circuit-Voltage (OCV)

The open circuit potential difference of the cell is the voltage (expressed in Volts, V) established at its poles in open circuit conditions (in the absence of external electric current). It represents the maximum voltage available for the discharge, or the minimum value to be reached to carry out the charge of the cell. The value of this parameter in standard reference conditions can be obtained from the variation of Gibbs free energy in standard conditions due to the reactions occurring in the negative and positive electrode respectively (Equation 2.1).

$$OCV\ cell = E^0_{anode} - E^0_{cathode} = \Delta E^0 = -\frac{\Delta G^0}{n \cdot F} \qquad [2.1]$$

II. Overvoltage or overpotential

The overpotential (η) is defined as the difference between the OCV and the cell potential, during the discharge phase, or as the difference between the cell potential and its OCV, during the charge phase.

III. Current density

The current density (j) is defined as the ratio of the total current (I) which flows through the electrode, and the normal surface of the electrode (A).

$$j\,(t) = \frac{I\,(t)}{A} \qquad [2.2]$$

Its units are normally in A m^{-2}.

IV. Cell Capacity

The capacity Q, measured in Coulomb [C] or [Ah], with 1Ah = 3600 C, represents the quantity of electrical charge accumulated during the charging phase, or available during the discharging phase. The capacity of the cell accumulated/released in a time range [t1; t2] can be defined by Equation 2.3 which, in conditions of constant current, can be written as in Equation 2.4.

$$Q = \int_{t1}^{t2} I(t)\,dt \qquad [2.3]$$

$$Q = I \cdot t \qquad [2.4]$$

The theoretical capacity Q_t, equal to the maximum electric charge from the cell, can be obtained based on the amount of active material present inside the cell through Equation 2.5:

$$Q_t = x \cdot n \cdot F \qquad [2.5]$$

Where x represents the number of moles of active material present inside the electrode, n the number of equivalent electrons involved in electrochemical reactions and F is the Faraday constant.

The specific capacity of an electrochemical cell is the amount of charge that a battery can accumulate/deliver expressed per unit of mass (Ah g^{-1}) or volume (Ah cm^{-3}).

V.   C – Rate

The C-rate is a measure of the rate at which a battery is charged (or discharged) relatively to its maximum capacity. This parameter can be associated with the time required for the cell to charge/discharge completely. A charge at C/5 and 2C mean, for example, that the charging current is such as to determine a necessary time to completely charge the cell equal to 5 and 0.5 hours, respectively.

VI.   Coulombic Efficiency

The coulombic efficiency, Y, is the ratio between the capacity provided during the cell discharge phase ($Q_{discharge}$) and the capacity accumulated during the previous charge phase (Q_{charge}):

$$Y = \frac{Q_{discharge}}{Q_{charge}} \qquad [2.6]$$

VII.   Energy

The Energy (E) that an electrochemical power source can supply, expressed in Joule (J) or more commonly in Watt hour (Wh), is related to the capacity and the voltage through the equation:

$$E = Q \cdot V \qquad [2.7]$$

where V is the average operating voltage delivered by the system and Q is the capacity. It is generally expressed in Watt-hours [Wh, $1Wh = 3600$ J].

VIII. Power

The power (P) delivered by a material or a power source is defined as the average working voltage multiplied by the flowing current, it is related to the energy transferred per unit of time:

$$P = V \cdot i = \frac{Q \cdot V}{t} = \frac{E}{t} \qquad [2.8]$$

The power is expressed in Watt [W].

IX. Cycle life

The Cycle life is a measure of the ability of a secondary battery to withstand subsequent charge/discharge cycles. It usually describes the number of charge/discharge cycles that give rise in a battery to the capacity fade at a fixed percentage of the original capacity (usually 80 %). The cycle life depends on the working conditions, *e.g.* charge/discharge rate.

X. Shelf life

Shelf life is the period of time over which a battery can be stored without significant deterioration, therefore still meeting specified performance criteria.

XI. Self-discharge

Self-discharge is the loss of capacity of a battery under open-circuit conditions as a result of internal chemical reactions and/or short-circuits.

2.3 Li-ion battery fundamentals

Nowadays Li-ion batteries have become the most popular battery chemistry, due to their high gravimetric and volumetric energy density, as compared to the other rechargeable battery chemistries [13].

A generic Lithium-ion battery is made of one or more power-generating units called cells. Where the cell consists of two electrodes which are isolated by a separator and soaked in electrolyte solution to promote the movement of ions, avoiding short circuits.

A scheme of a generic Li-ion cell is shown below in Figure 2.2:
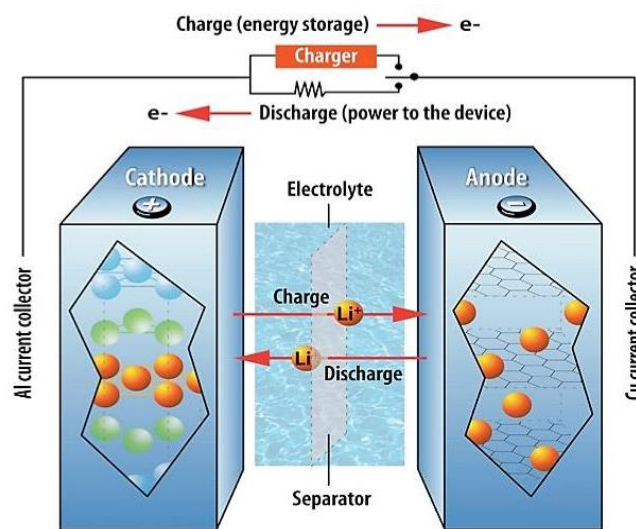
Figure 2.2: Lithium-ion cell general scheme (illustration by Argonne National Laboratory).

The Li-ion cell is composed by four main components [8]:

- o <u>Anode (-)</u>: electrode at which oxidation reaction occurs and electrons are releases.
- o <u>Cathode (+)</u>: electrode at which reduction reaction occurs and electrons are captured.
- o <u>Electrolyte</u>: phase containing mobile ions to carry the current. An electrolyte typically contains a solvent in addition to a dissociated salt. It is normally added to the separator.
- o <u>Separator</u>: electronically insulating material that segregates the anode from the cathode, forming an isolator for electrons but allowing ions to pass through. A separator may also help provide mechanical rigidity to a cell.

In an electrochemical cell a set of reactions occurs at the electrode/electrolyte interfaces and current flows in the form of electrons through an external circuit, and in the form of ions through the separator, maintaining the charge balance of the system.

The more negative electrode is designated the anode, whereas the cathode is the more positive one. During the electrochemical discharge reaction, the anode, gives up electrons to the external circuit and is oxidised, while the cathode, accepts electrons from the external circuit and is reduced. The electrical circuit is completed by the flow of anions and cations to the respective poles (electrodes), through the electrolyte.

During the charge process the electron flow is reversed, forcing the non-spontaneous redox reaction to take place.

It is common to use the terminology anode and cathode for the negative and positive electrodes, respectively, although the electrodes play alternatively the role of anode and cathode during the charge and discharge process.

Li-ion batteries are also referred to as rocking chair batteries because the lithium ions are reversibly removed or inserted into the active materials by an intercalation process and without a significant structural change to the host. By this way, the anode can be considered as a "lithium sink" while the cathode as a "lithium source" of lithium ions [8].

The first modern Li-ion battery was commercialized by Sony in 1991 [14]. The commercialization of the first "*rocking chair battery*" was allowed thanks to several studies on stable intercalation materials able to reversibly accommodate Li ions. These were done in the late 1970s by Basu and Yazami [15] groups on graphite and by Goodenough and Muzichima on $LiCoO_2$ [16].

This cell based on $LiCoO_2/C$ gained a wide diffusion and is still in use in today's high-performance portable electronic devices thanks to high energy density ($\approx$180 Wh kg^{-1}) and high discharge potential (3.7 V). The main peculiarity of Li-ion cell is that lithium is directly incorporated in layered or three-dimensional transition metal oxides, Li_xMO_2 (M = Co, Ni or Mn) rather than in the pure metallic form. Since metallic lithium is not present in the cell, Li-ion batteries are chemically less reactive, safer, and offer longer cycle life in comparison to rechargeable lithium batteries that employ pure lithium metal as the negative electrode material.

As mentioned before the reactions occur at the electrode/electrolyte interface. During charge process, the Li^+ ions are de-inserted/de-intercalated from the positive electrode, with relative oxidation of the active material ($LiMO_2$). The as formed lithium ions migrate across the electrolyte and are inserted into the crystal structure of the negative active material (C), which is reduced. At the same time, the compensating electrons travel in the external circuit and are accepted by the host to balance the reaction. The process is completely reversible therefore the discharge process is just the opposite [17].

In the following scheme, LiMO$_2$ represents the metal oxide positive material, such as LiCoO$_2$, and C the carbonaceous negative material, such as graphite [18].

Positive electrode (LiMO$_2$):

$$Li_{(1-x)}MO_2 + xLi^+ + xe^- \rightleftharpoons LiMO_2 \tag{2.9}$$

Negative electrode (LiC$_6$):

$$Li_xC_6 \rightleftharpoons 6C + xLi^+ + xe^- \tag{2.10}$$

Full reaction:

$$Li_xC_6 + 2Li_{(1-x)}MO_2 \rightleftharpoons 6C + 2LiMO_2 \tag{2.11}$$

The schematic illustration of (LiMO$_2$/C) rocking chair battery is shown in Figure 2.3.
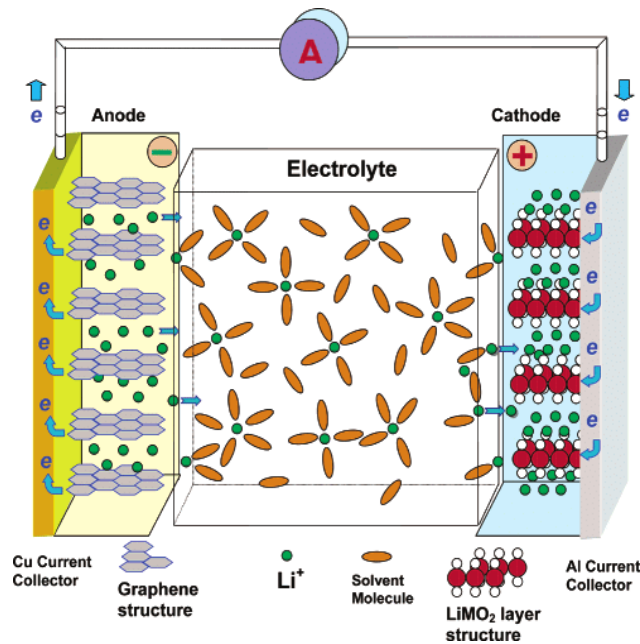
Figure 2.3: schematic description of a "lithium ion rocking chair" cell that employs graphitic carbon as anode and transition metal oxide as cathode [18].

In addition to active materials, a polymeric binder, typically polyvinylidene fluoride (PVdF), copolymer polyvinylidene fluoride–hexafluoropropylene (PVdF-HFP), or greener binder such as carboxymethylcellulose (CMC) derivate, is used to hold the electrode structure together and bond it to the current collector.

In the meantime, a conductive additive, typically a high-surface-area carbon black, is added to the active material particles to improve the contact between the

particles and the electrical conductivity. This is particularly important for common Li-ion positive active materials which have limited conductivity. Therefore, additives like carbon, have to be added to increase the conductivity of the porous electrode.

The pore structure of the electrode, with the combination of conductive carbon, guarantees good contact among the particles which is essential for the maximum availability of the active materials and for a good efficiency during high rate performances [13][19].

In standard Li-ion cells the system is completed by a microporous polyethylene or polypropylene separator film soaked with a liquid electrolyte, while the separator is replaced by a gel-polymer electrolyte in gel-polymer batteries, or by a layer of solid electrolyte in solid-state batteries [13].

In general, the amounts of electric energy per mass or volume that a cell can deliver strictly depends on the chemical energy stored within the electrodes. All the redox reactions which occur originate a change in the Gibbs free energy (ΔG).

From a thermodynamic point of view ΔG represents the net useful energy available from a given reaction.

The net available electrical energy from a reaction is given by the following equation:

$$\Delta G = -xnFE \hspace{4cm} [2.12]$$

where ΔG is the Gibbs free energy, x is the molar quantity of the active materials involved during the reaction, n is the number of electrons transferred per mole of reactants, F is the Faraday constant (96485 Coulombs per mole) and E is the standard potential which depends on the type of the active material integrated into the cell [8].

The Equation 2.12 implies that, assuming constant the number of electrons exchanged, the higher the cell potential (E), the higher the capacity of the electrochemical cell. So, to maximize the energy of an electrochemical cell, the difference between the cathode and anode potentials (open circuit voltage, OCV) has to be as large as possible [13] [20].

On the other side the detailed mechanism of battery electrode reactions often involves a series of physical, chemical, and electrochemical steps, including charge-transfer and charge transport reactions. This means that the practical batteries deviate from thermodynamic equilibrium condition when current is withdrawn, because of kinetic limitations.

The rates of each individual steps determine the kinetics of the electrode and, consequently the performance of the cell.

Therefore, the final available energy is lower than the stored chemical energy, and this is due to polarisation effect (of the electrodes) which is lost in the form of heat.

The types of polarization are mainly three:

1. activation polarization: required to drive the electrochemical reaction. It is related to the kinetics of the electrochemical redox (or charge-transfer) reactions taking place at the electrode/electrolyte interfaces of both the electrodes;
2. ohmic polarization: which causes a voltage drop during the operation. It is proportional to the current delivered, and related to the resistance of individual cell component as well as to the resistance due to contact problems between them;
3. concentration polarization: which is due to the differences in concentration between the reactants or products at the electrode surface, in comparison to the bulk of the solution, which are strictly related to mass transport limitations during cell operation.

The polarization, η, is given by:

$$\eta = E_{ocv} - E_t \qquad\qquad\qquad [2.13]$$

where E_{OCV} is the voltage of the cell at open circuit and E_t is the terminal cell potential when current (I), is flowing [8][11].

The polarization effects can be better explained observing a typical discharge curve of a battery as shown in Figure 2.4.
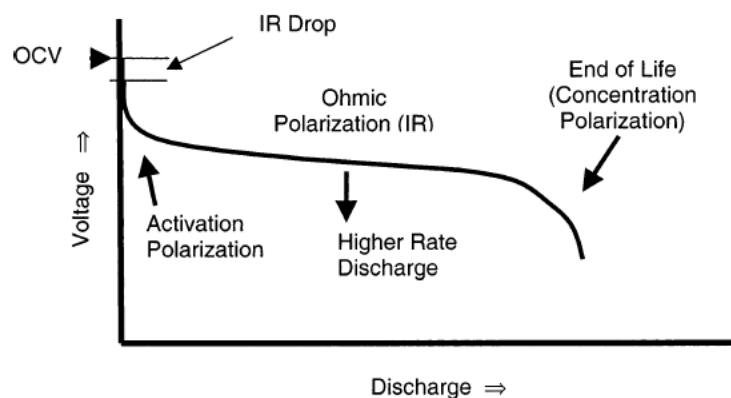
Figure 2.4: discharge curve of a battery and the effects of different types of polarization [8].

13

The discharge curve in useful to calculate the total capacity of the cell, and to understand the effects of temperature or different current regimes (C-rate) on the cell capacity.

The available energy of a cell depends on the chemistry of the total system and principally the electrochemical reaction occurring at both electrodes. Anyway, there are some additional factors, which affect the kinetics of the charge-transfer reaction, or the diffusion rate and degree of the energy loss, such as: the electrode construction, cell engineering, electrolyte conductivity and nature of the separator *etc*.

In conclusion, most of the improvements are attributable to the engineering, the structuring, and processing of the materials inside the battery [12].

2.4 Materials for LiB

The selection of the most suited active material is strongly dependent on the application itself. A selection has to be made considering which key property (energy density, power density, cost and lifetime) is the most important for the considered application [3].

Theoretically, the capacity of a cell is calculated from the amount of active materials and is expressed as the total quantity of electricity produced (in terms of Coulombs or Ampere-hours) by the electrochemical reactions.

As mentioned in the previous paragraph a typical battery electrode includes more components which can be divided into three categories: active material, conductive (carbon) additive and binder. It is worth noting that each of these components is vital to the operation of the cell, and electrode materials represented the 66 % of the total battery cost [3].

2.4.1 Anode active materials

An ideal active anode material should fulfil the following requirements [21]:

- o It must be light and accommodate as much Li as possible to optimize the gravimetric capacity.
- o Its redox potential with respect to Li^0/Li^+ must be as small as possible. (this way the overall voltage of the cell, will be higher).
- o It must possess good electronic and ionic conductivities which means higher power density of the cell.

- o It must not be soluble in the solvents of the electrolyte and not react with the lithium salt.
- o It must be safe
- o It must be cheap and environmentally friendly.

Pure metallic lithium is the lightest metallic element with a density of 0.53 g cm^{-3} and it presents the lowest standard electrode potential (-3.045 V vs. SHE) as illustrated in Figure 2.5 [11]. Due to these properties, metallic lithium became the first anodic materials in reversible lithium-based energy storage systems.
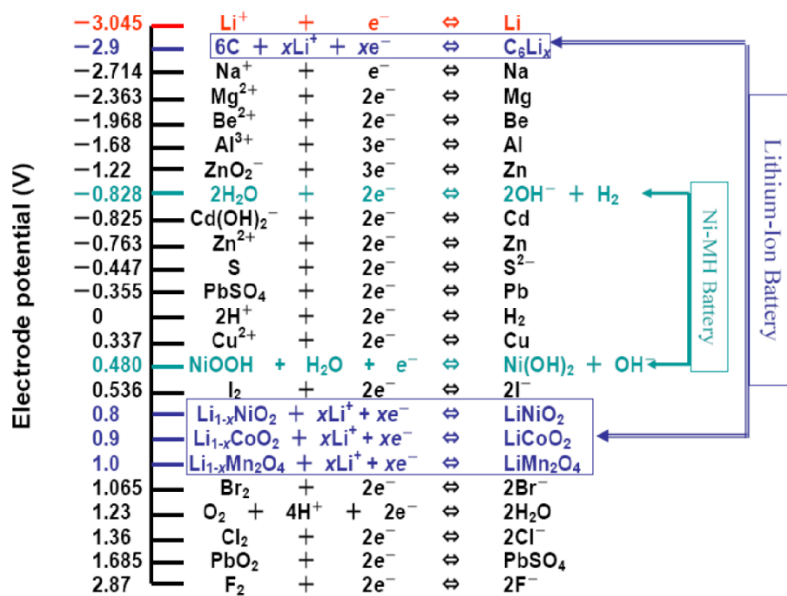
Figure 2.5: standard potential of the most common electrodes at 25°C.

Unfortunately metallic lithium suffers from several problems which hinder its implementation in most of the commercial cell [12]. The most important are mentioned below:

- o dendrites formation during charge process (Figure 2.6);
- o unavoidable strongly and continuous reactions with the commonly used electrolyte solutions;
- o poor capacity retention when practical specific charge (per cm^2) is modified upon cycling.
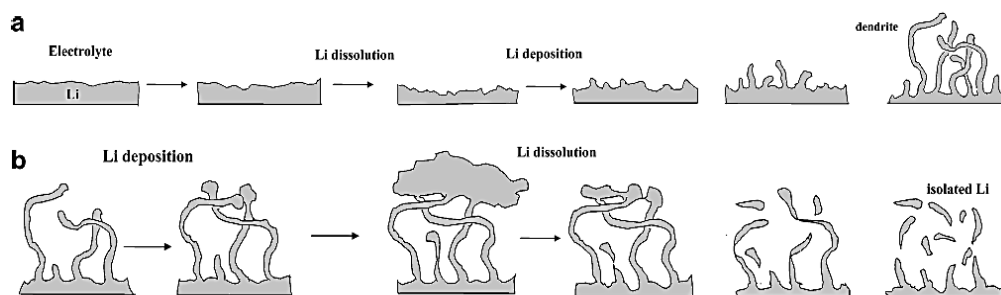
Figure 2.6: schematic description for the growth of dendrite crystals on a Li surface [18].

Anyway, the safe use of Li metal anodes is possible in some systems like solid-state batteries, in which the electrolyte systems are based on polymeric or solid matrices [12].

As a consequence of the instability and safety related problems associated to metallic Lithium, carbonaceous materials like graphite (ABAB layers) or hard carbon (polycondensation of oil pitch) are still the most used anode materials, in commercially available Li-ion.

Graphitic carbon is the dominant anode material due to its favourable electrochemical properties (*i.e.*, low and flat operating voltage of ~0.25 V vs. Li^0/Li^+), low cost, and chemical and mechanical stability [13]. The theoretical specific capacity of graphite is 372 mAh g^{-1} which corresponds to the lithiated formula LiC_6.

Non-graphitic carbons such as hard carbons are able to incorporate Li^+ as well, both in the space between crystal particles and between the layers. They have higher specific capacity (200 - 600 mAh g^{-1}) combined with a good cycle life, and lower cost of production. Usually, the problem with hard carbon are the poor rate capability coming from the slow diffusion process resulting from the random alignment of the graphene sheets, the low density, and hysteresis in the voltage profile [13].

All the carbonaceous materials suffer from some drawbacks including low specific energy capacity and strong electrolyte reactivity at the surface. Another important drawback is the proximity of the intercalation potential (around 0.3 V) to the potential for lithium metal plating which means that at high current range Li metal plating can occur and dendrites can be formed and they can easily penetrate the separator inducing the short-circuit of the cell.

During the operation of LIBs, graphite and other carbon materials are involved in a side reaction with the electrolyte solution. This reaction induces the deposition of various species directly on the electrode surface, forming the so called solid electrolyte interphase (SEI) [22].

Generally, the SEI layer formation occurs during firsts cycles of charge when the electrolyte components decompose into various species leading the formation

of a variety of layers on the electrode surface. This is caused by salts and solvents reduction at potentials higher than the intercalation potential of lithium ions.

The SEI layer is a good Li-ion conductor but an insulator to electron flow which means that SEI layer limits further electrolyte decomposition improving the cycle life of the system.

It is widely accepted that the SEI layer formation is essential in the electrochemical process and has a relevant impact on the initial capacity loss, self-discharge characteristics, cycle life, rate capability and safety of the battery.

On the other side, it is difficult to control the homogeneous formation and growth of the SEI layer, because its chemical composition, morphology, and stability depend on several factors [22][23]. Considering this, many efforts have been made to identify electrolyte additives able to help a rational SEI layer formation.

In order to avoid the problems related to graphite, researchers have been focused in the development of alternative anode materials which can guarantee both higher capacities and slightly higher intercalation potential (Figure 2.7) [13] [24].
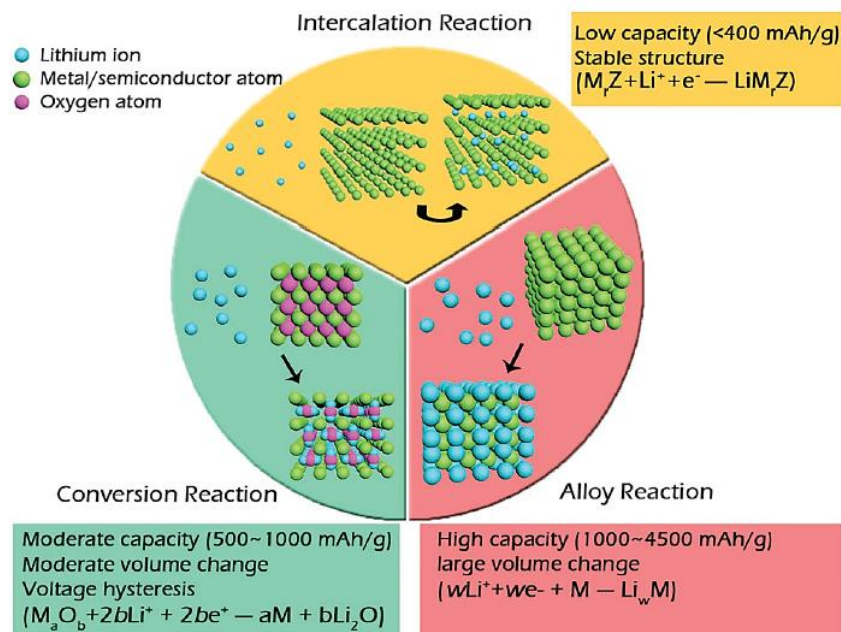
Figure 2.7: three main common reaction mechanisms between lithium ion and anodic electrode materials [24].

Materials such as Li metal alloys have been deeply investigated as potential alternatives to carbonaceous anode materials thanks to their higher gravimetric capacity. A great number of elements (Al, Si, Sn, Sb, Ga, Ge etc.) are known to form alloys with lithium, when polarized to sufficiently low potentials vs. lithium [12].

Elements like silicon and tin can be alloyed with 4.4 moles of lithium, with a consequent volume expansion during charge process. The large volume changes (up to 300 %) during Li^+ insertion/de-insertion, induces the loss of electrical contact between the active material and the current collector with dramatic impact on the cycle life of the cell [11] [25].

The cracks thus formed, continuously expose fresh active Li-alloy surface to the electrolyte solution leading to ongoing side reactions which consume the electrolyte solution and prevent the formation of a stable SEI layer on the alloy anodes, ultimately resulting in low Coulombic efficiency [12] [26].

To compensate the wide volume expansion and consequently avoid the electrode disaggregation, the most efficient action is embedding the Li metal alloys into a buffer matrix (typically a carbon matrix) [11] [27]. For example, carbon shells create a buffer zone between the silicon surface and the electrolyte inhibiting the direct reaction, but after many cycles the carbon coating can lose its structural integrity, and fresh Si surfaces are eventually exposed.

Another possible route to alleviate the electrode disaggregation of metal alloys is to nanosize the metallic clusters. The nanosize of the active material particles can help to suppress the strains, enhancing the reversibility of the alloying reaction. However, nanocomposites electrodes still suffer large capacity loss in particular in the first cycles [11].

As mentioned, silicon-based materials (silicon and its composites) can be employed as negative electrode materials for lithium-ion batteries.

These electrodes are very interesting because Silicon is cheap, and its specific capacity is very large, about 4200 mAh g^{-1} when highest Li content is achieved ($Li_{4.4}Si$). Moreover, its onset voltage potential is quite low, 0.3 - 0.4 V above the Li^0/Li^+ redox potential.

However, Silicon capacity fades very quickly because it changes from the amorphous state to the crystalline one, and the nanoparticles aggregate during the reversible lithium insertion, causing a very large volume expansion (440 %) [28].

Metallic tin presents high research interest because of its high theoretical specific capacity (991 mAh g^{-1}) and the consequent possibility of obtaining batteries with elevated power and energy densities [29]. However, tin based electrodes show fast capacity fading upon cycling as well, generally ascribed to the large volume expansion associated to the alloying reaction with Li.

Tin oxide compounds show high theoretical specific capacities of 1491 mAh g^{-1}, due to a double step reaction combining conversion reaction and the following alloying reaction. The electrochemical behaviour of tin oxide will be better explained in chapter 6.

Lithium titanate $Li_4Ti_5O_{12}$ (LTO) is another common anode material used in LIB that was disclosed in the middle 1990s by Ohzuku [30]. LTO has a defective spinel-framework structure and is characterized by a two-phase electrochemical process evolving with a flat voltage profile. Its theoretical specific capacity is 168

mAh g^{-1}, and the average discharge voltage plateau is around 1.56 V. Since its capacity is much lower than that of graphite, the energy density of lithium-ion battery, using LTO as anode, is generally lower than the one of graphite. Moreover, the electronic conductivity of $Li_4Ti_5O_{12}$ is poor, and needs to be improved by doping, coating, or other methods.

However, LTO is a zero-strain material and its crystal structure is very stable during lithiation process (< 4 %), and it doesn't need much solid-electrolyte-interface (SEI) film. Hence, batteries using LTO have demonstrated long cycling life and high reliability.

Another widely studied negative electrode material is Titanium Oxide. TiO_2 has some peculiar characteristics like a high potential for lithium intercalation (about 1.75 V), thus avoiding the lithium dendrite formation; great chemical stability and negligible volume change during lithium intercalation/deintercalation which means good cycling and lifetime. In particular Anatase crystal phase has a theoretical capacity around 330 mAh g^{-1}. In practice, only half of the capacity is usually achievable because there is strong Li–Li intercalation in the TiO_2 crystal, which practically impedes further intercalation of Li when the lithium intercalation coefficient is above 0.5. Like LTO, TiO_2 exhibits good electrochemical performance, even if its electronic conductivity is poor and has to be increased. Tailoring the particle size and combining TiO_2 with materials of high electronic conductivity (graphene), it is possible to increase the specific surface area and decrease the diffusion distance of Li$^+$ ions in the solid phase [31].

In the following table (Table 2.1) are reported and compared the pros and cons of the most commonly studied anode materials for LIB [32].

Table 2.1: comparison of the most common studied anode materials for LIB [32].

Active anode material	Theoretical capacity (mAh g^{-1}) [Reference]	Advantages	Common issues
Insertion/de-insertion materials			
A. Carbonaceous	200-600	➢ Good working potential	❖ Low coulombic efficiency
a. Hard carbons	1116	➢ Low cost	❖ High voltage hysteresis
b. CNTS	780/1116	➢ Good safety	❖ High irreversible capacity
c. Graphene			
B. Titanium oxides	175	➢ Extreme safety	❖ Very low capacity
a. LiTi$_4$O$_5$	330	➢ Good cycle life	❖ Low energy density
b. TiO$_2$		➢ Low cost	
		➢ High power capability	
Alloy/de-alloy materials			
a. Silicon	4212	➢ Higher specific capacities	❖ Large irreversible capacity
b. Germanium	1624	➢ High energy density	❖ Huge capacity fading
c. Tin	993	➢ Good safety	❖ Poor cycling
d. Antimony	660		
e. Tin oxide	790		
f. SiO	1600		
Conversion materials			
a. Metal oxides(Fe$_2$O$_3$, Fe$_3$O$_4$, CoO, Co$_3$O$_4$, Mn$_x$O$_y$, Cu$_2$O/CuO, NiO, Cr$_2$O$_3$, RuO$_2$, MoO$_2$/MoO$_3$ etc.)	500−1200	➢ High capacity ➢ High energy ➢ Low cost ➢ Environmentally compatibility	❖ Low coulumbic efficiency ❖ Unstable SEI formation ❖ Large potential hysteresis ❖ Poor cycle life
b. Metal phoshides/sulfides/nitrides (MXy; M = Fe, Mn, Ni, Cu, Co etc. and X = P, S, N)	500−1800	➢ High specific capacity ➢ Low operation potential and Low polarization than counter oxides	❖ Poor capacity retention ❖ Short cycle life ❖ High cost of production

2.4.2 Cathode active materials

A variety of positive electrode materials has been developed. The positive electrode materials are typically, intercalation-type materials based on transition metal oxides and many of these are commercially available.

Basically, there are three types of cathodes:

1. Layered oxides which have two-dimensional Li ion diffusion channels (such as $LiCoO_2$)
2. Spinels (such as $LiMn_2O_4$) which have three-dimensional Li ion diffusion channels
3. Olivines (such as $LiFePO_4$) which have one-dimensional Li ion diffusion channels

The crystal structures of these three main types of intercalation cathodes are shown in Figure 2.8.

layered $LiCoO_2$ spinel $LiMn_2O_4$ olivine $LiFePO_4$

2D   3D   1D

Dimensionality of the Li^+-ions transport
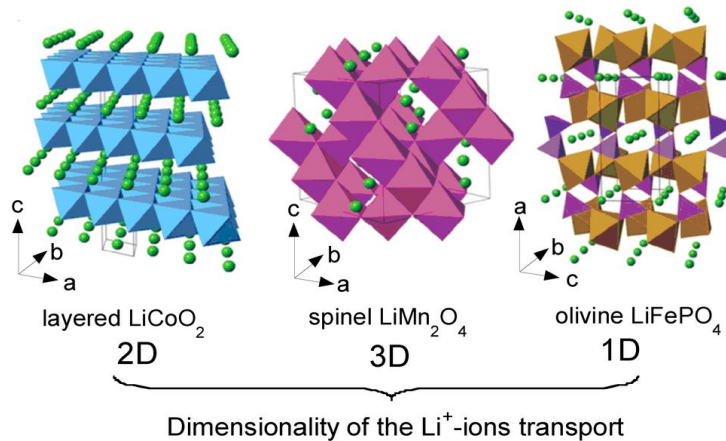
Figure 2.8: Representative crystal structures of three main types of cathode materials for LIB: 2-D (layered), 3-D (spinel) e 1-D (olivine) [24].

The first positive active material adopted in Li-ion batteries was $LiCoO_2$ developed by Goodenough and Mizushima [11][16]. $LiCoO_2$ is a layered oxide type cathode material that presents a practical capacity of 140 mAh g^{-1} and average voltage of 3.9 V vs. Li^0/Li^+.

By a practical point of view only half of the lithium (*i.e.*, $1 > x > 0.5$) stored in Li_xCoO_2 could be extracted because further Li extraction (corresponding to upper

cut-off voltage of 4.2 V) triggers structural transition from a hexagonal to monoclinic phase resulting in quick degradation of the cycle life.

After almost three decades, $LiCoO_2$ is still used in commercial batteries employed in some devices like cell phones, laptops, etc., Unfortunately higher cost and both environmental and safety issues limit its application in the systems where low cost and higher energy are required, such as hybrid (HEV) and pure electric vehicles (EV) [11].

Furthermore, cobalt is less abundant and more expensive if compared to the other transition metals, and also presents political and ethical issues related to its mining in some countries especially in Africa [33] [34]. So cheaper cathodes have been developed that substitute all or some of the cobalt with other metals.

Another layered oxide type cathode material is $LiNiO_2$ which has a lower cost compared to $LiCoO_2$. Unfortunately, synthesis conditions significantly affect $LiNiO_2$ compositional and structural properties impeding the widespread utilization of this material as cathode [35]. Furthermore, $LiNiO_2$ exhibits similar structural transformations as $LiCoO_2$ and at high voltage (4.2 V) its cycle-life quickly decays. In addition, the material becomes catalytic toward electrolyte oxidation and some nickel ions may migrate to lithium anode side. For all these reasons $LiNiO_2$ was never really commercialized for LIBs application [11].

$LiMnO_2$ (LMO) is another popular layered metal oxide. Similarly to $LiNiO_2$ it is a low cost and attractive cathode material if compared to $LiCoO_2$, because manganese is a quite abundant material and in particular because it is environmentally benign [11] [36] [37].

From an electrochemical point of view, $LiMnO_2$ shows a specific charge capacity of 190 - 220 mAh g^{-1} in the voltage range of 2.0 V to 4.25 V, with 99.9 % capacity retention [12].

Unfortunately, once lithium is deintercalated, $LiMnO_2$ suffers from a simple rearrangement of the lattice that leads to $LiMn_2O_4$ transition. This rearrangement is quite significant and a large portion of the active material is transformed into the $LiMn_2O_4$ spinel after few cycles [12]. LMO, is also affected by a relevant capacity fading upon cycling which is due to its intrinsic structural instability causing the dissolution of Mn^{3+} into the electrolyte at elevated temperature [11] [38]. For these reasons, its implementation in commercial Li-ion cell has been strongly reduced.

Another strategy to lower the content of Co is to partially substitute Co with Ni, Mn (or other metal, eventually) developing intercalation compounds based on all three transition metals with the general formula $Li[Ni_{1-x-y}Co_xMn_y]O_2$ [11] [39].

In these types of "mixed" metal oxide cathodes, the transition metal ratio has to be controlled in order to balance aspects like high capacity (more nickel) or better cycle stability (more cobalt) and safety/cost (more manganese).

Such kind of materials have caught a lot of interest in the last years resulting in some of the most commercialized cathode materials.

Two examples are $LiNi_{1/3}Mn_{1/3}Co_{1/3}O_2$ (NMC), and $LiNi_{0.8}Co_{0.15}Al_{0.05}O_2$ (NCA), which derive directly from $LiCoO_2$, where cobalt is simply replaced by other metals like Al, Ni, Mn etc. [13].

$LiNi_{1-y-z}Co_yAl_zO_2$ (NCA) is currently used in some commercial batteries, it has a specific capacity of ~136 mAh g^{-1}, in the potential range 3.2 - 4.2 V.

Li(Ni,Mn,Co)O_2 (NMC) was first synthesized by Liu [40] which observed many advantages in the partially substitution of cobalt with combination of nickel and manganese.

In the last years NMC has been intensively studied attracting great interest thanks to its good reversible capacity, high capacity retention even at elevated temperature, and high reversible capacity [21].

Spinel $LiMn_2O_4$ is easy to synthesize and it is also inherently safe because Mn is a low cost, environmental friendly and an earth abundant element [13].

From the electrochemical point of view, the major problems associated with $LiMn_2O_4$ are related to Mn dissolution especially at high operating or storage temperatures (i.e., 55 °C).

The Mn dissolution is a function of surface area of the oxide and can occurs at both 3 V and 4 V voltage plateaus. Mn acts as a catalyst at high open circuit voltages and oxidizes the non-aqueous electrolyte producing harmful products, and it can also migrate to the anode side and precipitate as Mn metal where it can catalyse some parasitic reactions and damage the structure of the solid electrolyte interface [41].

Recently many efforts have been done to replace the lithium-cobalt oxide used in the first generation of commercial lithium-ion batteries by materials with low cost and environmental concerns. The future challenge is to develop cathodes with twice the energy density at a voltage lower than 4.5 V.

In the last decade the spinel $LiNi_xMn_{2-x}O_4$ (0 < x < 0.5) (LNMO) arose as a promising high-voltage cathode material for high-energy Li-ion batteries. In LNMO the reversible oxidation of Ni^{2+}/Ni^{3+} and Ni^{3+}/Ni^{4+} occurs at 4.70 and 4.75 V vs Li^0/Li^+, leading to a high nominal operating voltage as well as a high theoretical specific capacity (146.7 mAh g^{-1}) [12].

In addition, LNMO is also promising as a competitive material considering the battery costs, since this cathode material is the cheapest among LIBs.

About 1/5 of the LNMO total capacity is provided by the oxidation of Mn^{3+} whereas the other 4/5 is provided by the oxidation of Ni^{2+}. An order-disorder phase transition can occur associated with oxygen loss, where part of the Mn^{4+} ions are reduced to Mn^{3+} to keep the electric neutrality. This affects the electrode performance since Mn^{3+} has a larger ionic radius expanding the lattice, which benefits Li^+ diffusion. However, a disproportionation reaction may occur, where Mn^{3+} forms Mn^{2+} which is dissolved into the electrolyte. These manganese ions migrate and deposit on the graphite anode where they catalyse decomposition reactions of the electrolyte and increase Li^+ retention in the solid electrolyte

interphase (SEI). For this reason, the cell is subjected to a gradual capacity fade and some relevant safety problems [12][42][43].

Phospho-olivine $LiFePO_4$ (LFP) is one of the most commercialized electrode materials because it is plentiful, environmentally benign, low-cost, non-toxic [13][44]. $LiFePO_4$ is highly cost-competitive because Fe is one of the most abundant elements on Earth's crust and it is even less costly than Mn [13]. From the electrochemical point of view $LiFePO_4$ has an average operating voltage of 3.4 V vs. Li^0/Li^+, and a competitive theoretical specific capacity of 170 mAh g^{-1} (corresponding to one Li^+ per $LiFePO_4$ formula unit). The enhanced cycle life and safety of $LiFePO_4$ are strictly associated to its operating voltage that is quite lower than other cathode materials such as $LiCoO_2$ (*i.e.*, 4.2 V) and $LiMn_2O_4$ (*i.e.*, 4 V). The flat voltage profile with a single plateau at ca. 3.4 V vs. Li^0/Li^+ makes LFP more stable in non-aqueous electrolyte solutions. Unfortunately, $LiFePO_4$ has one-dimensional Li-ion diffusion channels leading to poor ionic conductivity, and it has also an intrinsic low electronic conductivity $< 10^{-9}$ S cm^{-1} [12]. Moreover, $LiFePO_4$ density is lower (i.e., 3.6 g cm^{-3}) than the layered oxides and spinels (~5 g cm^{-3}) which means poor volumetric energy density. However, to overcome low electrical conductivity, LFP can be subjected to various carbon coating techniques. Thus, the consequent intimate contact between LFP and a conductive carbon layer leads to an increased electrical conductivity.

Thanks to long cycle life, thermal stability (safety), low cost and environmental impact LFP is nowadays of great interest for cathodes in a wide range of battery applications, such as stationary applications where long cycle life is a key aspect [12] [45].

Vanadium is a valuable transition metal for plenty of scientific and industrial applications, as it is abundant in the Earth crust, cheap, and presents a large variety of oxidation states, ranging from +2 to +5, forming several oxides like VO, VO_2, V_6O_{13} or V_2O_5, [46][47]. In particular, V_2O_5 has been extensively investigated as promising alternative cathode material over the last years for LIBs [30][32].

The layered crystal structure of V_2O_5 allows the reversible intercalation of ions [51]. In particular, the theoretical capacity is 294 mAh g^{-1} with the intercalation/deintercalation of 2 Li^+ per unit formula. Typically, when Li^+ is inserted into the layers of V_2O_5 the material suffers some phase transformations. Thus, the intercalation of lithium ions into the structure of V_2O_5 leads to the formation of different $Li_xV_2O_5$ phases [52]. Hence, the structural behaviour of V_2O_5 during the insertion of lithium in its structure is complex.

Despite several advantages, practical application of V_2O_5 as cathode materials for LIBs has been hampered since bulk V_2O_5 suffers both low electronic (10^{-7} - 10^{-6} S cm^{-1}) and ionic conductivities, poor structure stability and low diffusion coefficient of lithium ions (10^{-12} - 10^{-13} cm^2 s^{-1}), resulting in limited rate capability and long-term cycling stability [53][36][37].

To overcome these problems, nanostructured materials have substantial impact on the performance of cathodes in LIBs, influencing the diffusion distance of lithium ions and the electrode/electrolyte contact area [56]. Thereby, various V_2O_5 nanostructures, such as nanorods [57], nanowires [58], nanotubes [59], nanosheets [60] and three-dimensional nanoflowers [61], have been widely proposed to improve V_2O_5 performance as electrode material.

The following table (Table 2.2) reports and compares the pros and cons of the most commonly studied cathode materials for LIB [7].

Table 2.2: comparison of main cathode electrode materials in relation to their main characteristics: crystal structure, theoretical/experimental/commercial gravimetric and volumetric capacities, average potentials, and level of development [7].

Crystal structure	Compound	Specific capacity (mAh g^{-1}) (theoretical/experimental/typical in commercial cells)	Volumetric capacity (mAh cm^{-3}) (theoretical/ typical in commercial cells)	Average voltage (V)	Level of development
Layered	$LiTiS_2$	225/210	697	1.9	Commercialized
	$LiCoO_2$	274/148	1363/550	3.8	Commercialized
	$LiNiO_2$	275/150	1280	3.8	Research
	$LiMnO_2$	285/140	1148	3.3	Research
	$LiNi_{0.33}Mn_{0.33}Co_{0.33}O_2$	280/160	1333/600	3.7	Commercialized
	$LiNi_{0.8}Co_{0.15}Al_{0.05}O_2$	279/199	1284/700	3.7	Commercialized
	Li_2MnO_3	458/180	1708	3.8	Research
Spinel	$LiMn_2O_4$	148/120	596	4.1	Commercialized
	$LiCo_2O_4$	142/84	704	4.0	Research
Olivine	$LiFePO_4$	170/165	589	3.4	Commercialized
	$LiMnPO_4$	171/168	567	3.8	Research
	$LiCoPO_4$	167/125	510	4.2	Research
Tavorite	$LiFeSO_4F$	151/120	487	3.7	Research
	$LiVPO_4F$	156/129	484	4.2	Research

Another recent approach to overcome the operational limits of some cathode materials is blending together two different active materials. The active material in a 'blended' cathode is made of a physical mixture of two or more distinct lithium intercalation compounds.

The reason for mixing two (or more) active materials is to achieve a more balanced performance of the electrode compared to what is possible with any individual compound.

The blending strategy enables the cathode materials to complement each other, so what is generally a weakness of one material alone is strengthened in the blend.

In a blended cathode, each material may be influenced by the other and the electrochemical characteristics of both cathode materials influence the charge/discharge profile of the blended system. In fact, one of the major outcomes of a blended cathode system is the modification of the voltage profile in comparison to that of parent cathode materials.

More generally blended cathode systems can offer advantages over using a single cathode material, including reduced capacity loss, longer cycle life, reduced cost and improved thermal stability [62].

2.4.3 Non active materials

As mentioned in paragraph 2.3, LIB cell is also composed by materials not directly involved in Li ions intercalation. These materials are called inactive materials and they are: current collector, separator, electrolyte, binder and carbon additive.

The inactive components do not contribute to the cell capacity therefore it is critical to minimize their content; however, they play a remarkable role in the operation and safety of a battery.

One of the most important inactive components inside the electrode is the binder. The binder plays a decisive role in the electrode performance, despite its rather low content (up to 5 wt.%, but usually 2 wt.%) with respect to the total electrode composition. In fact, it serves as a polymeric matrix able to connect active materials to each other and to the current collector, also accommodating volume changes inside the electrodes during lithiation/de-lithiation process [13].

An ideal binder have to fulfil some criteria [63]:

- o   guarantee cohesion and adhesion between the active material particles, additives and the current collector;
- o   help electrode processing;
- o   avoid solubility in the electrolyte and electrolyte swelling;
- o   possess high chemical, thermal, and electrochemical stability, while not detrimentally affecting the electron and ion transport in the electrode composite;
- o   provide low additional cost, ideally being also environmentally friendly.

Since the first development of the LIB, poly(vinylidene difluoride) (PVdF) and copolymers of the vinylidene difluoride (VdF) and hexafluoro-propene (HFP) monomers, so-called PVdF-HFP have been employed as electrode binder, thanks to their good electrochemical stability, binding capability and ability to absorb electrolyte [63] [64].

Unfortunately, PVdF is strictly connected to the environmentally unfriendly N-methyl Pyrrolidone (NMP) used as solvent in the process of electrodes preparation [65]. NMP is a heterocyclic compound, liquid at room temperature with a boiling point around 200 °C, which is part of the so-called volatile organic compounds (VOC), and is classified, by the European Union, as teratogen, toxic and irritant to eyes, respiratory system, and skin [63].

Moreover PVdF is also affected by some other drawbacks, for example it is very sensitive to the environmental humidity and, as many fluorinated polymer, at

elevated temperatures it also shows a certain reactivity against lithium metal or lithiated graphite (Li_xC_6), producing some low conductive species (as LiF and -C=CF–) on the electrode surface, which may trigger the onset of thermal runaway [63].

Alternatively, to the PVdF/NMP couple, some water-soluble binders have been investigated. Aqueous binders present some indisputable advantages: eco-compatibility, lower cost, do not require strict control of the drying process during electrode fabrication [66][67].

In this frame biopolymers and their derivatives would represent one of the more sustainable choice. Polysaccharides, for example, are naturally occurring polymers that can be extracted from a variety of natural sources. These generally present the same glucose monomer as building block, with different glycosidic bonds and substituents on the pyranose ring which define the peculiar properties of each polymer (e.g., cellulose, alginate, starch, etc.) [68].

Sodium Carboxymethyl Cellulose (Na-CMC) is the most famous bio-derived compound used in the current state-of-the-art production of LIB negative electrodes in combination to styrene-butadiene rubber (SBR) [69][70]. The price of Na-CMC is lower compared to PVdF (about 1-2 euro/kg) and it has the advantage to ease the recycling of LIBs electrode [71].

Beyond the CMC/SBR couple [69][70][71][72] a lot of water soluble binders have been studied and used in LIBs: Li-CMC [73], Gelatin [74][75], Sodium Alginate, Xanthan Gum, Chitosan and derivate, Agar-Agar, Carrageenan, Guar Gam [68] [76][77] and many other polymer as polyacrylonitrile (PAN), polyacrylic acid (PAA), polymethyl acrylate (PMA), polyvinyl alcohol (PVA), methyl acrylate copolymer latex (AMAC), acrylonitile methyl metacrylate (AMMA), Polyimide [78][79][80][81][82][83]. All of them have been reported as promising new binder system for Li-ion battery replacing PVdF. Table 2.3 reports different properties comparison for the most common binders adopted in lithium-ion battery.

Table 2.3: comparison of different properties for most common binder used in Li-ion battery [63].

Name of Binder (incl. the corresponding derivatives)	F-free	Processability	Synthesis	Sustainability	Ease of disposal	"Green score"
State of the art						
CMC	+	+	+	+	+	+5
PTFE	−	+	−	−	−	−3
PVdF	−	−	−	−	−	−5
Alternatives						
Agar-agar	+	+	+	+	+	+5
Alginate	+	+	+	+	+	+5
Amylose	+	+	+	+	+	+5
Arabic gum	+	+	+	+	+	+5
Carrageenan	+	+	+	+	+	+5
Caseine	+	+	+	+	+	+5
Chitosan	+	+	+	+	+	+5
Cyclodextrines (carbonyl-beta)	+	+	+	+	+	+5
Ethylene propylene diene monomer (EPDM) rubber	+	+	0	−	0	+1
Gelatine	+	+	+	+	+	+5
Gellan gum	+	+	+	+	+	+5
Guar gum	+	+	+	+	+	+5
Karaya gum	+	+	+	+	+	+5
Cellulose (natural)	+	+	+	+	0	+4
Pectine	+	+	+	+	+	+5
PEDOT-PSS	+	+	+	−	+	+4
Polyacrilic acid (PAA)	+	+	0	−	0	+1
Poly(methyl acrylate) (PMA)	+	+	+	−	0	+2
Poly(vinyl alcohol) (PVA)	+	+	0	−	0	+1
Poly(vinyl acetate) (PVAc)	+	+	+	−	0	+2
Polyacrylonitrile (PAN)	+	+	+	−	0	+2
Polyisoprene (PIpr)	+	+	0	+	0	+3
Polyaniline (PANi)	+	+	+	−	0	+2
Polyethylene (PE)	+	+	0	−	0	+1
Polyimide (PI)	+	+	0	−	0	+1
Polystyrene (PS)	+	+	0	−	0	+1
Polyurethane (PU)	+	+	0	−	+	+2
Polyvinyl butyral (PVB)	+	+	0	−	0	+1
Polyvinyl pyrrolidone (PVP)	+	+	+	−	+	+3
Starch	+	+	+	+	+	+5
Styrene butadiene rubber (SBR)[b]	+	+	0	−	0	+1
Tara gum	+	+	+	+	+	+5
Tragacanth gum	+	+	+	+	+	+5
TRD202A	−	+	n.a.	n.a.	−	n.a.
Xanthan gum	+	+	+	+	+	+5

Another vital part of any given battery technology is the electrolyte solutions. Generally, the electrolyte solutions for LIBs are complicated systems consisting of a solvent mixture, salt and any number of additives.

The electrolyte solutions actually used in LIBs consist of ethylene carbonate (EC) and linear carbonates (e.g. ethyl methyl carbonate (EMC), dimethyl carbonate (DMC)) as solvents in combination with $LiPF_6$ as a lithium salt.

These solutions provide a reasonably wide electrochemical window for 4 - 5 V Li batteries, thanks to complicated passivation phenomena of SEI layer formation.

The electrolyte solution needs a number of attributes to be useful for LIBs application [12]:

o   wide operating temperature range (low meting point, high boiling point);

- low viscosity of the solvent mixture that promotes good ionic conductivity;
- good solubility and dissociation of the used lithium salt in the solvent mixture (high relative permittivity) that promotes ionic conductivity;
- large electrochemical window to operate with low voltage anodes and high voltage cathodes.
- possibly non-toxicity, environmental benignity, low cost.

Taking into account all these optimal properties, only polar-aprotic solvents, able to dissolve an adequate amount of lithium salt thus forming solutions with high ionic conductivity are relevant. Therefore, the spectrum of useful solvents is limited to esters, ethers, alkyl carbonates, nitriles and sulfones. Fluorinated solvents may also be used as flame retardants in LIB but mostly as co-solvents due to their higher viscosity [12][84].

Generally, the common practical approach for an electrolyte solution consists in using a combination of two solvents: one with low viscosity combined with one with high viscosity and high dielectric constant.

$LiPF_6$ is the most used salt in LIBs due to its high solubility and ionic conductivity, and also thanks to the stable SEI layer formation in combination with EC [18]. However, $LiPF_6$ can decompose and form HF when traces of water are present. HF dissolves transition metal cations which can migrate to the anode side, reacting with graphite and damaging the anode passivation, and consequently, lowering the safety, stability and capacity of the electrode.

LiBOB (Li-bioxalato-borate) is also widely used as LIB salt. The electrochemical stability window is over 4.5 V, which makes LiBOB a potential candidate for high voltage spinel cathodes [12][85].

LiBOB demonstrates also high temperature and cycling stability, giving no reaction with water. On the other side the solubility of LiBOB is lower than that of $LiPF_6$ leading to a lower ionic conductivity [12][86].

LiTFSI (Bis(trifluoromethane) sulfonamide; $LiN(SO_2CF_3)_2$) is quite popular candidate to replace $LiPF_6$. LiTFSI shows a reasonable ionic conductivity, good thermal stability and is not prone to HF formation [12][87][88]. The biggest drawback is the Al corrosion, especially when the battery is in full state of charge [12][89].

The electrolyte is quite important in a LIB cells where the magnitude of the open-circuit potential is constrained to OCV < 5 V not only by the attainable difference of the electrochemical potentials of the anode reductant and the cathode oxidant, but especially by the energy gap E_g between the HOMO (highest occupied molecular orbital) and the LUMO (lowest unoccupied molecular orbital) of the liquid electrolyte.

As illustrated in Figure 2.9, the chemical potential μ_a, which is the Fermi energy ε_F of a metallic reductant anode, must lie below the LUMO of a liquid electrolyte to achieve thermodynamic stability against reduction of the electrolyte by the reductant.

Similarly, the chemical potential μ_c, which is the LUMO of the Fermi energy of a metallic oxidant cathode, must lie above the HOMO of a liquid electrolyte to achieve thermodynamic stability against oxidation of the electrolyte by the oxidant.

$$V_{OC} = (\mu_A - \mu_C)/(-nF) \qquad\qquad [2.14]$$

Moreover, "window" E_g of the electrolyte has to match the energies μ_a and μ_c of the reactants in order to maximize the OCV [90].

Operatively, the electrolyte is chosen to match the cathode potential and to provide kinetic stability at the anode-electrolyte interface. The traditional carbonate-based electrolytes undergo reduction processes at ca. 1 V vs. Li^+/Li^0 with the formation of the solid electrolyte interphase. The so formed SEI layer while limiting further reduction of the electrolyte, also affects other important battery parameters such as the capacity fade and power density. Anyway the formation of a spontaneous SEI causes a noticeable reduction in battery capacity, which is detrimental for the system, for this reason the application of a bifunctional electrolyte is generally adopted [91][92].
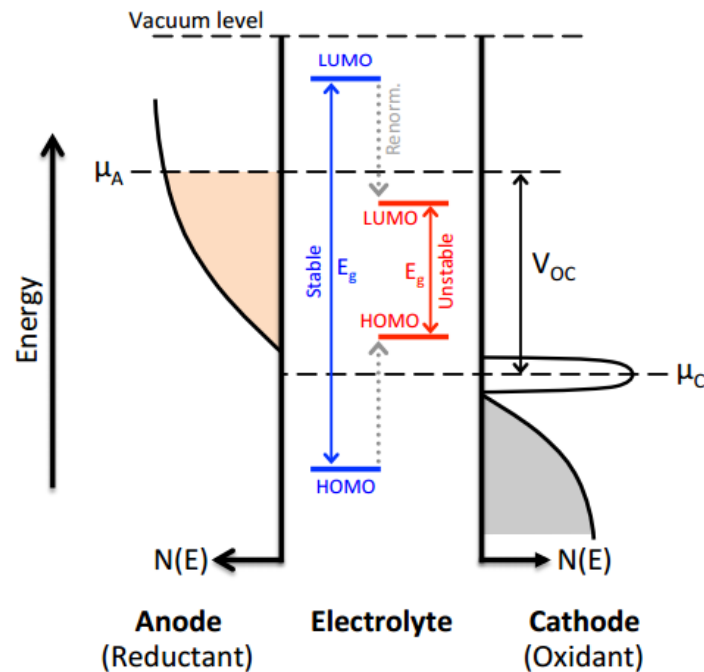
Figure 2.9: position of electrolyte HOMO/LUMO levels respect to the density of states of a battery anode and cathode [93].

The separator is another inactive component in Li-ion batteries, which plays a critical role in the operation and safety of batteries. The separator physically separates the anode and cathode to prevent the electrical short circuit, allowing Li-ion diffusion thanks to its porous structure during cycling of a cell.

An ideal separator should be a good electronic insulator, mechanically robust, chemically inert under the operating conditions of the battery, and should have good wettability in non-aqueous liquid electrolytes [13][94]. The most common types of Li-ion battery separators are microporous separators which are mainly made of polyolefins such as polyethylene (PE) and polypropylene (PP). The multilayer structure (PP/PE/PP) separators are used to prevent the thermal runaway of the Li-ion battery via thermal shut-down mechanism [13][95]. Table 2.4 reports the most important requirements for separators for Li-ion application [96].

Table 2.4: general requirements for separators used in lithium-ion batteries [96].

Parameter	Requirement
Chemical and electrochemical stabilities	Stable for a long period of time
Wettability	Wet out quickly and completely
Mechanical property	>1000 kg cm^{-1} (98.06 MPa)
Thickness	20–25 μm
Pore size	<1 μm
Porosity	40–60%
Permeability (Gurley)	<0.025 s μm^{-1}
Dimensional stability	No curl up and lay flat
Thermal stability	<5% shrinkage after 60 min at 90 °C
Shutdown	Effectively shut down the battery at elevated temperatures

Chapter 3

3 Rechargeable lithium-sulphur battery (Li-S)

As widely mentioned in the previous chapters, Li-ion batteries are now beginning to enter deeply into electric vehicles market and grid storage applications.

Unfortunately, the current Li-ion technology is reaching the intrinsic limits in terms of energy density and specific capacity which are strongly referred to the insertion-compound chemistry [97]. Therefore, alternative anode and cathode materials which can offer higher capacities and energy densities need to be developed and implemented.

Beyond Li-ion battery, one of the most promising next-generation energy storage system is lithium-sulphur (Li-S). Li-S technology is expected to offer 2-3 times higher (about 2600 Wh kg^{-1}) energy density than actual Li-ion batteries. Moreover, Sulphur is one of the most abundant elements on earth and could be recovered in desulphurization processes by oil and gas industries, so it is also useful to reduce the overall battery price and the environmental impact. Figure 3.1 shows the graphic comparison of gravimetric and volumetric energy density of various electrochemical energy storage systems [98].
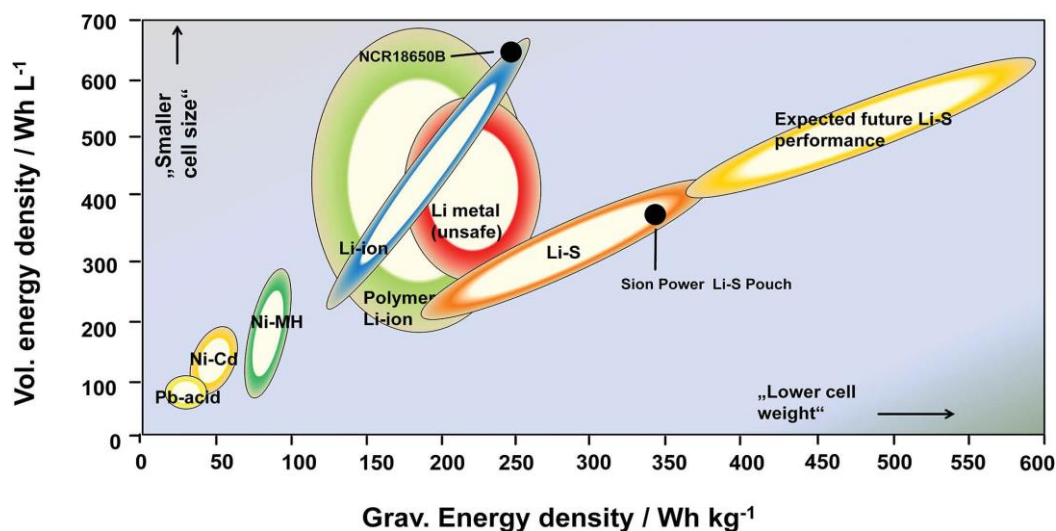
Figure 3.1: energy density of various electrochemical storage systems and expected future Li-S performance [98].

However, some limitations of this system hinder its complete technological transfer to commercial market. Significant progresses were made during past years, however, there are still many challenges to overcome, so that this technology can deeply enter into the market.

The next paragraph presents the basic operation and the limitation of the Li-S batteries.

3.1 Lithium-sulphur battery: principle of operation

The lithium-sulphur system was first studied in the 1960s by Herbert and Ulam [99], but over the next forty years, this technology was only used as primary battery due to its complicated chemistry [100]. In recent decades lithium-sulphur technology has returned to arouse great interest because it guarantees high gravimetric and volumetric energy densities.

In particular, sulphur offers many advantages as electrode active material, if compared to other LIBs cathode materials. From a commercial perspective, sulphur is earthly abundant, geographically well-distributed, non-toxic and its cost production is only 0.5 % of the conventional cathode material (roughly $150 - 200 per ton) [101][102]. As possible to see in Table 3.1, Li-S battery price per kilowatt-hour is less than one-fourth of Li-ion battery price at cell level. This makes lithium-sulphur technology a cost-effective candidate for future energy storage [102].

Table 3.1 Cost comparison between Li-ion and Li–S batteries [102].

	Unit	Li-ion		Li–S	
Cathode	$ kg^{-1}	LiCoO$_2$	40	S	0.2
Binder	$ kg^{-1}	PVDF	10	PVDF	10
Anode	$ kg^{-1}	Graphite	12	Li	50
Separator	$ m^{-2}	PP/PE/PP	2	PP/PE/PP	2
Electrolyte	$ L^{-1}	LiPF$_6$/EC:EMC	18	LiTFSI/DME:DOL	50[a]
Current Collector	$ m^{-2}	Al	0.8	Al	0.8
		Cu	1.8	–	–
Cell cost	$ (kW h)$^{-1}$		600		<150

[a] Estimated based on the prices of components.

The Li-S battery configuration is quite similar to traditional lithium-ion battery because it consists of a sulphur cathode and a lithium metal anode immersed in an electrolyte solution. However, the electrochemistry associated to Li-S systems, is completely different from the insertion/intercalation process which are commonly involved in Li-ion batteries [103].

Li-S system is based on the electrochemical reaction of sulphur (α-S$_8$) with lithium to form lithium sulphide (Li$_2$S). The open circuit voltage (OCV) of a Li-S cell directly depends on the electrochemical potentials of lithium anode (E° = - 3.040 V) and sulphur cathode (E° = - 0.445 V) and is normally around 2.4 - 2.5V.

In contrast to Li-ion cells, the operation of Li-S batteries starts with discharge, because sulphur is in the oxidized state. Therefore, during discharge, lithium metal is oxidized at the negative electrode to produce lithium ions and electrons. The lithium ions stripped from the anode migrate, through the electrolyte, to the cathode side, while electrons flow at the same way through an external circuit. Consequently, the octoatomic elemental sulphur (α-S$_8$) is reduced to form lithium polysulfides (LiPSs) with different chain length (Li$_2$S$_x$, x = 8 $\leq$ n $\leq$ 2) which gradually convert to lithium sulphide (Li$_2$S), the end-discharge product. During charge, the lithium ions migrate back to the negative electrode where they react with electrons to reform lithium metal, while the Li$_2$S converts reversibly toward pure sulphur [104].

The overall redox reaction is:

$$S_8 + 16Li \rightarrow 8Li_2S \qquad\qquad\qquad [3.1]$$

In the complete redox reaction is possible to observe that each atom of sulphur can accept 2 electrons, this is the reason behind the very high theoretical specific capacity (1675 mAh g^{-1}) of this system. The gravimetric capacity of sulphur is higher than any other solid cathode material, this explains why the low potential of 2.15 V vs Li^0/Li$^+$ is not detrimental for the practical applications of this system [103][105].

As mentioned before, the reaction between sulphur and lithium is quite different to the typical solid-state intercalation process of the lithium-ion battery. In particular, the reduction of solid sulphur involves the formation of numerous soluble intermediates species Li$_2$S$_x$ (8 $\leq$ x $\leq$ 2), so called lithium polysulfides. By

virtue of that, to better understand the lithium-sulphur reaction, it's preferable to split the overall discharge reaction in a multi-step process [106]. The three main steps are reported below:

Step I: solid-state sulphur (α-S_8) is opened to form long chain LiPSs (Li_2S_x, $4 < x < 8$), which are dissolved into the liquid electrolyte. The three main products as shown in Equations below (3.2 - 3.4):

$$S_8 + 2Li^+ + 2e^- \rightarrow Li_2S_8 \qquad \text{(2.39 V vs Li}^0\text{/Li}^+\text{)} \qquad [3.2]$$

$$3Li_2S_8 + 2Li^+ + 2e^- \rightarrow 4Li_2S_6 \qquad \text{(2.37 V vs Li}^0\text{/Li}^+\text{)} \qquad [3.3]$$

$$2Li_2S_6 + 2Li^+ + 2e^- \rightarrow 3Li_2S_4 \qquad \text{(2.24 V vs Li}^0\text{/Li}^+\text{)} \qquad [3.4]$$
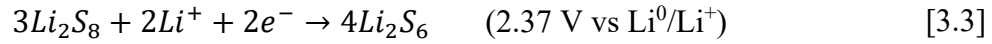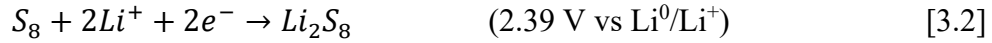
During this step disproportionation reactions and chain growth occur, resulting in the simultaneous coexistence of multiple species [103]. Anyway, Li_2S_6 and Li_2S_4 are generally reported as the most probable stable polysulfides in the electrolyte solution [106].

This reaction contribution is about 25 % of the total sulphur capacity and correspond to the upper voltage plateau ($\approx$ 2.4 V vs Li^0/Li$^+$).

Step II: the soluble species Li_2S_4 are reduced to insoluble Li_2S_2, as shown in Equations 3.5:

$$Li_2S_4 + 2Li^+ + 2e^- \rightarrow 2Li_2S_2 \qquad \text{(2.22 V vs Li}^0\text{/Li}^+\text{)} \qquad [3.5]$$

This way the high order LiPSs are reduced to short chain LiPSs (Li_2S_x, $1 < x < 4$). This stage contributes to the major portion of the capacity (around 75 %) and correspond to the lower voltage plateau ($\approx$ 2.1 V vs Li^0/Li$^+$).

Step III: Li_2S_2 are reduced to final product Li_2S by solid-to-solid reaction, as shown in Equation 3.6:

$$Li_2S_2 + 2Li^+ + 2e^- \rightarrow 2Li_2S \qquad \text{(2.15 V vs Li}^0\text{/Li}^+\text{)} \qquad [3.6]$$
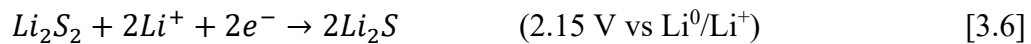
It's worth noting that this is a very simplified description of the complicated and not well-understood electrochemical mechanism of Li-S and most of the common steps of reaction involved in the mechanism are based on mathematical modelling [107][108]. Moreover, each individual step does not produce any specific product but rather multiple reduction species [106].

A characteristic cycling profile of the Li-S cell is shown in Figure 3.2 [109].
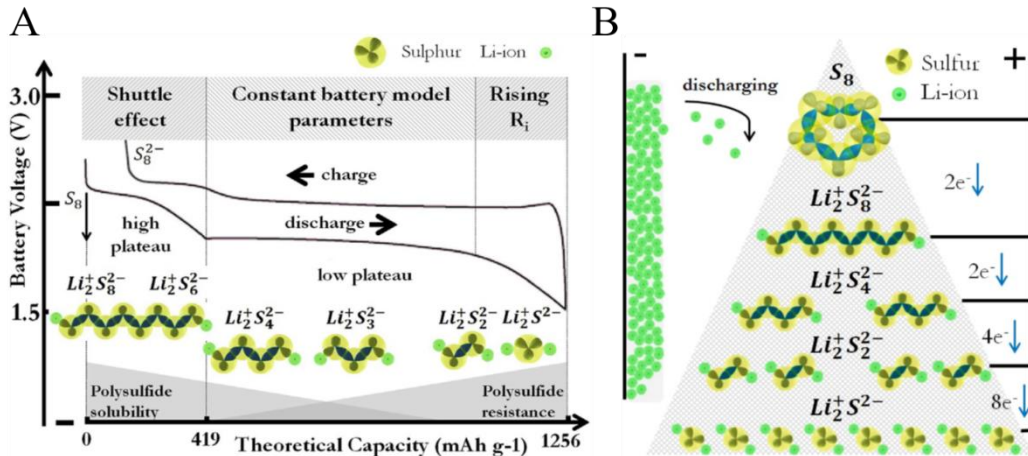
Figure 3.2: typical cycling profile of the Li-S cell [109] .

In the discharge curve is possible to individuate two distinct voltage plateaus, one around 2.4 V and the second around 2.1 V. These two plateaus are related to the: first reduction reaction of S_8 to soluble polysulfides and to the second reduction reaction of high order polysulfides to insoluble Li_2S, respectively. The two plateaus are delimited by a so-called "supersaturation point", which corresponds to a supersaturated solution of S^{2-}, before its precipitation.

During the first step of reaction the voltage constantly decreases while the electrolyte viscosity rises, and this is mainly affected by the increasing of long chain polysulfides concentration. After this step the concentration of Li_2S_4 (or S_4^{2-}) gradually decreases due to the slow kinetic reactions. The voltage stays between 2.1 and 2 V for a long time (second plateau), until the cathode is largely covered by the nonconductive Li_2S. At the end, Li_2S greatly increases the cell resistance, blocking charge transfer and the voltage quickly drops, ending the reaction.

In the reverse reaction, the charge curve shows an over-potential and then a long slopping curve. The presence of this over-potential (or energy barrier) is attributable to the oxidation of insoluble Li_2S. In fact, insulating Li_2S needs to be activated by a large activation energy to convert back to the liquid phase (LiPSs). After the activation step two quasi-plateaus can be observed, representing the oxidation of insoluble short-chain polysulfides to soluble long-chain polysulfide species (Li_2S_x, $4 < x < 8$), and the oxidation reactions from the soluble long-chain polysulfide species to elemental sulphur [110].

The species formed in the different steps have different physical properties. Typically, S_8 and Li_2S are solid and insoluble in common electrolytes, while the intermediate polysulphides species are soluble in organic solvents. This complexity of the Li-S is the basis of some important drawbacks of this system.

3.2 Challenges to Li-S battery system

Regardless of the mentioned advantages, the widescale commercial use of lithium-sulphur technology is still limited by some key challenges that have to be addressed [103].

Three are the main obstacles making Li-S far from industrial requirements to this day:

- o the insulating nature of sulphur and final product Li_2S;
- o huge volume fluctuation;
- o shuttle effect of polysulfides.

Elemental sulphur has a very low electronic conductivity (5×10^{-30} S cm^{-1} at 25 °C.) [106]. The insulator nature of sulphur and final discharge product (Li_2S) leads to a large polarization and a slow kinetic process, limiting sulphur utilization as pure active materials.

For this reason, sulphur needs to be intimately mixed with a conductive additive such as carbon. Unfortunately, the "dilution" of sulphur and the large amount of conductive additives introduced into the cathode, deeply affect the mass loading of the electrode and consequently reduce the energy density of the system [104].

The second problem of Li-S is related to the huge volume expansion occurring during the solid-liquid-solid transition process. The end product Li_2S exhibits lower density (1.66 g cm^{-3}) than elemental sulphur (2.06 g cm^{-3}). It means that the conversion of S_8 to LiPSs, during lithiation, results in a volumetric expansion up to 80 % of the initial volume of the positive electrode.

This expansion involves severe mechanical stress with structural and morphological changes of the cathode, leading to a deep capacity fade of the cell. On the other hand, the nonconductive agglomeration of Li_2S_2 and Li_2S forms insulating layers on the electrode, which results in voltage drop and poor long-term cycling performances [106][111][104].

The most problematic issue of Li-S system is related to polysulfide dissolution. The polysulfide dissolution is beneficial to full active-material utilization, because thanks to continuous PSs dissolution into the electrolyte, bulk sulphur can be exposed to the electrolyte solution and participate to the reaction [102].

Unfortunately, the dissolved polysulfide can diffuse out from the cathode and migrate toward the anode side, driven by chemical potential and concentration gradient between the two electrodes [106].

In particular, when long chain polysulfides diffuse to the anode side, they directly react with metallic lithium creating nonconductive and insoluble Li_2S precipitated on its surface. This process is known as "polysulfide shuttle effect" which results in anode corrosion and consequent irreversible loss of active material, low capacity retention and low coulombic efficiency.

Moreover, during cell resting, sulphur reacts directly with the lithium ions dissolved into the electrolyte producing soluble lithium polysulfides with consequent self-discharge of the cell [104][106][111].

For all these reasons polysulfide shuttle effect is actually considered the most fatal challenge affecting Li-S. In Figure 3.3 the degradation mechanism of Li-S is graphically illustrated.
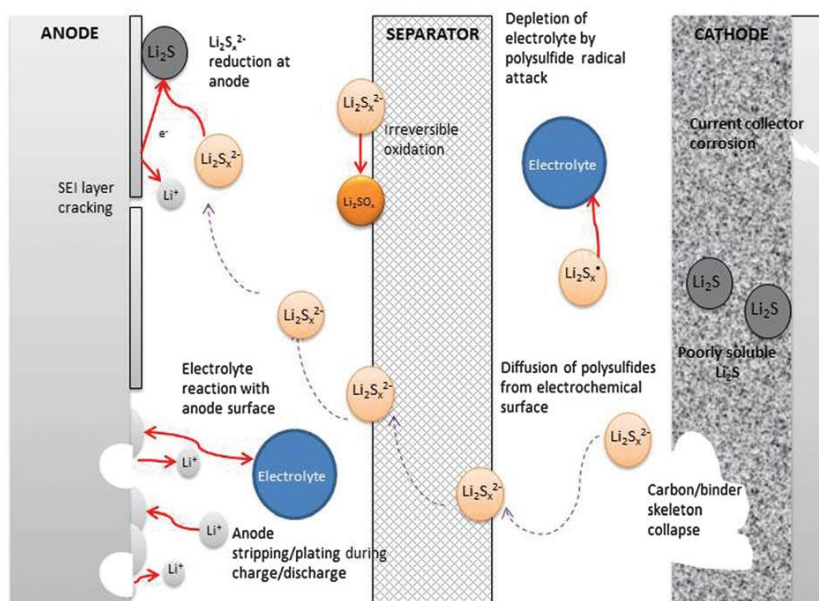
Figure 3.3: degradation mechanisms of Li-S [108].

Other important challenges are also associated to the most commonly used anode in Li-S batteries: metallic lithium [104].

On one side, pure lithium is a lightweight material (0.59 g cm^{-3}) with a very low standard reduction potential, 3.04 V (vs SHE), and high theoretical capacity of 3860 mAh g^{-1}, which offers a high energy density to Li-S system [112].

But on the other side, the reaction involving pure lithium is a plating and stripping reaction, which has some intrinsic problems. The most relevant one is the growth of Li dendrites which can penetrate the separator causing the short-circuit of the cell with consequent safety hazard. The second relevant problem ascribed to pure Lithium anode is the instability of SEI layer, which induces a continuous electrolyte depletion and consequent capacity loss [112].

Therefore, anode engineering is an important pathway toward overcoming side reactions and related problems. The most important strategy is protecting Li anode with solid membranes. A second solution is the repletion of metallic lithium with less reactive pre-lithiated anode materials such as silicon, alloys or

carbon group metals. Unfortunately, most of these alternatives result in lower power and energy density of Li-S cell [102].

3.3 Strategies to overcome Li-S challenges

In the last years different approaches and methods have been adopted to solve the issues and drawbacks which affect Li-S, with the purpose of realizing industrial production and the commercial diffusion of this technology [111].

3.3.1 Cathode engineering

Most of the work was done on design and development of a suitable cathode nanocomposite.

Many composites with conductive substances such as carbon and conducting polymer were proposed.

As mentioned in the previous chapter carbon additives can increase the electrical conductivity and can also provide structural integrity to accommodate the volumetric expansion occurring during lithiation. The strategy to confine the sulphur into a porous-controlled carbon host structure was first proposed by Nazar group [113]. In particular, it was observed that a proper porosity sensibly affects the sulphur loading, and is helpful for physically-adsorbing active materials, mitigating the undesired shuttle effect. Mesoporous carbon (2 - 50 nm) was individuated as optimal framework to hinder soluble polysulfides diffusion outside the anode guaranteeing, at the same time, high sulphur loadings and enough space for Li^+ migration [104]. On the contrary, micropores (< 2nm) provide high surface areas and close contact but guarantee low sulphur loadings, while macropores (> 50 nm) allow high loadings, but reduced contact areas.

Sulphur cathodes has been realized with zero dimensional solid or hollow carbon spheres, one dimensional (1D) carbon nanotubes (CNT) and nanofiber, two-dimensional (2D) graphene or three-dimensional (3D) carbon aerogels and sponge structures.

Many studies were also done considering different approaches of sulphur impregnation inside the carbon host [111].

The main synthesis approaches to produce S/C nanocomposite can be classified into four groups:

       o   Melt or vapour phase infiltration: sulphur is heated to its melting or boiling point temperature and then filled into carbon. This is possible

because melt sulphur has low viscosity, which facilitates filling of the carbon pores by capillary deposition.

o Solution infiltration: sulphur is solubilized into a few substances, such as carbon disulphide CS_2, and then filled into carbon. Subsequent to the solution-based infiltration, the solvent is removed, usually by evaporation

o Chemical reaction deposition: sulphur is deposited by chemical reaction, starting from different precursors such as Na_2S.

o Mechanical intrusion: sulphur and carbon are intimately mixed by a mechanical procedure (ball-milling). These mechanical treatments also reduce the particle size of sulphur, increasing the surface area of sulphur particles and their contact area with carbon. However, ball-milling method usually originate sulphur cluster and weak contact with hosts.

Figure 3.4 graphically summarizes the most common used of S/C production strategies.
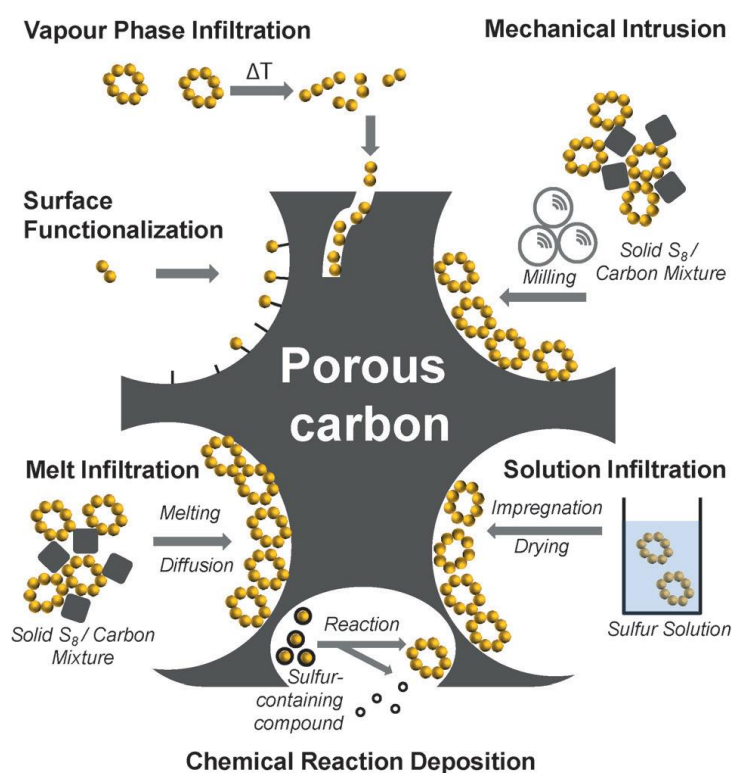
Figure 3.4: different approaches for introducing sulphur into carbon [104].

As a result, a large amount of conductive active material has to be added to sulphur into the cathode, with consequent depletion of gravimetric capacity. It was observed that by all these methods the sulphur loadings in S/C composites is generally in the range of 50 % to 80 %, which correspond to from 600 to 1000 mAh g^{-1} in terms of gravimetric capacity.

3.3.2 Electrolyte formulation

The second important strategy used to improve the Li-S performance, was implemented directly on electrolyte formulation.

Initially, traditional liquid electrolytes used for LiBs were used also in Li-S batteries. Unfortunately, most of these electrolytes possess high polysulfide solubility, with consequent polysulfide shuttle. This leaded to avoid traditional electrolyte solution (such as esters, carbonates, and phosphates) in lithium sulphur battery. Besides, most of conventional lithium salts (LiPF$_6$, LiBOB, LiBF$_6$, *etc*.) shown a strong reactivity with lithium polysulfides [114].

Many studies individuated lithium bistrifluoromethanesulfone imide (LiTFSI) in a 1,3-dioxolane (DOL)/dimethyoxyethane (DME) solvent mixture as more suitable liquid electrolyte [115]. Unfortunately, this electrolyte formulation presents a low boiling point, making it too volatile for a real commercial use [116]. Alternative solvents commonly used in electrolyte formulation for Li-S are: tetraethylene glycol dimethyl ether (TEGDME), polyethylene glycol dimethyl ether (PEGDME), tetrahydrofuran (THF) and ionic liquids [111].

Some additive like LiNO$_3$ were deeply studied and are now added to electrolyte solution with the aim to create a passivating film on metallic lithium, protecting it from the effects of the polysulfide shuttle. Typically LiNO$_3$ oxidizes the Li$_x$S moieties in solution forming an effective and protective solid-electrolyte interphase (SEI) on lithium anode [101].

However, LiNO$_3$ gets reduced on the positive electrode at a potential below 1.8 vs. Li^0/Li$^+$, giving rise to irreversible capacity loss during cycling.

It is worth noting that, in Li-S, the electrolyte amount is a critical factor. Electrolyte excess increases the cost but also the weight, lowering the energy density of the cell. At the same time a small quantity of electrolyte causes high PSs concentration, amplifying their negative influence on the cell performance [102].

Therefore, liquid electrolytes suffer from high PSs solubility, high flammability, and high volatility, leading to short cycle life, poor safety, and marked self-discharge.

Solid state electrolytes (SSEs), both inorganic or polymer compounds, can prevent the dissolution of polysulfide and, at the same time, protect lithium anode from detrimental effects. Moreover, solid electrolyte can also accomplish the role

of separator. The SSEs can be divided into four types: gel electrolyte, SPE, ceramic electrolyte, and composite electrolyte.

SPE referred to a polymer matrix (like PAN, PMMA, PEO, PVdF) swollen with lithium salts. SPE are light and possess good electrochemical stability, interfacial compatibility with electrode, and high transference number. While their main disadvantage is the low ionic conductivity at room temperature (10^{-7} S cm^{-1}). To enable the use of SPE also at room temperature plasticizer agents have to be added into polymer skeleton to obtain gel electrolyte (GPEs) with higher ionic conductivity.

Ceramic electrolytes (like NASICON) are totally inorganic and possess excellent thermal stability, low flammability, and wide electrochemical window, but low ionic conductivity.

Composite electrolyte contains inorganic and organic portions, combining the advantages of each component such as high ion conductivity, good mechanical strength and good interfacial contact. Therefore, the presence of both inorganic and organic species can deeply alleviate the dendrite formation and shuttle effect of sulphur but also improve the ionic conductivity at room temperature. In Table 3.2 are reported the advantages and disadvantages of different types of electrolyte.

Table 3.2: comparison of advantages and disadvantages of different electrolytes.

Classification	Advantages	Disadvantages
Liquid	High ionic conductivity	Poor thermal stability
	Low interfacial impedance	Severe LiPSs shuttling
		Severe Li dendrite growth
Gel	High ionic conductivity	Poor thermal stability
	Low interfacial impedance	Low mechanical strength
	Suppressing LiPSs shuttling	
Solid-state polymer	Low interfacial impedance	Low ionic conductivity
	Suppressing LiPSs shuttling	Low mechanical strength
	Good thermal stability	
Ceramic	High ionic conductivity	High interfacial impedance
	Excellent thermal stability	Poor processability
	Preventing LiPSs shuttling	
	Suppressing Li dendrite growth	
Polymer/ceramic composite	Low interfacial impedance	Low ionic conductivity
	Good thermal stability	
	Suppressing LiPSs shuttling	
	Suppressing Li dendrite growth	

Unfortunately, solid electrolytes still suffer from lower lithium conductivity and high resistance in comparison to liquid electrolyte, which strongly affect the performance of the battery [111], so the next step will be to develop solid state

electrolyte with high ionic conductivity at room temperature and good interfacial capability with both sulphur and Li metal electrodes [110].

3.3.3 Shuttle effect inhibition

In any way, to this day, the greatest research effort for improving Li-S performances was has been carried out with the aim of suppressing LiPSs shuttle.

Indeed, suppressing the shuttle effect inside Li-S cell is fundamental to better understand the chemistry of the main actors involved in this process: lithium polysulfides.

Polysulfides are a class of chemical compounds containing multiple sulphur atoms linked by covalent bonds. Polysulfides anions mainly exist in two forms: the singly charged radical monoanion ($Sn^{.-}$) and the dianion (Sn^{2-}) which are generally symbiotic and in equilibrium in the solution (Equation [3.7]).

$$S_{2n}^{2-} \rightleftarrows 2S_n^{.-} \qquad [3.7]$$

Moreover, each PS anions coexist with each other in disproportionation/co-proportionation equilibria due to their close Gibbs free energies.

PSs present high chemical reactivity and high sensitivity to air and moisture, and their status and behaviour strictly depend to solvent selection [102]. As a consequence of these complex equilibria, it is extremely difficult to isolate and characterize individually each PSs compound.

However, despite these known issues, PSs are not replaceable in the Li-S system because dissolution of PSs enhances the reaction kinetic, promoting active material redistribution and reducing electron and ion transfer resistance [102].

The PSs management can be divided into two different approaches: PS-bypass and PS-retain strategies. One possibility to avoid PSs shuttle phenomena is directly bypassing the formation of long chain polysulfides. This could be done exploiting some sulfurized organics additives or implementing the use of Solid-state electrolytes (SSEs).

Though, the most promising strategy consists in retaining PSs species. Retention strategy is a less radical method, which permits to preserve the positive contribution of polysulfides.

In general, the PSs confinement is mainly realized by immobilizing PS species within the cathodes via physical and/or chemical adsorption.

In the last decade, considerable improvements of battery performance have been achieved through PSs confinement strategies [110]. Some of them are reported below:

o building physical barriers to block the LiPSs diffusion like confining molten sulphur into porous carbon or other materials. In general, physical confinement of LiPSs alleviate the shuttle effect and it includes: coating, loading and separating process. Coating confines active material within a limited space; loading anchors active materials into a matrix; separating prevents LiPSs migration through separators [117].

o chemically adsorbing LiPSs molecules by bonding with polar host materials. PSs are inherently anionic polar species, presenting great affinity towards polar adsorbents which have positive surface charges, such as metallic oxide, transition metal sulphide, heteroatom-doped carbon material, or metal-organic frameworks (MOFs). Moreover, according to Lewis' theory, PSs with lone electron pairs are Lewis base which can strongly interact with Lewis acid materials such as MOFs or MXene. Lastly, some polymers like polyacrylonitrile (PAN) and polyaniline (PANi) can be sulfurized and anchor the sulphur with strong chemical bonding [117][118][119].

o accelerating the conversion process of LiPSs by catalysts able to reduce the LiPSs conversion potential barrier. These types of catalysts are called electrocatalytic materials and can be classified into three main categories. The first category includes polar hosts, such as: graphitic carbon nitride (g-C_3N_4), phosphorene nanosheets, metal particles, metal oxides (like MoO_2/MoO_3, VO_2, RuO_2, etc), NiFe-layered double hydroxide (NiFe-LDH), sulphides (like Co_xS_y, MoS_{2-x}, TiS_2, WS_2, etc), nitrides (like TiN, VN, etc), carbides (WC and NbC), and some metal compounds. The second category include δ-MnO_2, CuO, and V_2O_5, which are able to form thiosulfate groups ($S_2O_3^{2-}$) on the host surface to mediate the redox reaction of sulphur species. The third category of materials consists of Te-doped sulphur, which is the only material, actually known, that can accelerate the lithiation/de-lithiation reaction [119].

In Figure 3.5 are resumed all the materials which give chemical and electrocatalytic reaction with PSs.
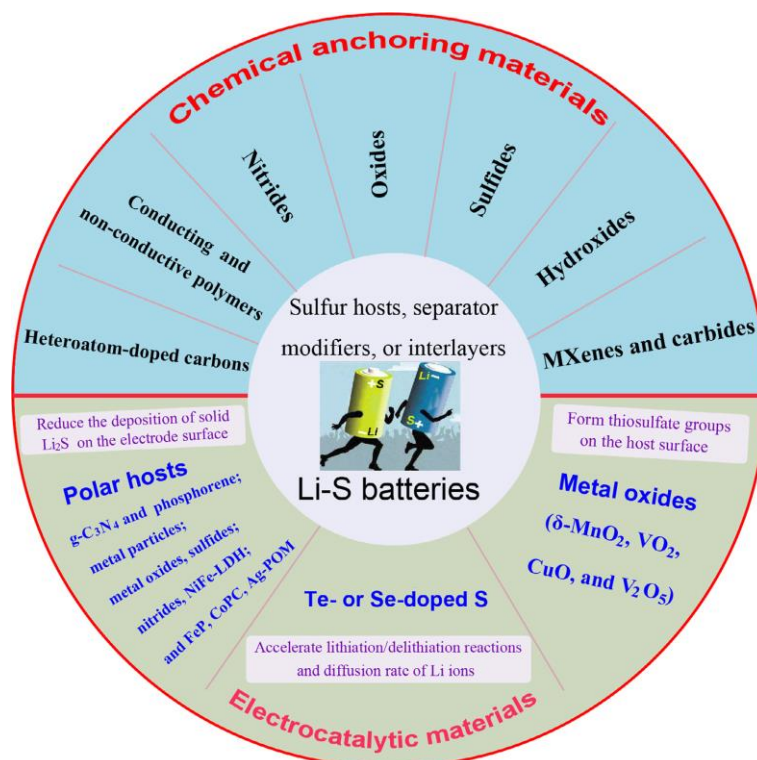
Figure 3.5: schematic illustration of chemical anchoring and electrocatalytic materials for Li–S batteries

Materials with just physical adsorption cannot confine polysulfides completely, while chemical bonding materials suffer from low specific surface area and low sulphur loading. So physical or chemical process, if used alone, show limited improvement of Li-S batteries. Thus, the combination of both physical and chemical process, exploiting their synergy, is the most promising strategy for addressing shuttle effect of PSs [117].

Another quite recent and interesting PS blocking strategy is using functionalized interlayer or separator, because the PSs permeation from cathode to anode can be effectively inhibited by employing an ion selective layer between the electrodes [111].

An interlayer is a freestanding film inserted between the separator and electrode, while a functionalized separator is a traditional separators subjected to a physicochemical functionalization process [120]. Polyolefin separators including polypropylene (PP) and polyethylene (PE) are widely used in Li-S batteries due to their chemical stability, mechanical strength, high porosity, and low cost. However, polyolefin separators, alone, could not confine soluble polysulfides into the cathode side. Therefore, coating the commercial separators with specific materials able to chemically interact or physically confine PSs was individuated

as an effective way to limit the shuttle effect. For this purpose, conventional separator modified with PSs absorber such as carbon materials (MWCNT, graphene oxide), functional polymers (Nafion, PANi, PPy) or metal oxides/sulphides/carbides/nitrides can be used as well as coating interlayer [111] [102].

The concept of ''interlayer'' and its relative use in Li-S was proposed for the first time by Manthiram group [121], which showed the possibility to insert an electrolyte-permeable microporous carbon paper, acting as ''polysulfide stockroom'', between the sulphur cathode and the separator [122]. In the last year, many others carbon based, metal-based, and polymer-based interlayers have been deeply investigated, with the aim of improving the electrochemical performances of Li-S [120][123].

However, in spite of the great improvements in terms of electrochemical performances there are several additional problems which arise when considering the commercial application of the above-mentioned approaches [122][124][125]:

- o preparation of an interlayer is relatively complicated because it commonly involves filtration;
- o integration of interlayer in the cell is still difficult in practical continuous production;
- o interlayers possess low flexibility which cannot satisfy the requirement of roll-to-roll assembly procedures;
- o the thickness/weight of the applied interlayer is high, with consequent detrimental effect of gravimetric capacity of the cell.
- o the presence of void space inside the interlayers lead to a faster consumption of the electrolyte, while the poor conductivity results in an internal resistance increase

Recently Huang *et al.* [124] developed and integrated a selective double layer structure for PSs diffusion mitigation, simply by coating the surface of a S/C cathode with a thin graphene/TiO$_2$ film. TiO$_2$ was selected because it can improve the surface adsorption of PS through the electrostatic attraction of negatively charged polysulfide and O-Ti$^{\delta+}$. With this simple coating strategy, they were able to achieve 1040 mAh g^{-1} over 300 cycles at 0.5 C.

At the same time Zhang *et al.* [125] reported a simple double-coating technique to develop an interlayer directly spread on the cathode surface, which acts as a LiPSs barrier layer.

They simply spread a second layer of carbon nanospheres (Super P), with a thickness of 10 μm, directly on the pre-formed S/C cathode. With this double coating technique, they observed a specific capacity of ~ 695 mAh g^{-1} at 0.5 C after 100 cycling.

More recently Lei and Chei group [126] deposited on a S/CNT cathode a boron nitride nanosheet functionalized with positively charged amino groups

(FBN)/ graphene film. The FBN/graphene film was able to trap the PSs directly on cathode surface, exploiting the electrostatic interaction of the positive -NH$_2$ functional groups of FBN which act as ion-attracting sites of negatively charged polysulfide. The authors affirm that, with the implementation of the FBN/graphene film, the Li-S cell shows an improved cycle life (over 1000 cycles), with an initial specific capacity of 1100 mAh g^{-1} at 3 C, and a cycle decay as low as 0.0037 % per cycle.

Following the same rational scheme, Sun and co-workers [127] designed and developed a cathode modified by a double-coating layer. They selected a functionalized graphene containing an in situ grown MnO$_2$ nanoparticles (MnO$_2$@GP) layer, able to chemically interact with PSs, and catalysed they reactions. As a result, the MnO$_2$@GP double-layer cathode showed a specific capacity of about 1395 mAh g^{-1} at 0.5C, with a coulombic efficiency close to 100 % with a fade rate of 0.3 % for the first 100 cycles.

Last year Dai *et al.* [128] developed a 2D carbon-based composite with a laminated structure constituted by graphene and g-C$_3$N$_4$ as an interlayer, directly spread on the cathode surface.

They combined the graphene properties, like good ionic and electronic conduction, to accelerate charge transfer and Li$^+$ diffusion, and the g-C$_3$N$_4$ properties as physical and chemical trapping agent for the dissolved polysulfide species. With this double-layer approach the Li-S cell was able to deliver an initial discharge capacity of 612.4 mAh g^{-1} at 1C after 1000 cycles.

In conclusion a variety of strategies have been tried to solve the above-mentioned polysulfide shuttle effect: various porous structures are supposed to physically trap the soluble polysulfides, carbon hosts have been doped by various heteroatoms (N, B, O, P, S, etc.), decorated by metal compounds (metal oxide or sulphide), or coated by polymer able to chemically interact with PSs.

In particular, the rational design of a double layer approach seems to be an effective way to mitigate polysulfides shuttling. Moreover, this approach can be easily applied for the variety of existing S/C cathodes which makes it very interesting for industrial scale-up.

For this reason, chapter 5 focused on the optimization of an effective double layer approach, using g-C$_3$N$_4$ as polysulfides trapping agent. The next chapters will give a brief overview on g-C$_3$N$_4$ properties.

Chapter 4

4 Graphitic Carbon Nitride

4.1 Structure and chemistry

Carbon nitrides are defined as a class of polymeric materials consisting mainly of carbon and nitrogen. Carbon nitride can be considered one of the oldest synthetic polymers reported in literature. It was first studied in 1834 by Jöns Jakob Berzelius, which first synthesized a carbon nitride material simply heating mercury(II)thiocyanate (Hg(SCN)), but it was Justus von Liebig who discovered the general formula $(C_3N_3H)_n$ corresponding to this compound. Liebig identified several amorphous C/N compounds which he arbitrarily named melamine, melam, melem and melon [129] [130].

Many years passed before Franklin, in 1922, first described the structure of this compound, introducing the concept of "carbonic nitride", suggesting that it can be obtained as the final deamination product by heating melon [131]. Lastly, in 1937, Pauling and Sturdivant suggested a coplanar tri-s-triazine unit as the basic structural motif of carbon nitride.

Considering the chemical structure, tri-s-triazine (heptazine) rings, and related melon polymer, were recently confirmed as the most energetically favoured (30 kJ mol^{-1}) basic units of carbon nitride [132]. The aromatic tri-s-triazine rings (C_6N_7) are cross-linked to each other by trigonal nitrogen atoms forming a π-conjugated planar layer, like graphite. For this reason, the most stable allotrope of carbon nitride is named "graphitic" (g-C_3N_4), which possesses a stacked 2D layered structure, where single-layers are bounded by van der Waals forces.

The characteristic XRD pattern of bulky g-C_3N_4 powders presents two distinct diffraction peaks located at 27.4 and 13.0 degrees, which can be attributed to (002) and (100) diffraction planes for graphitic materials, respectively (JCPDS 87-1526) [133][134].

The diffraction plane (002) reveals an interplanar stacking distance of about 0.325 nm, which is similar to that of graphite (0.34 nm) indicating that the g-C_3N_4

presents a typical flake-like structure. The interplanar stacking distance confirms a high packing density perpendicular to the layers, which can be attributed to the localization of the electrons and stronger binding between the layers [135].

The tri-s-triazine ring structure and the high degree of condensation are the basis for the high thermal and chemical stability of g-C$_3$N$_4$. In fact, the thermal decomposition of carbon nitride starts at 630 - 650 °C with a complete decomposition of the structure at 700 - 750 °C, resulting in no material residue. This temperature is quite high for an organic material if compared to other typical high-temperature polymers [136] and deeply extend the use of g-C$_3$N$_4$ in a wide range of application.

Carbon nitride is also incredibly stable and resistant to chemical attack by acid, base or organic solvents. In particular, g-C$_3$N$_4$ doesn't show any detectable solubility and reactivity versus the most common solvents as: water, alcohols, dimethylformamide, tetrahydrofuran, diethyl ether and toluene, *etc.* [137]. This chemical stability in a variety of different solvents makes carbon nitride an interesting material also for liquid-phase reactions.

Only treating g-C$_3$N$_4$ with molten alkali metal hydroxides leads to a hydroxolysis of the structure, while the treatment with concentrated acids leads to sheet-like dissolution resulting in colloidal dispersion. However, all these treatments are fully reversible [138].

By optical and photoelectrochemical point of view carbon nitride is a semiconductor with a tunable bandgap of about 1.8 - 2.7 eV and light adsorption at 460 - 698 nm, as confirmed by its typical pale-yellow colour [135].

Graphitic carbon nitride also owns rich surface properties, such as basic surface functionalities, electron-rich properties, H-bonding motif, etc., which are particularly attractive for many applications [135][134].

The presence of hydrogen indicates that the structure is not completely condensed, and some surfaces defects are present. This characteristic can be particularly useful in catalysis, for example, promoting the electron re-localization on the carbon nitride surface, and leading to typical Lewis-base behaviour, as depicted in Figure 4.1 [139].
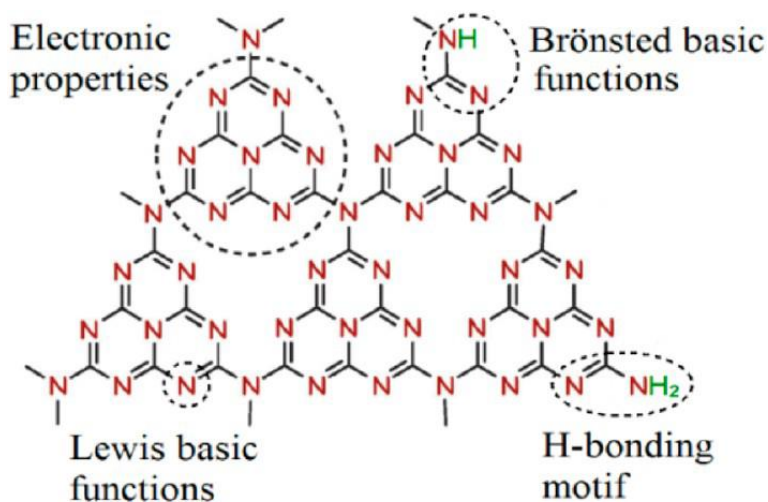
Figure 4.1: surface functionalities of g-C$_3$N$_4$

As mentioned before g-C$_3$N$_4$ consists essentially of only two earth-abundant elements, carbon and nitrogen (with a theoretical C/N molar ratio of 0.75), which makes this material bio-compatible, non-toxic, easy to prepare and with low cost [134]. All these properties inevitably expand the range of application.

The most common precursors used for the synthesis of g-C$_3$N$_4$ are typically nitrogen-rich compounds, containing C-N bond.

The thermal condensation reaction starting from cyanamide to dicyandiamide, melamine and subsequent C/N materials, first described by Liebig, is still the most simple and available synthetic routes to generate slightly defective g-C$_3$N$_4$ [139][136].

Most precisely, the thermal condensation reaction of carbon nitride is properly a combination of a polyaddition and polycondensation reactions. In the reaction pathway the precursors are first condensed towards melamine, up to 350 °C, while the typical tris-s-triazine units are formed via melamine rearrangement at 390 °C. The subsequent condensation of tris-s-triazine units to polymer network, and to the finally polymeric g-C$_3$N$_4$, occur at 520 °C. During these condensation steps a huge amount of ammonia is eliminated. At 600 °C the material become unstable and completely disappears around at 700 °C, generating nitrogen and cyano fragments [135].

Both experimental data and DFT calculation confirmed that melam (melamine dimers) are formed as metastable intermediates and the polymerization takes place through the connection between adjacent molecules (in the melem crystal) to form di-melem molecules. The so-formed di-melem molecules condense into melon, a linear polymer of tris-s-triazine units, by further release of NH$_3$. The final step of the polymerization is the release of other NH$_3$ to form the pure carbon nitride [135]. In Figure 4.2 is reported the thermal condensation pathway for the formation of g-C$_3$N$_4$ starting from cyanamide.
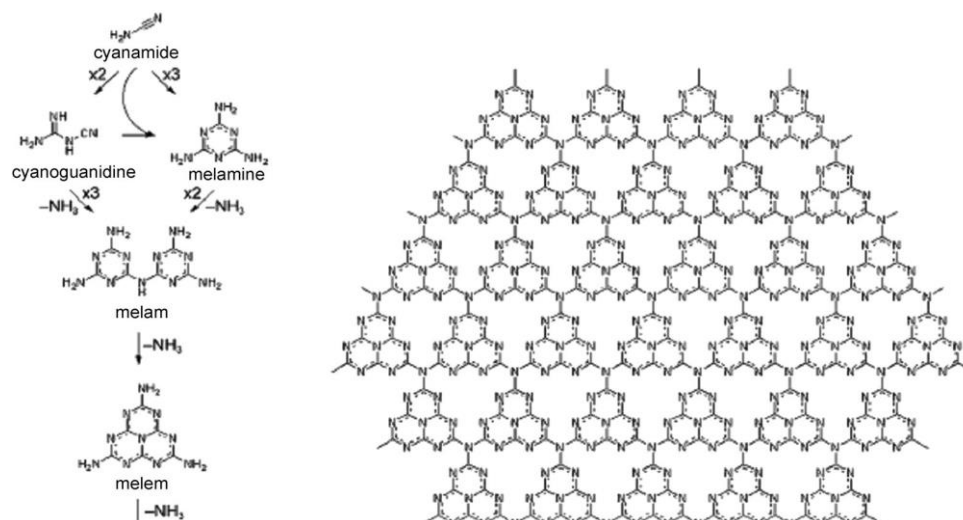
Figure 4.2: thermal condensation reaction pathway starting from cyanamide as precursor.

The thermal condensation synthesis can be conducted either in inert (N_2, Ar) or in air atmosphere, with no significant changes in the bulk structure but resulting in some differences in product yield, degree of condensation and surface properties.

Since cyanamide is expensive and explosive material, it could be preferable to use some derivatives such as dicyanamide, melamine or several other low-cost N-rich organic solid precursors such as urea, thiourea, and guanidine hydrochloride which are less problematic precursor [134].

Other different strategies such as iono-thermal synthesis, molecular self-assembly, microwave irradiation and ionic liquid can be used to obtain condensed carbon nitride (Figure 4.3) [134].
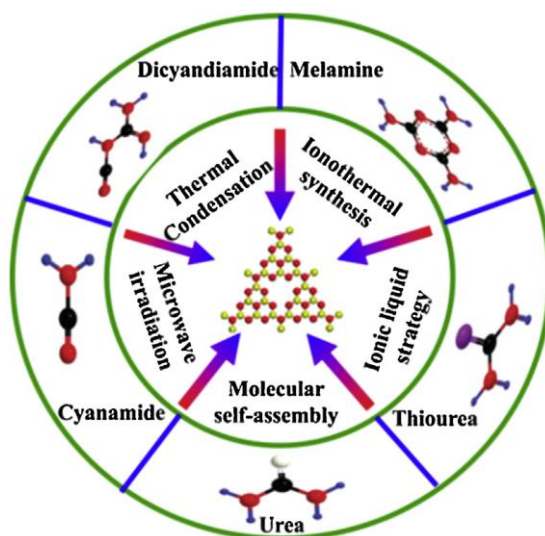
Figure 4.3: different synthetic strategies and
precursors to produce g-C_3N_4 [134].

It is worth noting that synthetic routes, condensation temperatures, material compositions and surface functionalities are important factors which deeply affect the structure and morphology of carbon nitride and consequently strongly influence its properties and applications range [130]. Crystalline perfection only contributes to the bulk properties, such as thermal and chemical stability or semiconductor electronic structure [136]. While g-C_3N_4 rich of defects is quite useful and interesting in catalysis, especially in heterogenous catalysis, since surface terminations and defects are considered as the real active sites of the reaction.

The nitrogen-rich functional groups and the electronic delocalization properties confer to g-C_3N_4 complex interaction mechanism, involving π-π conjugation, hydrogen bond interaction, electrostatic interaction and hydrophobic effect.

In particular, pyridinic N atoms of g-C_3N_4 possess a strong electron-accepting ability, serving as active site for the electrochemical reactions. While g-C_3N_4 basic surface defects exhibit nucleophilic character, able to give strong interaction with ionic compounds (cations) by electrostatic interaction. These basic surface

functionalities are essentially due to the presence of basic primary and/or secondary amine groups (CNH_2 and C_2NH), attributable to the incomplete polycondensation process and small quantity of hydrogen impurity [140][134][141].

To tailor and increase the number of surface basic groups, reinforcing the catalytic behaviour of g-C_3N_4, one possible strategy is replacing carbon atoms in the aromatic rings by nitrogen or other elements such as phosphorus, sulphur, boron and fluorine.

Typical doping strategy involves the in-situ synthesis in which additives are directly mixed with the CN precursor. By this way heteroatoms are directly incorporated into the g-C_3N_4 matrix.

For example, ionic liquids like 1-butyl-3-methylimidazolium hexafluorophosphate ($BmimPF_6$) or butylmethylimidazolium tetrafluoroborate were used as phosphorus or boron source for doping carbon nitride.

Zhang *et al.* demonstrated that mixing 1-butyl-3-methylimidazolium hexafluorophosphate ($BmimPF_6$) with dicyandiamide before the thermal treatment is a possible strategy to obtain P-doped mesoporous g-C_3N_4. The doping is possible because PF_6^- can react with amine groups, and therefore be incorporated in the CN framework. Phosphorus heteroatoms can change the electronic structure and increase the electric conductivity of carbon nitride [142][143].

Many other phosphorus sources have been applied as doping agents such as diammonium hydrogen phosphate [144], 2-aminoethylphosphonic acid [145], (hydroxyethylidene) diphosphonic acid [146], hexachlorocyclotriphosphazene [147], ammonium hexafluorophosphate [148], and phosphorous acid [149].

Sulphur has also been used to modify the electronic structure of g-C_3N_4, treating pure CN powder directly with gaseous H_2S [150], or directly using thiourea as precursor or co-precursor [151].

Lastly boron-doped carbon nitride was synthetized via heating the mixture of melamine and boron oxide [152], while doping fluorine-doped g-C_3N_4 was obtained using NH_4F as dopant agent [153].

Another quite used approach to tailor the surface properties of carbon nitride is the so-called post-treatment functionalization. g-C_3N_4 was reversibly protonated by the simple treatment with HCl. The protonation process tuned the electronic bandgaps, increased the ionic conductivity and improved the dispersion in aqueous solutions of carbon nitride [138]. While hydrophilicity of g-C_3N_4 can be improved through introducing oxygen-containing functional groups (hydroxyl and carboxyl) by chemical oxidation process [134][130].

The surface area of g-C_3N_4 obtained by direct thermal self-condensation of nitrogen-rich precursors is normally around 10 m^2 g^{-1}, which is too low for typical catalytic applications.

For this reason, many strategies were individuated to increase the surface area of carbon nitride.

The first strategy is to tailor the porous structures of g-C$_3$N$_4$, with the purpose to create channels and more accessible active sites and, at the same time, facilitate the molecular mass transfer and the charge migration.

Porous architecture of g-C$_3$N$_4$ have been widely fabricated through self-assembly induced by structure-directing agents (SDAs) strategies, such as hard templating (nanocasting), soft templating or self-templating (supramolecular self-assembly) [134] [135].

For example, mesoporous carbon nitride (mpg-C$_3$N$_4$) was simply obtained by adding silica nanoparticles [154].

Unfortunately, the hazardous agents necessary for removing the silica templates, such as NH$_4$F or HF, are harmful for environment, and this inevitably restricts the practical large scale applications of hard-templating process [134] [135].

Soft-template route has proved a "greener" alternative strategy to produce g-C$_3$N$_4$ with controlled porosity, avoiding the use of hazardous agents [155].

For example, Triton X-100 [156], Pluronic P123 [157] and some ILs [158] were adopted as soft template to increment the specific surface area of g-C$_3$N$_4$ at 70 - 400 m^2 g^{-1}.

The main drawbacks of soft template like ionic liquids and polymers, are related to the high cost, and the inevitable carbon residue in the final product, which limit their extensive practical applications at a large scale [134][135].

Another way to significantly enhance the surface area of g-C$_3$N$_4$ is obtaining nanosheets. As mentioned before the carbon nitride layer are stacked with each other by weak intermolecular van der Waals or electrostatic forces. Typically, these interlayer interactions can be destroyed by physical or chemical approaches, and g-C$_3$N$_4$ nanosheets could be obtained by two distinct synthetic strategies: the top-down exfoliation of layered bulk g-C$_3$N$_4$ materials and bottom-up 2D assembly of precursors.

By these ways it is possible to synthetize 2D few-layer g-C$_3$N$_4$ nanosheets with surface areas (up to 300 m^2 g^{-1}) which are several times larger than that of bulk layered carbon nitride. The larger surface area inevitably increases the number of accessible active sites, with consequent improving the catalytic activity of the material. The most common strategies are ultrasonication-assisted liquid exfoliation, chemical exfoliation, thermal oxidation etching, or a combination of them [134][159].

Many ultrasonication treatments adopting different solvents such as water, alcohols, N-methyl-pyrrolidone, dimethyl formamide (DMF), acetone, acetonitrile, 1,4-dioxane, etc. or their mixtures, have been studied. Unfortunately, these process are affected by long sonication exfoliation time and low yield [134].

Acid-exfoliation method with low cost and controlled exfoliation degree, liquid ammonia-assisted lithiation by the intercalation of LiCl ions [160] and thermal exfoliation through direct oxidation "etching" [161] or employing agents

like NH$_4$Cl [162] have been deeply exploited to achieve the large-scale exfoliation of bulk g-C$_3$N$_4$ materials.

In conclusion the adsorption properties of carbon nitride are strongly dependent from both its porous structure and surface chemical functionalities. A wide variety of species can be adsorbed on the multiple different functional groups and defect sites through different types of interactions such as physical adsorption, electrostatic attraction, or chemical interaction.

In relation to some indisputable advantages such as simple composition, facile synthesis, low cost, and rich chemistry, g-C$_3$N$_4$ is still an useful candidate in some applications of sustainable chemistry and energy storage like catalysis, photocatalysis, water splitting, sensing, fuel cell, supercapacitors and so forth [163].

A detailed description of g-C$_3$N$_4$ properties and its application as PSs trapping agent will be given in the next paragraph.

4.2 g-C$_3$N$_4$ application in Li-S batteries

In the last five years, g-C$_3$N$_4$ has been studied as suitable polysulfides trapping agent in Li-S battery. As shown in Figure 4.4 more than 25 papers were published since 2015. Multiple and different approaches were investigated with the aim to better understand the carbon nitride role inside the lithium-sulphur chemistry, finding the best strategy to implement it inside the cell.
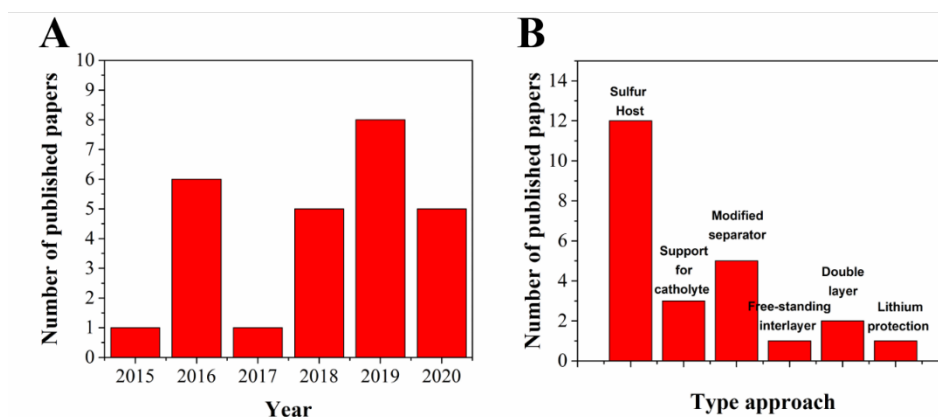
Figure 4.4: histogram of published papers concerning the use of g-C$_3$N$_4$ in Li-S battery in the last 5 years (a) and different research approaches (b).

A lot of investigations payed particular attention to better understand the origin of the strong interaction between carbon nitride and lithium polysulfides.

For example, Liang *et al.* [164] confirmed and validated the existence of a strong electrostatic affinity between carbon nitride and LiPSs, by density

53

functional theory (DFT) simulations and experimental data. The most interesting conclusion of this work was the kinetic contribution of g-C$_3$N$_4$ to LiPSs redox reaction. For the authors, the high surface polarization of carbon nitride can alter the molecular configurations of the adsorbed LiPSs, inevitably affecting the electron transport between them and kinetically facilitating their redox conversion reaction.

Generally, LiPSs molecules have similar charge distributions, Li atoms are positively charged (with 0.86 electrons), while the S atoms are negatively charged (with 0.06 to 0.68 electrons, depending on the location of S atoms in the molecule). For this reason, the positively charged Li atoms of LiPSs can be subjected to strong electrostatic attraction by negatively charged N of carbon nitride. Calculating the charge transfer from Li$_2$S$_6$ to g-C$_3$N$_4$, the authors excluded the formation of strong ionic bond, preferring an electrostatic interaction without relevant charge transfer between the two materials. Typically, a chemical interaction mainly comes from charge transfer (ΔQ) for ionic bonding or charge density overlap for covalent bonding, but in this case, the authors found that charge transfer or charge density overlap is insignificant between LiPSs and g-C$_3$N$_4$, confirming the prevalently physical nature of this interaction. The mentioned DFT prediction were also validated by XPS analysis, in which no evident peak shifts were observed in carbon nitride spectra, after its interaction with LiPSs.

In support of this theory Pang and Nazar [165] observed that the intrinsic high charge polarity of g-C$_3$N$_4$ (due to nitrogen group) provides superior LiPSs absorptivity, through Li$^+$−N$^{\delta-}$ interaction. By the combination of DFT calculations and spectroscopic experimental studies they evidenced that the binding energy between Li$_2$S$_2$ or Li$_2$S$_4$ and g-C$_3$N$_4$ increases in relation to the concentration of doped N, concluding that accessible pyridinic nitrogen adsorption sites are the key factor for the improvement of electrochemical performance.

In 2017 Zheng *et al.* [166] presented a systematic and exhaustive theoretical study to fully investigate the anchoring effect of some non-metallic layered materials such as boron nitride, graphene, and carbon nitride for all the most common LiPSs species.

DFT calculation suggested to the authors that lithium polysulfides have a much stronger interaction with carbon nitride, because LiPSs present higher binding energies on g-C$_3$N$_4$ (or C$_2$N) materials than on boron nitride and graphene. g-C$_3$N$_4$ evidenced high binding energies (Eb: from -1.14 to -8.70 eV) for LiPSs proving and supporting previous studies about the effective trapping ability and shuttle effect mitigation.

In their study, the authors supposed that LiPSs do not remain intact when adsorbed at vacant sites of g-C$_3$N$_4$, but Li atoms detach from the polysulfides molecules and bind to the vacant site (−N= sites) of g-C$_3$N$_4$, originating Li$_{2-x}$PS species. This is partially in contrast to Liang's study, suggesting that the Li-N bond, between LiPSs and g-C$_3$N$_4$, is a kind of ionic bond and the consequent molecular configuration distortion can promote the redox reaction kinetics. By analysis of physical dispersion interaction, Zheng e co-workers highlighted a

decreasing of dispersion interaction ratio from Li_2S_8 (28%) to Li_2S (4%), demonstrating that S_8 and LiPSs with more S atoms are physisorbed on carbon nitride mainly through dispersion interaction. Accordingly, the dispersion interaction is largely contributed by S atoms. Charge transfer analysis further confirmed that the charge is mostly transferred from g-C_3N_4 to long chain LiPSs. Besides, these theoretical studies demonstrate that Li_2S species prefer anchoring on g-C_3N_4 rather than nucleating into larger lithium sulphide clusters. Besides, the binding energies between LiPSs and carbon nitride are higher than that of the DOL/DME solvents and LiPSs, suggesting that the anchoring effect of C_3N_4 overtakes the dissolution.

Similar conclusions were achieved by other studies, combining theoretical calculations with experimental analysis. For example, Fan *et al.* [167] reported DFT calculation highlighting the presence of C-S interaction in addition to the well discussed N-Li one. Many studies reported similar conclusions about the strong dipole–dipole electrostatic interaction between the Li atom of PSs and the pyridinic-N sites of g-C_3N_4, confirming the effective contribution of carbon nitride to trap and promote redox reaction kinetics of LiPSs [168][169].

Starting from the theoretical predictions many and different strategies were adopted to completely exploit the g-C_3N_4 properties as PSs trapping agent by experimental point of view.

Carbon nitride was largely adopted and investigated as sulphur host. A pioneer work was done by Liu *et al.* [170] in 2015, which was the first study to report the employment of porous oxygenated carbon nitride (OCN) nanosheets as sulphur host. They used a bottom-up process, exploiting a sustainable two step solid-state pyrolysis of urea and biomass (such as glucose) as reactive molecular precursors. Glucose was added as reactive carbon and oxygen sources but also to produce pores inside the structure, avoiding the addition of other template agents. The as obtained micro-mesoporous carbon showed high specific surface area (605.97 m^2 g^{-1}) and was successively loaded with 56 wt.% of sulphur.

The S/OCN cathode was able to deliver an initial capacity of 1407.6 mAh g^{-1} at 0.05C with a coulombic efficiency of about 98%, and a long-term cycling of 447.3 mAh g^{-1} over 500 cycles at 0.5C with a capacity decay of 0.1% per cycle.

Despite the interesting electrochemical results, it is important to note that in this work the authors used carbon nitride prevalently as template to produce nitrogen and oxygen rich carbon. Therefore, it is only partially included in the studies which effectively investigated the PSs trapping properties of g-C_3N_4.

One year later, Pang and Nazar [165] produced a pure and lightweight mesoporous g-C_3N_4 (~ 5 nm) with high surface area of 615 m^2 g^{-1} and a final nitrogen concentration of 53.5 atom %, by hard-template approach.

The cathode with a final sulphur loading of 1.5 g cm^{-2} (75 wt.% of sulphur) was produced by a melt diffusion method and presented an ultralow long-term capacity fade rate of 0.04 % per cycle over 1500 cycles at 0.5C rate and retained electrode capacity of 620 mAh g^{-1} capacity after 500 cycles, at 0.2C. The authors ascribed the good electrochemical performances to the 53.5 % of N present in the

carbon nitride, which was sufficient to adsorb all the polysulfides originated by the cathode and, at the same time, to the structural role to carbon nitride, as flexible material able to accommodate the cathode volume expansion.

Analogously, Han and co-workers [171] synthetized a graphene-like g-C_3N_4 nanosheets (GCN), with high nitrogen content (56 wt.%) and high specific surface area of 209.8 m^2 g^{-1}, as host material for sulphur. The final S/GCN cathode (with 70.4 wt.% of sulphur) exhibited an initial reversible capacity of 1250 mAh g^{-1} at 0.05C and a discharge capacity of 578.0 mAh g^{-1} at 0.5C over 750 cycles with a fade rate of 0.053 % per cycle. By XPS analysis, the authors, also supported the thesis of the electron transfer from electron-rich N atoms of carbon nitride to $Li^{\delta+}$ of Li_2S_4, attributing the high and long-term cycle performance of S/GCN cathode to the abundant nitrogen anchor sites present on carbon nitride and at the same time to the high specific surface area of the material. Li *et al.* [172] synthesized a polar and porous g-C_3N_4 host materials by a facile and scalable production method, using thiourea and ammonium chloride respectively as precursor and soft-templating agent. The cathode containing the as produced carbon nitride delivered an initial specific discharge capacity of 1050 mAh g^{-1} at 0.05C and a retained specific capacity of 600 mAh g^{-1} after 200 cycles at 0.1C.

Yao *et al.* [173] conduced an interesting investigation, producing g-C_3N_4 at different temperatures (520, 550, 580, 610) by direct thermal-condensation. In particular, they observed a decrease of specific surface area and morphology changes with the temperature rising, selecting carbon nitride obtained at 550 °C as optimal sulphur host. The CN550/S cathode, with a final mass loading of 2.3 mg cm^{-2}, delivered an initial specific capacity of 1262.1 mAh g^{-1}, and a reversible capacity of 605.4 mAh g^{-1} over 500 cycles imposing a current of 0.39 mA cm^{-2}. By XPS post-cycling analysis the authors evidenced the presence of sulphate and thiosulfate specie, which are intermediate products obtained by the gradual reaction of g-C_3N_4 with polysulfides. They also observed a significant decreasing in pyridinic-N signal, in the post-cycling electrode (if compared to the pristine one), attributing to the adsorption and deposition of polysulfides by active-sites of nitrogen.

Similar approaches were used by many other researchers, often coupling carbon nitride with other and more conductive materials such as graphene.

For example, Wang *et al.* [174] designed a 3D hierarchically porous g-C_3N_4/graphene hybrid material (GCN) host, exploiting the polycondensation of urea directly in a rGO hydrogel and creating a large meso- and macro-pores structure with an increased accessibility to the nitrogen active sites. The GCN-10/S electrode with a sulphur mass loading of 1.1 mg cm^{-2} (65 wt.% of sulphur) showed a specific capacity of 505 mAh g^{-1} for 600 cycles at about 0.06C, with 0.087 % of capacity decay per cycle. The authors ascribed the electrochemical performances to the synergistic combination of spatially confining, chemically anchoring, and rapidity of LiPSs catalytic conversion, of g-C_3N_4 and reduced graphene oxide hydrogel.

Another porous two-dimensional sulphur host composed of g-C_3N_4 and N-doped graphene was developed by Ma et al [175]. In this case porous g-C_3N_4

(PCN) was synthetized by hydrothermal method and then uniformly mixed and spread on the graphene nanosheets surface, obtaining a hybrid hetero-structured sulphur host (PCN/NG) with a specific surface area of 120.8 m^2 g^{-1}. The resulting PCN/NG/S cathode, with a final sulphur content of 69.5 wt.% delivered an initial discharge capacity of 1028.6 mAh g^{-1}, and 615.6 mAh g^{-1} after 500 cycles with a capacity retention of 59.8 % (average capacity decay of 0.08 % per cycle) and a coulombic efficiency above 99 %, at 0.2C. Lastly, Deng *et al.* [176] designed a hierarchical porous g-C_3N_4/reduced graphene oxide sulphur cathode (g-C_3N_4/r-GO/S), able to deliver an initial charge capacities of 1039.4 mAh g^{-1} at 0.5C and a reversible capacity of 589.6 mAh g^{-1} after 100 cycles at a current rate of 2 C.

Graphitic carbon nitride was also combined with other carbonaceous materials like carbon nanotubes (CNTs) [177] or with totally different kinds of material such as MoS_2 [178].

For example, graphitic carbon nitride was coated over a carbon core-shell structure containing sulphur (S@HCS@ g-C_3N_4). In this case the cavity and mesopores present in the hollow porous carbon nanospheres (HCSs) accommodate the volume change of sulphur during cycling while the g-C_3N_4 layer blocks LiPSs by strong chemisorption [179]. The cathode obtained delivered an initial discharge capacity of 1420 mAh g^{-1} at 0.2C, which decayed to 885 mAh g^{-1}, after 100 cycles.

Majunber *et al.* exploited the synergetic interaction of MoS_2 and nitrogen rich g-C_3N_4 heterostructures designing a molybdenum disulphide/graphitic carbon nitride porous nanosheets sulphur host. They observed that MoS_2 nanosheets improved the cycling performances thanks to its polar nature, remarkable flexibility and high lithium ion conductivity while light-weight porous g-C_3N_4 nanosheets provided huge amount of lithium polysulfide adsorption sites, limiting PSs shuttle. The as obtained MoS_2/g-C_3N_4/S electrodes delivered a reversible specific discharge capacity of 952 mAh g^{-1} at 0.5C, and especially the high reversible specific capacity of 430 mAh g^{-1} rate after 400 cycles at 8C [178].

Alternatively to g-C_3N_4 as sulphur host, which inevitably needs to be mixed with conductive carbon, many studies were oriented to separator modifications or interlayer design.

A first simple coating approach was reported by Fan and co-workers [167]. They coated a commercial glass fibre separator (Whatman) with a slurry composed of g-C_3N_4, carbon black, and PVdF, obtaining a final porous layer of about 26 μm.

The as obtained coated separator was successively inserted in a LiS cell which delivered a reversible capacity of 773.2 mAh g^{-1}, 840 mAh g^{-1}, 732.7 mAh g^{-1} respectively at 0.2, 0.5 and 1C after 400 cycles. The authors assumed that the microsized g-C_3N_4 contributes to mechanical strength of the coated separator if compared to the simple carbon coated one.

Analogously, Jiang *et al.* [180] coated the glass fibre separator with a lightweight 2D boron doped g-C_3N_4 nanosheets (BCN). The boron doping increases the surface area, improves electrical conductivity, and chemically anchors more polysulfides through B-S bond. As a result, the Li-S cell with the

BCN modified separator delivered a large discharge capacity of 1197 mAh g^{-1}, with a retained capacity of 553 mAh g^{-1} after 500 cycles at 1C.

Instead of glass fibre separator Huangfu et al. [181] exploited the possibility to combine g-C$_3$N$_4$, with a more suitable PP separator. They used a simple vacuum filtration technique to cover a commercial PP separator with an ultrathin g-C$_3$N$_4$ film with low areal loading of about 0.15 mg cm^{-2}. The maintained good lithium ion conductivity of the covered separator was evaluated by Li$^+$ transference number. While electrochemical impedance spectroscopy (EIS) measurement showed that the introduction of the g-C$_3$N$_4$ film on the separator did not increase the total battery resistance. Considering the electrochemical performances, the Li-S cell containing the modified separator showed an initial specific capacity of 990 mAh g^{-1} and a discharge capacity of 829 mAh g^{-1} after 200 cycles at 0.2C, corresponding to 83.7 % of the initial capacity. Despite the good performance, the battery with g-C$_3$N$_4$ separator showed higher polarization, especially at higher C-rates, if compared to Li-S cell with simple PP separator. Furthermore, in their experiment the authors used a huge amount of electrolyte (20 ml mg^{-1} of sulphur), which clearly exceeds the optimal declared ratio.

Similarly, Do et al. [182] designed a polyolefin separator covered by phosphorus doped carbon nitride, containing 22 wt.% of P (CNP22/PF). By DFT calculations the authors evidenced the existence of P-S coordination, in addition to the already mentioned Li-N and C-S interactions, which play a supplementary role in the mitigation of LiPSs shuttle and the prolongation of battery cycle life. The CNP22/PF separator was implemented in a Li-S cell, which delivered a discharge capacity of 850 mAh g^{-1} after 700 cycles with a decay rate of 0.041 % cycle and lastly, in pouch cell containing a high sulphur loading cathode (6.1 mg cm^{-2}), which showed a promising specific capacity of 699 mAh g^{-1} after 74 cycles at 0.2C.

Chen et al. [183] investigated a metal coordinated graphitic carbon nitride combined with crystalline carbon. They directly spread the metal coordinated g-C$_3$N$_4$/C on a PP separator, with the aim to evaluate the advantages of combining the above-mentioned properties of carbon nitride and the catalytic feature of metals.

Three transition metals (M = Fe, Co, Ni) were directly inserted in carbon nitride structure during the synthesis process, and deeply investigated under morphological and electrochemical point of view. The authors concluded that, the M-C$_3$N$_4$ can immobilize the lithium polysulfides, but also accelerate their kinetic conversion during the cycling process. In particular, Ni-C$_3$N$_4$/C revealed remarkable activity for PSs redox conversion reaction, showing a specific capacity of 999 mAh g^{-1} and good cycle stability with 89.4 % capacity retention after 300 cycles.

Another adopted strategy was using g-C$_3$N$_4$ as an interlayer, between the cathode and the anode. For example, Wutthiprom et al. [169] inserted an interlayer of graphitic carbon nitride coated on flexible and conductive carbon fibre paper (g-C$_3$N$_4$/CFP) between a sulphur impregnated 3D nitrogen-doped reduced graphene oxide aerogel (NGae), acting as cathode, and the polymer

separator. The as prepared cell delivered a specific capacity of 1271 mAh g^{-1} at 0.1C with excellent stability over 400 cycles, with a low capacity fading of 0.068 % per cycle. Moreover, the presence of the interlayer increased the specific capacity of about 23 - 57 %, in relation to the different NGae/S ratio.

Some papers also reported the implementation of carbon nitride in free-standing electrode, used in combination of catholyte solution. In this frame, Liao *et al.* [168] coated a commercial carbon fibre mesh (CFM) with pure g-C$_3$N$_4$ using a catholyte solution of Li$_2$S$_6$ for adsorption and electrochemical tests. The final cell showed a specific capacity of 800 mAh g^{-1} after 100 cycles with a capacity fading rate of 0.115 % per cycle. Unfortunately, the authors detected a quite low sulphur loading (0.6 mg cm^{-2}), due to the use of a catholyte solution instead of a solid sulphur cathode, which is one of the most important drawbacks of this approach, which inevitably limit its practical application. To limit the issue of a low sulphur amount Wu *et al.* [184] fabricated g-C$_3$N$_4$/CNTs membrane as a freestanding Li$_2$S$_6$ catholyte electrode with a sulphur amount of 4.74 mg which displayed an initial specific capacity of 876 mAh g^{-1} and a retained capacity of 633 mAh g^{-1} after 300 cycles at 0.5 C.

Lastly, other authors directly covered the sulphur cathode with a carbon nitride interlayer, following the same strategy already reported for different kinds of materials, such as graphene or polymers. A particular mention to Qu *et al.* [128] which developed a 2D laminated composite constituted by graphene and g-C$_3$N$_4$ nanosheets (g-C$_3$N$_4$/GS), directly spread on the sulphur cathode surface. The main idea of the authors was to assemble a laminated channel structure able to hinder the shuttle effect by physical and chemical interactions, exploiting the properties of both carbon nitride and graphene as trapping agents. Graphene was also added to create a conductive network and to accelerate charge transfer and Li$^+$ diffusion in the interlayer.

By a detailed XPS analysis, performed at different SOC of the cell, the authors verified the synergic contribution of both materials to chemically and physically anchor long-chain polysulfides. EIS and CV measurements also evidenced an increasing of Li$^+$ diffusion coefficient and of charge transfer at the electrode/electrolyte interface. As a consequence of the fast electrochemical reaction kinetics, the S/KB@C$_3$N$_4$/GS cathode (mass loading was 0.9 - 1.1 mg cm^{-2}) was able to achieve a discharge capacity 37 % higher than pristine cathode and delivered an initial specific capacity of 1167.8 mAh g^{-1} with a retained capacity of 612.4 mAh g^{-1} at 1C and 407.4 mAh g^{-1} at 2C after 1000 cycles.

In a similar study Zhao *et al.* [185] directly covered a sulphur graphene aerogel foam (S-GF) cathode with a carbon nitride film (g-C$_3$N$_4$) by a facile, inexpensive, and scalable spray-coating method. The spray-formed g-C$_3$N$_4$ film was uniformly dispersed with a final thickness of 70 nm and a total content of g-C$_3$N$_4$ of 13 - 15 wt.%.

The as prepared S-GF/g-C$_3$N$_4$ cathode (with the sulphur loading of 5 mg cm^{-2}) achieved a reversible capacity of 927 mAh g^{-1} at 0.2 C and long cyclic stability of 720 mAh g^{-1} after 280 with a capacity retention up to 78 %.

In addition, g-C_3N_4 was investigated also as lithium anode protective layer. Recently Xiong *et al.* [186] proposed a bifunctional artificial lithium protective layer, composed of graphitic carbon nitride nanosheets joined together by a polyvinylidene fluoride binder. With the bifunctional protective layer, the Li-S battery maintains a high capacity of about 800 mAh g^{-1} after 180 cycles, compared to 500 mAh g^{-1} with unprotected lithium anode. A brief summary of different approaches adopted is reported in Table 4.1.

Table 4.1: approach and performance comparison of Li-S containing g-C$_3$N$_4$ reported in literatures.
(* partial information provided)

Synthesized composite	Sulphur loading (mg cm^{-2})	Sulphur content (wt. %)	Electrolyte amount (µL mg^{-1})	C-rate	Long cycling capacity (mAh g^{-1})	Number of cycles	Year of publication	Ref.
Sulphur host								
Graphene-like oxygenated g-C$_3$N$_4$	-	56	-	0.5	447. 3 229.7	500 2000	2015	[170]
Light-weight nanoporous g-C$_3$N$_4$	1.5	75	15	0.5 1	620 730	500 200	2016	[165]
Graphene-like g-C$_3$N$_4$ nanosheets	-	70.4		0.5	578.0	750	2016	[171]
g-C$_3$N$_4$ into the 3D graphene framework	1.1	-	43	0.06	505	600	2018	[174]
g-C$_3$N$_4$	2.3	-	38	0.1	605.4	500	2018	[173]
Porous g-C$_3$N$_4$				0.1 1	600 400*	200	2018	[172]
g-C$_3$N$_4$ carbon nanotubes with MnO$_2$ compound		70.3		0.2	792	200	2019	[177]
Hierarchical porous g-C$_3$N$_{4r}$/reduced graphene oxide compound	2.5	75		2	589.6	100	2019	[176]
Porous two-dimensional (2D) g-C$_3$N$_4$ and N-doped graphene compound		69.5		0.2	615.6	500	2019	[175]
Porous structure of g–C 3 N 4		60		0.2 0.5	806 600	100 500	2020	[187]
g-C$_3$N$_4$-coated dual core–shell structured	1.0	70	15.6	0.2 1	885 718.7	100 500	2020	[179]

61

Material								
$Mo_2S/g\text{-}C_3N_4$ porous nanosheets	1.5 - 4.3	59.1	18	1 8	569 430	400 400	2019	[178]
Catholyte								
$g\text{-}C_3N_4$/graphene hybrid	-	50	-	0.2	700	280	2016	[164]
$g\text{-}C_3N_4$ coated on carbon fibre mesh	0.6	-	-	0.1	801	100	2016	[168]
$g\text{-}C_3N_4$/carbon nanotubes hybrid membrane	4.74 mg*	-	-	0.5	633	300	2020	[184]
Modified separator								
$g\text{-}C_3N_4$ coated on glass fibre separator	1.7	-	-	0.5 1	840 732.7	400 500	2016	[167]
Lightweight 2D boron doped $g\text{-}C_3N_4$ nanosheets coated on glass fibre separator	1.2	-	60 µL*	1	553	500	2020	[180]
$g\text{-}C_3N_4$ coated on commercial polypropylene separator	4.0	45	20000	0.2	829	200	2018	[181]
Phosphorus doped $g\text{-}C_3N_4$ coated on polypropylene separator	3.2	-	-	0.5	850	700	2019	[182]
Transition metal coordinated $g\text{-}C_3N_4$ with crystalline carbons coated on polypropylene separator	4.6	-	6	3.3	999	300	2020	[183]
Freestanding interlayer								
$g\text{-}C_3N_4$ coated on flexible and conductive carbon fibre paper	2.21–2.66	-	-	0.1	600	400	2017	[169]
Double layer								
2D carbon-based laminated graphene/$g\text{-}C_3N_4$ layer	0.9 - 1.1	50.9	-	1 2	612.4 407.4	1000 1000	2019	[128]
Uniform film of $g\text{-}C_3N_4$	5	-	20	0.2	720	280	2019	[185]

In conclusion the high polysulfides adsorption ability of graphitic carbon nitride due to the intrinsically high charge polarity of the pyridinic-N functional groups was largely verified. In addition, the chemical and physical intrinsic properties of carbon nitride make it a suitable material for many kinds of approaches relevant in Li-S cell. In many cases, different strategies involving g-C_3N_4 were effectively useful to improve the electrochemical performances of the cell. Many types of doping, many morphologies, and many precursors of carbon nitride were used and investigated in different studies. To date, no systematic studies comparing the role of different carbon nitride precursors, different temperature of synthesis, different doping are reported, using the same test procedures. In fact, most of the reported researchers are difficult to compare, because of different test parameters, such as sulphur mass loading, electrolyte uptake, in addition to the already mentioned different type of adopted strategies.

For these reasons, in my Phd work I decided to compare g-C_3N_4, synthetized starting from different precursor and at different temperatures. A double layer approach was selected as investigation strategy. A more detailed description of the systematic work will be given in the next chapter.

Chapter 5

5 Graphitic Carbon Nitride as interlayer for Li-S system

5.1 Graphitic-Carbon nitride synthetized from different precursors

5.1.1 Structural and morphological characterization

Graphitic carbon nitride can be easily prepared by the direct pyrolysis of various organic precursors, as mentioned in the previous chapter.

The intrinsic physicochemical properties of g-C_3N_4, including morphology, thermal stability, surface area, pore volume, and yield can be closely related to the precursor [188].

In order to investigate the effects of different physicochemical properties of g-C_3N_4 on LiPSs trapping, three different carbon nitride materials were prepared starting from urea ($\geq$ 98 % Sigma Aldrich), dicyandiamide (DCDA, $\geq$ 99.0 % Sigma Aldrich) and melamine (MLM, $\geq$ 99 % Sigma Aldrich), respectively and using the same synthesis conditions.

Urea, dicyandiamide and melamine were used because they are not toxic, cheap and are easily available. In a typical condensation process 6 g of urea, dicyandiamide or melamine were put into a semi-closed alumina boat and heated to 550 °C in a tubular furnace for 3 h with a heating rate of 2.5 °C min^{-1}.

After the reaction, the furnace was cooled to room temperature and the resultant g-C_3N_4 powders were grounded into powder, washed several times with water and ethanol and centrifuged at 10000 - 12000 RPM for 15 minutes.

The different g-C_3N_4 powders prepared starting from urea, dicyandiamide, melamine, were named as: CN-U, CN-D, CN-M, respectively.

XRD analysis was carried out by a PANalytical X'Pert (Cu Ka radiation) diffractometer. Data were collected with a 2D solid state detector (PIXcel) from 10 to 80° 2θ with a step size of 0.026 2θ and a wavelength of 1.54187 Å.

Fourier Transform Infrared Spectroscopy (FTIR) was measured with a Nicolet™ iS50 FTIR spectrometer (Thermo Scientific™) equipped with ATR tool. 32 scans were collected with a resolution of 4 cm^{-1} from 4000 to 400 cm^{-1}.

FESEM analysis was carried out by Zeiss SUPRA™ 40 with Gemini column and Schottky field emission tip (tungsten at 1800 K). Acquisitions were made at acceleration voltage of 3 kV and working distance (WD) between 2.1 - 8.5 mm, with magnification up to 1000 KX.

The Brunauer-Emmett-Teller specific surface area (SSA) was determined by nitrogen physisorption at 77 K using a Micrometrics ASAP 2020 instrument. The specific surface area was calculated with the BET model in the relative pressure range of 0.07 - 0.30 by assuming 0.162 nm^2/molecule as the molecular area of nitrogen.

X-ray photoelectron spectroscopy (XPS) measurements were carried out using a PHI Model 5000 electron spectrometer equipped with an aluminium anode (1486 eV) monochromatic source, with a power of 25.0 W, and high-resolution scan with 11.75 eV pass energy. The instrument typically operates at pressures below 5×10^{-8} mbar.

The yields of the thermal condensation reaction starting from the three different precursors, using the same synthesis condition was evaluated.

The results show that a higher yield was obtained by using Melamine (50 %), followed by dicyandiamide (30 %), while it was significantly lower, around 5 % for urea. This behaviour is due to the chemical structure of the precursors, in fact melamine presents aromatic structure with a 1,3,5-triazine skeleton, on the contrary dicyandiamide and urea are not aromatic compounds, therefore more precursor is loss during the thermal condensation.

Table 5.1: reaction yields of g-C_3N_4 for the three different precursors: melamine, dicyandiamide, urea.

	C_3N_4-M	C_3N_4-D	C_3N_4-U
Yield	~ 50 %	~ 30 %	~ 5 %

The crystal phases of the samples were analysed by X-ray diffraction (Figure 5.1). XRD pattern of the three carbon nitride samples clearly show two peaks at 27.6° and 13.5°, which were assigned to (002) and (100) planes, respectively. The main peak at 27.6 ° (002) was attributed to the strong interplanar stacking of the conjugated aromatic systems while the less pronounced peak at 13.5° was attributed to the in-plane tri-s-triazine units which formed one-dimensional (1D)

melon units [188]. These two diffraction peaks are consistent with the XRD patterns of the g-C$_3$N$_4$ (JCPDS 87-1526).

Analysing the spectra, no particular difference can be seen in the position of XRD peaks for g-C$_3$N$_4$ powders prepared from different precursors, confirming an identical crystal structure of g-C$_3$N$_4$ among all samples [189]. The interplanar d-spacing was calculated considering the strong peak at 27.6° and was approximately around 3.26 Å for all the samples.

In the XRD spectra of carbon nitride obtained from urea the two main peaks are broader and have lower intensity, presumably as a consequence of smaller crystalline domains [190]. The possible explanation for this different peak's shapes of C$_3$N$_4$-U can be attributed to the alternative polycondensation route (see the reaction pathway in the previous chapter) [189]. In fact, according to some authors, during the thermal condensation of urea, heptazine-based structure might not be completely formed, and some structural defects can be present in the final product [190].

The FWHM of the Bragg lines of the g-C$_3$N$_4$ powders, obtained from different precursors was calculated in order to compare the size of crystallites. The average crystallites sizes were 13.18, 40.94 and 31.02 nm respectively for C$_3$N$_4$-U, C$_3$N$_4$-D and C$_3$N$_4$-M.
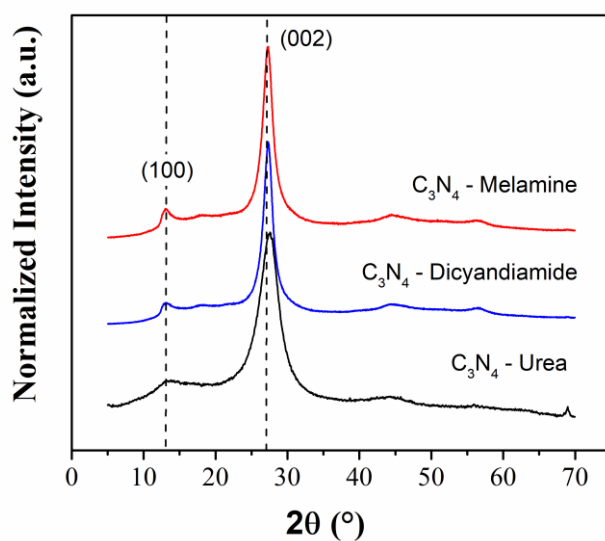
Figure 5.1: XRD patterns for the g-C$_3$N$_4$ samples prepared starting from different precursors.

In conclusion, the XRD patterns are all attributable to carbon nitride structure but the intensity and breadth of the peaks are strictly related to the different nanostructures and morphologies of the as-prepared g-C$_3$N$_4$ samples [188].

The FT-IR spectra of g-C$_3$N$_4$ samples obtained from different precursors are shown in Figure 5.2

All the samples showed some evident groups of signals centred in three different regions of the spectra: 3000 - 3500, 1200 - 1700 and around 800 cm^{-1}.

Absorption peaks in the 700 - 800 cm^{-1} region are typically assigned to the bending vibration mode of carbon nitride heterocycles, in particular the band at 801 cm^{-1} is characteristic of out of plane bending vibration mode of the triazine units [188].

The several bands in the 1200 - 1650 cm^{-1} region corresponds to the typical stretching vibration modes of the heptazine heterocyclic ring (conjugated C=N).

The 2172 cm^{-1} peak is observable only in the C$_3$N$_4$-U spectra and can be assigned to C≡N triple bonds. The presence of this peak indicate that the aromatic unit of g-C$_3$N$_4$ was partly broken and defected [191].

Another interesting difference between the three samples is visible in the 3000 - 3500 cm^{-1} region, where the absorption band at 3170 cm^{-1} is assigned to the stretching mode of O-H while the band at 3336 cm^{-1} can be attributed to the N-H vibration mode [191], indicating the existence of uncondensed amino groups and absorbed H$_2$O molecules in all the samples.

It is worth noting that, in the total spectrum range, the peaks intensity of CN-U is stronger than that of CN-D and CN-M, indicating that urea could improve the polycondensation of g-C$_3$N$_4$ [188]. However, all samples basically maintain the classic carbon nitride structure.
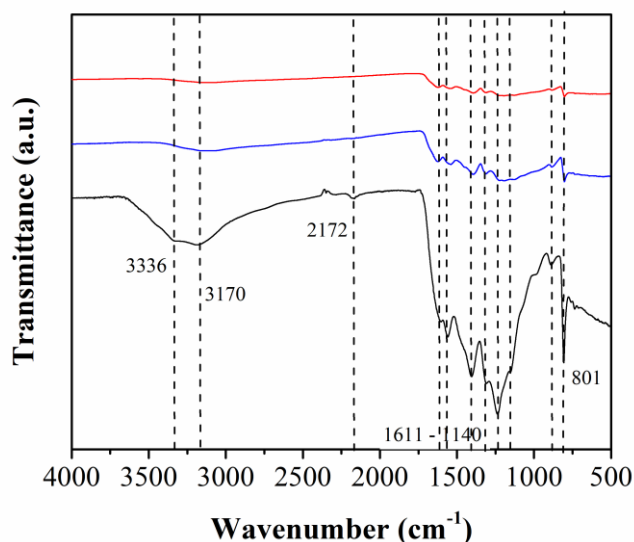
Figure 5.2: FT-IR/ATR spectra comparison of carbon nitride derived from different precursors.

Elemental analysis was further carried out to evaluate the C/N ratio for the different samples. The three carbon nitride samples showed a C/N ratio of 0.57 - 0.58 which is less than the theoretical value of 0.75 or the average value usually found in literature (*e.g.* 0.70). The similar C/N ratio of the different carbon nitride confirms the excess of nitrogen in all the three samples, if compared to the

theoretical values. These observation can be attributed to the incomplete condensation of amino functions, which is correlated to the small, but significant, amounts of hydrogen still present in the compounds [135]. This is the reason why many authors prefer to report the general formula of carbon nitride as $C_xN_yH_z$ [192]. In some cases the determination of C:N:H ratios can be affected to the presence of other elements or the exposure of the sample to air or moisture which can be incorporated into the samples [192]. For example, the evident missing amount reported for CN-U in Table 5.2 can be attributed to oxygen or moisture still present in the sample.

Table 5.2: elemental analysis of carbon nitride obtained from different precursors.

SAMPLE	CARBON %	HYDROGEN %	NITROGEN %	MISSING AMOUNT %	C/N RATIO
C_3N_4-D	35	2.0	60	3.0	0.58
C_3N_4-M	34	2.1	60	3.9	0.57
C_3N_4-U	31	2.5	53	13.5	0.58

To better investigate the chemical state of different element and the surface composition and functionalization, the three different synthetized carbon nitrides were analysed by X-ray photoelectron spectroscopy (Figure 5.3).

The comparison of survey spectra reveal that all the samples predominantly contain C and N elements with some O. The three wide spectra also revealed that there is no significant shift in the binding energy of C1s, N1s and O1s signals, indicating that the surface chemical state of the carbon nitride synthesized by the three different precursors is almost the same. Moreover, the intensity of C1s and N1s are very close, suggesting that the amount of carbon and nitrogen is quite similar in each sample.

To better understand the carbon nitride chemical structure, calculating the C/N ratio and quantify the N species present in the samples the C1s and N1s spectra were deeply investigated at high resolution (Figure 5.3 b-g). Unfortunately, the quantitative XPS analyses of carbonaceous materials is hindered by the presence of an ''adventitious'' C1s signal deriving from the carbon tape used to mount the samples. However, a small signal of silicon was also detected and used to evaluate the contribution of carbon tape to the C1s spectra.

The C1s core level spectra for all samples was deconvoluted into four components: sp^2 hybridized C atoms (284.8 eV), C–O (286.2 eV), N–C=N (288.0 eV) and C=O (288.9 eV). The C1s spectrum of CN-D, was deconvoluted in five components instead of four, and in addition to the already mentioned peaks, also a peak centred to 290.2 eV, attributable to O=C–O was individuated. The CN-D analysis was repeated, obtaining the same results and confirming the presence of five contributes.

Unfortunately, as mentioned before, the presence of carbon tape signals, could interfere with the measure. Typically, the carbon tape C1s spectra presents a main C–C peak at 284.8 eV and weak peaks at higher binding energy values due to C–O (286.1 eV) and O–C=O (288.7 eV) species, attributable to surface oxidation of the carbon film [192].

For these reasons the high definition N1s spectrum deconvolution can be helpful to give more information about the carbon nitride surface chemistry.

The N1s spectra of the analysed samples were deconvoluted into three main components. In particular, the peak at 398.5 eV was attributed to hybridized nitrogen in C–N bonds (C=N–C) of triazine rings, the second fitted peak at 399.6 eV was assigned to tertiary nitrogen N–(C)$_3$ groups, lastly the peak at 401.1 eV was assigned to H–N–(C)$_2$ groups. No signals were detected at 403 eV attributable to N–O species.
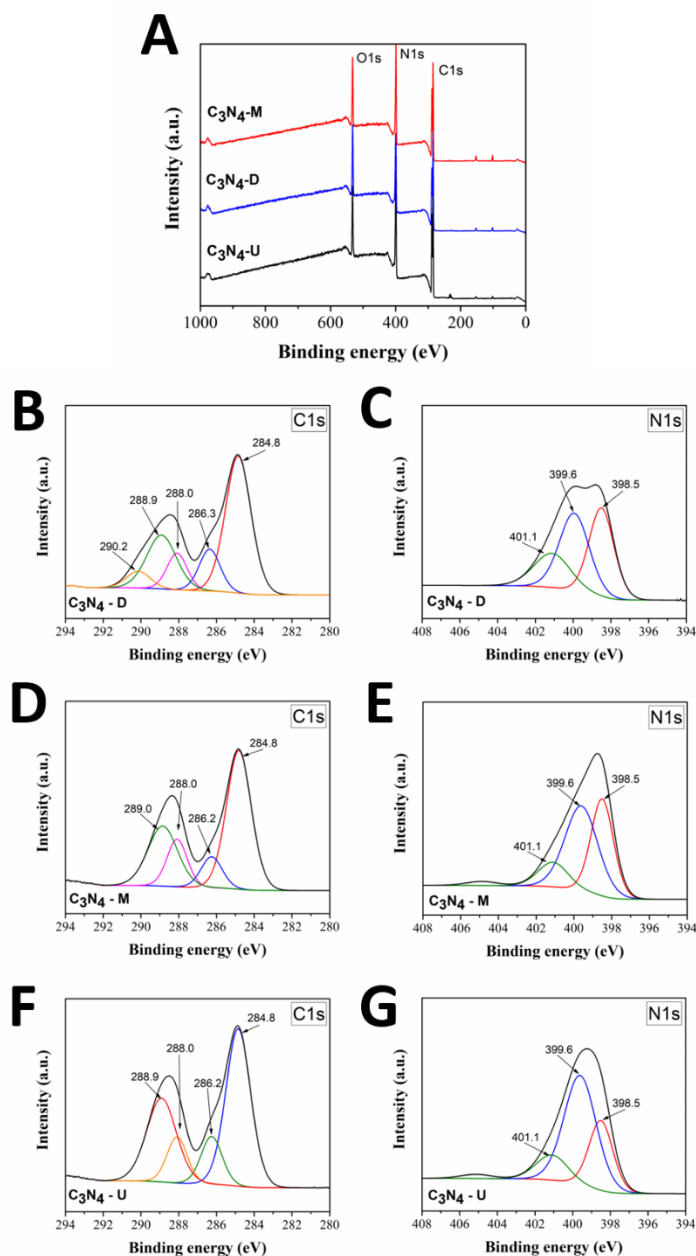
Figure 5.3: XPS survey spectra comparison (a), C1s and N1s of CN-D (b, c), CN-M (d, e) and CN-U (f, g).

In conclusion the 288 eV peak in C1s can be reasonably assigned to sp^2 bonded C atoms associated with triazine or heptazine units. At the same time 398.6 eV peak in N1s spectra can be assigned to C–N=C units within triazine or heptazine rings, while 401.1 eV peak is indicative of C–N–H uncondensed amino groups, and 399.9 eV is attributable to the central N atoms bridging between three heptazine rings (N–(C)$_3$ units) [192].
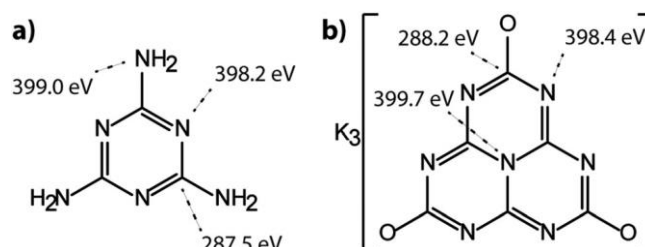
Figure 5.4: molecular representations of carbon nitrides with characteristic binding energies indicated for specific sites and groups within the compounds: melamine (a) and simil-heptazine (b) [192].

Table 5.3 shows the deconvolutions results of C1s and N1s spectra for all the samples. The labels "Area" refers to the relative areas of the species within the all analysed signal, while "Area relative" refers to the area of the species in relation to C and N peaks. In the calculation of % C *, the contribution of the carbon tape signals was subtracted.

Table 5.3: relative percentage of C and N species area of CN-D, CN-M and CN-N calculated by high resolution XPS spectra deconvolution.

Binding energy (eV)	Specie	CN-D		CN-M		CN-U	
		Area %	Area relative %	Area %	Area relative %	Area %	Area relative %
398.5	C=N–C	38.25	10.74	37.37	10.82	27.40	8.20
399.6	N– (C)$_3$	40.04	11.24	47.74	13.82	57.29	17.16
401.1	H–N(C)$_2$	21.71	6.10	12.65	3.66	13.13	3.93
403.0	N–O	-	-	-	-	-	-
284.8	Csp^2 Csp^3 Cadv	49.32	35.47	50.31	35.75	46.91	32.86
286.3	C–O	12.32	8.87	9.56	6.79	12.10	8.48
288.1	N–C=N	10.35	7.44	14.06	9.99	11.15	7.81
288.9	C=O	22.37	16.09	26.07	18.53	29.83	20.90
290.1	CO$_3^{-2}$	5.62	4.04	-	-	-	-
	%N	32.48		35.25		38.26	
	%C*	67.52		64.75		61.75	
	N/C	0.48		0.54		0.62	

The morphological characterization of the prepared samples was performed by FE-SEM investigation. The FE-SEM images of g-C_3N_4 samples derived from different precursors are depicted in Figure 5.5.

It can be seen that all the g-C_3N_4 particles exhibit wrinkles and irregular shapes. In particular, CN-D and CN-M consist of large amounts of dense and thick nanosheets with irregular shape assembled together, resulting in a condensed morphology (Figure 5.5 a, d, b, e).

On the contrary CN-U presents dispersed smooth and thin irregular flakes with characteristic porous morphology (Figure 5.5 c, f). The typical porous structure was due to the different reaction pathway of urea instead melamine and dicyandiamide.
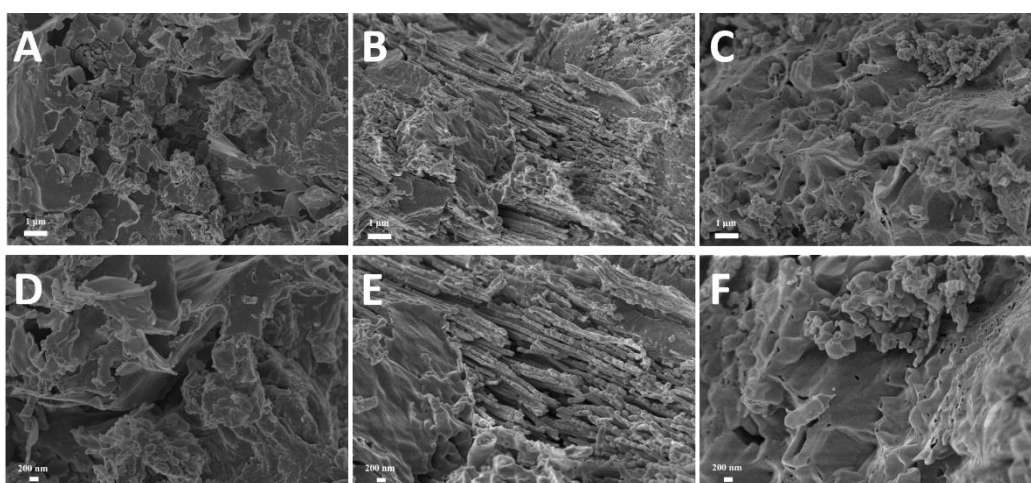
Figure 5.5: FESEM micrographies of STD+CN-D (a, d), STD+CN-M (b, e) and STD+CN-U (c, f) at 25 and 50 KX respectively.

The morphological observations are in good agreement with the surface area values and pore distribution, obtained by the BET method (Figure 5.6).

All the synthetized samples have similar nitrogen adsorption-desorption isotherms, and all belong to the Type IV isotherm with H3 loop corresponding to monolayer coverage and multilayer adsorption typical for non-rigid aggregates of plate-like particles [193]. The specific surface areas were 4.5, 5.1 and 44.8 m^2 g^{-1} for CN-D, CN-M and CN-U respectively, while pore volume calculations let us to suppose that all samples have negligible microporosity and some disordered interparticle mesoporosity. CN-U shows higher specific surface area and higher porosity, confirming the different morphology of this sample in comparison to the other obtained from different precursor.

71
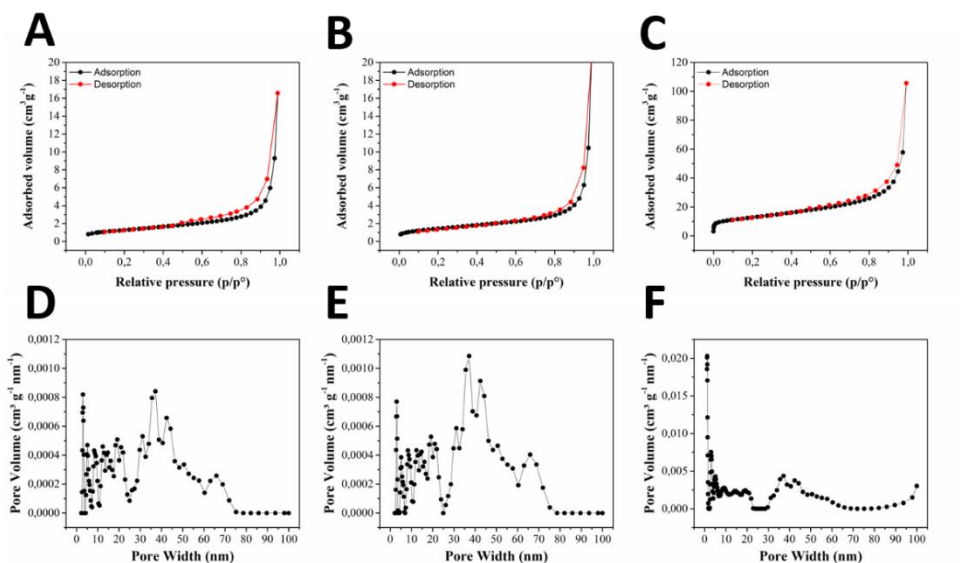
Figure 5.6: N_2 adsorption-desorption isotherms and the corresponding pore-size distribution curves for: CN-D (a, d), CN-M (b, e) and CN-U (c, f).

More precisely, both the specific surface areas and pore volumes of CN-U are one order of magnitude higher than the ones of CN-D and CN-M, as reported in Table 5.4. The different morphological characteristics obtained for CN-U are probably due to the particular synthetic route of carbon nitride from urea, which induce the formation of large amount of gas such as NH_3 and H_2O favouring the expansion of the packing layers and porous structure. In particular the presence of oxygen heteroatom in urea, influence the thermal condensation process, originating water vapor which can act as "soft template" producing porous structure and inducing the expansion of carbon nitride layers [190].

Table 5.4: specific surface area and pore volume for carbon nitride obtained from different precursors.

Sample	SSA$_{BET}$ (m² g^{-1})	Pore volume (cm³ g^{-1})
CN-D	4,5671	0,025650
CN-M	5,1441	0,032037
CN-U	44,8938	0,069018

As previously observed, the higher porosity and the higher specific surface areas of the urea-derived g-C_3N_4 can enhance the electrochemical properties of the carbon nitride [190]. In particular, the higher surface area facilitates the mass transfer providing more active sites for surface-dependent reactions. At the same time structural defects resulting from the lack of a proper s-triazine structure can generate more catalytic active sites for PSs interaction [190].

To further evaluate the polysulfide adsorption capability of various carbon nitrides a visual adsorption test under argon atmosphere was performed. More precisely a solution 0.1 M of Li_2S_6 was prepared directly reacting Li_2S and S_8 (ratio 1:5 in weight) into a mixture of DME and DIOX (1:1 by volume) for 72 h at 70 °C, under continuous stirring in argon atmosphere. Li_2S_6 was chosen because it is a representative soluble long-chain polysulfide species

The resulting brownish-red Li_2S_6 solution was then diluted to 1 mM for the polysulfide adsorption test. Successively, a quantity of different carbon nitride equivalent to 0.5 m^2 surface area was added to 20 μL of 1 mM of Li_2S_6 solution diluted in 2 mL of DME:DIOX 1:1 v/v mixture and left to interact for 12 hours [194].

After adding carbon nitrides materials to the Li_2S_6 solutions the colour appears yellow, for all three samples as depicted in Figure 5.7 (a). The solution containing CN-U appears paler, due to the intrinsic colour of carbon nitride obtained from urea, which is closer to pale yellow.

After resting the samples for 12 hours, without any form of stirring, only the solution containing carbon nitride obtained from urea results transparent (Figure 5.7 b). On the contrary, the solution containing carbon nitride synthetized from melamine presents no observable colour fading, while the one containing CN-D shows only a mild discolouration. Accordingly, the interaction between CN-U and LiPSs is stronger than carbon nitride obtained from other precursors.

The consistent colour fading, clearly observable after 12 hours, confirms the strong interaction between lithium polysulfides and carbon nitride, especially for the one synthetized from urea. It is worth noting that, the added amount of 0.5 m^2 for CN-U is definitely less in comparison to the others based on the surface area, so the active sites accessibility is particularly important for a good physico-chemical interaction.

To better investigate the interaction of synthetized materials and LiPSs, other 20 μL of 1 mM of Li_2S_6 were added to the solution (Figure 5.7 c) and once again after 12 hours the solution in contact with CN-U presents a remarkable colour fading as depicted in Figure 5.7 (d). On the contrary the colour fading for the other two solutions, containing respectively CN-D and CN-M, was not so consistent.
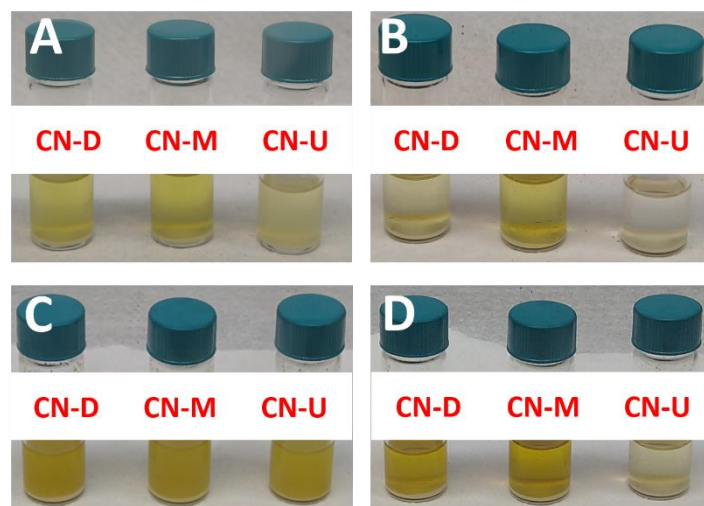
Figure 5.7: lithium polysulfides adsorption test: 20 μL of Li_2S_6 1 mM at 0 h (a), after 12 h (b), 40 μL of Li_2S_6 1 mM at 0 h (c) after 12 h (d).

Lastly Figure 5.8 shows the comparison between a pure Li_2S_6 reference solution, a Li_2S_6 solution with 0.5 m^2 of KjB and Li_2S_6 solution with CN-U at 0 hours and after 12 hours.

It is possible to observe in Figure 5.8 b LiPSs solution containing CN-U showed an evident discoloration after 12 hours, confirming that carbon nitride has relevant adsorption capability for LiPS. On the contrary KjB, involved only a mild discoloration of the Li_2S_6 solution, confirming that the interaction of KjB is not sufficient for high sulphur loadings.
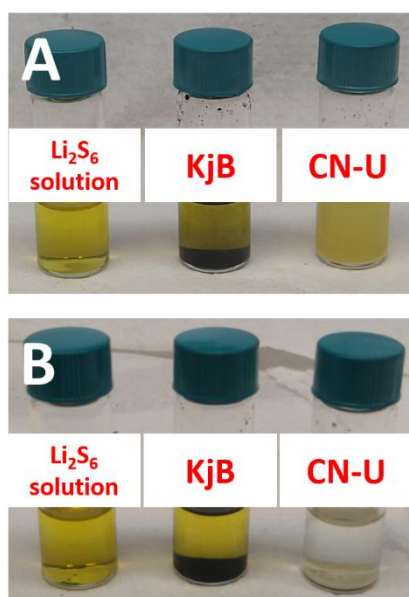
Figure 5.8: lithium polysulfides adsorption test: 40 μL of Li_2S_6 1 mM at 0 h (a), after 12 h (b).

In summary, carbon nitride obtained from urea seems the best candidate to be used for lithium polysulfide trapping. The reason of better interaction can be assigned to the morphology, because CN-U presents a SSA one order of magnitude higher than the other samples, this inevitably increase the active sites able to give interaction with LiPSs. On the other side the different surface chemistry of CN-U, which is particularly rich of pyridinic nitrogen can be the second reason of the interesting reaction with LiPSs species.

To investigate the possible direct application of carbon nitride as additive in lithium sulphur battery a double layer approach was adopted, and the electrochemical results will be discussed in the next paragraph.

5.1.2 Electrochemical characterization

The carbon nitride behaviour was investigated using a double layer approach, inside a lithium sulphur cell.

This approach was chosen to guarantee a good interaction between LiPSs (originated during the charge/discharge processes) and carbon nitride. Moreover, carbon nitride, which has neither an optimal mesoporosity nor an optimal electronic conductivity, is not mixed directly with sulphur in the standard cathode formulation. Hence, in the first layer, sulphur is directly in contact with the conductive carbon, which is a good electron conductor for the electrochemical reaction, while the second layer allows a good distribution of carbon nitride and higher possibility for this material to carry out its trapping function (Figure 5.9).
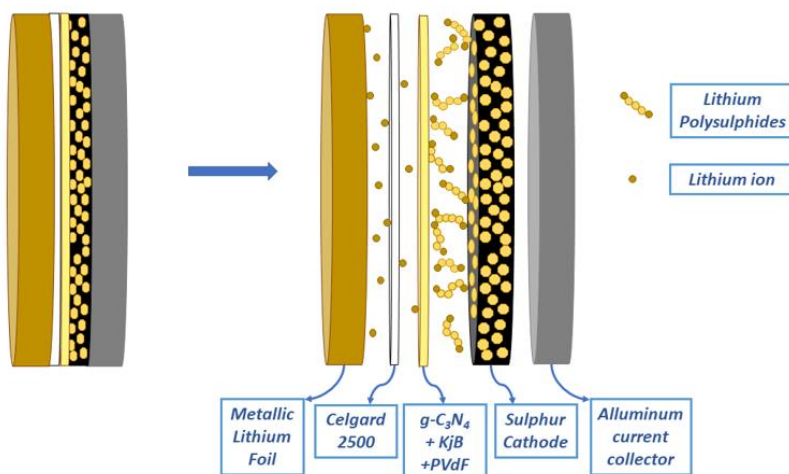
Figure 5.9: schematic configuration of a Li-S cell with a double layer cathode electrode.

All the working electrodes used in the experimental part were prepared by solvent tape casting method. The so called "standard" sulphur cathode electrode was prepared using pure sulphur (≥ 99.5 % Sigma Aldrich) as active material,

Ketjenblack® (EC-300J, AkzoNobel), as conductive carbon additive and poly(vinylidenedifluoride) (PVdF, Solvay; 10 wt.% in N-methyl-2-pyrrolidinone solution) as polymeric binder.

The "standard" electrode composition was set up 60/30/10 wt.% respectively for (S/KjB/PVdF), for all the experiments of this section. This ratio was arbitrarily chosen, with the aim to obtain a cathode with high sulphur loading, using a simple mixing procedure and keeping in mind the practical application of the electrodes and their industrial scale-up.

The precise amounts of sulphur and Ketjenblack®, were first manually grinded together in an agate mortar and then transferred in a 2 mL Eppendorf tube, where an appropriate amount of PVdF solution (10 wt.% in NMP) was added and an additional volume of NMP was also incorporated in order to obtain an optimal viscosity of the ink. At the end the Eppendorf tube was inserted in a jar and ball milled for 15 minutes at 30 Hz.

The final mixture was mechanically deposited on the aluminium current collector by Doctor Blade technique. The blade was adjusted for 200 μm deposition using an automatic film applicator (Sheen 1133N) with a speed of 50 mm s^{-1}. After the slurry deposition the coated aluminium foil dried at 50 °C in air.

A similar procedure was used to obtain the double layer cathode. The dried standard electrode was first obtained following the previously mentioned procedure, which was subsequently coated by a second layer containing carbon nitride. The ratio between CN, KjB and PVDF, contained in the second layer slurry was 80:10:10, while the adopted blade thickness remains 200 μm, as depicted in Figure 5.10.

After solvent evaporation in air, disks of 2.54 cm^2 were punched out, vacuum dried at 40 °C (in a Büchi Glass Oven B-585) for 4 h, then transferred into an Argon filled dry glove-box (MBraum Labstar, H$_2$O and O$_2$ content < 1 ppm) for cell assembly.

The active material loading of the "standard" sulphur cathode electrode was ~ 1 mg cm^{-2}.

The electrodes were assembled in 2032 coin-type cells with lithium disk (Chemetall Foote Corporation, Ø 16 mm) as counter electrode and PP polymeric membrane (Celgard 2500, 25 μm thickness, Ø 19 mm) as separator. The electrolyte used for the experiments was a solution of 1,2-dimethoxyethane (DME) and 1,3-dioxolane (DIOX) 1:1 (v/v) with 1 M lithium bis(trifluoromethanesulfonyl)imide (CF$_3$SO$_2$NLiSO$_2$CF$_3$, LiTFSI) and 0.25 M LiNO$_3$ (LiNO$_3$, ≥ 99.9 % Sigma Aldrich). The electrolyte amount for each kind of experiment never exceeds 20 μL, corresponding to ~ 11 μL mg^{-1} (referred to S quantity).

The electrolyte was prepared in an argon-filled glove box by dissolving lithium nitrate and LiTFSI, in a 1:1 (v/v) mixture of DME and DIOX. Lithium nitrate was selected as an additive because of its beneficial effect against polysulfide shuttle. The solution was stored in argon filled glove box for at least 12 h before the use.
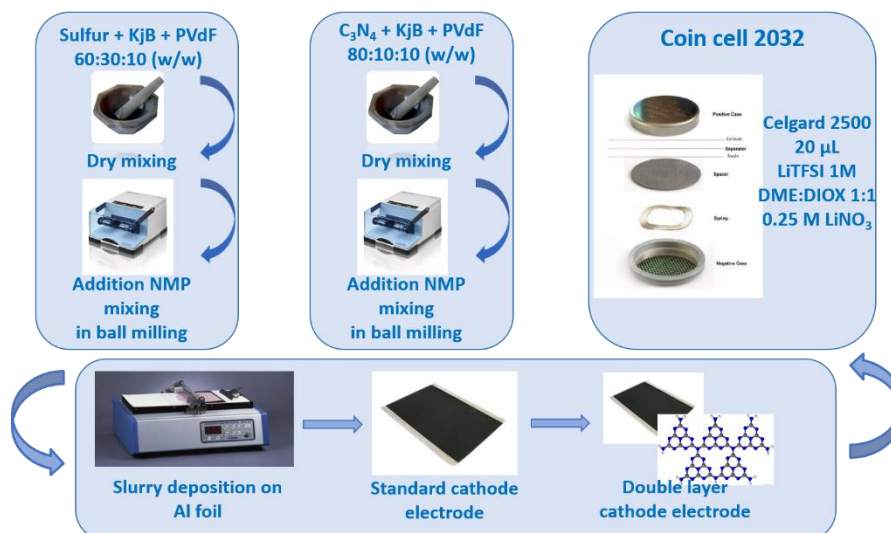
Figure 5.10: double-layer electrode preparation scheme.

The cycling performances of the cathodes were investigated by means of galvanostatic discharge-charge cycling (GC) using an Arbin LBT-21084 battery tester at room temperature. Galvanostatic discharge-charge test were carried out in the potential interval 1.8 - 2.6 V vs. Li^0/Li^+ at different current rates. The C-rate is calculated using a theoretical capacity of sulphur (1672 mAh g^{-1}). For cyclic voltammetry (CV), the electrode potential was reversibly scanned between an extended range from 1.7 to 2.8 V vs. Li^0/Li^+ at 0.1 mV s^{-1}.

It is worth underlining that all results reported here were carefully selected to keep the best reproducibility and reliability. In most cases, the data were obtained from few cells tested in parallel. Nevertheless, experimental results could be affected by some error, such as the non-homogenous morphology of the electrodes, associated to the manual preparation of the electrodes.

For all these reasons the obtained electrodes have been carefully selected based on their weight and morphology. The electrodes with obvious discrepancies were appropriately discarded.

Below (Figure 5.11) is shown the chart reporting the weight distribution measured for about 90 standard cathode electrodes. The statistical evaluation reported an average weight around 12.3 mg with a standard deviation of 0.45 with a minimum and maximum value respectively of 11.2 and 13.3 mg. According to the statistical analysis only the samples in the range of 11.8 - 12.8 were considered.
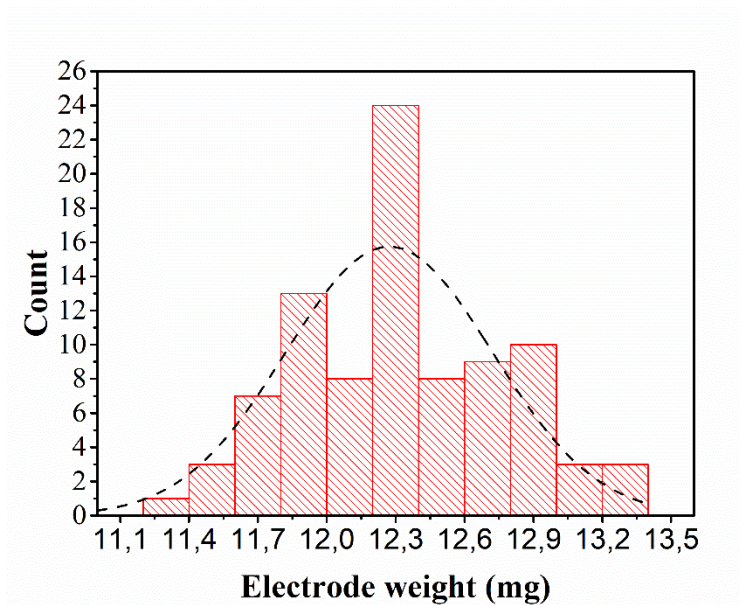
Figure 5.11: weight distribution of prepared standard cathode electrodes

In Figure 5.12 is reported the picture of the dried electrode (left) and the FESEM micrography of the electrode cross section (right, STD+CN-U electrode). In the left image of the picture the aluminium foil, the single layer and the double layer are easily distinguishable. In particular, the single layer "standard electrode" presents a black colour, due to the huge amount and wide distribution of the carbon black, while the second layer, containing around 80 wt.% of carbon nitride, appears grey coloured. Thus, the presence of a second layer is properly visible. In the cross section, obtained by FESEM, it is also possible to distinguish the standard Li-S cathode (bottom layer), where only the KjB particles are clearly visible, while the second layer (top layer), is rich of flakes structure, typical of carbon nitride.
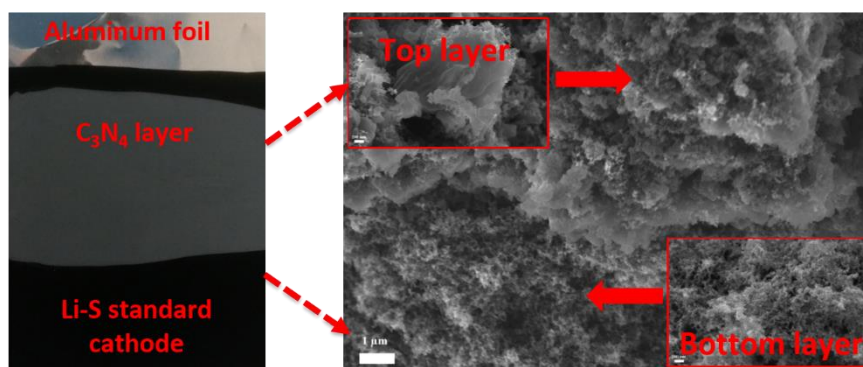
Figure 5.12: picture of dried electrode (left), FESEM micrography of STD+CN-U electrode cross section (right).

The top cathode electrode morphology was also investigated by FESEM (Figure 5.13). The morphology of the single layer standard electrode does not appear smooth, but some evident prominences are visible (Figure 5.13 a). These are due to sulphur agglomerates, which are covered and enrobed by Ketjen black particles. The standard electrode morphology is reasonable because no melt infusion or solvent impregnation were used for the active material fabrication.

On the contrary, the electrodes with the second layer of carbon nitride, seem less wrinkled (Figure 5.13 b, c, d). In particular, the surface of the electrode with CN from urea (Figure 5.13 d) appears homogeneous, compared to the other samples. In CN-U the superficial cracks are less pronounced compared to CN-D and CN-M, this behaviour is probably correlated to the different morphology of the sample.

The magnification of the electrode surface (Figure 5.13 e, f, g, h) confirms a good distribution of carbon nitride in the electrode with CN-U. For all double-layer electrodes, only carbon nitride and Ketjen black are visible and no sulphur agglomerates are directly detected. The absence of sulphur agglomerates is due to the high temperature reached by the electron source and the concomitantly low melting point of S_8, which immediately melts under the electron gun.

The electrodes with CN-D (Figure 5.13 f) and CN-M (Figure 5.13 g) presents a large amount of typical dense and thick nanosheets with irregular shape already observed in the morphology of pure CN powders. At the same time the electrode with CN-U shows well dispersed porous, smooth and thin irregular flakes immersed in KjB matrix (Figure 5.13 h).
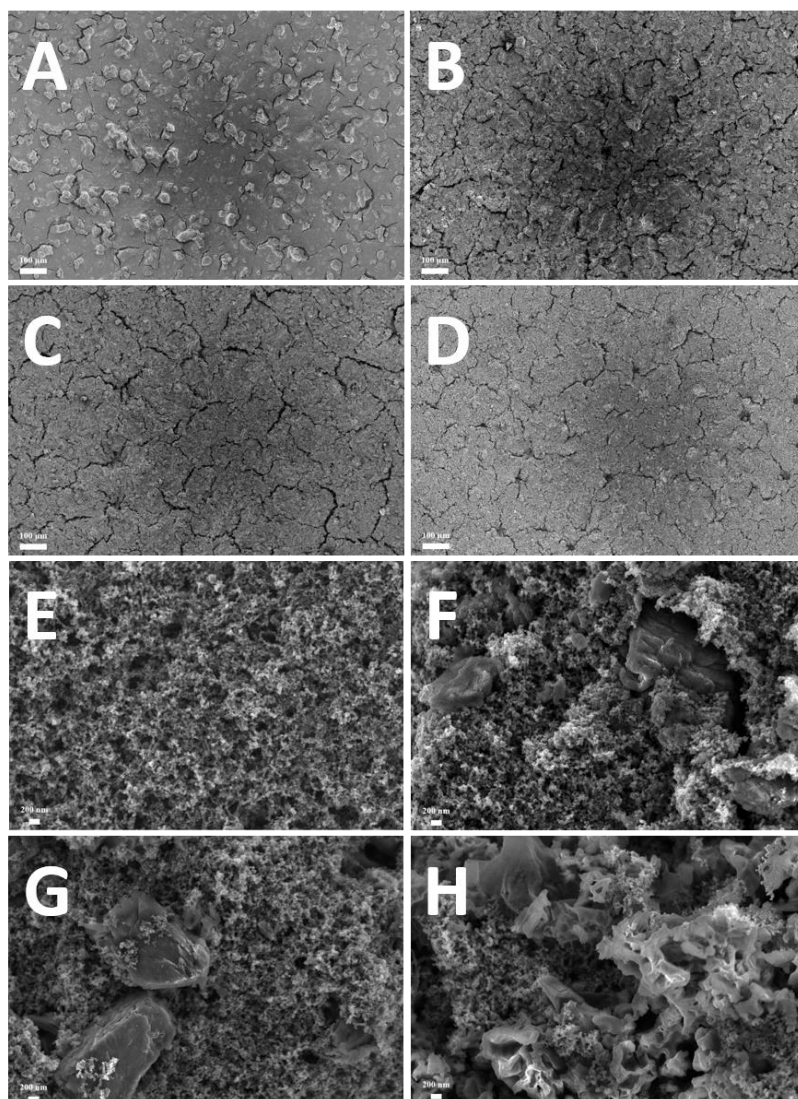
Figure 5.13: FESEM micrographies of sulphur cathode electrode at 250 X for: STD KjB/S cathode (a), STD+CN-D (b), STD+CN-M (c), STD+CN-U (d). FESEM micrographies of sulphur cathode electrode at 50 KX for: STD KjB/S cathode (e), STD+CN-D (f), STD+CN-M (g), STD+CN-U (h).

EDS analysis was carried out to investigate the superficial elemental distribution in the electrodes (Figure 5.14). For each sample at least 3 areas were investigated to obtain a general information about the distribution of the elements. For the standard electrode only carbon, fluorine and sulphur were detected (Figure 5.14 a, Table 5.5). Fluorine comes from to the binder and is present in all the samples less than 10 % by weight. The sulphur amount in standard electrode is around 21 wt.%, while is 7.6, 6.4 and 5.5 respectively for double layer with CN-D, CN-M and CN-U (Table 5.5).

The carbon amount is reasonably high for standard electrode while stands around 33 - 36 wt.% for the double layer cathodes.

Nitrogen was not detected in single layer cathode, but it was detected for all the double layer electrodes, in particular the percentage amount is sensibly higher

for electrode containing CN-U, in which is attested around 38 %wt (Figure 5.14 d, Table 5.5).
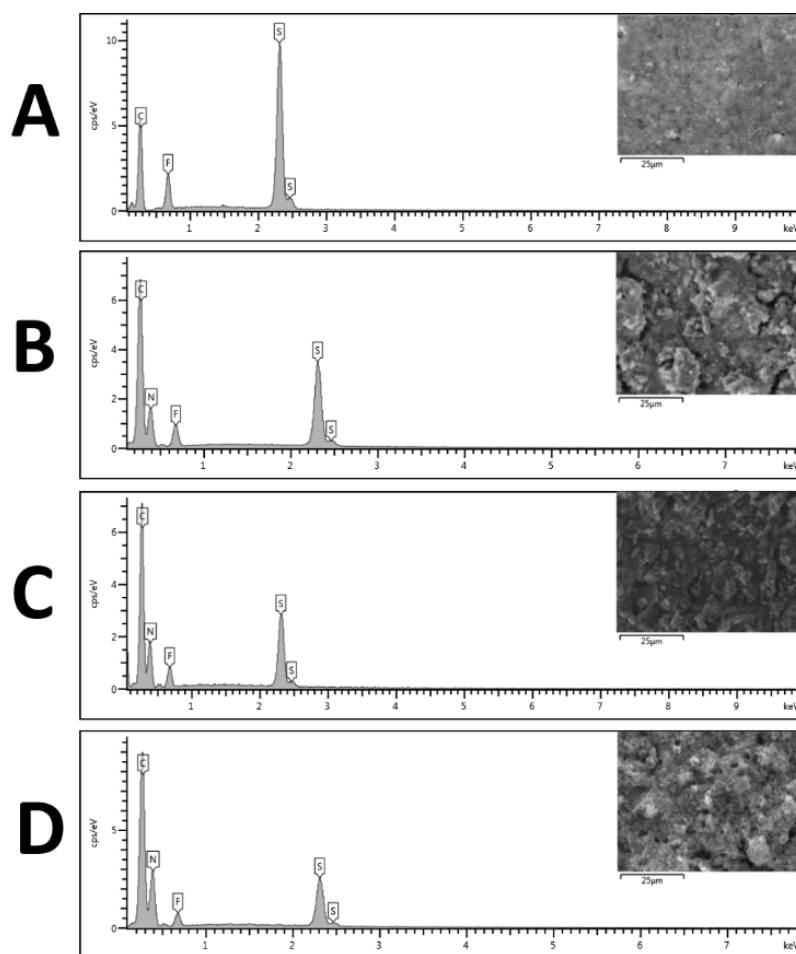
Figure 5.14: EDS superficial analysis for standard (a) and double layer electrodes containing: CN-D (b), CN-M (c) and CN-U (d).

Table 5.5 reports the weight and atomic percentages for all the elements detected in each sample.

Table 5.5: EDS element analysis for standard and double layer electrodes.

	STD		CN-D		CN-M		CN-U	
Element	Wt%	Atomic %	Wt%	Atomic %	Wt%	Atomic %	Wt%	Atomic %
C	55.51	81.26	35.56	56.42	33.65	54.10	36.45	49.56
N	-	-	25.62	34.86	27.71	38.20	38.37	44.75
F	7.79	7.21	4.21	4.22	3.79	3.85	3.33	2.86
S	21.03	11.53	7.58	4.50	6.39	3.85	5.54	2.82
Total:	84.33	100.00	72.97	100.00	71.54	100.00	83.70	100.00

Figure 5.15 shows the cyclic voltammetry profiles for ten successive cycles at a scan rate of 0.1 mV s^{-1}, within the cut-off potentials of 1.6 - 2.8 V. All the curves demonstrate typical sulphur cathode CV behaviour. As expected, the two peaks detected during the initial cathodic reduction process, correspond to two different redox processes. The first reduction peak at 2.23 V corresponds to the reduction of sulphur (S$_8$) to soluble long-chain lithium polysulfide (Li$_2$S$_x$, 4 < x < 8), while the second reduction peak centred at 1.95 V is assigned to the further conversion of long-chain LiPSs to insoluble short-chain lithium polysulfides (Li$_2$S$_2$ or Li$_2$S). By contrast, during the oxidation process, two nearly overlapping anodic peaks at 2.45 V and 2.55 V were observed. These peaks represent the formation of both higher order polysulfides and successively elemental sulphur, by the oxidation of lower order LiPSs.

As observable in Figure 5.15 (e) the reduction and oxidation peaks potential of double layer coated electrodes are shifted if compared to single layer electrode peaks positions. More in detail the two reduction peaks of double-layer electrodes are shifted at lower potential while the oxidation peaks move toward higher potential if compared with the single-layer standard cathode. This phenomenon can be related first to the semiconducting nature of carbon nitride, secondly to the presence of the second layer which inevitably increases the polarization of the electrode [175]. This observation is particularly true for the first cycle, while for the other cycles a slight shift of the peaks, minimizing the polarization, is clearly visible for all three double-layer electrodes (Figure 5.15 a, b, c, d).

Lastly, the intensity of CV curves slightly decreases during cycling for all the samples (Figure 5.15 a, b, c, d), but for the electrode containing CN obtained from urea (Figure 5.15 d) the peaks current underwent very little change as the cycle proceeded and the curves are more overlapped showing a good reversibility of the systems.
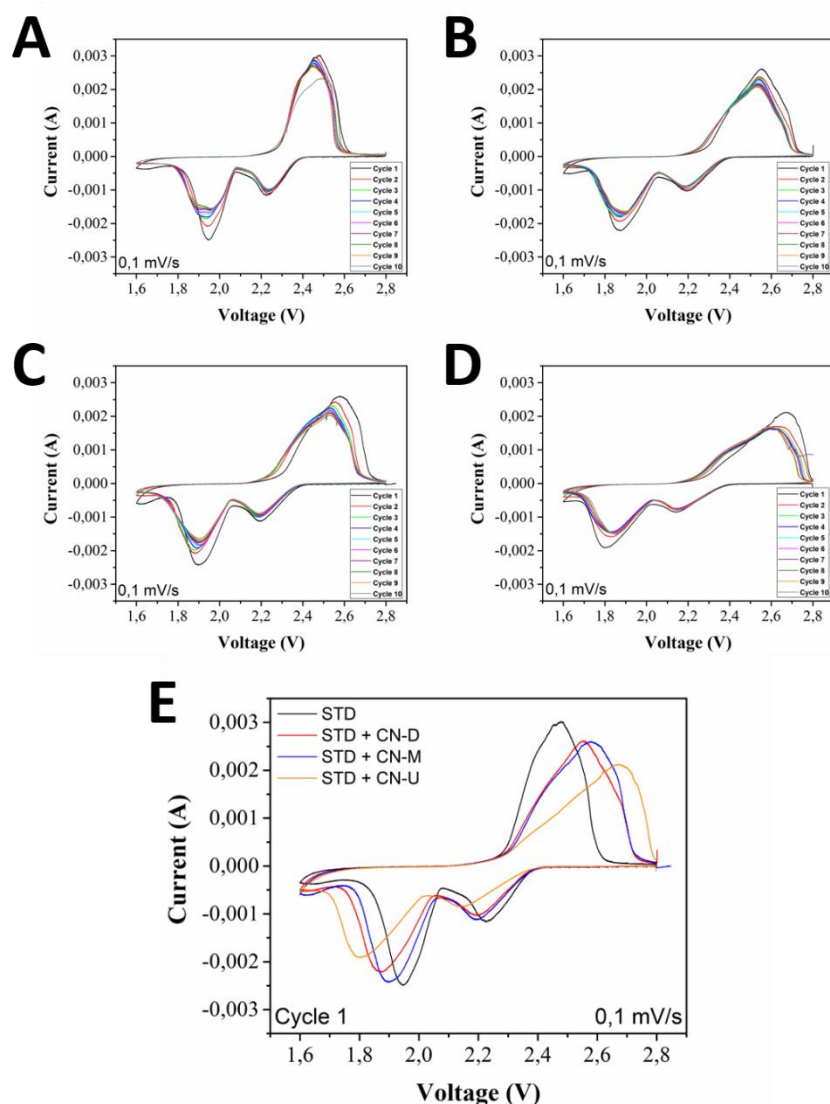
Figure 5.15: cyclic voltammetry curves at 0.1 mVs-1 for single-layer standard cathode (a), double-layer cathode CN-D (b), CN-M (c), CN-U (d) and first cycle comparison (e).

The galvanostatic charging and discharging behaviour of the cathodes was compared at C/5 for 200 cycles, after three activation cycles at C/10 (Figure 5.16 a).

Figure 5.16 (b) shows the first-cycle galvanostatic voltage profiles at C/10 of standard single-layer and the three double-layer electrodes, which all exhibit the typical two plateau discharge curves. The first, at 2.3 V, is attributable to the reduction of sulphur to long-chain LiPSs, and the second at 2.1 V corresponds to the reduction into short-chain LiPSs.

The four cathodes delivered an initial discharge capacity at C/10 of about 780, 870, 1010 and 1150 mAh g^{-1} for STD, STD+CN-D, STD+CN-M and STD+CN-U respectively.

The initial higher capacity of double-layer electrodes could be due to the contribution of g-C$_3$N$_4$ which, according to Qu *et. al.* [128], delivers a discharge capacity of about 93.6 mAh g^{-1}, in the considered potential range, during the first

5 cycles. A second possible explanation for the higher initial capacity can be a partial rearrangement of the active sulphur material after the initial charge-discharge cycle, in particular the carbon nitride-based second-layer can reduce the capacity loss originating from the rearrangement of sulphur during the first cycles [128].
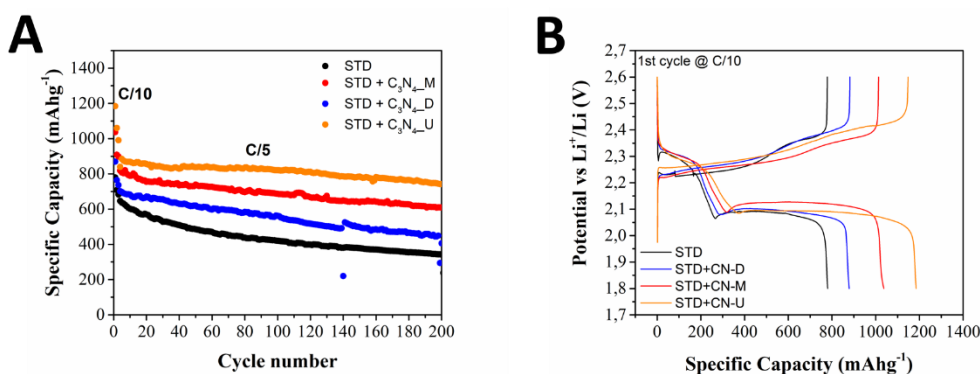
Figure 5.16: cycle performance comparison (a) and first cycle galvanostatic charge–discharge profiles comparison at C/10 (b) between single-layer cathode and double-layer cathodes.

After 200 cycles, the discharge capacity at C/5 was attested around 340 mAh g^{-1} for the single layer electrode while it was 406, 609 and 740 mAh g^{-1} for the double layer electrodes containing CN-D, CN-M and CN-U (Figure 5.16 a), respectively.

The capacity retention (considering the first and last cycle at C/5 after 200 cycles) is higher for the double-layer electrodes resulting 88.1 % for STD+CN-U and 73.9 %, 58.0 % and 52.6 % for STD, STD+CN-M and STD+CN-D, respectively. This means that the capacity fade of the STD+CN-U is only 0.06 % per cycle. The coulombic efficiency at 200th cycle is higher than 99 % for all the samples (Table 5.6).

Table 5.6: electrode performances comparison between single-layer cathode and double-layer cathodes.

	Specific capacity @ 1st cycle @ C/5 (mAh g^{-1})	Specific capacity @ 200th cycle @ C/5 (mAh g^{-1})	Capacity retention (4th – 200th cycle) (%)	Coulombic efficiency 200th cycle (%)
STD	780	340	52.6	99.16
STD+CN-D	870	406	57.9	99.27
STD+CN-M	1010	605	73.9	99.59
STD+CN-U	1150	740	88.1	100.00

In general, double-layer electrodes show good cycle performances, suggesting an enhanced interaction between the polysulfides and carbon nitride. In particular,

the electrode containing carbon nitride synthetized from urea shows the best performances in terms of specific capacity, capacity retention and coulombic efficiency, suggesting that CN-U has better chemical and morphological feature towards LiPSs trapping. For this reason, the electrochemical behaviour of CN-U was further investigated.

Galvanostatic charge–discharge curves of single- and double-layer cathodes of the first cycle at C/10 rate are reported in Figure 5.17 (a, b).

The overpotential of the electrodes was calculated measuring the voltage hysteresis (ΔE) between charge and discharge curves at 50 % of the total discharge capacity ($Q_{1/2}$) for the first cycle. The single-layer standard sulphur cathode presented an initial polarization potential of 0.17 V, whereas the double layer cathode polarization reached 0.23 V.

The large overpotential observed in first cycles should be ascribed to the initial wetting process between the cathode and the electrolyte, and this is particularly true for the double-layer electrode, where sulphur is confined in the bottom layer and so the electrolyte needs more time to reach it. Moreover, the presence of carbon nitride in the electrode surface decreases the conductivity of the double-layer cathode, which inevitably exhibits a slightly larger overpotential than that of the single-layer cathode.

Regarding the first cycle discharge capacity of single-layer cathode, the upper plateau capacity (Q_1) and the lower plateau capacity (Q_2) were respectively 269 and 510 mAh g^{-1} respectively, corresponding to a total discharge capacity of about 779 mAh g^{-1} which is definitely lower than sulphur theoretical value of 1675 mAh g^{-1}. On the contrary the upper plateau discharge capacity of double-layer cathode was 374 mAh g^{-1} while the lower plateau capacity was around 808 mAh g^{-1}, which summed together correspond to a total discharge capacity of 1182 mAh g^{-1}, which means a 34 % higher capacity than the standard single-layer cathode.

The corresponding Q_1 and Q_2 values of the single-layer electrode are approximately 35 and 65 %, respectively, while they are 32 and 68 % for the double-layer, which means that the percentage contribution of upper-plateau discharge, due to long-chain LiPSs is lower for the cathode containing carbon nitride.

Considering the charge/discharge curves from the 1st to 200th cycle (Figure 5.17 c, d), the polarizations increases as current density rises, from C/10 to C/5. Larger polarization of double-layer electrode is seen at higher C-rate, while the overpotential of single-layer standard cathode is quite constant at C/5.

As depicted in Figure 5.17 (d), the polarization of STD + CN-U increases from C/10 to C/5 (3rd to 5th cycle) but decreases from 5th to 200th cycle at a constant C-rate of C/5. This means that after some "activation" cycles, the initial polarization effect is mitigated, due to the presence of carbon nitride.

The decrease of specific capacity (ΔQ) related to the upper plateau, between the 1st and 200th cycle, is around 147 mAh g^{-1} for the single-layer and 115 mAh g^{-1} for STD + CN-U electrode (Figure 5.17 c, d).

85

As thoroughly mentioned in the previous chapter, the region of the upper discharge plateau is ascribable to the formation of soluble long-chain polysulfides. Therefore, it is possible to assume that the decrease of specific capacity (ΔQ) related to the upper plateau, is mainly due to the formation and diffusion of soluble polysulfides into the electrolyte medium, which induces the irreversible loss of active sulphur. For this reason, the values of ΔQ can be directly correlated to the suppression of polysulfide diffusion [195]. The lower ΔQ observed for double layer cathode means a lower irreversible loss of active sulphur and consequently an effective lower LiPSs dissolution, due to the presence of carbon nitride.
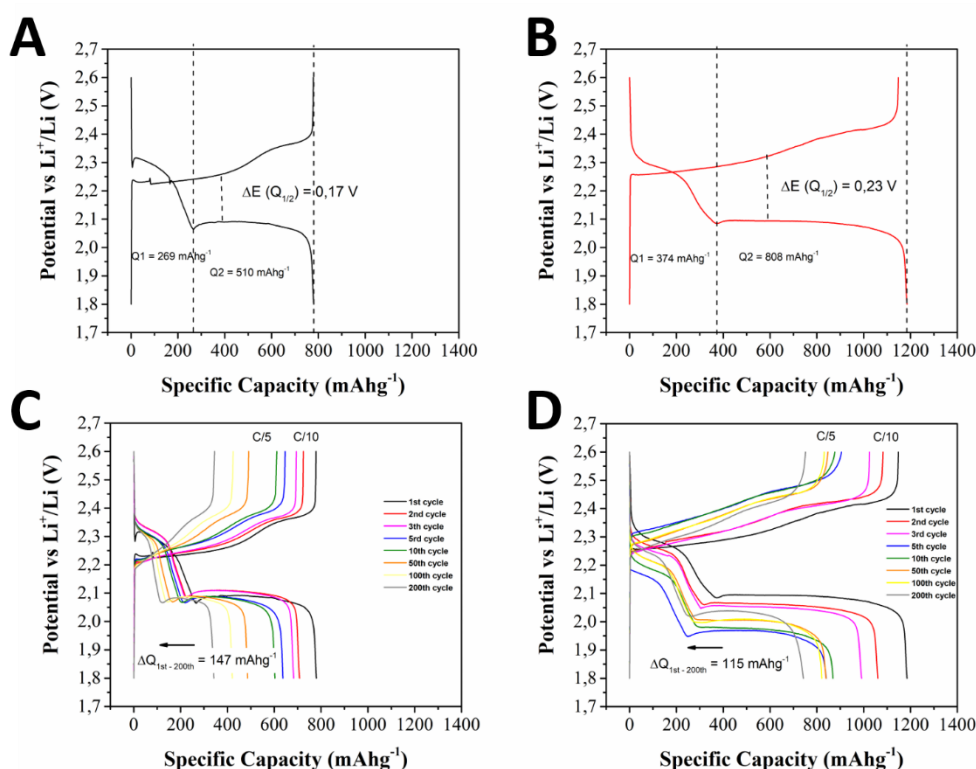
Figure 5.17: first cycle charge/discharge voltage profile at C/10 for single-layer (a) and double-layer with CN-U (b) cathode. Charge–discharge curves at different cycle number for single-layer (c) and double-layer with CN-U (d) cathode.

The results indicated that the carbon nitride layer not only enhanced the specific capacity of the cell but also reduced the capacity loss originating from the rearrangement of the active sulphur materials during cycling.

To confirm the effect of carbon nitride layer the cells were disassembled after 200 cycles. In the cell containing the single-layer cathode the surface of lithium disks (Figure 5.18 a) appeared darker compared to the one of double-layer cell (Figure 5.18 b). At the same time the celgard 2500 separator in contact with the single-layer electrode was clearly yellow, while the separator of the cell containing the double-layer cathode was less coloured, appearing pale yellow. The

differences observed comparing the two cells are presumably due to the greater polysulfide migration attributable to the single-layer cathode, where the LiPSs trapping of carbon nitride is absent.
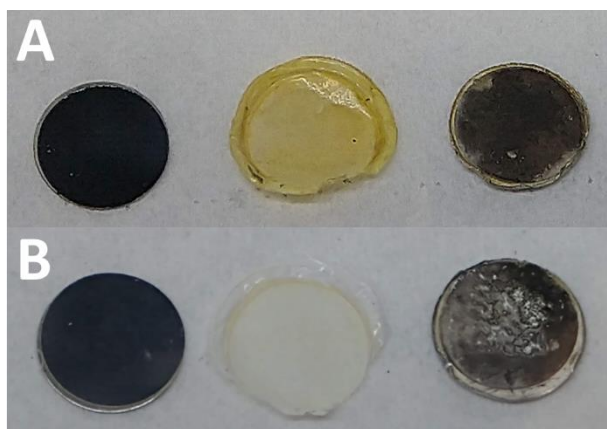
Figure 5.18: photo images of cathode, separator and lithium anode disassembled after 200 cycles for single-layer (a) and double-layer (b) cells.

The inhibition of g-C_3N_4, synthetized from urea at 550 °C, on self-discharge behaviour of lithium-sulphur battery was depicted in Figure 5.19.

To evaluate the self-discharge of the battery a standard single-layer cell and a double-layer STD+CN-U cell were cycled at C/10 for one cycle and then rested for 20 days, as shown in Figure 5.19. During the rest phase the open circuit potential of the cells were measured once per minute, and two more charge/discharge cycle were performed at the end of the rest time. This type of measurement was performed in order to evaluate the static stabilization of Li-S cells and the decay of open-circuit voltage (self-discharge) due to polysulfides diffusion which is the main cause of irreversible capacity fading. The OCV and capacity retention after the rest time were used to evaluate the effect of the carbon nitride-based double-layer on discharge behaviour of the cell.

The single-layer electrode delivers an initial capacity of 780 mAh g^{-1} (at C/10), while the double-layer electrode delivered an initial capacity of 980 mAh g^{-1}. After 20 days-rest, the specific capacity of STD electrode was still 650 mAh g^{-1} with a capacity retention of 83 %, while the STD + CN-U specific capacity successfully recovered to 910 mAh g^{-1} with a capacity retention of 93 %.

After the long-time rest the standard single-layer cell exhibits a severe capacity fading, 10 % higher than the one observed for the cell containing the carbon-nitride double-layer electrode.

Figure 5.19 b and c displayed the open circuit voltage (OCV) variation trends for single-layer and double-layer electrode, respectively. Both the cells demonstrated an initial voltage of 2.37 V, after the first cycle at C/10. After resting for 20 days the single-layer cell voltage showed an OCV of about 2.227 V, indicating a voltage decay of 145 mV. After the same time of rest, the cell

containing the double-layer electrode, showed a final voltage of 2.314 V, with a voltage decay of about 61 mV, which is consistently lower than the OCV decay observed for the standard electrode. These results can be reasonably attributed to the trapping polysulfides action and the consequent self-discharge inhibition due to g-C_3N_4 present in the double-layer cathode.
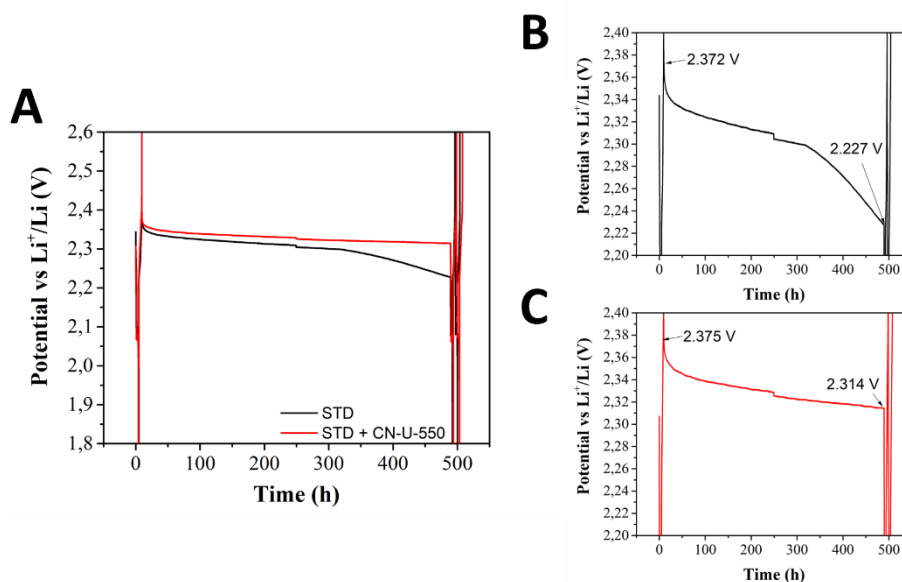
Figure 5.19: self-discharge comparison of single-layer standard electrode and carbon nitride-based double-layer electrode (a), open circuit voltage variation after 20 days for standard cell (b) and double-layer cell (c).

The electrochemical kinetic of polysulfide redox reaction on the g-C_3N_4 surface was elucidated by exchange current measurements using linear scanning voltammetry (LSV) with a Li_2S_6 catholyte solution. For simplicity a single-redox behaviour was assumed (considering Li_2S_6) even though more than one polysulfide may be present in Li-S system.

In this case, the working electrode containing g-C_3N_4, KjB and PVdF in the weight ratio of 80:10:10 was directly cast on a gas diffusion layer (GDL) and a pure lithium disk was used as counter/reference electrode. The cell was assembled using a 0.3 M Li_2S_6 solution directly prepared in the LiTFSI (1 M) in DME:DIOX 1:1 v/v + 0.25 M $LiNO_3$ electrolyte, which was used as catholyte solution.

For comparison a reference electrode containing only KjB: PVdF (in weight ratio of 90:10) was prepared and subjected to the same electrochemical test.

The scan speed of the LSV experiment was set at 0.1 mV s^{-1}, and the voltage range was limited to 30 mV from open-circuit voltage (OCV).

The overpotential (η) and the current response from the LSV experiment were fitted on the semi-logarithmic plot (V/log|I|) using the linear Tafel:

$$\eta = a - b \log(|I|) \tag{5.1}$$

$$\eta = \frac{RT}{aF}\ln i_0 - \frac{RT}{aF}\ln i \qquad [5.2]$$

where the two fitting parameters a and b correspond to the position and slope of the Tafel line, respectively. In particular, the linear region obtained in the semi-logarithmic Tafel plot was fitted and extrapolated to obtain the exchange current density (i_0).

$$b = -2.3\frac{RT}{aF} \qquad [5.3]$$

$$a = 2.3\frac{RT}{aF}\ln i_0 \qquad [5.4]$$

In conclusion the linear region of the semi-logarithmic Tafel plot was manually fitted and extrapolated to obtain the exchange current density according to the Bulter-Volmer equation.

$$i = i_0 \left[\exp\left(\alpha_{an}\frac{F}{RT}\eta\right) - \exp\left(-\alpha_{cat}\frac{F}{RT}\eta\right)\right] \qquad [5.5]$$

Where i is the current density of the reaction, i_0 is the exchange current density, α is the transfer coefficient, η is the overpotential of the electrochemical reaction, F is the Faraday constant, R the universal gas constant and T the temperature in Kelvin [196].

Figure 5.20 shows the Tafel plots comparison of g-C_3N_4 and KjB, derived from linear sweep voltammetry scans in which the linear part of the plots was used to calculate the exchange current density by linear fit as shown by the straight dashed lines.
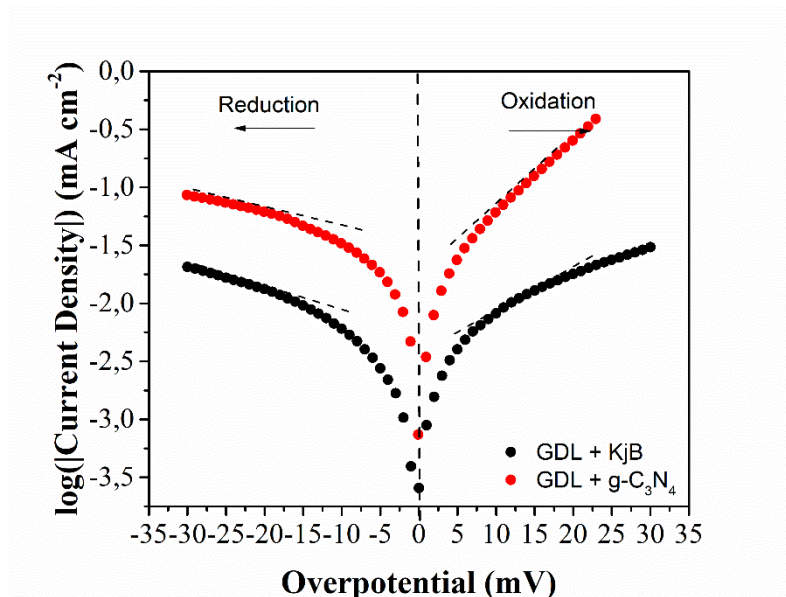
Figure 5.20: Tafel plot comparison of the Li_2S_6 solution redox derived from linear sweep voltammetry scans, on GDL + KjB and GDL + g-C_3N_4. The linear part of the plots was fitted to calculate the exchange current density, as shown by the straight dashed lines.

As possible to observe in Table 5.7, g-C_3N_4 presents higher exchange current density, of about 0.015 - 0.02 mA cm^{-2} which is one order of magnitude higher than that calculated for pure KjB carbon (0.0045 - 0.0034 mA cm^{-2}).

This behaviour seems to demonstrate the superior reaction kinetics of carbon nitride surface, towards lithium polysulfides conversion process [197]. One possible explanation can be related to the surface-mediated charge transfer of carbon nitride (with polysulfide anions) and its semi-conductive nature. This is also a possible explanation of the superior charge/discharge performances of the double-layer electrode.

Table 5.7: reduction/oxidation exchange current density calculated for GDL + KjB and GDL + g-C_3N_4.

	Exchange current density oxidation (mA cm^{-2})	Exchange current density reduction (mA cm^{-2})
GDL + KjB	0.0045	0.0034
GDL + g-C_3N_4	0.0151	0.0205

In conclusion the results for double layer cathode indicate that the introduction of carbon nitride enables effective improvement of the specific capacity despite of the larger overpotential due to the inherent lower electronic conductivity of CN. Moreover, the ''shuttle effects'' can be effectively restricted inserting carbon nitride as double layer material.

However, the higher overpotential highlights the necessity for a comprehensive balancing between the electrical conductivity and the anchoring-conversion ability of LiPSs in the STD + CN-U electrode. A possible way to achieve this compromise is to reduce the thickness of the second layer or reducing the amount of carbon nitride. A detailed description of different approaches to reduce the polarization of the cell will be given in paragraph 5.3.

5.2 Graphic carbon nitride obtained from urea at different temperature

5.2.1 Morphological characterization

Starting from the conclusions of the previous section, in which urea was individuated as optimal precursor to obtain graphitic carbon nitride, able to strongly interact with lithium polysulphides, the effect of temperature synthesis was investigated in this section. In particular, the influence of the heating temperature, adopted in the thermal condensation process, on the crystalline quality, surface morphology, physical properties and to the consequent LiPSs adsorption ability of carbon nitride was deeply examined.

Different g-C$_3$N$_4$ samples were synthesized by a facile thermal condensation process, already discussed in the previous chapter. Typically, 5 g of urea ($\geq$ 97.0 %, Sigma Aldrich) were transferred into a semi-closed alumina boat, which was put into a tubular furnace and heated to a chosen temperature for 3 h in an argon atmosphere. Urea was treated at five different annealing temperatures: 450 °C, 500 °C, 550 °C, 600 °C, and 650 °C respectively. All the obtained sample discussed in this section were labelled as CN-U-x, where x refers to the specific annealing temperatures.

The synthetized powders were first analysed by morphological and structural point of view.

The FESEM micrographies of the prepared samples are shown in Figure 5.21. At the process temperature of 450 °C, the carbon nitride shows a regular morphology composed of wavy and smooth flakes with a low presence of visible pores. Increasing the temperature to 500 °C, the typical flakes are still present, but some rolled and conical structure start to appear. The presence of conical and rolled structure increase with the temperature annealing (550 °C), originating a visible porosity into the sample. Reaching 600 °C the morphology of carbon nitride is similar to the sample obtained at 500 and 550 °C but some flakes start to be wrinkled due to the thermal degradation of the structure. The thermal degradation is particularly evident in the sample obtained at 650 °C, where the original large flakes are seriously degraded, and higher porous structure is visible.
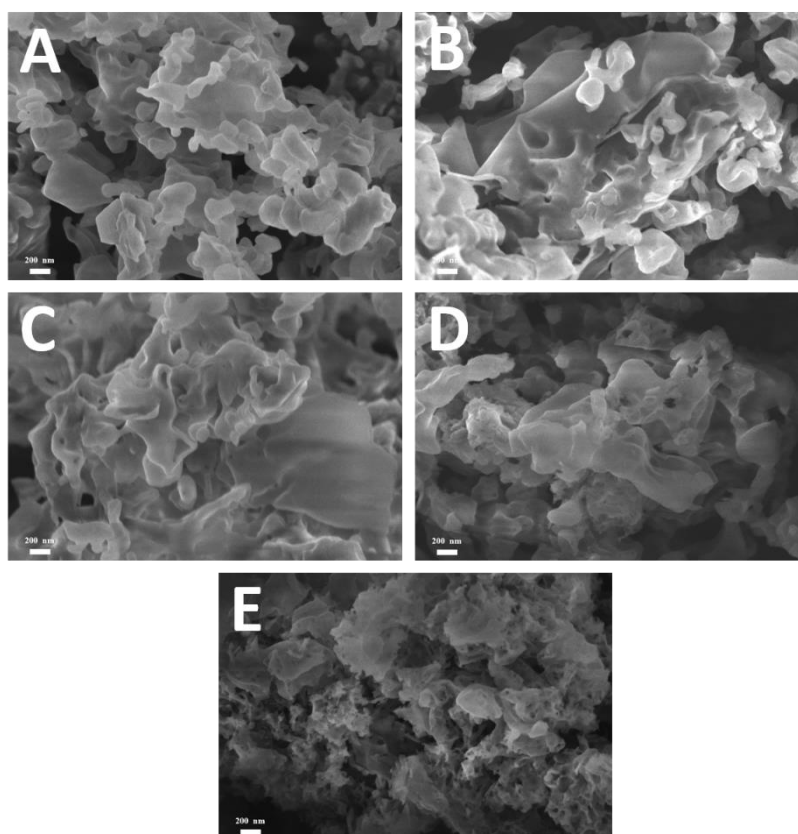
Figure 5.21: FESEM micrographies (50 KX) of carbon nitride powder
obtained at: 450 °C (a), 500 °C (b), 550 °C (c), 600 °C (d) and 650 °C (e).

To confirm the different pores distribution and the consequent different surface area of the synthetized samples, the nitrogen adsorption-desorption isotherms and pore size distribution (PSD) were evaluated by BET method.

Considering the similar morphology of some samples, observed by FESEM investigation only the SSA and PSS of three samples obtained respectively at 450, 550, 650 °C were investigated.

The nitrogen adsorption-desorption isotherm is similar for all the samples, it is ascribable to type IV isotherm with an H3-type hysteresis loop, which is typical for mesoporous materials (Figure 5.22 a, b, c) [198][199].

The pore size distribution was estimated using NLDFT method, from the desorption branch of the isotherm which denotes the mesoporous structure for all the carbon nitride samples (Figure 5.22 d, e, f).

In particular, CN-U-450 and CN-U-550 presents small mesopores at about 3-5 nm and also some larger mesopores at about 35 - 45 nm. Interestingly, the CN-U-650 pore distribution is wider and more heterogeneous, presenting huge amount of mesopores of about 35 - 45 nm and, in addition to mesopores at 3 - 5 nm, also a microporosity referred to some pores at 2 nm.

This behaviour can be due to the splitting of the nanosheets layers during the thermal condensation and exfoliation process of carbon nitride. Particularly small

mesopores may be originated by this nanosheets splitting, while larger mesopores can be prevalently formed by the packing process of g-C_3N_4 layers [198][199].

The characteristic PSS of CN-U-650 is attributable to the thermal exfoliation occurring at high temperature and the consequent structure degradation which originates a huge amount of pores.

The generation of porous structure results in a significant enhancement of specific surface area which similarly increases as the process temperature rises.
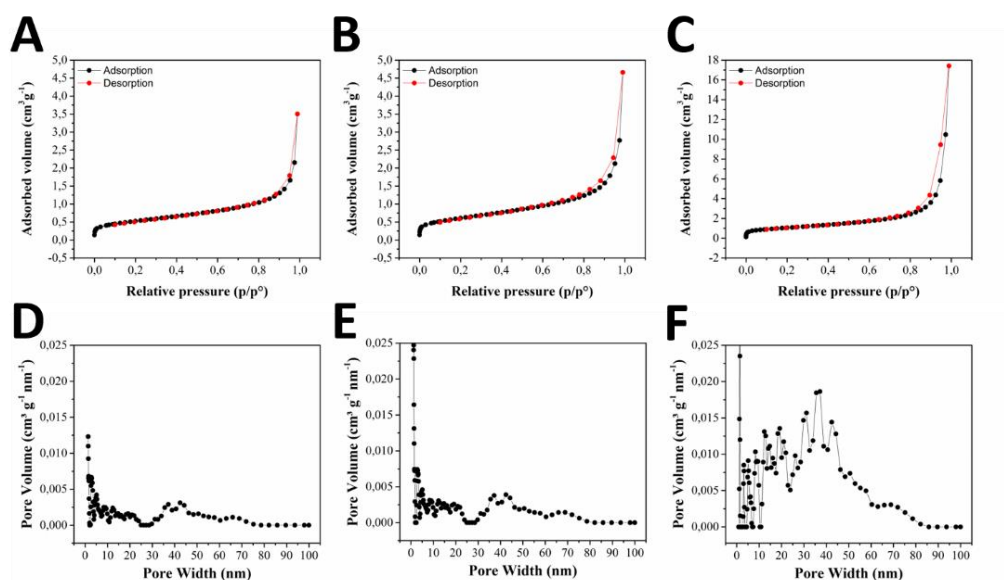
Figure 5.22: N_2 adsorption-desorption isotherms and the corresponding pore-size distribution curves for: CN-U-450 (a, d), CN-U-550 (b, e) and CN-U-650 (c, f).

Similarly, to the average pore size, the BET surface area values increase as the process temperature rises Table 5.8. The specific surface areas of CN-U-450 is about 42 m^2 g^{-1} which is not so different from the SSA obtained at 550 °C (48 m^2 g^{-1}). On the contrary the specific surface area was twice for the sample obtained at 650 °C, which is about 84 m^2 g^{-1}.

In general, the BET surface area of g-C_3N_4 increases with the polycondensation temperature, because the rise of temperature promotes the separation of layers in g-C_3N_4 leading to the enhanced specific surface area. In addition, the increment of temperature over 600 °C, induces the decomposition of carbon nitride layer networks, creating additional pores in the structure and a characteristic "sponge-like" morphology.

Table 5.8: specific surface area and pore volume for carbon nitride obtained from different precursors.

Sample	Specific surface area (SSA) (m² g⁻¹)	Pore volume (PSS) (cm³ g⁻¹)
CN-U-450	41.91	0.057
CN-U-550	48.37	0.073
CN-U-650	84.11	0.214

XRD pattern comparison of carbon nitride samples obtained at different temperatures are reported in Figure 5.23.

The X-ray diffraction pattern indicates that g-C_3N_4 was already formed even at low annealing temperature of 450 °C, and it is still present at high temperature (650 °C). This is confirmed by the presence of the two typical diffraction peaks located around 13° and 27.5° corresponding to (001) and (002) planes, respectively (JCPDS file no. 87–1526).

No particular shift of the main peak is observable in the samples, indicating that no evident structural changing occurs increasing the temperature. The main peak results slightly shifted from 27.26 to 27.52° with the increasing of annealing temperature (from 450 to 600 °C), but it is around 27.36 for the sample obtained at 650 °C. However, the interplanar d-spacing, attributable to the interlayer stacking of conjugated aromatic system, is quite similar for all the samples, reaching d = 3.25 Å. Moreover, the shape of peak located at 27.5° seems broader for CN-U-450 and CN-U-650, if compared to the other three samples. From these considerations, samples obtained from 500 to 600 °C are quite similar, while more discrepancies are observed for the other two carbon nitrides.
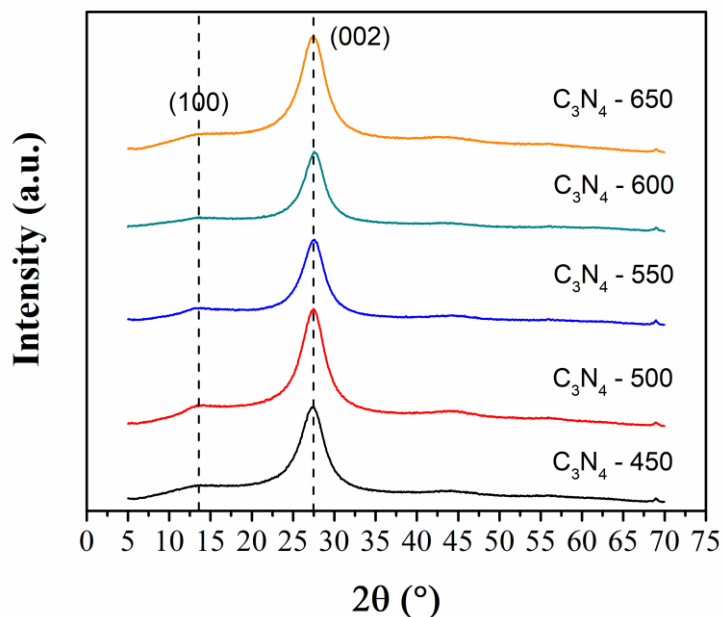
Figure 5.23: XRD patterns for the g-C_3N_4 samples prepared at different temperatures starting from urea.

The chemical structures of the samples are further analysed by FT-IR/ATR spectroscopy (Figure 5.24). All spectra show the typical absorption bands of carbon nitride. The narrow peak at around 805 cm^{-1} represents the out-of-plane bending vibration of tri-s-triazine units in g-C_3N_4 [200][201]. However, the spectra are dominated by several absorption peaks appearing in the range of 1650 - 1200 cm^{-1} which correspond to different stretching and bending modes. The peaks are very close to each other, but bands centred at 1559 cm^{-1} and 1616 cm^{-1} can be assigned to N–H bending modes in primary (-NH_2) and secondary amino group (-NH). While all the other bands located in this region can be ascribed to the stretching modes of C–N bonds of aromatic primary and secondary amine [198][200][202]. The high intensity of peaks attributable to C–N bonding of aromatic secondary and tertiary amines, are typically due to the formation of di-melem molecules which indicate the higher polycondensation degree of carbon nitride structure, as already observed in XRD spectra [198]. Lastly the broad peaks in the range of the 3000 - 3700 cm^{-1} are attributed to the symmetric and asymmetric N–H stretching modes from residual amino groups and the O–H band from adsorbed H_2O molecules [198]. These absorption peaks are sharper for the samples obtained at 650 °C, indicating that more C–NH_2 groups and C–NH–C bridges between heptazine units are present into the structure [202]. This is attributable to a greater fraction of small polymer segments containing only a few heptazine units with -NH/NH_2 groups at the terminals [202].

To conclude, the increment of the polymerization temperature can promote the planarization of g-C_3N_4 layers, weakening the interactions between the two adjacent atoms respectively located in two adjacent tri-s-triazine rings [201].

95
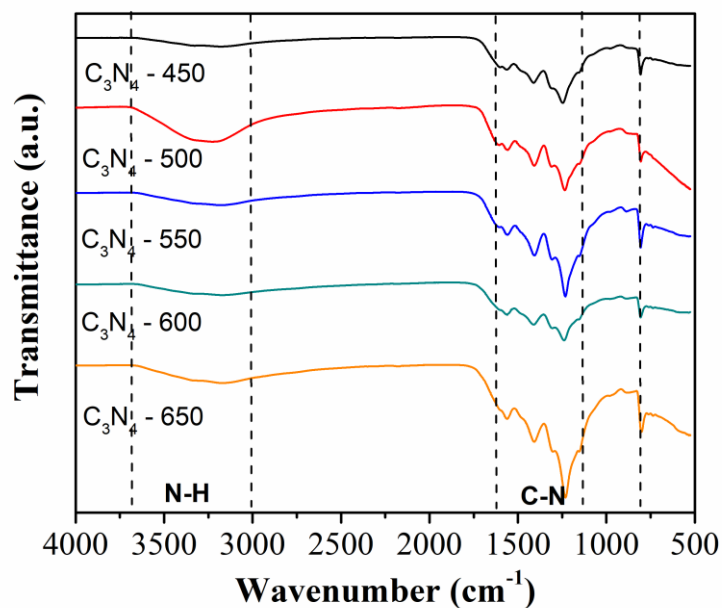
Figure 5.24: FT-IR/ATR spectra comparison of carbon nitride derived from urea at different temperatures.

In general, both XRD and FT-IR analysis confirmed the formation of carbon nitride for all the investigated synthesis temperatures.

The carbon, nitrogen and hydrogen stoichiometry were determined by elemental analysis Table 5.9. The results indicate that the C/N atomic ratio is constant for carbon nitride samples obtained at 450, 500 and 550 °C, while it increased for samples obtained at 600 and 650 °C attesting respectively at 0.57, 0.58 and 0.61. So, C/N ratio increases with the increasing process temperature, but in all cases, it was lower than the theoretical value of 0.75.

Table 5.9: elemental analysis of carbon nitride obtained from different precursors.

Sample	Carbon %	Hydrogen %	Nitrogen %	Missing Amount %	C/N ratio
CN-U-450	30	3.0	52	15	0.57
CN-U-500	30	2.9	52	15.1	0.57
CN-U-550	30	2.8	52	15.2	0.57
CN-U-600	28	3.5	48	20.5	0.58
CN-U-650	30	2.9	49	18.1	0.61

EDS area analysis was carried out (Figure 5.25) to investigate the superficial elemental distribution of carbon nitride samples. For each sample at least 3 areas were investigated to obtain a general information about the distribution of the elements.

The analysis detected only three elements for all the samples: carbon, nitrogen and oxygen. Only a small amount of oxygen is present in each sample, but it increases with the rise of synthesis temperature. The presence of oxygen is due to adsorbed water and atmospheric oxygen. The increasing trend amount is probably due to the higher porosity of the sample obtained at higher temperature, as confirmed by nitrogen adsorption–desorption isotherms analysis and FESEM micrographs.

The C/N (wt.%) ratio (Table 5.10) is the same for carbon nitride obtained at 500, 550 and 600 °C, around 0.56, while it is higher for samples obtained at 450 and 650 °C, respectively 0.59 and 0.61. Similarly, the atomic percentage C/N ratio confirms that the amount of carbon is higher for carbon nitrides obtained at 450 and 650 °C (C/N = 0.7), while it is lower (~ 0.65) for the other three samples.

EDS analysis shows that at 450 °C the amount of carbon in the CN structure is still high, while at 650 °C the degradation of the material induces a sensible nitrogen loss. The three samples synthetized at middle temperatures are similar, presenting a higher C/N ratio and consequently a higher relative amount of nitrogen species.

It is worth noting that EDS analysis provide approximate content of carbon, so this analysis was only used to support the previous investigation.
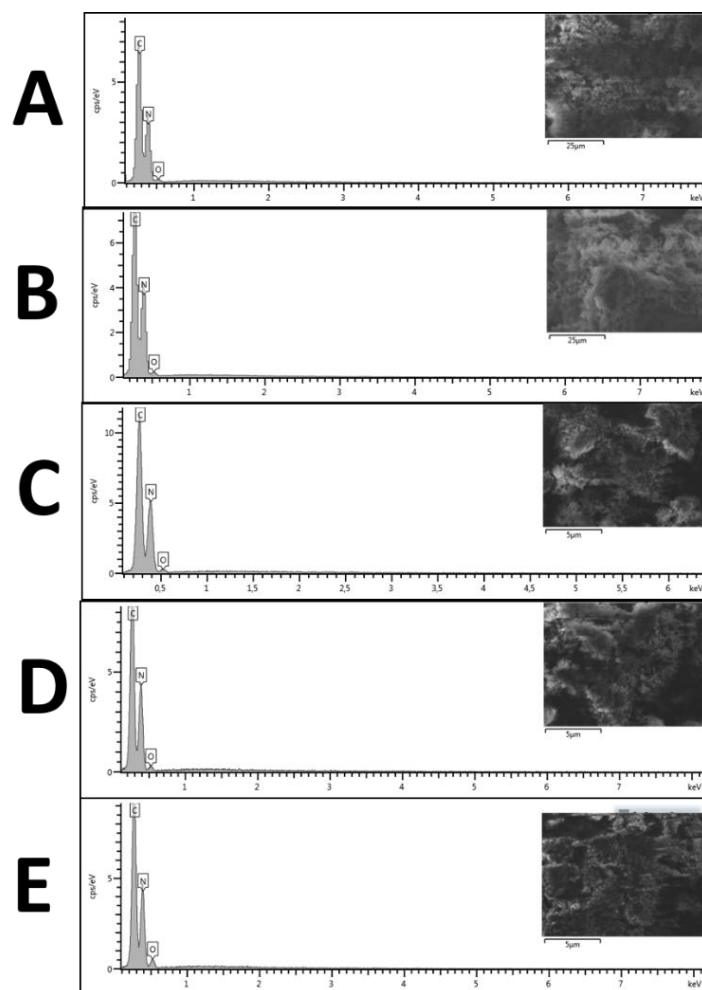
Figure 5.25: EDS superficial analysis for CN-U-450 (a), CN-U-500 (b), CN-U-550 (c), CN-U-600 (d) and CN-U-650 (e) powders.

Table 5.10: EDS element analysis for carbon nitrides obtained at different temperature starting from urea.

Element	CN-U-450		CN-U-500		CN-U-550		CN-U-600		CN-U-650	
	Wt%	% atom.	Wt%	% atom.	Wt%	% atom.	Wt%	% atom.	Wt%	% atom.
C	36.71	40.46	35.03	38.71	35.18	38.88	35.16	38.89	36.18	40.06
N	61.05	57.69	62.54	59.27	62.25	58.99	61.66	58.47	58.34	55.39
O	2.24	1.85	2.43	2.02	2.56	2.13	3.18	2.64	5.47	4.55
Total	100.00	100.00	100.00	100.00	100.00	100.00	100.00	100.00	100.00	100.00

The surface chemical composition of the synthetized samples was also evaluated by XPS analysis (Figure 5.26).

The survey spectra for all g-C_3N_4 samples reveal three main peaks, respectively at 288, 400, and 532 eV belonging to carbon, nitrogen and oxygen (Figure 5.26 a).

The presence of oxygen is more pronounced in samples obtained at 550, 600 and 650 °C and it can be attributed to some residual oxygen, also present in the precursor or to some adsorbed air.

The C1s spectra (Figure 5.26 b), for all five samples were deconvoluted in four main subpeaks. In particular, the C1s peak at 284.8 eV arises from the adventitious carbon (Csp^2, Csp^3) [203], while the weak C1s peak at 286.2 eV is attributable to the presence of nitrogen-related defects in the graphitic carbon nitride system (N–CH=N) or C–O bonding. The intense C1s peak around 288.1 eV was identified as typical sp^2-hybridized carbon (N–C=N) in the aromatic s-heptazine ring and the other peaks at 289 - 290.1 eV can be assigned to C=O or O=C–O species.

The high-resolution N1s spectra of carbon nitride samples (Figure 5.26 c) were deconvoluted into three subpeaks respectively centred around 398.5, 399.6, and 401.1 eV. The peak centred at 398.5 eV corresponds to sp^2-hybridized nitrogen in triazine rings (C–N=C), while the peak at 399.6 eV is attributable to tertiary nitrogen N–(C)$_3$ groups. Lastly the weaker peak at 401.1 eV can be attributed to quaternary N (H-N–(C)$_2$) [198][204] .
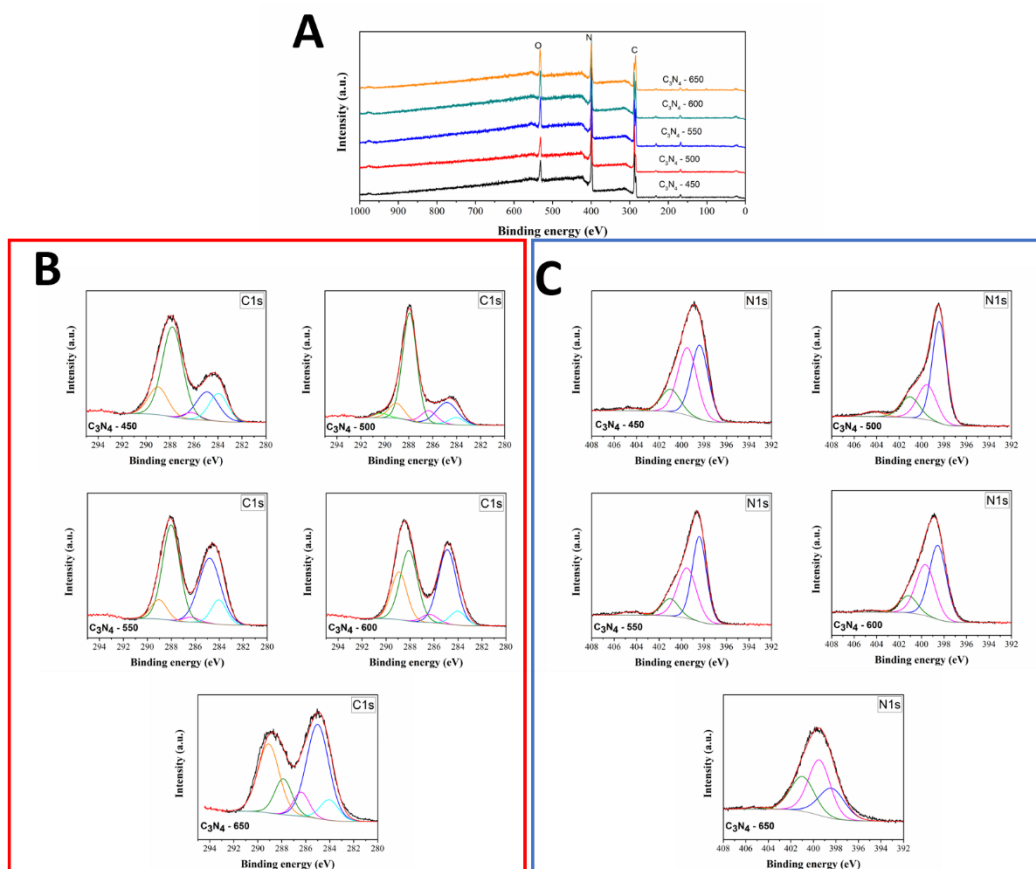
Figure 5.26: XPS survey spectra comparison (a), C 1s high resolution spectra (b), N 1s high resolution spectra (c) for CN-U-x: 450, 500, 550, 600, 650.

To better understand the influence of synthesis temperature on the surface chemical composition of different samples the peak-area ratio between C=N–C and N–(C)$_3$ was calculated (Table 5.11). The samples obtained at 500, 550 and 600 °C present a higher percentage of secondary nitrogen species (C=N–C ~ 47-56 %) and a lower percentage of tertiary nitrogen species (N–(C)$_3$ ~ 25 – 38 %), while the sample with a lower temperature (450 °C) shows a similar percentage of both species. On the contrary the sample obtained at 650 °C shows a different behaviour from the other samples, presenting N–(C)$_3$ as the abundant species, while C=N–C and H–N–(C)$_2$ species are present in lower percentages, close to 30 %.

Comparing the results, the peak-area ratio of 0.99, 2.22, 1.3, 1.3 and 0.6 respectively for CN-U 450, 500, 550, 600 and 650 was measured. The lower value of C=N–C/N–(C)$_3$ ratio indicates the presence of nitrogen vacancy in the triazine rings site. The relative intensity of the two main peaks reveals that as the synthesis temperature rises more tertiary nitrogen (N–(C)$_3$) is formed in contrast to pyridinic nitrogen (C=N–C) [198][203]. In particular, the results indicate that increasing the temperature up to 600 °C, involves the chemical transition from pyridinic nitrogen to tertiary nitrogen with the consequent degradation of the g-C$_3$N$_4$ sheets.

100

Table 5.11: relative percentage of C and N species area of CN-U obtained at different temperatures, calculated by high resolution XPS spectra deconvolution.

Binding energy (eV)	Specie	CN-U-450		CN-U-500		CN-U-550		CN-U-600		CN-U-650	
		Area %	Area rel %	Area %	Area rel %	Area %	Area rel %	Area %	Area rel %	Area %	Area rel %
398.5	C=N-C	16.07	41.81	24.68	55.64	16.32	47.91	17.47	49.40	8.03	27.25
399.6	N-(C)$_3$	16.26	42.31	11.29	25.46	12.86	37.77	13.39	37.86	12.56	42.66
401.1	H-N(C)$_2$	5.44	14.17	6.71	15.12	3.96	11.64	4.05	11.45	8.54	29.01
403.0	N-O	16.07	41.81	2.68	55.64	1,32	47.91	17.47	49.40	8.03	27.25

As previously done for carbon nitride obtained from different precursors, 20 µL of 1 mM of Li_2S_6 solution diluted in 2 mL of DME:DIOX 1:1 v/v mixture were directly added to a quantity equivalent to 0.5 m^2 surface area of CN 450, 550, and 650 for the polysulfide adsorption test (Figure 5.27).

After resting the samples for 12 hours, without any form of stirring, the solution containing carbon nitride obtained at 550 °C showed the already discussed colour fading. Moreover, the solution containing CN-650 showed a visible colour fading, but of reduced intensity compared to CN-550. While CN-450 still showed a yellowish solution, demonstrating a lower interaction with Li_2S_6.
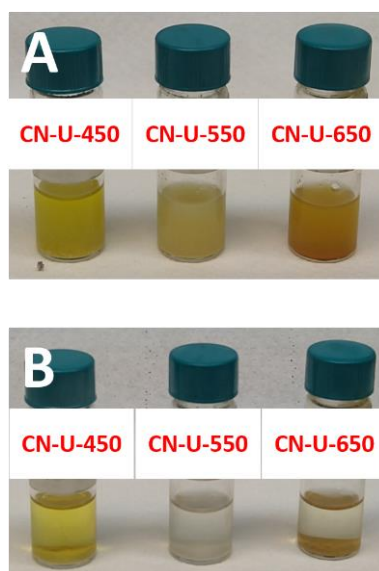
Figure 5.27: lithium polysulfides adsorption test comparison for CN-U-450, 550, 650: 40 µL of Li_2S_6 1 mM at 0 h (a), after 12 h (b).

The structural and morphological analysis confirm that carbon nitride is formed in all the temperature conditions investigated. However, the two samples obtained at 450 and 650 °C present some relevant differences in terms of specific surface area, pore distribution and surface chemistry, while the samples synthetized at 500, 550 and 600 °C are quite similar to each other. This behaviour agrees with the assumption that carbon nitride samples obtained at different temperatures behave differently in the lithium-sulphur cell, so the next paragraph will be dedicated to the electrochemical investigation of these materials.

5.2.2 Electrochemical characterization

The standard and double-layer working electrodes were prepared by solvent tape casting method and the cell were assembled as described in paragraph 5.1.2.

Each synthetized carbon nitride was used to prepare a respective double-layer electrode, which for simplicity was labelled as STD + CN-U-x, where x is referred to the temperature used for the carbon nitride thermal condensation.

The electrochemical performances of the electrodes were evaluated assembling coin cell 2032, as already described in previous chapters. The as assembled cells were subjected to galvanostatic charge/discharge procedures.

The sulphur mass loading of each electrode was settled between 1 and 1.2 mg cm^{-2}, while the S/CN ratio was kept in the range of 0.5 - 1.

In Figure 5.28 specific charge and discharge capacities were compared for each sample, for 200 cycles. The cells were cycled at C/10 for the initial 3 cycles and then cycled at C/5. As possible to observe in Figure 5.28 the electrodes containing the double layer with CN-U-500, CN-U-550 and CN-U-600 displayed a higher specific capacity if compared to single layer standard electrode.

The initial specific capacity of single-layer standard cathode was 800 mAh g^{-1} at C/10, which is significantly lower if compared to specific capacity of double-layer electrodes, which is higher than 1000 mAh g^{-1} for all the samples.

At higher C-rates (*e.g.* C/5), after 200 cycles, the cathode electrodes containing CN-U-500, CN-U-550 and CN-U-600 delivered respectively 550, 750 and 700 mAh g^{-1}, which are significantly higher than the specific charge/discharge capacity obtained for standard cathode (345 mAh g^{-1}).

On the contrary, double-layer cathodes containing CN-U-450 and CN-U-650 showed very low specific capacity after long-cycling test. In particular, CN-U-450 cell failed after 195 cycles, while CN-U-650 cell delivered a specific capacity of 250 - 300 mAh g^{-1} after 200 cycles at C/5.
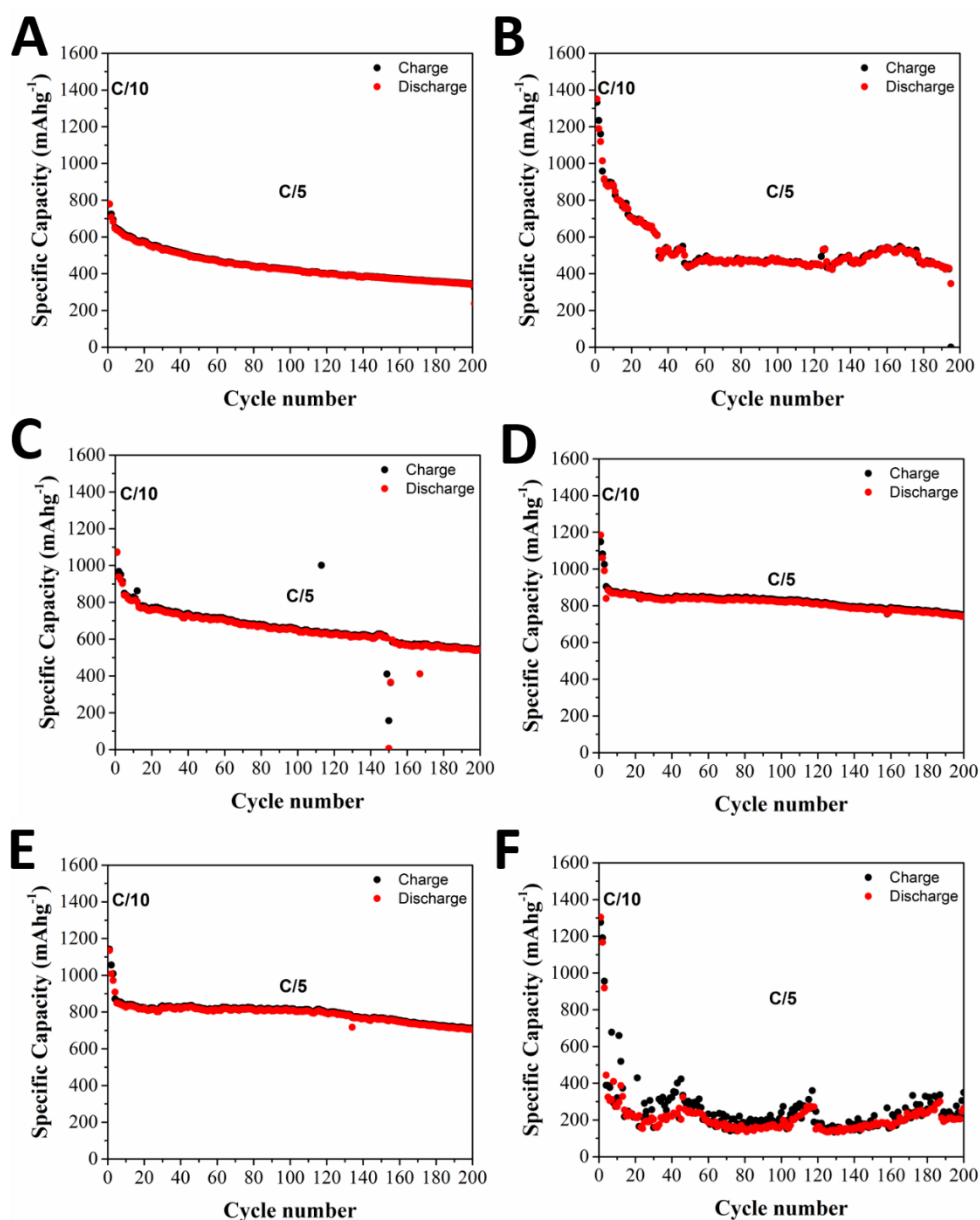
Figure 5.28: specific charge and discharge capacities for standard single-layer (a), STD+CN-U-450 (b), STD+CN-U-500 (c), STD+CN-U-550 (d), STD+CN-U-600 (e) and STD+CN-U-650 (f) electrodes.

For better understanding of the real behaviour of double-layer electrodes and consequently discern the contribution of different carbon nitride samples, specific capacity at 5th and 200th cycles are reported in Table 5.12, with the corresponding capacity loss (% per cycle) at the current density of C/5.

As it is possible to see in the table below, the capacity loss between the 5th and the 100th cycle is 0.23 % per cycle for the standard single-layer cathode. A similar capacity loss was also observed for STD + CN-U-450 electrode, while it sensibly decreased for the other double-layer electrodes. In particular, STD + CN-U-550 and STD + CN-U-600 showed a capacity loss which is almost one third of

the one of standard cathode. The low capacity loss observed for these double-layer cathode also reflects their good capacity retention.

The capacity loss per cycle was low also for STD + CN-U-650, but in this case the specific capacity was low if compared to the other double-layer electrode. Moreover, as depicted in Figure 5.28 (f) the capacity trend of STD + CN-U-650 is generously irregular, which means that the capacity decrease is not constant during cycling.

Table 5.12: specific capacity at 5th and 200th cycles at C/5 for single-layer and double-layer electrodes.

Sample	5th cycle charge capacity (mAh g^{-1}) at C/5	200th cycle charge capacity (mAh g^{-1}) at C/5	Capacity loss (% per cycle)
STD	646	345	0.23
CN-U-450	913	-	0.28
CN-U-500	850	550	0.18
CN-U-550	895	750	0.08
CN-U-600	862	711	0.09
CN-U-650	387	350	0.05

The different electrochemical behaviour between double-layer cathodes obtained using CN-U-450 or CN-U-650 and the carbon nitride synthetized at intermediate temperatures is particularly evident also comparing the coulombic efficiency (Figure 5.29).

The coulombic efficiency of the standard cathode with STD + CN-U-500, STD + CN-U-550 and STD + CN-U-600 is very close to 100 %, reflecting a good charge and discharge efficiency for each cycle. On the contrary, this is not true for STD + CN-U-450 and in particularly for STD + CN-U-650, for which the CE is dramatically changing. The particular behaviour of STD + CN-U-650 can be attributable either to parasitic reactions unrelated to conventional charge and discharge mechanism, or to the interaction between carbon nitride obtained at high temperature and some lithium-sulphur reaction products. The low and irregular coulombic efficiency can also be linked to the occurrence of shuttle mechanism responsible for longer charge.
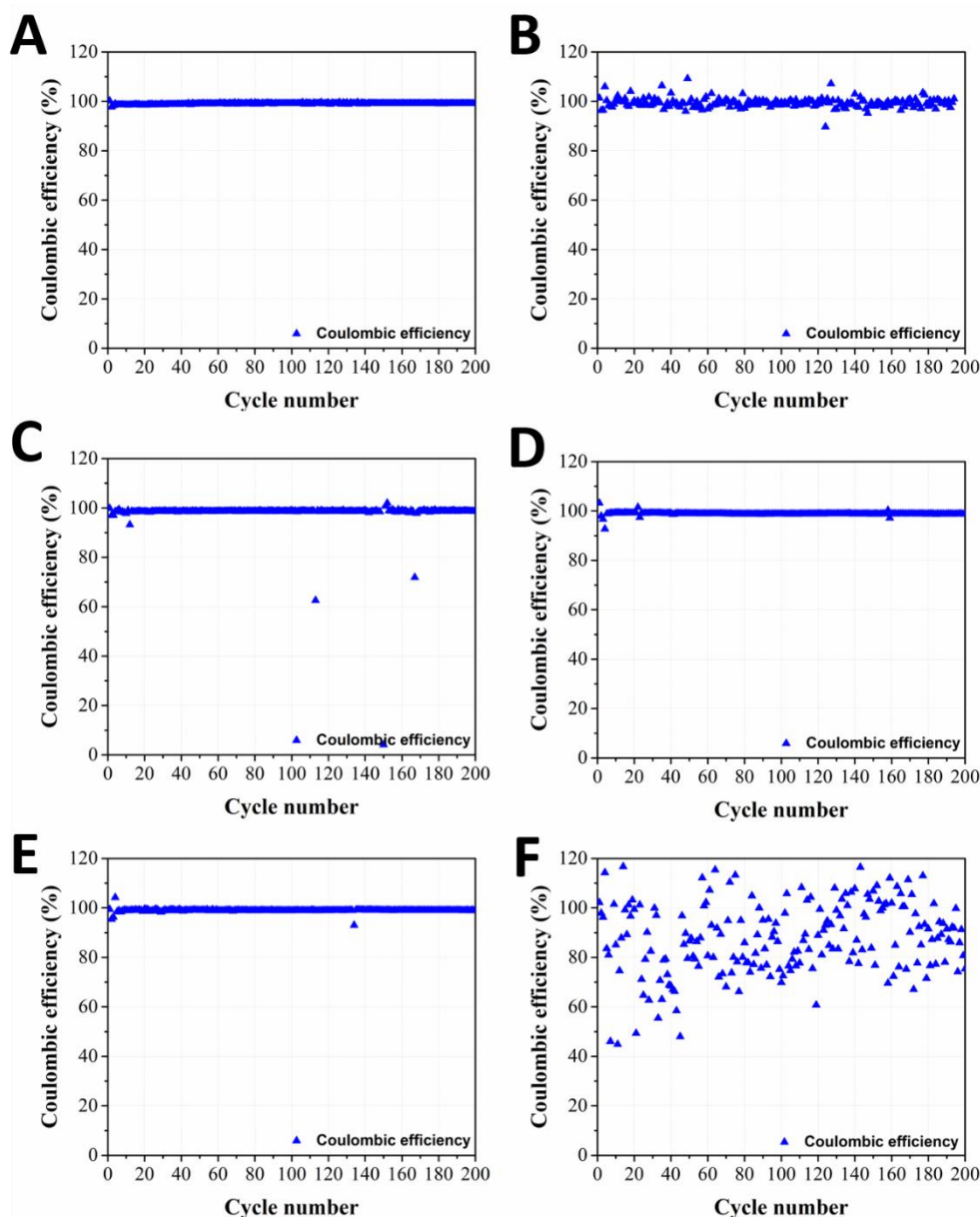
Figure 5.29: coulombic efficiency comparison for standard single-layer (a), STD+CN-U-450 (b), STD+CN-U-500 (c), STD+CN-U-550 (d), STD+CN-U-600 (e) and STD+CN-U-650 (f) electrodes.

Comparing the specific (charge) capacity of the first 10 cycles (Figure 5.30), it is higher for all the double-layer cathode as compared to standard single-layer cathode, when the current range is C/10. On the contrary, increasing the current at C/5, the specific capacity of STD + CN-U-650 rapidly decrease reaching values lower than standard cathode. The specific capacity of STD + CN-U-450 deeply decreases after 30 cycles, reaching a value comparable to the standard one. As already mentioned, the STD + CN-U-450 failed after 195 cycles, as a consequence of a specific capacity increase, probably due to parasitic reaction and/or shuttle phenomenon.

In Figure 5.30 are depicted and compared the charge/discharge curves of the different electrodes of the first cycle (at C/10, Figure 5.30 c) and the 100th cycle

(at C/5, Figure 5.30 d). In the curves at low C-rate the two characteristic plateaus are well discernible and the polarization between the charge and discharge curve is similar for all the samples. At higher current density (C/5, 100th cycle), all the double-layer electrodes show an increased polarization, if compared to the standard single-layer cathode or to the initial curves at lower C-rates. This behaviour was already observed and discussed in the previous paragraphs, and is due to the intrinsic nature of carbon nitride double-layer and the concomitant increasing of the current density.

It is important to note that both the samples STD + CN-U-450 and STD + CN-U-650 show higher polarization compared to the other double-layer cathodes. The abnormal polarization of both these electrodes can be strictly related to some parasitic reactions occurring on the surface of the double-layer and the formation of reaction products, which inevitably reduce the performances of the cell.
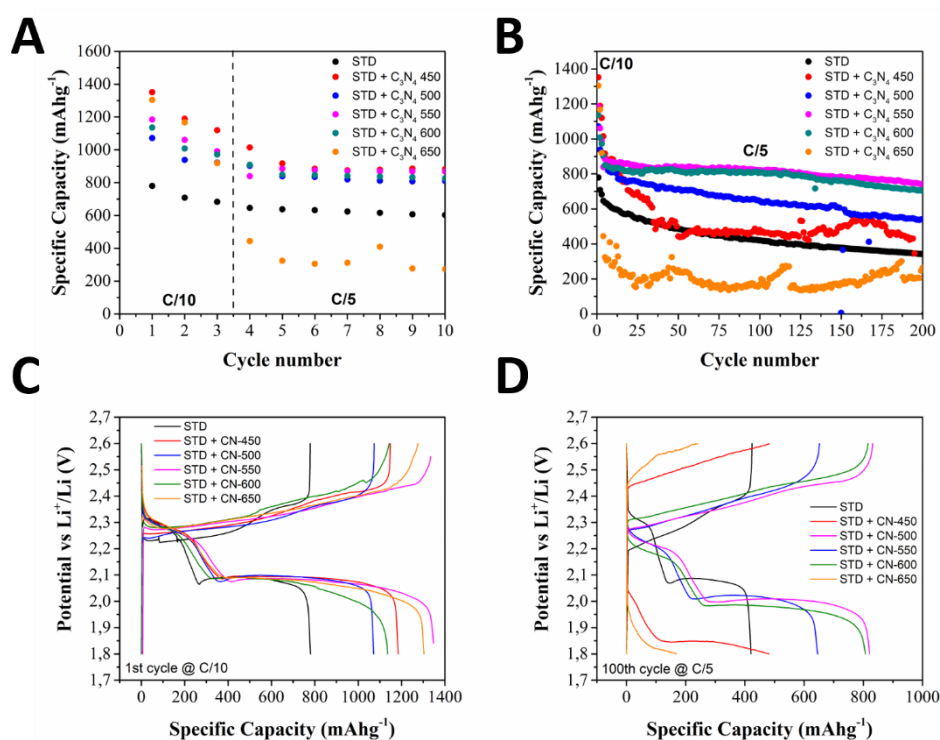
Figure 5.30: galvanostatic charge/discharge performances comparison for the first 10 cycles (a), for 200 cycles (b), first cycle galvanostatic charge/discharge profiles comparison at C/10 (c), galvanostatic charge/discharge profiles comparison at C/5 at 200th cycle (d) double-layer cathodes with different g-C_3N_4 obtained at different temperatures.

In conclusion, the electrochemical results revealed a different behaviour between the as prepared electrodes. In particular, adopting carbon nitride synthetized at 450 or 650 °C, in the double-layer, reveals worse electrochemical properties. This behaviour can be correlated to the structural and morphological properties of these materials, which are quite different to the others as reported in Paragraph 5.1. The differences in terms of specific surface area, pore distribution and general morphology can inevitably contribute to the final electrochemical

performances. However, the different surface chemistry, and the different amount of nitrogen species is reasonably one of the major contributions to the different behaviour. In fact, the samples synthetized at 550 and 600 °C demonstrate similar surface chemistry and consequent similar electrochemical performances, because the presence of pyridinic nitrogen instead of tertiary nitrogen. On the contrary, the huge amount of tertiary nitrogen in the CN-U-650 sample and the concomitant low amount of pyridinic nitrogen can be one of the most relevant causes of the low electrochemical performance. Further investigations will be necessary to better understand the surface interactions and reactions which are responsible for the mentioned behaviour.

5.3 Double-layer thickness optimization to reduce polarization

The conclusions drawn in paragraph 5.1.2 highlights the necessity for a comprehensive balancing between the high specific charge/discharge performance and the higher overpotential observed in the double-layer electrode containing carbon nitride. The first way to investigate this compromise was reducing the thickness of the second layer.

In order to modify the second layer thickness a dried standard electrode was first obtained following the previously mentioned procedure (paragraph 5.1.2).

The standard electrode was subsequently coated by a second layer containing carbon nitride (obtained from urea at 550 °C), KjB and PVdF, in the ratio 80:10:10 (wt.%) adopting different blade thickness, from 100 to 200 μm. After the second slurry deposition the coated aluminium foil was air dried at 50 °C in oven for 30 minutes.

The final thickness, after the complete evaporation of the solvent, was evaluated by FESEM analysis, observing and comparing the cross section of the dried electrodes.

Figure 5.31 reports the cross section micrographies of standard (single-layer) electrode (a, b, c) and double-layer electrodes obtained with a blade thickness of 100 (d, e, f) and 200 μm (g, h, i). Three different orders of magnification (5, 25 and 150 KX) are reported for each sample, with the purpose of highlighting the presence of g-C$_3$N$_4$ in both the double-layer electrodes.

The single-layer electrode showed an average thickness of 15 - 20 μm, and these values were also observed for all the double-layer electrodes. The double-layer electrode obtained with a blade distance of 100 μm (named DL-100 μm) presented a final top-layer thickness of 25 - 30 μm. While the double-layer electrode obtained with a blade distance of 200 μm (named DL-200 μm) showed a final top-layer thickness of about 45 μm. The micrographies at higher magnification confirmed the different morphology of the two double-layer cathodes in comparison to the single-layer cathode. In particular, carbon nitride

sheets were clearly visible in the top-layer, well distributed with the KjB particles. On the contrary carbon nitride was not observed in any bottom-layer.
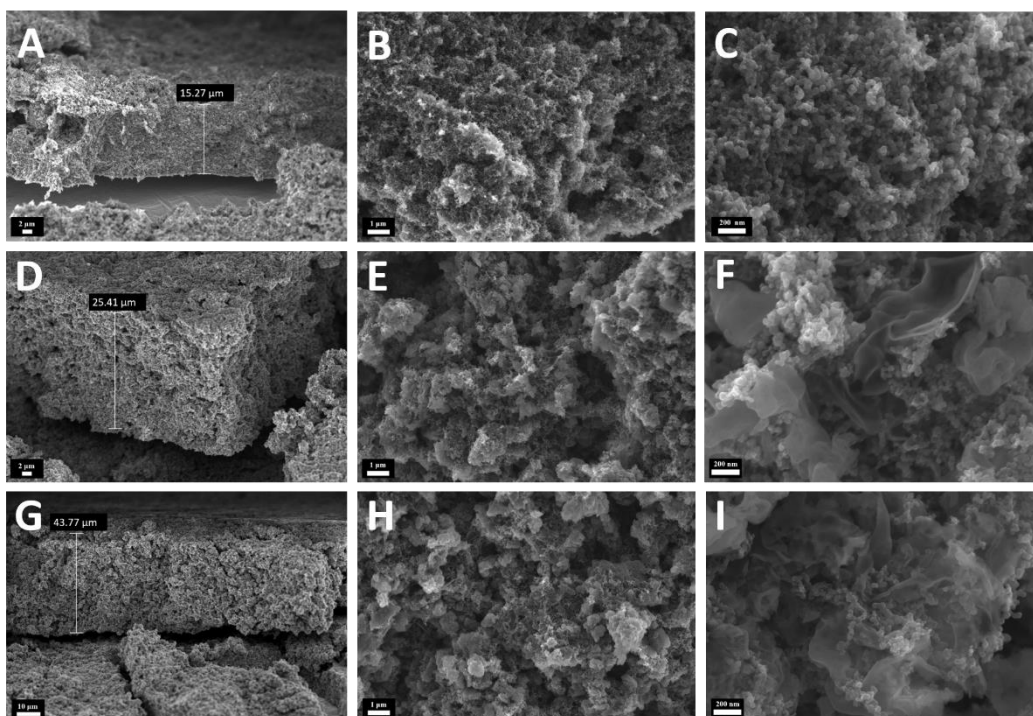
Figure 5.31: FESEM micrographies of single-layer electrode: cross section at 5KX (a) top at 25 KX (b) and 150 KX (c). FESEM micrographies of double-layer electrode 100 μm: cross section at 5KX (d) top at 25 KX (e) and 150 KX (f). FESEM micrographies of double-layer electrode 200 μm: cross section at 5KX (g) top at 25 KX (h) and 150 KX (i).

The electrochemical performances of the electrodes were evaluated assembling coin cell 2032, which were subjected to galvanostatic charge/discharge procedures, at C/10 for the initial 3 cycles and then cycled at C/5, as already described in previous chapters.

The sulphur mass loading of each electrode was settled between 1 and 1.2 mg cm^{-2}, while the S/CN ratio was kept in the range of 0.8 - 1, in order to have a comparable S/CN ratio for both the double-layer samples.

In Figure 5.32 (a, b) specific charge/discharge capacities and coulombic efficiency were reported for the two double-layer electrodes with different thickness. Both the samples showed a good coulombic efficiency, very close to 99 %.

In Figure 5.32 (c) the specific charge capacities of single-layer and two double-layer electrodes with different thickness were compared. The cell containing the electrode with thinner double-layer presented a capacity fade of about 0.13 % per cycle (at C/5). While the cell containing the electrode with 200 μm double-layer presented a capacity fade of about 0.09 % per cycle (at C/5). In the same conditions, the single-layer standard electrode showed a capacity fade of 0.24 % per cycle. This trend underlines that the effect of double-layer thickness is consistent and can induce a better capacity retention of the cell.

Figure 5.32 (d) compares the first cycle charge and discharge curves of the three samples at the current range of C/10. Two representative discharge plateaus at around 2.38 and 2.10 V are observed, corresponding to the reduction of sulphur to long-chain lithium polysulfides (Li_2S_x, $3 \leq x \leq 8$) and the subsequent formation of short-chain Li_2S_2/Li_2S, respectively.

The figure also depicts the voltage hysteresis (ΔE) between charge and discharge curves at the point of 50 % of the discharge capacity. The voltage hysteresis value is an important parameter to evaluate the cell polarization and the consequent energy efficiency of the sulphur cathode. The single-layer cathode shows a $\Delta E = 0.17$ V for the first cycle at C/10, which is reasonably smaller than the one observed for the two double-layer electrodes, which is 0.25 and 0.23 V respectively for DL-100 μm and DL-200 μm. As already observed in the previous chapter, the presence of a second layer, based on g-C_3N_4, affects the polarization of the cell, which results higher than the single-layer one.
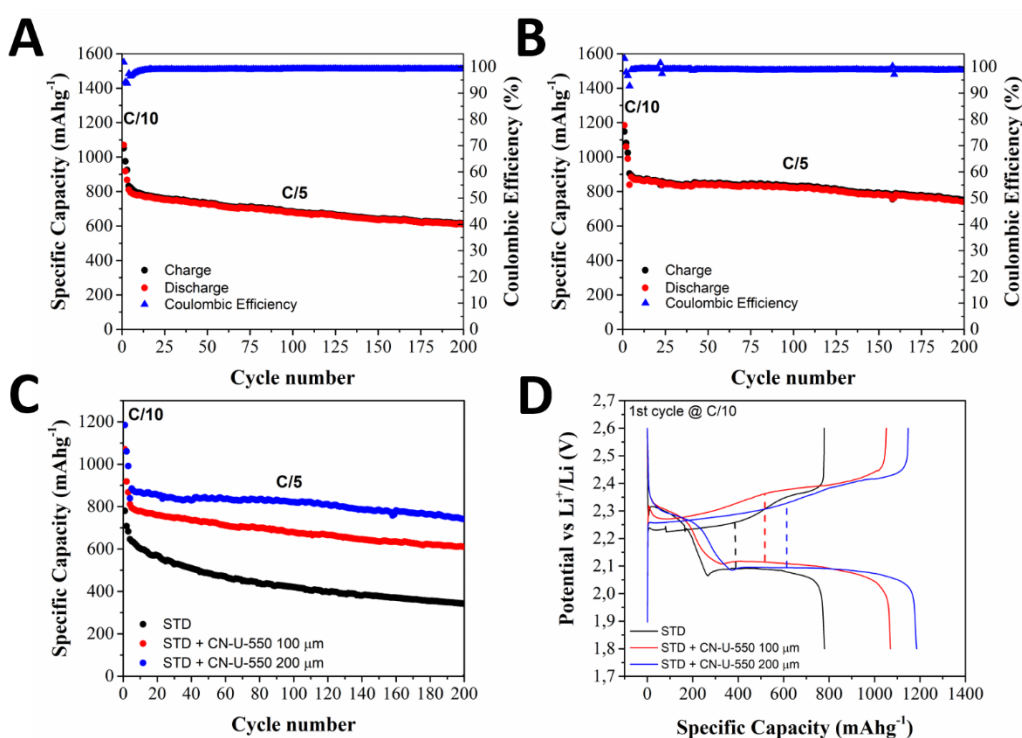
Figure 5.32: specific charge and discharge capacities and coulombic efficiency for double-layer electrode 100 μm (a), double-layer electrode 200 μm (b), specific charge capacity comparison vs. single-layer electrode (c), first cycle galvanostatic charge/discharge profiles comparison at C/10 (d).

The voltage hysteresis increased as the rate increased, so it was also compared at C/5, at different cycles, as depicted in Figure 5.33.

In particular, at 5th cycle, the ΔE of all the cathodes increased, if compared to the previous cycle at lower rate. The ΔE of the single-layer cathode increased to 0.2 V, while it increased to 0.33 and 0.44 V, for DL-100 μm and DL-200 μm, respectively. According to these values, the higher thickness of the top-layer

containing carbon nitride strongly affects the polarization of the cell, especially at higher C-rates.

Observing the charge/discharge curves at higher number of cycle (50, 100, 200), as reported in Figure 5.33 (b, c, d), the calculated voltage hysteresis remains approximately constant for standard electrode, with a slight increase from 0.20 to 0.22 V (after 200 cycles). Similarly, for DL-100 μm, a slight increase is noticeable, from 0.33 V to 0.36 V, after 200 cycles. On the contrary, the voltage hysteresis of DL-200 μm decreases as the number of cycle increases passing from 0.44 to 0.31 V. This means that after 200 cycles the polarization of the two double-layer cathodes is quite similar, in spite of the different thickness.

The ΔE trend of DL-200 μm appears opposite to the other electrodes, because after the expected increasing of the polarization from C/10 to C/5, it decreases during cycling, as shown in Table 5.13.

It is generally accepted that polarization increases upon discharge due to the passivation layer formed on the electrode surface, and due to the Li_2S formed on any available electronic conductive area of the positive electrode. In particular, the insulating layer composed of Li_2S may not be completely re-oxidized in the following charge reaction, with consequent loss of active material. This is the reason why, in the single-layer, a progressive capacity fading of about 0.24% is noticed.

On the contrary higher polarization is observed, in the first cycles at C/5, by DL-200 μm, if related to the low capacity fading of about 0.09 %. This can be ascribable to low connection between sulphur particles and the conductive agent. In fact, at C/5 the sulphur multi-step reaction is too fast and it takes place only at the extreme surface of the electrode, which is rapidly blocked and polarized. This behaviour could be due by the presence of carbon nitride, which is dispersed in a higher volume (higher thickness). Probably, the thick and porous architecture of the second layer, makes the void space totally accessible for the electrolyte, only after few cycles. This also means that the initial polarization is affected by the time needed for the species to diffuse through the double-layer. For the double-layer electrodes the polarization can be also due to the charge accumulation.

In conclusion, the decreasing of polarization after 200 cycles observed for DL-200 μm, let us suppose that the polarization is not attributable to a passivation layer due to Li_2S formation, because it is not linked to a drastic capacity fading.
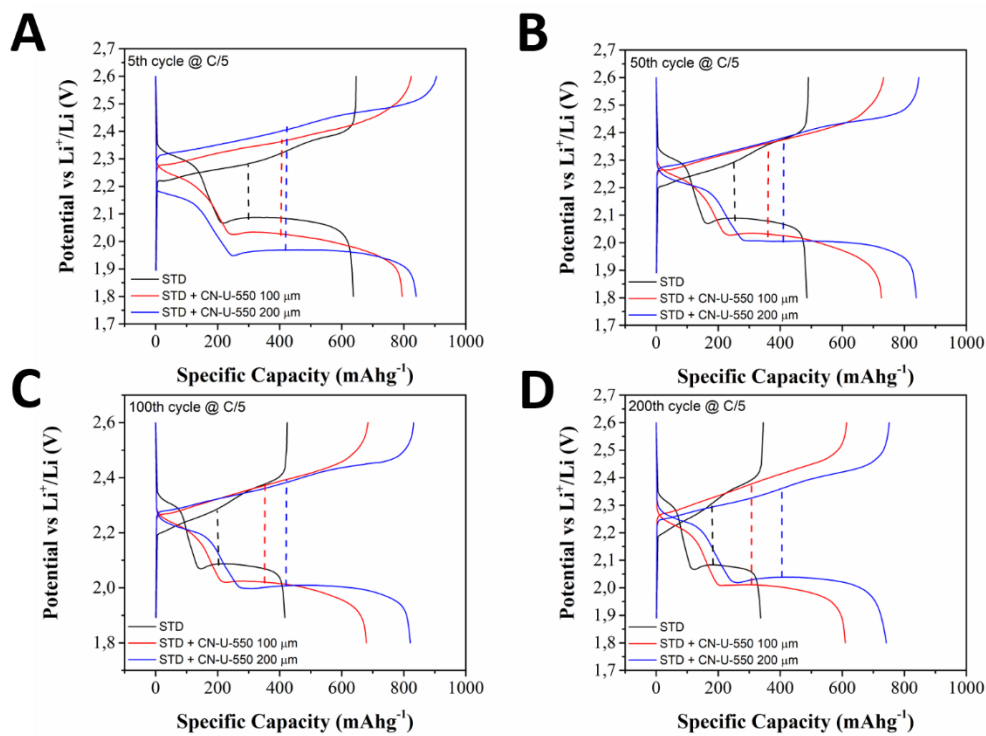
Figure 5.33: charge/discharge profiles comparison corresponding to cycle 5 (a), cycle 50 (b), cycle 100 (c) and cycle 200 (d) at C/5 of single-layer cathode and double-layer cathodes at different thicknesses.

Table 5.13: voltage hysteresis at different cycle number for single-layer and double-layer electrodes.

| Cycle (@ C/5) | Voltage hysteresis (ΔE) | | |
	standard single-layer	g-C$_3$N$_4$ double-layer 100 µm	g-C$_3$N$_4$ double-layer 200 µm
5th	0.20	0.33	0.44
50th	0.20	0.33	0.38
100th	0.21	0.35	0.38
200th	0.22	0.36	0.31

5.4 Influence and modulation of sulphur loading and sulphur/carbon nitride ratio in double-layer electrodes

Starting from the conclusion of the previous paragraph, regarding the influence and the optimization of the thickness in the double-layer electrode, in this paragraph the influence of sulphur loading and the sulphur/carbon nitride ratio is evaluated.

The single-layer electrode was prepared following the as mentioned solvent-casting method by doctor-blade technique. In this case a carbon coated aluminium current collector was used, in order to improve the adhesion and the conductivity of the standard cathode. The "standard" electrode composition was set up to 60/30/10 wt.% and 70/20/10 wt.% (S/KjB/PVdF), in order to obtain cathodes with different sulphur mass loading. The resulting sulphur mass loading was 0.84 and 1.42 mg cm^{-2} for the two different composition, respectively.

A standard cathode composition of 80/10/10 wt.% was also investigated, but it showed worse performances due to the low amount of carbon black, and therefore was not considered for further investigation.

The two different standard electrodes were subsequently coated by a second layer containing carbon nitride (obtained from urea at 550 °C), KjB and PVdF, in the ratio 80:10:10 (w/w%) adopting a blade thickness of 100 μm. The blade thickness of 100 μm was chosen in order to reduce the polarization effect of the second layer, also in the initial cycles, as discussed in the previous paragraph.

The final sulphur/carbon nitride (S/CN) ratio was 1.59 for the electrode with the lower sulphur mass loading (named STD-S-60) and 2.69 for the electrode with the higher sulphur mass loading (named STD-S-70). The relevant S/CN ratio between the two samples allows to obtain more information about the effect of carbon nitride on its optimization.

The electrochemical performances of the electrodes were evaluated using the same protocol adopted in the previous paragraphs. The cells were subjected to charge/discharge cycling at C/10 (calculated on sulphur amount) for three cycles and at C/5 until 200 cycles.

The results are reported in Figure 5.34. Both the double-layer electrodes show a high coulombic efficiency, very close to 100 %, after only few cycles. The specific capacity trend is quite similar for both the electrodes at different mass loading. The initial specific capacity is 1270 mAh g^{-1} and 1060 mAh g^{-1} for STD-S-60 and STD-S-70. The different initial capacity can be attributed to the lower amount of sulphur accessible for the electrochemical reaction. This means that, in the higher mass loading electrode, the amount of sulphur which takes part to the reaction is lower. This claim could seem contradictory, but it is reasonable considering that, the higher is the amount of sulphur, the lower is the contact with carbon black particles, and therefore lower is its availability. However, the

capacity fading observed for both the electrodes is quite similar and is around 0.35 % per cycle at a current range of C/5 (considering 4th to 200th cycles).

The Figure 5.34 (c and d) also reports the comparison of the double layer electrodes with the respective single-layer standard cathodes. The STD-S-60 double-layer electrode showed a specific discharge capacity 160 mAh g^{-1} higher than the co-related single-layer electrode, after 200 cycles. On the contrary, STD-S-70 double-layer electrode showed a lower specific capacity discrepancy from the co-related single-layer electrode, corresponding to only 80 mAh g^{-1}.
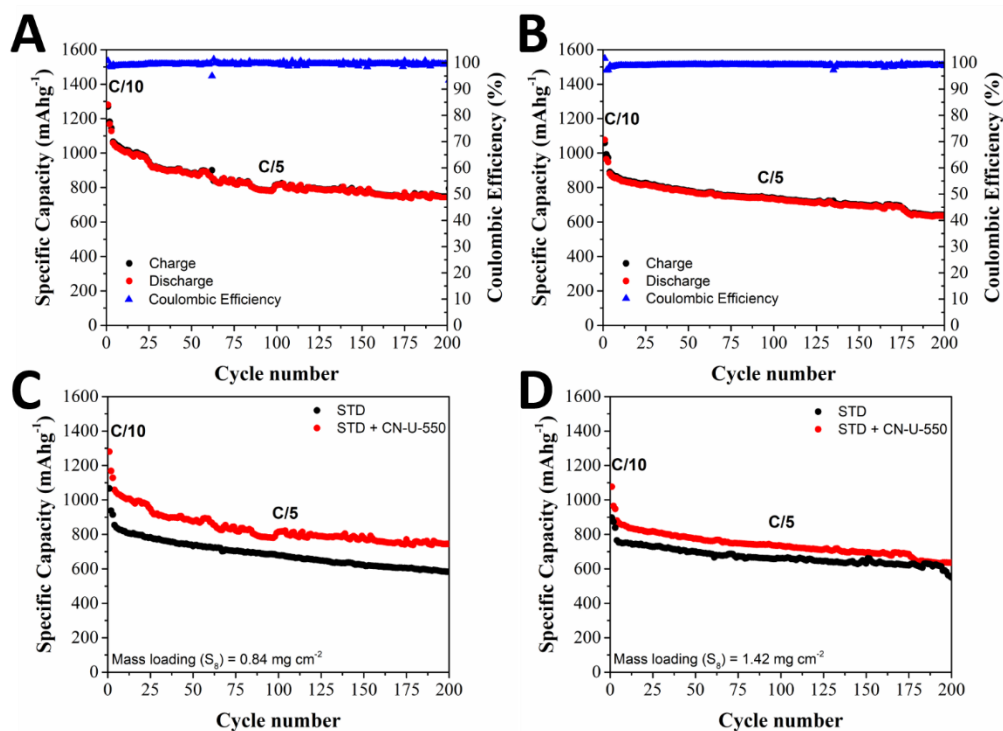
Figure 5.34: specific charge and discharge capacities and coulombic efficiency for double-layer electrode at lower sulphur loading STD-S-60 (a), and higher sulphur loading STD-S-70 (b), specific charge capacity comparison vs. single-layer electrode for lower sulphur loading STD-S-60 (c) and higher sulphur loading STD-S-70 (d).

Figure 5.35 shows the charge/discharge curve profiles for the standard single-layer electrodes (a, c) and the correlated double-layer electrodes (b, d), at different sulphur mass loading.

For all the electrodes a polarization effect due to the transition from lower current (C/10) to higher current (C/5) was observed. The polarization phenomenon is more evident for the cells containing a higher amount of sulphur. This is reasonable because of the insulating nature of sulphur and the higher sulphur/carbon black ratio in the STD-S-70 based electrodes.

On the contrary, adopting an initial second layer thickness of 100 µm, resulting in less than 20 µm after the drying process of the electrode, as discussed

in the previous chapter, seems not to influence the polarization of system during cycling.

Moreover, the single-layer electrode with higher amount of sulphur showed a deterioration of the electrochemical performances, clearly visible in the discharge curve profile of the 200th cycle. In particular, the lower discharge plateau presents an abnormal slope.
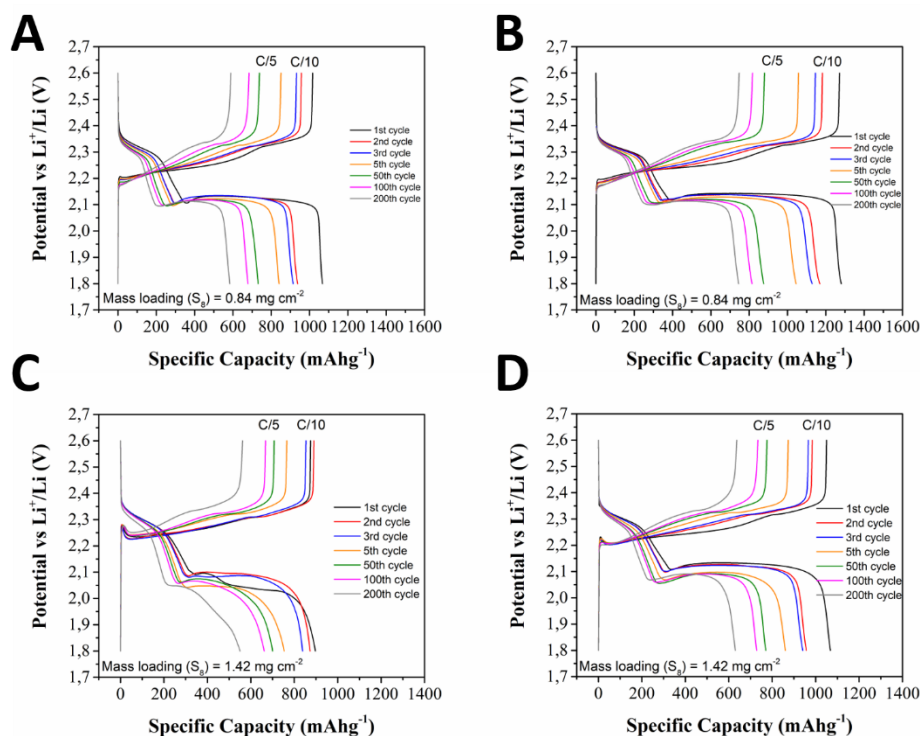
Figure 5.35: charge-discharge curves at different cycle number for single-layer (a, c) and corresponding double-layer lower sulphur loading STD-S-60 (b) and higher sulphur loading STD-S-70 (d).

The voltage hysteresis (ΔE) was evaluated at the 200th cycle and it was compared with the voltage hysteresis of single-layer electrodes (Figure 5.36).

For the STD-S-60 electrode the voltage hysteresis is the same for single and double-layer electrodes, with a value of 0.17 V (Figure 5.36 a).

In the case of STD-S-70 electrodes the ΔE for the double-layer electrode is ~ 0.22 V which is lower if compared to the voltage hysteresis calculated a Q ½ for the standard single-layer electrode (0.27 V) (Figure 5.36 b).

Hence, the overpotential phenomenon could be attributed to the higher sulphur amount present in the cathode, which is less accessible and less conductive. While, the contribution of carbon nitride to the overvoltage is less evident and masked by sulphur mass loading contribution.
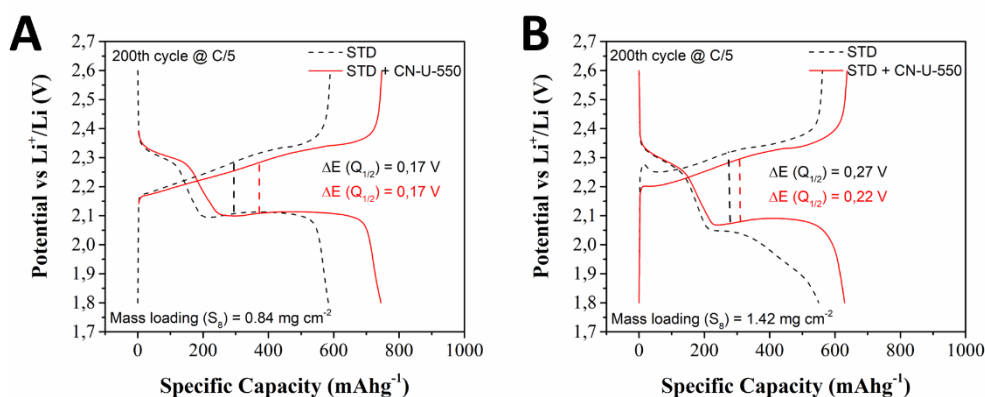
Figure 5.36: 200th cycle charge/discharge voltage profile at C/5 comparison for: lower sulphur loading single-layer and double-layer electrode (a) and higher sulphur loading single-layer and double-layer electrode (b).

All the cells were cycled for more than 200 cycles at C/5, in order to evaluate the long cycling stability and the capacity retention of the systems.

As possible to see in Figure 5.37 (a) the cathodes with 0.84 mg cm^{-2} cycled for 500 cycles. The final capacity of double-layer STD-S-60 electrode was 580 mAh g^{-1}, meaning 55 % of the initial capacity at C/5 and corresponding to 0.9 mAh g^{-1} depletion each cycle. The single-layer cathode, presenting the same amount of sulphur, showed a final specific capacity of 415 mAh g^{-1}, 165 mAh g^{-1} lower than the one observed for double-layer.

The higher loading electrodes showed lower cyclability (Figure 5.37 a), the single-layer standard cathode failed after 250 cycles, while the double-layer electrode cycled for more than 400 cycles. The final double-layer STD-S-70 specific capacity was 445 mAh g^{-1} at 450th cycle, corresponding to 50 % of the initial capacity at C/5. After 450 cycles the cell failed.

The lower cyclability for the high loading cathodes, can be attributed to the higher amount of sulphur and the higher polysulfides formation during cycling. In fact, the single-layer cathode with a 1.42 mg cm^{-2} faded after only 250 cycles instead of 500 cycles achieved by the cathode with lower sulphur amount.

At the same time, the higher cyclability observed in the double-layer cathode with higher amount of sulphur, if compared to the correlated single-layer electrode, passing from 250 cycles to 450 cycles, can be attributed to the presence of carbon nitride. The specific capacity difference, though, is not as evident as it is in the STD-S-60 sample.

115
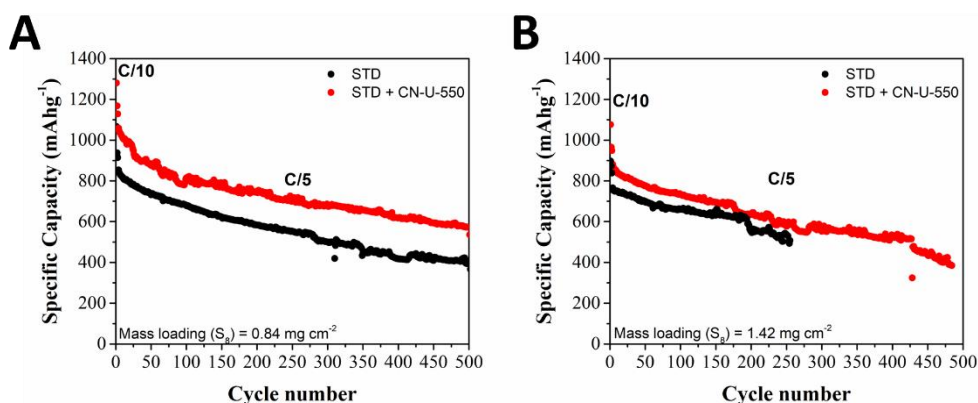
Figure 5.37: long cycling specific charge capacity comparison vs. single-layer electrode for lower sulphur loading STD-S-60 (a) and higher sulphur loading STD-S-70 (b).

It is worth noting that the sulphur/carbon nitride ratio is sensibly different in the two double-layer electrodes, hence the cycling performance are inevitably affected by this aspect. This is a confirmation of the active role of carbon nitride in the improvement of the cell performances.

The STD-S-60 and STD-S-70 double-layer cathodes were also subjected to rate capability evaluation (Figure 5.38). The electrodes were cycled at C/10 for three cycles and at C/2, C/5 and 1C for 10 cycles, respectively. Lastly, the C-rate was reduced again to C/10, with the aim of evaluating the capacity retention after high current regimes.

At C/10 and C/5 the specific capacity of the two samples was comparable, while the at higher current densities (C/2 and 1C) a great discrepancy was observed.

For STD-S-60 the capacity values slowly decreased rising the current density from C/10 to 1C, while for STD-S-70 the specific capacity drastically dropped at higher C-rate (C/2 and 1C).

In particular, the specific capacity at C/10 was higher than 900 mAh g^{-1} for both samples, and it was around 800 mAh g^{-1} for STD-S-70 and 850 mAh g^{-1} for STD-S-60. On the contrary, at C/2 the specific capacity for the higher loading electrode was 220 mAh g^{-1} instead of 770 mAh g^{-1} for the lower loading electrode. At 1C, the specific capacity decreased to 680 and 180 for STD-S-60 and STD-S-70, respectively.

Observing the charge/discharge curves of the two samples (Figure 5.38 c, d), the polarization obviously increases, increasing the current densities. Considering the oxidation process, this behaviour is reasonable because, at high current rate, the oxidation reactions induce a larger polarization and the cut-off voltage is reached faster.

Interestingly, at higher current densities, STD-S-70 presented a unique sloping plateau. This means that the current is too high to reduce all the sulphur through the typical multi-step process. Hence, the reaction takes place only at the

116

extreme surface of the electrode, which is consequently blocked and polarized. The particular, the behaviour observed at high C-rate can be also associated to the mass transport limitation, because the lower plateau is assigned to the formation of insulating species which cover the electrode surface. Anyway, returning back to slow C-rates, the specific capacity was almost the same for both the electrodes and its corresponded to the initial values.
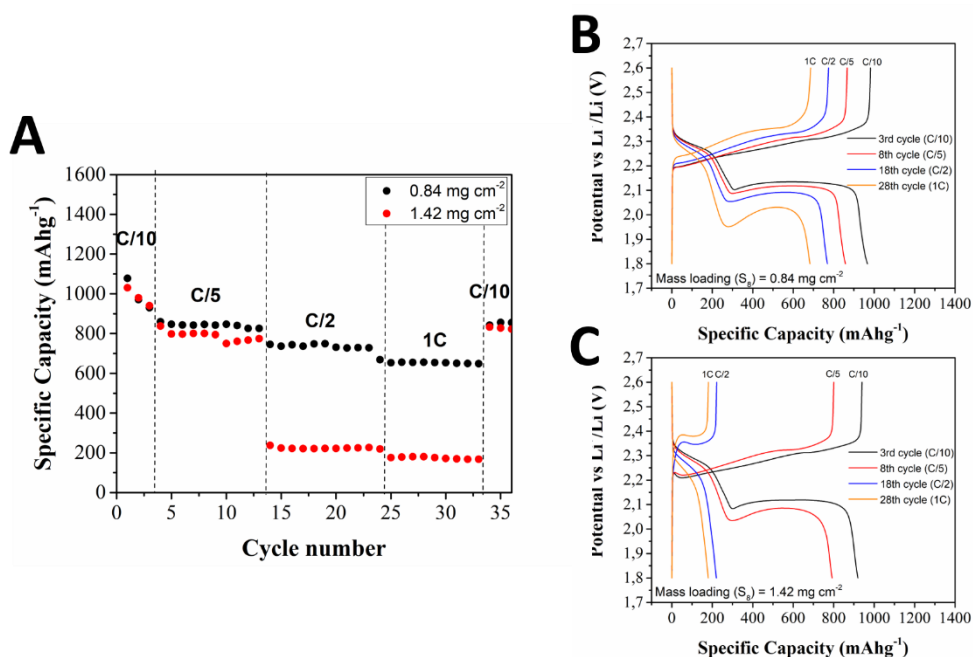
Figure 5.38: galvanostatic charge/discharge performances comparison at high current regimes between low sulphur loading electrode and high sulphur loading electrode (a), galvanostatic charge/discharge profiles comparison at different C-rates for low sulphur loading electrode (b), and for high sulphur loading electrode (c).

In conclusion, the different behaviour of the two samples can be due to the worse conductivity of the electrode containing higher amount of sulphur which results in slow electrochemical reaction kinetics (from long-chain to short-chain lithium polysulfides). In addition, proportion of carbon nitride being the same in both samples (0.9 mg, 0.5 mg cm^{-2}) its contribution to rate capability is not consistent.

5.5 Galvanostatic intermittent titration technique measurements (GITT) to evaluate the internal resistance of the cell.

Galvanostatic intermittent titration technique (GITT) is a measurement where a series of constant current cycling steps are alternated with a relaxation time, during which no current passes through the cell and the potential quickly increases/decreases to reach equilibrium potential.

Generally, numerical data extracted from the GITT experiments give valuable information about the kinetic evolution of the equilibrium voltage and the relaxation behaviour of the system but also give some information about the thermodynamic behaviour of the active material present in the positive electrode.

In addition, GITT can be used as a tool to achieve qualitative information about the relaxation rate of the Li/S cell and its dependency with the depths of discharge [205][206].

In this paragraph the reason for the improved electrochemical behaviour of double-layer electrode containing carbon nitride was studied using the method proposed by Lacely and co-workers [207][208]. They presented a novel method for visualising and quantifying the changes in cell resistance, based on a regression analysis of the voltage change, during intermittent current interruption.

In general, internal resistance is an important indicator of state-of health of a battery system. Moreover, in the rechargeable Li/S system, it is well known that resistance changes considerably during charge and discharge processes as a result of compositional changes of the positive electrode and the electrolyte, and in relation with the state of charge (discharge). So, the continuous changes in internal resistance over cycling can be evaluated adopting a modified galvanostatic cycling program with short-duration intermittent current interruptions [207].

In this study the cells were cycled at constant current density of C/10 between the voltage limits of 1.8 and 2.6 V. GITT analysis was performed each 5 cycles, interrupting the current (set to rest) every 5 min for 0.5 s, for fifty cycles in total. The cell was conditioned for 4 cycles before the first GITT analysis.

Figure 5.39 reports the comparison of standard single-layer and double-layer cathode containing carbon nitride obtained from urea at 550 °C.

Both the cells presented an initial specific capacity of about 1200 mAh g^{-1}, which slightly decreased during cycling. The initial specific capacity also evidenced that the utilization of active sulphur was about 73% for both the electrodes.

The specific capacity, after 50 cycles, was 715 mAh g^{-1} and 798 mAh g^{-1} for STD and STD+CN-U-550 respectively. This means that, at the same current density, the capacity retention was approximately around 62.7 % for the standard cathode and 64.9 % for the double-layer cathode. This means that a slightly higher

capacity fading is observable in the first 50 cycles, for the standard cathode. The coulombic efficiency is close to 100 % for both the samples. In the figure below the cycles subject to GITT are evidenced by stars.
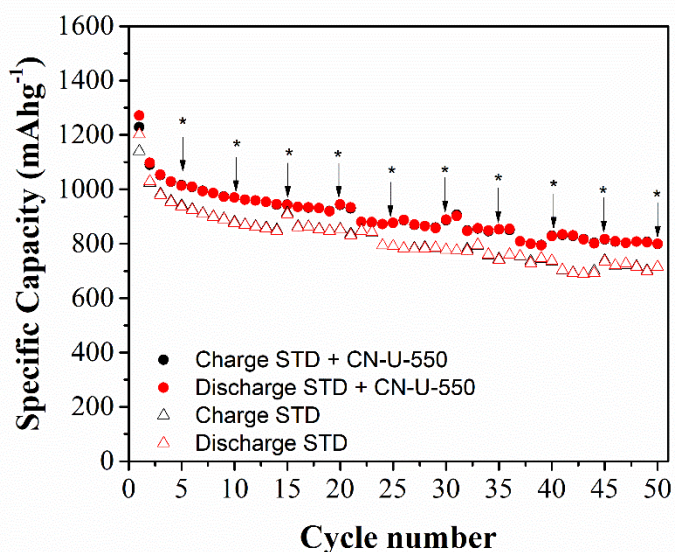
Figure 5.39: GITT measurements each 5 cycles at C/10 for standard single-layer and double-layer with CN-U-550 cathode.

Successively, the data collected were mathematically processed according to the procedure suggested by the authors in reference [207]. More in detail, for each individual current interruption, the cell resistance was calculated according to Ohm's law: R = dE/dI, where dE is the difference between $E_{i=0}$ (calculated by the regression of E vs $t^{1/2}$ to zero time following the current interruption) and E measured immediately before the interruption.

The resistance determined by this method can be reasonably associated to the sum of Ohmic electronic resistance of the electrode, ionic resistance of the electrolyte and charge transfer (kinetic) resistance. In addition, these measurements can be easily compared with EIS measurements.

In Figure 5.40 is reported the voltage profile of the 10th cycle, associated with the calculated internal resistance (for each point of current interruption) for the single-layer standard cathode and the double-layer carbon nitride-based cathode. Both the cells presented a visible increasing of the internal resistance during the upper plateau of discharge. The peak of resistance intensity was observed at about 250 mAh g^{-1} and is related to the transition from the upper to the lower voltage plateau, where the concentration of polysulfides in the electrolyte reaches a maximum (super-saturation point). This increase of resistance is reasonably attributable to the dissolution of long-chain lithium polysulfides into the electrolyte, which inevitably increases its viscosity and reduces its ionic conductivity. The successive resistance decreases, because of the variation of the electrolyte composition, due to the lithium polysulfides conversion (from long-chain polysulfides to Li_2S_2 or Li_2S).
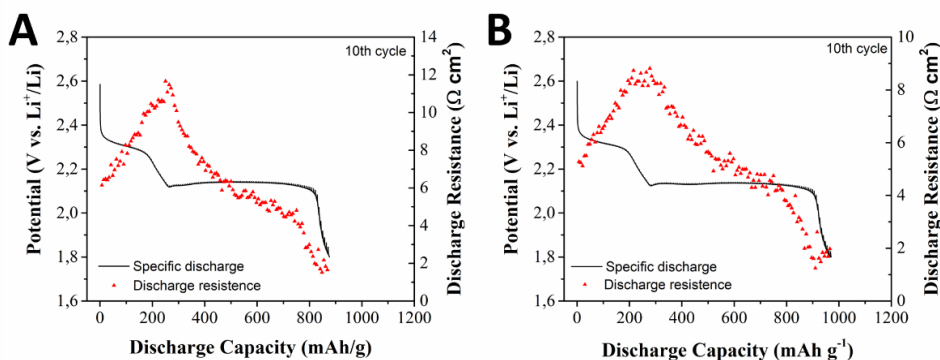
Figure 5.40: internal resistance vs. specific discharge capacity at 10th cycle for the standard single-layer (a) and double-layer with CN-U-550 cathode (b).

Comparing the internal resistance values during charge and discharge, at different cycles (5th, 10th, 25th and 50th), for both cells, it is possible to notice an evident asymmetry of the discharge and charge internal resistance profile (Figure 5.41). In fact, the resistance peak observed during the charge process appears broader and with a less obvious maximum. This behaviour can be explained as a result of the lower rate of change in polysulfides concentration during charge.

In general, during the charge process, the resistance variation can be explained as the release of conductive surface area and pore volume from the discharge products which filled the pores and passivated the surface of the electrodes. So, the resistance variations reflect a variety of physical and chemical changes within the cell, such as passivation by insoluble products, changes in reaction kinetics *etc*.
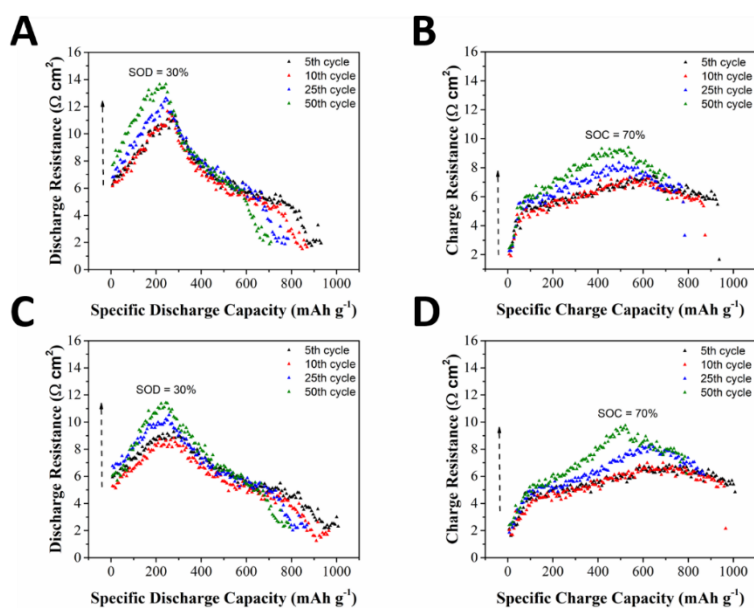
Figure 5.41: internal resistance variation for charge and discharge at the 5th, 10th, 25th, and 50th cycle for the standard single-layer (a, b) and double-layer with CN-U-550 cathode (c, d).

As mentioned before the maximum of internal resistance was observed at about 30% of state of discharge (SOD), and co-respective 70 % state of charge (SOC), which correspond to the point of transition between liquid-state reaction due to long-chain polysulfides and solid-state reaction due to short-chain polysulfides.

Considering the discharge profile trend of internal resistance, what is important to note is the increasing of resistance in percentage during the process. The percentual increasing of internal resistance was evaluated, for both cells, considering the initial resistance, when the discharge process starts, and the subsequent resistances calculated by intermittent current interruption. As possible to see in Figure 5.42, the maximum amount, observed in proximity of the super-saturation point, expressed in percentage, is sensibly higher for the single-layer standard cathode, if compared to the double-layer cathode. Only in the 45th and 50th cycles the values are comparable between the two cathodes, or the percentage of internal resistance increasing for the single-layer cathode appears lower. Assuming the previous conclusions which attribute the internal resistance observed for the upper discharge plateau to the higher viscosity of the electrolyte due to a long-chain polysulfides dissolution, we can conclude that the lower internal percentage variation of the double-layer cathode is attributable to a lower amount of LiPSs dissolved in the electrolyte.

The increasing of IR observed in the last three cycle subjected to GITT analysis can be due to a sort of saturation the carbon nitride, which directly interact with polysulfides. A better explanation of this behaviour could be obtained subjecting to GITT measurements the cell after long cycling procedure.
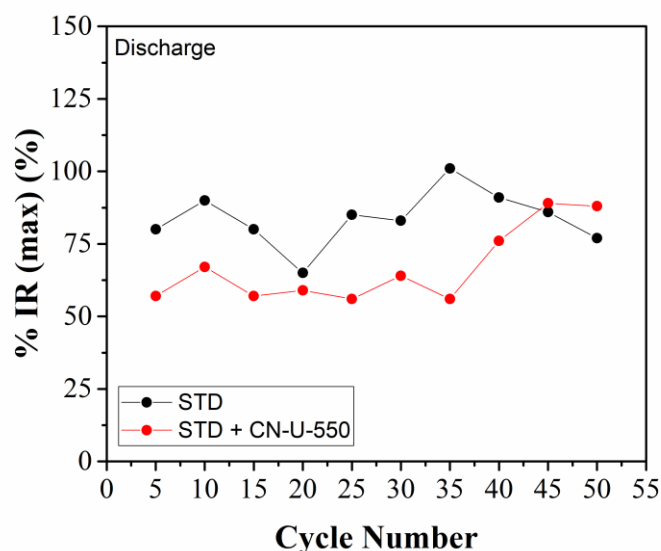
Figure 5.42: percentual increasing of internal resistance comparison, for standard single-layer and double-layer with CN-U-550 cathode, during discharge process.

In conclusion, as mentioned by Lacely [208] a rapid increase of the internal resistance brings to a gradual capacity fade of the cell. The rapid increasing of resistance can be due to the combination of inactivated polysulfide species and the consequent gradually decreasing of electrolyte conductivity and/or the passivation of the electrode surfaces by products of electrolyte decomposition. In our case the double-layer containing carbon nitride directly covering a simple sulphur cathode can hinder the fast dissolution of lithium polysulfides into the electrolyte and consequently, at least, delay or reduce the capacity fading of the cell.

5.6 Impedance response during discharge process

Electrochemical Impedance Spectroscopy tests (EIS) were performed with Bio-Logic® VSP-3e multichannel potentiostat, equipped with impedance modules.

Each spectrum was recorded in the frequency range of 100 kHz to 10 mHz, with an excitation potential of 5 mV and 10 points per decade. All EIS experiments were performed on classical two-electrode Li/S CR2032 coin cells, assembled as previously described.

The EIS measurement was performed at different voltage (2.8, 2.3, 2.1 and 1.7 V), during the discharge process of single-layer and doubled-layer electrode (sulphur loading 0.84 mg cm^{-2}) containing carbon nitride obtained from urea at 550 °C, at C/20 after a formation cycle at the same current range (Figure 5.43).

The EIS measurement was performed in order to evaluate the resistance variation during discharge at different stages.

It is worth noting that the impedance response is a contribution of all the components of the cell.
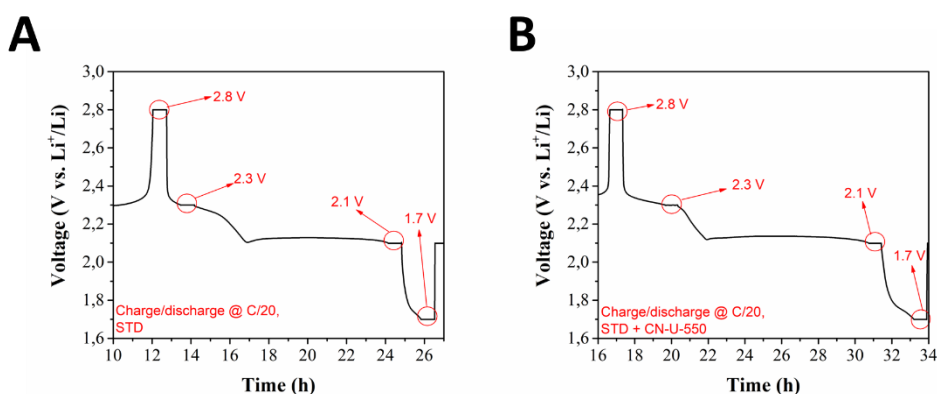
Figure 5.43: discharge voltage profile vs. time for standard single-layer (a) and double-layer electrode (b), circles indicate EIS measurements at different DOD.

Nyquist plot of double-layer electrode with carbon nitride obtained from urea at 550 °C and related contribution is reported in Figure 5.43, as an example.

It is worth noting that the number of semicircles that appear in the Nyquist spectra are strongly related with the depth of discharge/charge (DOD/DOC) of the Li/S cell.
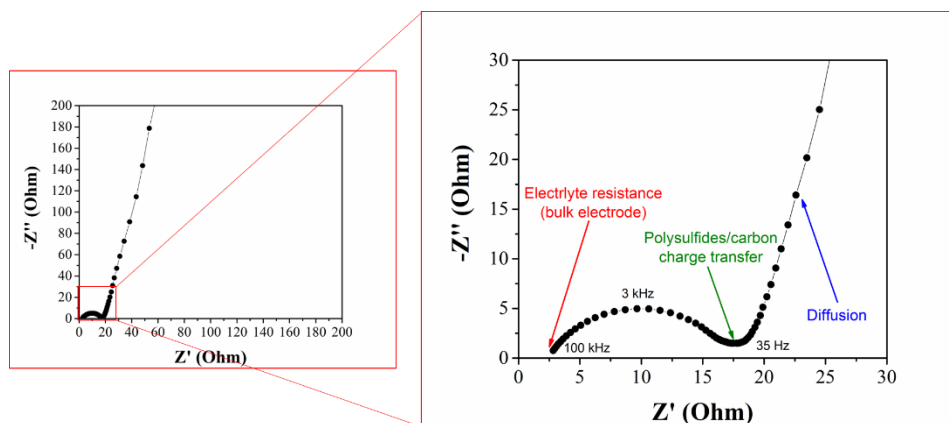
Figure 5.44: Example of Nyquist plot of double-layer cell.

The EIS spectrum for both the electrodes, recorded at 2.8 V, consist of a depressed semicircle at high to medium frequency regions and a bended line in the low-frequency region. In particular, the intercept along the Z' axis at high frequency is referred to the bulk resistance of electrolyte and electrode (Re), while the depressed semicircle observed at middle frequency values of Nyquist plot in Li-S battery is still controversial. Some authors attributed it to the charge transfer resistance of the positive electrode and its capacitance, or to the electronic contact resistance in the bulk electrode [209][210][211][212].

Typically, the Nyquist plot of a Li-S cell can be described by an equivalent electrical circuit consisting of an initial ohmic resistance (Rel) in series with one or more R//CPE elements (connected in parallel). A constant phase element (CPE) is prevalently preferred to a capacitor because of the non-ideal behaviour of the system. The possible multiple loop visible in the high-middle frequencies range (500 kHz - 100 Hz) may be associated to the charge transfer occurring at the anode surface, the charge transfer of sulphur intermediates, and the formation and dissolution of S_8 and Li_2S, respectively. At low frequency (1 Hz - 10 mHz) a CPE was chosen instead of Warburg element to describe the diffusion of lithium ion and/or the reaction of lithium polysulfides to form Li_2S. In a double-layer electrode, the constant phase element can also represent the double layer capacitance and the passivation film capacitance [209].

In general, the depressed semicircles observed in the EIS analysis could be the result of the superposition of many semicircles, corresponding to several parallel contributions (and reactions) occurring in the system [210].

The impedance profiles observed are composed of one depressed semicircle in high and a short Warburg line in low frequency regions. According to literature the anode contribution dominates the high frequencies region of the Nyquist spectrum, while at low frequencies the contribution of cathode is more evident [213].

Concerning the Nyquist plot fitting, several equivalent circuits for the Li-S systems are proposed in literature, in many cases different equivalent circuits are used in function of the different state of charge of the battery.

Based on these assumptions, the impedance spectra obtained in this work can be analysed respectively with the following equivalent circuit:
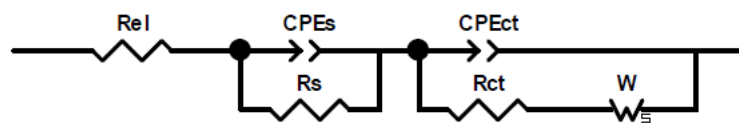
Figure 5.45: Equivalent circuits of Li-S cells for EIS adopted in this discussion

The equivalent electrical circuit consists in an ohmic resistance Rel in series with two R/CPE elements connected in parallel. Rel is the bulk electrolyte resistance, which can be strongly influenced by polysulfides dissolution, CPEs and Rs can be attributed respectively to the surface double layer capacity and surface resistance of lithium and sulphur electrodes. CPEct and Rct can be attributed to the pore double layer capacity and charge transfer resistance, respectively. W is the Warburg impedance due to the diffusion of the polysulfides within the cathode [209].

CPE is a constant phase element which was used instead of capacitance, taking into account the indefinite non-homogeneous morphology of the electrode surface.

Comparing the Nyquist plot, recorded at 2.8 V, for the two cathodes the initial resistance values (Rel) are different despite the identical assembling parameters (electrolyte amount and type). This could be attributed to a better electrolyte filling and diffusion in the double-layer electrode, due to the presence of carbon nitride with high surface area.

Proceeding with the discharge, a second EIS spectra was recorded at 2.3V, corresponding to a DOD of about 10 - 16 %.

Both cathodes showed a shift of Rel at higher values, as reported in Table 5.14.

In Li-S battery the shift observed for the electrolyte resistance (Rel), during charge/discharge process are normally attributed to electrolyte properties variation, such as chemical composition or viscosity. This is essentially due to the

dissolution of polysulfide as described in the previous paragraph. The maximum resistance is expected at the end of the first plateau in the discharge curve, corresponding to the higher concentrations of polysulfides and where the formation of solid Li_2S starts to occur.

The charge transfer resistance shows a similar trend, but more pronounced than that of Rel, because the dissolved polysulfides can diffuse to the anode surface where they can affect the passivation layer on the lithium surface and hinder the charge transfer of lithium ions. The characteristic frequency values are also shifted into higher range, due to the presence of polysulfides in the electrolyte.

Considering the EIS spectra recorded at 2.1 V, meaning a DOD of about 85 %, it is possible to observe a decreasing of the resistance values for both the electrodes. The decreasing is more evident for the double-layer cathode.

In general, in the lower plateau, a strong decrease of the semicircle diameter is observed (Figure 5.46). The lower resistance can be a consequence of the dissolution and reaction of sulphur. This means that the content of solid sulphur in the cathode sensibly diminishes and a more porous structure, with higher surface area and greater conductivity remains.

Therefore, the consumption of sulphur originates a better electronic contact interphase between particles, resulting in smaller semicircle.

The traditional diffusion line is replaced by an arc. This can be explained by the precipitation of insulating species directly on the electrode surface resulting in a blocking interface. This is also the reason why the resistance (in the equivalent circuit model) attributable to diffusion, could not always be determined as a result of an insufficient number of measured points at low frequencies.

At 1.7 V, where the discharge process is completed a lower electrolyte resistance is observed for the double-layer cathode instead of single-layer one (Table 5.14).

As mentioned before a lower value of Rel can be attributable to a lower amount of residual soluble species into the electrolyte. This let us suppose that a higher amount of soluble species is converted in Li_2S as a consequence of the presence of a second layer containing carbon nitride.

Concerning the charge-transfer and surface resistances, during discharge, Rs initially increases in correspondence of the first plateau at 2.3 V, for both the samples. The increment can be attributed to side phenomena, occurring on lithium surface, as SEI layer formation and long chain polysulfides reactions. However, as a concomitant variation of sulphur cathode surface occurs, its contribution to Rs increment cannot be excluded. During the second plateau (*e.g.* 2.1 V), where short chain polysulfides are formed, Rs decreases drastically, as expected. At the end of discharge process the Rs are comparable for both the cathodes.

The charge-transfer resistance is high at the beginning of the discharge for both the samples and decreases with the DOD increment. The significant decrease of Rct observed in the two plateau regions can be associated with the improved

electrochemical accessibility resulting from the consumption of insulating sulphur, during discharge. While the final increase of Rct, observed at 1.7 V (100 % DOD) could be ascribed to the generation and accumulation of insulating Li_2S and Li_2S_2 species on the cathode surface. The lower charge-transfer resistance value obtained for double-layer cathode, confirms the higher catalytic effect of carbon nitride in the polysulfide anchoring and conversion [211].

It is worth noting that the DOD of the two samples at 2.3 V is not the same, because the single-layer and double-layer cells reach this potential value at different time of their discharge process, so the EIS spectra are not properly comparable, and some discrepancies in the EIS analysis have to be taken into account.

Table 5.14: electrolyte and charge-transfer resistance at different state of discharge for single-layer and double-layer electrode.

Voltage (V)	Standard single-layer			Double-layer with g-C3N4		
	Rel	Rs	Rct	Rel	Rs	Rct
2.8	5.86	8.94	75.09	2.82	14.92	52.08
2.3	7.06	15.42	3.02	5.11	29.77	-
2.1	6.46	6.59	3.56	2.7	6.21	5.26
1.7	6.26	7.31	24.32	2.64	6.35	11.78
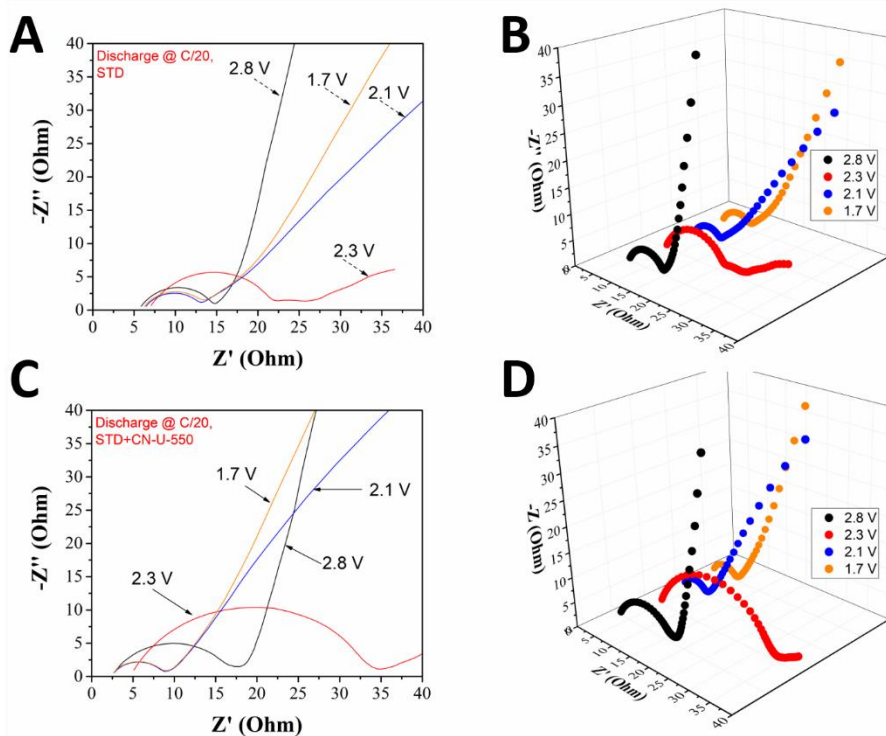
Figure 5.46: 2-D and 3-D Nyquist plot comparison at different DOD for single-layer electrode (a and b), and double-layer electrode (c and d).

In conclusion the EIS analyses are in good agreement with the results obtained with GITT measurements. In particular, the lower resistance values observed for the double-layer electrode seems to confirm a contribution of carbon nitride to the long-chain polysulfides conversion.

Chapter 6

6 Tin dioxide

Tin-based materials, particularly tin oxides, have been widely investigated since 1997 when Idota *et al.* from the Fuji Photo Film Celltec Co. (Japan) company reported SnO_2 as potential graphite substitutes for next generation LIBs [214].

SnO_2 gained great attention due to the high theoretical and volumetric capacity, biological compatibility, environmental friendliness, and rather low cost, but also to its low discharge potential [215].

The lithium reaction with SnO_2 is believed to proceed through two major steps: conversion and alloying [215][216].

This peculiarity explains the high theoretical specific capacity of tin oxide, which is four folds higher than that of graphite (782 mAh g^{-1} cycled in the voltage range of V = 0.005 - 1.0 V; and 1493 mAh g^{-1} cycled in the voltage range of V = 0.005 - 2.0 V) [217].

More in detail the electrochemical conversion of SnO_2 to metallic Sn and Li_2O occurs at 1.2 V *vs.* Li^0/Li^+. During this step, SnO_2 undergoes structural amorphization with the consequent formation of metallic tin dispersed in amorphous Li_2O, according to the following reaction:

$$4Li^+ + 4e^- + SnO_2 \rightleftarrows 2Li_2O + Sn \qquad (> 1.2 \text{ V vs } Li^0/Li^+) \qquad [6.1]$$

The conversion reaction is a typical reaction occurring between a metal oxide (MO) and lithium ions, involving the formation (and decomposition) of Li_2O, as shown in the following general mechanism [21]:

$$MO + 2Li^+ \rightleftarrows M + Li_2O \qquad [6.2]$$

where M is a 3d-metal (Mn, Fe, Co, Ni, Cu, Sn)

As mentioned, the reaction between lithium ions and MO induces the amorphization of the lattice, followed by the formation of metal particles embedded into a Li_2O matrix. Li_2O is electrochemically inert but it can participate indirectly to the anode performance by catalysing the reaction.

During charge (de-lithiation), MO is re-formed as a consequence of the decomposition of Li_2O [21].

Generally, the reversible capacity due to the alloying/dealloying reaction, occurring in the voltage range of 0.3 - 0.4 V $vs.$ Li^0/Li^+, which forms a series of Li_xSn-type alloys [217].

$$xLi^+ + xe^- + Sn \rightleftarrows Li_{x2}Sn \qquad (0 < x < 4.4) \qquad [6.3]$$

The conversion reaction (Equation 6.2) was initially believed to be the critical step to achieve the high capacity due to the irreversible conversion of Li_2O to SnO_2, driving the huge capacity loss (about 50 %) and the low Coulombic efficiency of SnO_2 anodes [217][218]. However, the specific capacity of SnO_2 still exceeds the one of graphite (372 mAh g^{-1}) even when considering only the step of alloying/dealloying.

Recent studies suggested that the conversion reaction is also partially reversible, if SnO_2 particles are in the nanometric form [219]. In particular, photoelectron spectroscopy (XPS) studies underlined the overlap of the conversion, alloy, and electrolyte decomposition reactions in the voltage range 1.2 - 0.4 V $vs.$ Li^0/Li^+, which induce the incomplete SnO_2 conversion and the consequent inability in regenerating the reduced SnO_2 in the oxidative process [220].

Some other studies on thin-film electrodes emphasized the presence of partially reversible intermediate phases (Li_2SnO_3 and Li_8SnO_6) during lithiation [221], which were experimentally individuated by Ferraresi et $al.$ [222] combining electrochemical studies with post-mortem XPS analysis, and SEM imaging. During de-lithiation, decomposition/dissolution of Li_2O is found to occur in parallel to the de-alloying reaction and the intermediate species are subsequently reduced to metallic Sn, which form Li_xSn alloys with increasing Li content (LiSn, $Li_{13}Sn_5$, Li_7Sn_2, up to $Li_{17}Sn_4$) [222].

Nevertheless, the problem of capacity fading has never been completely solved. Moreover, the other drawback that hampers SnO_2 application in LIBs, is the enormous volume expansion and contraction (up to 250 %) related to the formation and dealloy of Li_xSn during repeated charge/discharge cycling processes (Equation 6.3). This enormous volume expansion inevitably induces relevant stresses, loss of contact among particles and pulverization of active material [215]. Fortunately some experimental observations suggest that particle size reduction limits the stresses arising from the lithiation/de-lithiation process and it is recognized that most appropriate particle dimensions should be lower than 10 nm [223].

Furthermore, SnO_2 has poor electronic conductivity ($1.82 \cdot 10^{-8}$ S cm^{-1} [224]), meaning that it must be intimately contacted with electronically conductive additives.

To overcome all these issues, the main strategy is to achieve a good distribution of nanoparticles in a light matrix that restrains volume expansion and provides electronic conductivity.

In fact, similarly to other electrode materials with comparable properties, like silicon, reducing the particles to nanoscale dimensions is a promising strategy to mitigate the intrinsic drawbacks of SnO_2. The nano-structuration of the materials helps to accommodate volume expansion through built-in porosity and reduces the agglomeration of Sn clusters by a homogeneous dispersion within a Li_2O matrix but, does not reduce the extent of volume change. It follows that is necessary to design a hybrid compound in which the nanoscale SnO_2 is finely dispersed in a stable matrix which acts as a "buffer" [215].

Well-designed nanostructured composites of SnO_2 and carbon with graphene [223][225], carbon nanotubes (CNTs) [226][227], ordered mesoporous carbon nanospheres (OMCS) [228] and others carbonaceous materials [229] were developed to buffer SnO_2 volume expansion and prevent aggregation and pulverization of particles. However, the synthesis of composites generally involves two steps: preparation and/or surface activation of the carbon matrix followed by the growth of tin dioxide particles directly on the carbon support by hydrothermal [230][231][232], microwave-assisted hydrothermal [228] sono-chemical [233] or electrospinning [233] methods. Unfortunately, some of these approaches are expensive, require the use of solvents or complex techniques that make their scale-up extremely difficult and such complexity is not in line with requirements of cost affordable batteries.

Starting from these considerations, in my PhD work I focused my attention on hassle-free approach to prepare SnO_2/C composites using a simple, fully sustainable and economic synthesis process. The synthesis was carried out by wet impregnation without any acid treatment or high temperature process and tin oxide was in situ nucleated on commercial carbon black C-NERGY^{TM} Super C45 (Imerys Graphite & Carbon) in form of homogenously distributed nanoparticles. C-NERGY^{TM} Super C45 was selected because of its easy water dispersion, commercial availability and electronic conductivity [234]. The presence of surface oxide and carboxylic functional groups of C45 gather the possibility to tailor the nature of interaction with the metal oxide (SnO_2) especially when the wet impregnation technique is used in the preparation of the composites. In particular, the oxygen functional groups on the carbon surface provide anchorage sites for metal oxide precursor and act as active centres for nucleation. Moreover, such surface groups decrease the hydrophobicity of the carbon and this eases the access of metal precursor solutions [235].

Part of the results described in this chapter were previously published [236].

Chapter 7

7 Ultrasmall SnO$_2$ directly grown on commercial C45 carbon

7.1.1 Synthesis

The synthesis of SnO$_2$/C45 consists in two simple steps: in situ deposition of SnO$_2$ on C45 followed by elimination of the impurities. The first step was achieved by pouring an aqueous solution of SnCl$_2$·2H$_2$O (purity > 98 %, Sigma-Aldrich) on commercial carbon black (TIMCAL C-NERGY™ Super C45-Imerys) to obtain a semi-solid sludge with Sn/C = 2/3 (mass ratio). Typically, SnCl$_2$·2H$_2$O (1.2 g) was dissolved into Milli-Q® water (12 g) to obtain a milky suspension (9.0 wt.%, pH = 1.74). Then C45 (2.0 g) was added to the suspension under stirring at room temperature. Finally, the sludge was dried in oven (80 °C) overnight, to obtain the raw SnO$_2$/C45 material.

In the second step, the removal of impurities was carried out by washing the sample with water and centrifuging (10000 rpm for 15 minutes) several times until pH raised up to 4.0. The so obtained product was dried in oven (80 °C) overnight and labelled SnO$_2$/C45.

The steps involved in the synthesis of sub-5 nm SnO$_2$ nanoparticles spatially distributed on carbon black C-NERGY™ Super C45 are schematically illustrated in Figure 7.1.
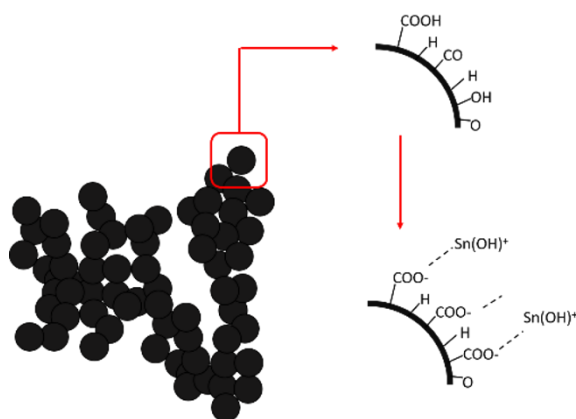
Figure 7.1: Schematic sketch of the interaction between C45 and SnO$_2$ precursor in the formation of SnO$_2$/C45 composite [236].

The strategy allows one-shot production of SnO$_2$/C composite exploiting the ease of the hydrolysis and the advantage of surface chemistry of C45, which contains high concentration of oxygen functional groups [234]. The chemical behaviour of SnCl$_2$ in excess of water depends on many factors such as the solution concentration, the pH and the presence of aerial oxygen. SnCl$_2$ is readily soluble in water where the following reaction (Equation 7.1) occurs [237][238][239]:

$$2SnCl_2 + O_2 + 2H_2O \rightarrow 2SnO_2 + 4HCl \qquad [7.1]$$

However, if the pH ranges in the interval of 1.24 - 4.13, Sn$_4$(OH)$_2$Cl$_6$ colloidal particles are formed as a result of the hydrolysis reaction 7.2 [239]:

$$4SnCl_2 + 2H_2O \rightleftarrows Sn_4(OH)_2Cl_6 + 2HCl \qquad [7.2]$$
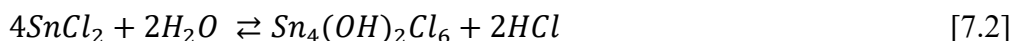
Generally, the Sn$_4$(OH)$_2$Cl$_6$ phase converts into SnO, and the hydrolysis of SnCl$_2$ requires HCl acid environment at pH down below 1.24 to obtain SnO$_2$ [239]. However, by wet impregnation, SnCl$_2$ undergoes direct hydrolysis/oxidation and acidification is not needed [237]. For the purpose, the easy dispersion of C45 in aqueous environment allows the use of a concentrated SnCl$_2$ solution to form a semi-solid slurry instead of a liquid mixture. First, a milky-white colloidal suspension is produced by solubilizing SnCl$_2$·2H$_2$O in distilled water, after addition of C45 to the colloidal suspension, the positively charged Sn(OH)$^+$ species [240] can be easily loaded on the carbon surface, by electrostatic interactions with the negatively charged surface groups of C45, where they experience hydrolysis:

$$Sn(OH)^+Cl^-(aq) + 2H_2O\ (l) \rightarrow Sn(OH)_2\ (aq) + HCl \qquad [7.3]$$
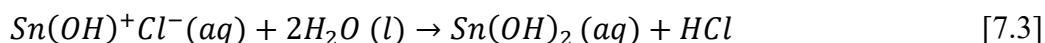
Owing to oxygen in air, tin (II) is oxidized to tin (IV) [241] so that $Sn(OH)_2$(aq) self-evolves into ultra-small SnO_2 nanoparticles on the surface of C45 (reaction 7.4), which supplies nucleation sites for the deposition:

$$Sn(OH)_2\ (aq) + \frac{1}{2}O_2\ (g) \rightarrow SnO_2\ + H_2O \qquad\qquad [7.4]$$
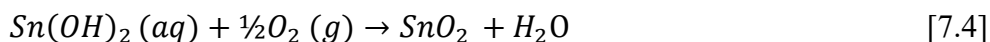
It is worth noting that C45 is essential to obtain SnO_2 nanoparticles because it presents oxide and carboxylic acid surface functional groups and lower degree of graphitization (sp^2 carbon concentration) in comparison to other commercial carbons. In this respect, C45 does not act as a mere carbon support but directs the homogeneous nucleation of SnO_2 nanoparticles. This is consistent with previous thermodynamic studies [242] demonstrating the tendency of tin ions to form complexes on activated carbon (AC) sites [243]. Particularly, oxygen containing groups on the carbon surface are responsible for the chemical attraction of positively charged tin species [228] and this stems from the fact that Lewis basicity associated to the aromatic rings in the activated carbons is weak [244] and the main basicity results from the oxygen containing groups [237].

7.1.2 Structural and morphological characterization

Figure 7.2 depicts the XRD spectra of bare C45 and SnO_2/C45 composite. Bare C45 XRD pattern evidenced the presence of two peaks at 25° and 44° which are assigned to (002) and (101) graphitic planes, respectively [245]. SnO_2/C45 XRD pattern shows three main broad peaks at 26.5°, 33.9° and 51.8°, corresponding to the (110), (101) and (211) planes of SnO_2 phase. The peak broadening is attributed to the small particle dimension of SnO_2, which average size is about 5.0 nm calculated using Scherrer's equation.
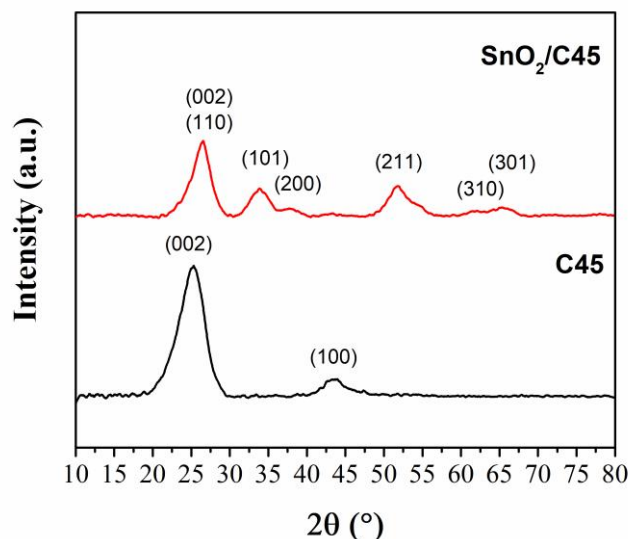
Figure 7.2: XRD spectra comparison of C45 (black line) and SnO$_2$/C45 (red line).

Thermogravimetric analysis (TGA) was performed on SnO$_2$/C45 and bare C45 under air atmosphere between 25°C and 800 °C in order to estimate the ratio of SnO$_2$ and C45 (Figure 7.3). The TGA curve of SnO$_2$/C45 points out two stages of weight loss. The initial weight loss in the temperature range of 25 - 200 °C is due to absorbed moisture, from the ambient atmosphere. In the temperature range of 200° - 450 °C a slight weight loss is attributable to the decomposition of surface functional groups of C45 [246], while the small inflection after 500 °C is reasonably due to the oxidation of residual stannous compounds. However, the significant weight loss occurs between 500 and 600 °C which is ascribable to the carbon combustion. Above 600 °C, the residue is attributed to pure SnO$_2$, corresponding to 29 wt.% of the total weight.

The TGA analysis was also carried out in the same experimental conditions, on the mixture consisting of commercial SnO$_2$ (Aldrich) and C45, mechanically mixed in the ratio 29:71 wt.% for comparison.

It's worth noting that combustion of SnO$_2$/C45 starts at lower temperature (about 500 °C) than that of the mechanically mixed commercial SnO$_2$-C45 powders, which is about 650 °C. This particular behaviour can be explained according to the catalytic effect known as Mars–van Krevelen mechanism [247], in which oxygen does not oxidize carbon directly, but is activated by transformation into high mobility lattice oxygen on the defective surface of SnO$_2$ [247][248]. Therefore, the resultant shift of the oxidation temperature requires the close proximity of tin dioxide to carbon and indirectly explains the metal oxide/carbon composite formation, confirming the strong chemical interaction between SnO$_2$ and C45 in obtained SnO$_2$/C45 compound.
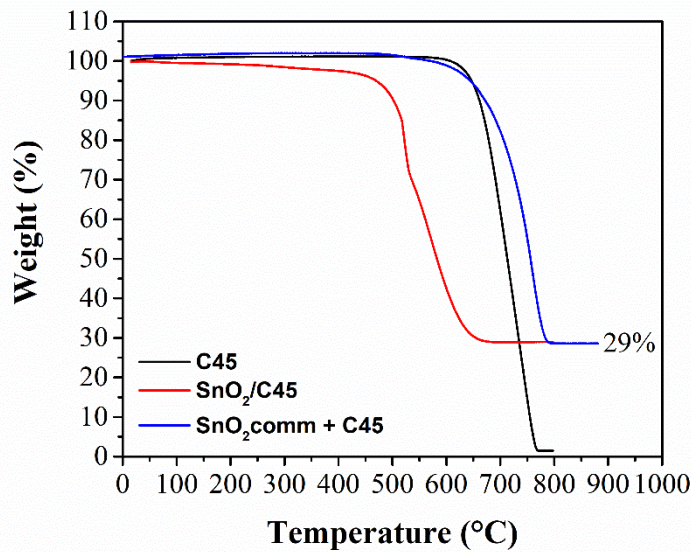
Figure 7.3: TGA analysis of C45, SnO_2/C45 and of commercial SnO_2 + C45 mixed in weight ratio 29:71.

The BET specific surface area (SSA) is evaluated by means of N_2 adsorption/desorption isotherms (Figure 7.4). The BET values of C45 and SnO_2/C45 are 52 m^2 g^{-1} and 65 m^2 g^{-1}, respectively. The slight increase in the SSA of SnO_2/C45 can be due to the SnO_2 nanoparticles placed on the C45 particles surface.
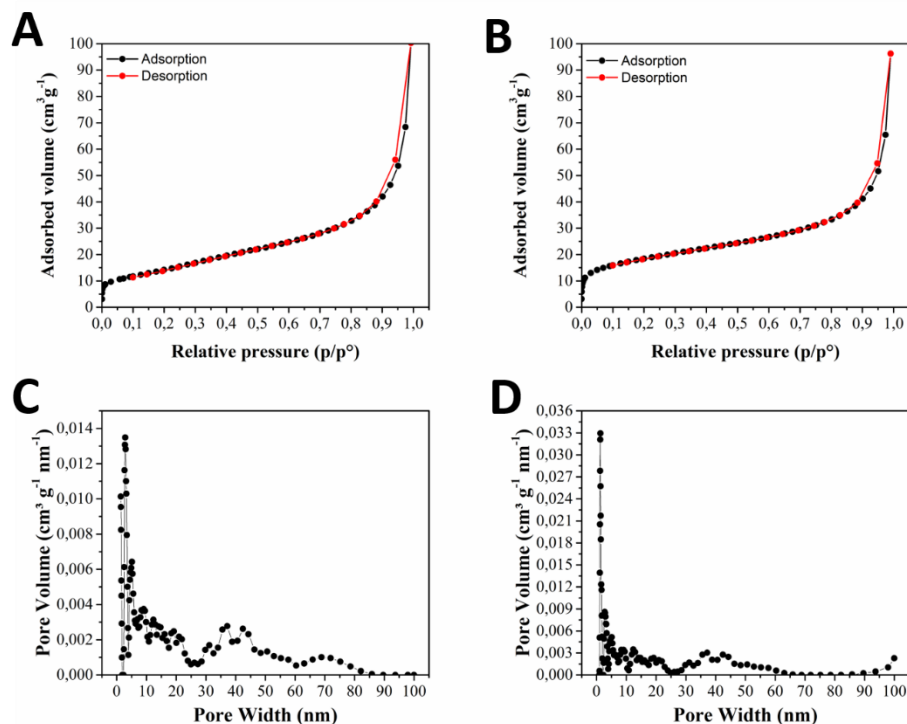
Figure 7.4: N_2 adsorption/desorption measurements of SnO_2/C45 (a) and C45 (b), pore distribution of SnO_2/C45 (c) and C45 (d).

The N$_2$ adsorption/desorption isotherms of pure C45 and SnO$_2$/C45 composite are compared in Figure 7.4 a and b. The curves show type II isotherms with a H3 type hysteresis at low p/p$_0$, typical for non-rigid aggregates with a pore network consisting of both mesopores and macropores (Figure 7.4 c and d). The SnO$_2$/C45 composite displays the same inhomogeneous micro-meso porosity of the parental carbon without any relevant change of porosity.

The fine dispersion of sub-5 nm SnO$_2$ nanoparticles on carbon surface is confirmed both by TEM and by FESEM analyses.

C45 consists of slightly large primary particles, with average particle diameter ascribed between 40 - 60 nm, as shown in Figure 7.5. FESEM micrographs of SnO$_2$/C45 highlight the presence of SnO$_2$ nanoparticles homogeneously dispersed on the C45 surface (Figure 7.5 b, c). Specifically, at high magnification (100000 KX), the surface of pure C45 appears smooth (Figure 7.5 c inset), while the surface of SnO$_2$/C45 is rough due to anchoring of SnO$_2$ nanoparticles (Figure 7.5 c).
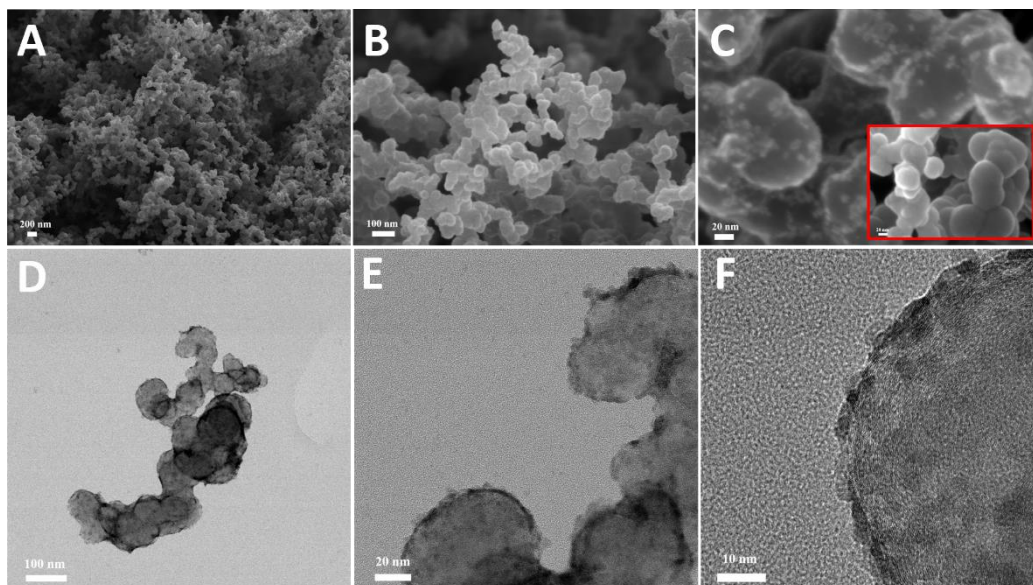
Figure 7.5: FESEM micrographs of SnO$_2$/C45 at low, intermediate and high magnifications (a, b, c), FESEM micrographs of bare C45 at high magnifications (inset). TEM micrographs of SnO$_2$/C45 at low, intermediate and high magnifications (d, e, f).

Observing the TEM micrography at high magnification (Figure 7.6) the lattice fringes of randomly arranged nanoparticles highlight inter-planar distances of 3.34 and 2.64 Å, which are in good agreement with (110) and (101) planes of SnO$_2$.

Moreover, TEM micrographics confirms SnO$_2$ average particle dimension of about 5.0 nm which evenly cover C45 surface.
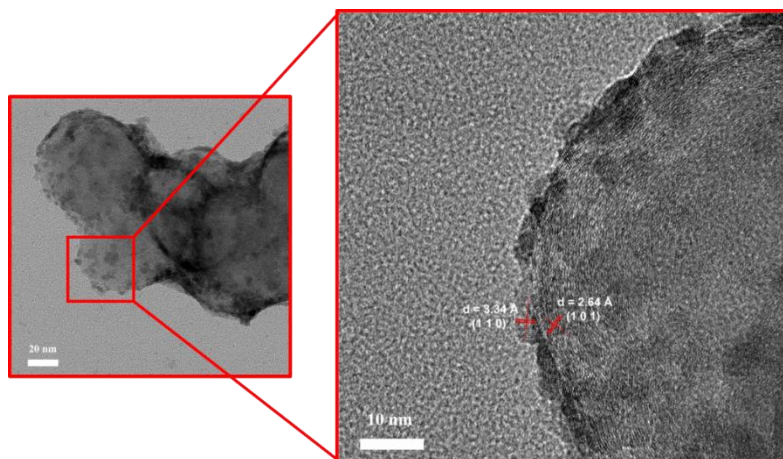
Figure 7.6: zoomed TEM micrography of SnO$_2$/C45 with evidenced lattice fringes.

In general, SnO$_2$/C45 shows a good interconnection among carbon particles to form a continuous network, ensuring the necessary electronic conductivity. The space among SnO$_2$ nanoparticles is desired to accommodate the large volume expansion during the alloying process, avoiding pulverization of the active material, so that the electrode can afford long cycling performances [249].

In order to get more information on the chemical species present in the starting materials and affecting the final electrochemical performance, EDS elemental analysis was performed (Figure 7.7, Table 2.1). The presence of carbon and a little amount of oxygen was detected in pure C45 sample, while in the composite sample tin was also identified, as expected. In the SnO$_2$/C45, chlorine is almost absent and the weight ratio C:Sn is about 1:3, indicating successful sample purification.
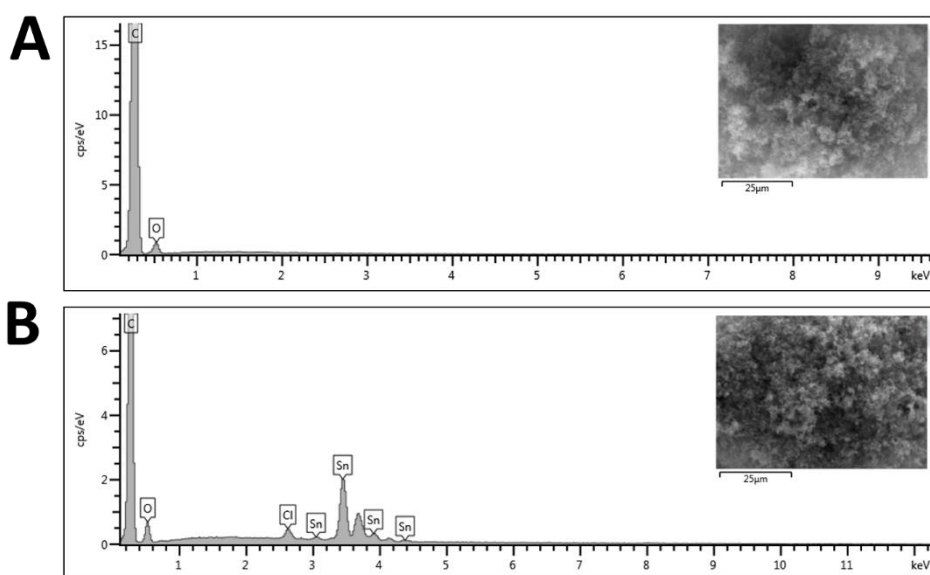
Figure 7.7: EDS analysis of (a) pure C45 and (b) SnO$_2$/C45.

Table 7.1: elemental surface amount of C45 and SnO$_2$/C45 from EDS analysis.

Elem.	C45		SnO$_2$/C45	
	Wt%	% atom.	Wt%	% atom.
C	92.31	94.11	69.07	88.62
O	7.69	5.89	8.54	8.23
Sn	-	-	21.58	2.8
Cl	-	-	0.81	0.35
Total	100.00	100.00	100.00	100.00

X-ray photoelectron spectroscopy (XPS) analysis was carried out to understand the SnO$_2$-carbon interaction (Figure 7.8). The XPS survey of SnO$_2$/C45 shows the presence of Sn, C and O and again, no chloride is detected, in agreement with the previous observations.

Deconvolution of the C1s peak for C45 results in two main contributions (Figure 7.8 b): the peak at 284.8 eV is attributed to C=C (72 %) and the peak at 285.6 eV is assigned either to C−OH or C−O−C (28 %). In SnO$_2$/C45 (Figure 7.8 c), the C1s peak is deconvoluted in four main components at 284.8, 285.9, 287.3 and 289.8 eV, which are associated to C=C (51 %), C−O and Sn−O−C (33%), C=O (13 %), −COOH (3%), respectively [233][250]. In both C45 and SnO$_2$/C45 samples, the major contribution is due to sp^2 bonded carbon, which is smaller in SnO$_2$/C45 (51 % at.) than in C45 (72 % at.). The 3.0 % of −COOH in the C1s of SnO$_2$/C45 can be explain through the entirely or partially oxidation of C−O−C into −COOH groups during the composite synthesis. More precisely, the oxidation of surface groups of the carbon into −COOH involves strong oxidizing species that originate from O$_2$ (air) and catalysed by SnO$_2$ during the oven-drying step at 80°C [237].

The presence of Sn-O-C peak at 285 eV supports the idea that SnO$_2$ nanoparticles are firmly anchored to the C45 surface, which is beneficial to preserve both stability and integrity of the composite during cycling [232]. The high-resolution spectrum of O1s of SnO$_2$/C45 (Figure 7.8 e) is deconvoluted in two peaks which are centred at 531.8 eV and 533.2 eV and attributed to Sn−O and C−O/C=O, respectively [251]. In the XPS Sn3d spectrum (Figure 7.8 d), two main peaks at 496.3 and 487.9 eV are assigned to Sn 3d$_{3/2}$ (~40%) and Sn 3d$_{5/2}$ (~60%) of Sn^{4+} (Sn bonded to O). The binding energy separation of 8.4 eV well agrees with the values reported in literature for SnO$_2$-based materials [252] moreover, no Sn (0) or Sn^{2+} are present [250]. Particularly, Sn directly bonded to C atoms should result in additional peaks Sn−C on the left-hand side of Sn 3d$_{3/2}$ and Sn 3d$_{5/2}$ peaks [253]. Those peaks are absent in SnO$_2$/C45 spectrum suggesting that SnO$_2$ preferentially interacts with C−O. This interaction should

contribute to modify the properties of pure tin dioxide and enhance lithium storage performance.
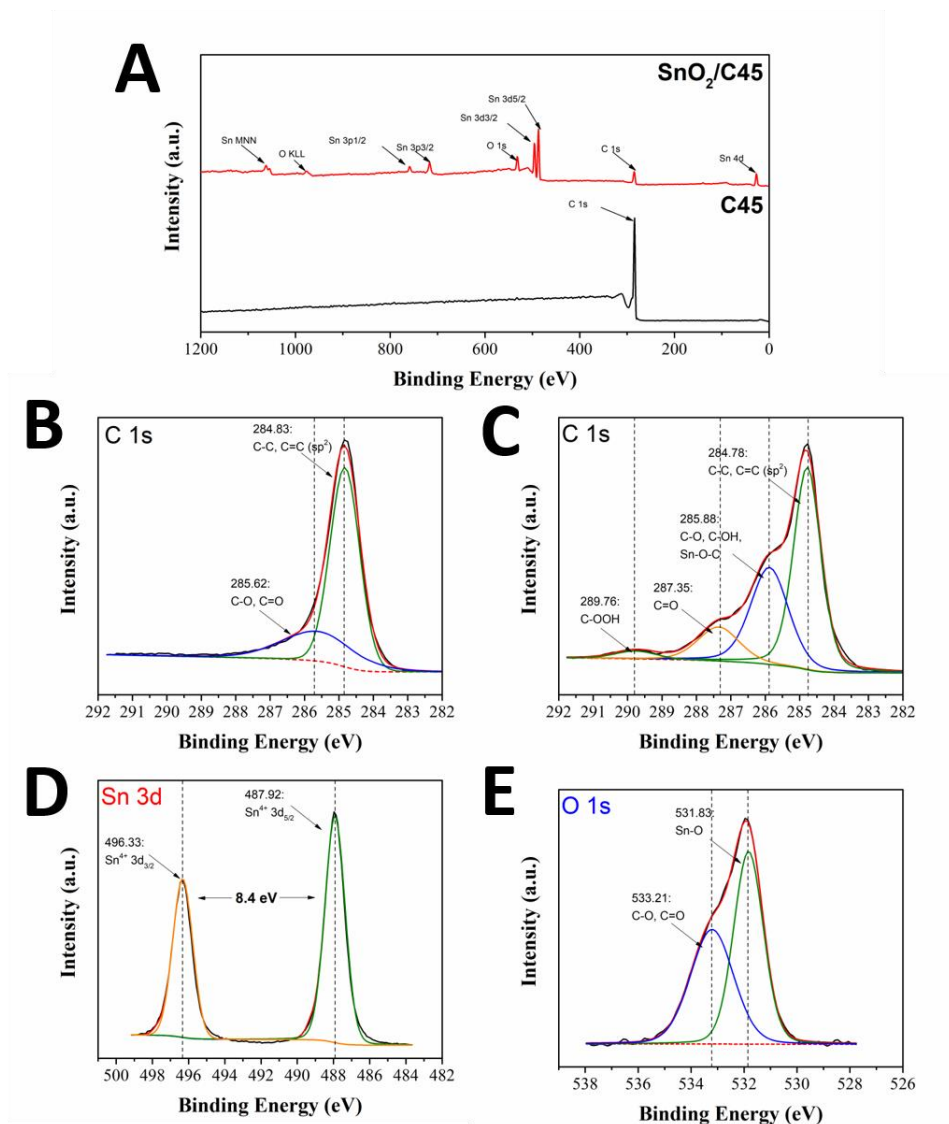
Figure 7.8: XPS survey spectra of SnO$_2$/C45 and pure C45 (a). High resolution C1s spectrum of C45 (b) and SnO$_2$/C45 (c). High resolution Sn2p spectrum of SnO$_2$/C45 (d). High resolution O1s spectrum of SnO$_2$/C45 (e).

7.1.3 Electrochemical characterization

To study the electrochemical processes of SnO$_2$/C45, cyclic voltammetry (CV) was carried out at a scan rate of 0.5 mV s^{-1} in a voltage range from 2.0 to 0.01 V *vs.* Li^0/Li$^+$ (Figure 7.9). The first five consecutive cycles are representative of the initial stages of the electrochemical processes because pulverization associated with large volumetric changes of active material is generally seen after

100 galvanostatic charge/discharge cycles. Typically, the first cathodic cycle shows higher current values through the whole potential range, which is due to SEI formation involving irreversible reactions at the electrode-electrolyte interface. The cathodic branch of the 1st CV cycle also shows a peak at 1.0 V related to the reduction of SnO_2 to Sn (0) with the simultaneous formation of Li_2O. This is followed by multistage lithium alloying process to form Li_xSn at 0.4V and 0.15 V, respectively. Similarly, in the anodic branch, the peak at 1.25 V corresponds to the reversed conversion reaction, indicating excellent reversibility of SnO_2/C45. While the oxidation peak at 0.5 V is due to the phase transition of the alloying, the process being diffusion-controlled as manifests a single-phase transformation [254]. Lastly, the peak at 0.05 V is ascribed to lithium ion intercalation in C45, as it clearly appears in the CV of C45 alone (at around 0.0 - 0.3 V; Figure 7.9 a). The process of Li insertion into C45 contributes to a small fraction of the total capacity delivered by SnO_2/C45 and partially accounts for the large irreversible capacity at the first cycle (Figure 7.9 c).
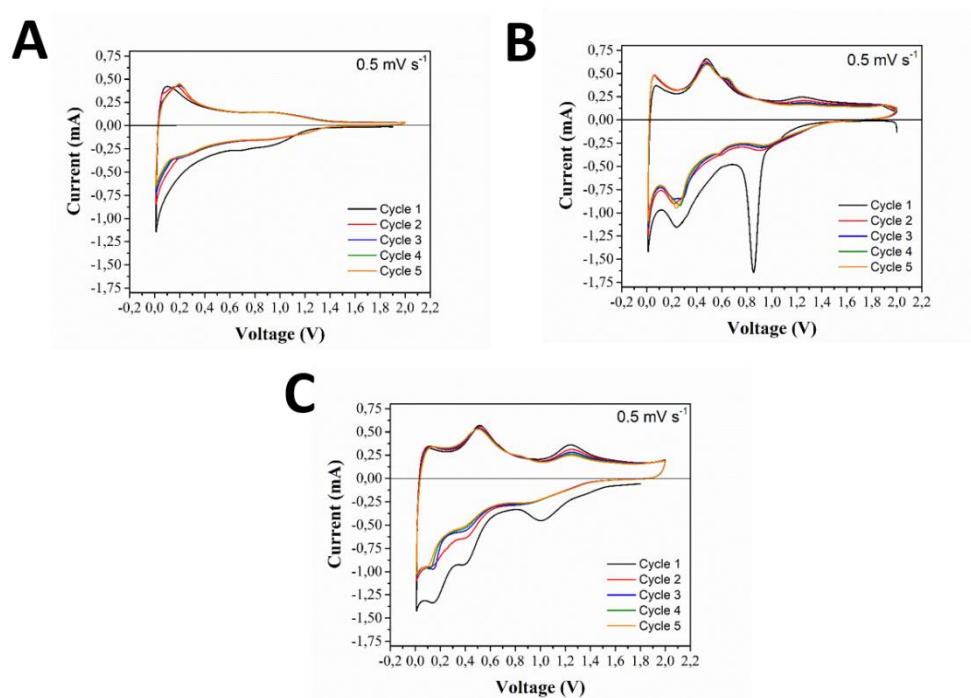
Figure 7.9: cyclic voltammetry at 0.5 mVs⁻¹ between 2.0-0.01 V *vs* Li⁺/Li of: C45 (a), commercial SnO_2 + C45 (b) and SnO_2/C45 (c).

It is worth noting that the anodic peak at 1.25 V is relatively more obvious and stable than expected. Since this peak is related to the backward reaction of Equation 6.1, it means that Sn produced from SnO_2 is oxidized back to SnO_2 and Li_2O is almost entirely decomposed. This implies that the conversion reaction is favoured by the small particle size of SnO_2 firmly anchored to C45 and by the high fraction of Sn/Li_2O interfaces during SnO_2 reduction. The good overlap of

the anodic and cathodic peaks from the 2nd to 5th indicate excellent cycling stability.

To analyse the relationships between structural features and electrochemical performance with a focus on the integrated structure of $SnO_2/C45$, the electrode consisting of commercial SnO_2 and C45 mechanically mixed in the ratio 29:71 wt.% was used as comparison Figure 7.9 b. The main difference is seen at the 1st cathodic branch of the CV curve. The performance marks a noticeable peak at 0.85 V that indicates extended presence of metallic Sn and Li_2O along with SEI formation. After the first cycle the process appears irreversible as the anodic peak at 1.25 V is almost inconspicuous and fast decreases upon cycling, which means that both SnO_x regeneration and Li_2O consumption are almost negligible [218]. During the subsequent cycles, in the cathodic branch, the peak shifts to 0.95 V due to the limited reduction of SnO_2 to Sn. While the single peak at 0.25 V refers to the alloying process which has its reverse reaction at 0.47 V in the anodic branch. The anodic branch of the pure C45 CV plot (Figure 7.9 a) shows that the peak near 0 V, and ascribed to lithium ions intercalation in C45, increases upon cycling, similar to what was previously observed with SnO_2 nanorod-planted graphite electrodes [255]. This result suggests that the contribution of C45 to the overall capacity is higher in the mixed samples (SnO_2 + C45), and the discharge/charge process is based on two steps: in the first step Li alloys with Sn, in the second step Li is intercalated in C45.

In conclusion, the CV curves comparison highlight the importance of an interconnected structure of $SnO_2/C45$ that controls preponderant Li_2O formation and maintains ultrafine Sn particles in the Li_2O matrix, resulting in the better reversibility of the conversion reaction.

To compare the real performance of the two composite materials $SnO_2/C45$ (29:71 wt.%), the reversible capacity has been calculated from following equation previously reported by Kisu *et al.* [246]:

$$Cap.SnO_2 = (Cap.SnO_2/C45 \; x \; 1.00 \; - \; Cap.C45 \; x \; 0.71) \; / \; 0.29 \qquad [7.5]$$

where *Cap.SnO2* represents the capacity purely ascribable to the SnO_2 particles, *Cap.SnO2/C45* is the capacity attributed to $SnO_2/C45$ (29:71) composite and *Cap.C45* is the capacity of pure C45. The reversible capacity *Cap.C45* was determined independently, through galvanostatic cycling tests, on a pristine C45 electrode (Figure 7.10), which was subjected to the same current density applied to $SnO_2/C45$ (0.31 mA cm^{-2}).
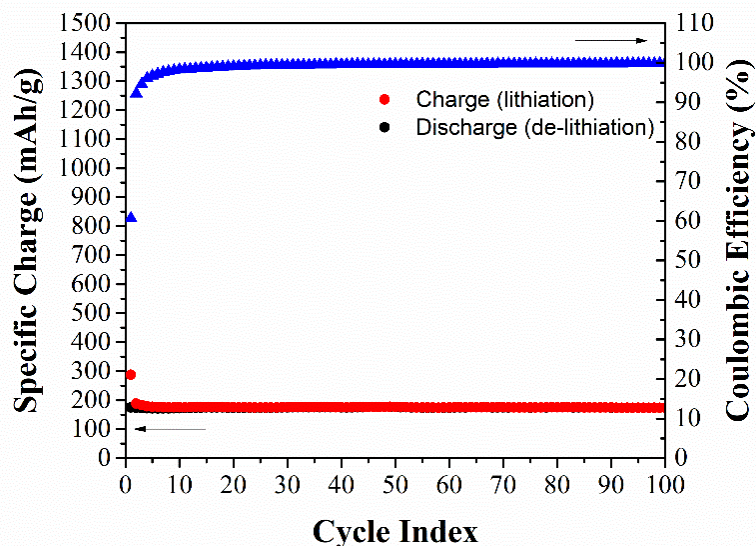
Figure 7.10: specific capacity vs. number of cycles of pure C45 electrode at 0.31 mA cm^{-2}.

The first galvanostatic charge/discharge voltage profiles *vs.* specific capacity carried out at C/10 = 0.148 A g^{-1} (assuming the theoretical specific capacity of tin dioxide: 1C = 1494 mA g^{-1}) are depicted in Figure 7.11. It is important to underline that the C-rate and the relative current was calculated considering the only amount of SnO_2 inside the electrode, but all the specific capacity results were given taking in account the contribution of C45, as described in Equation 7.5.
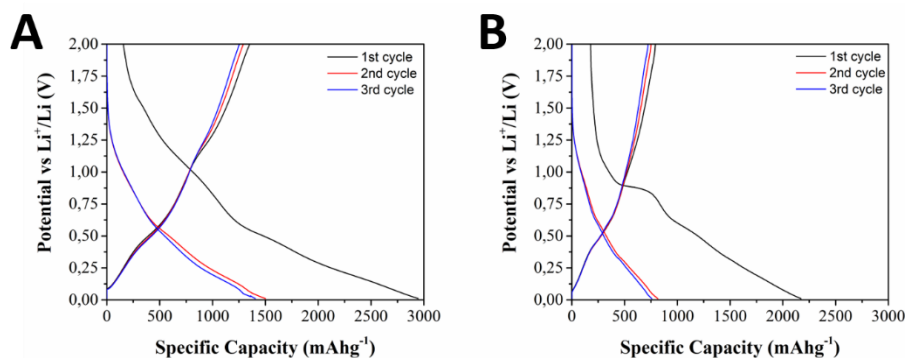
Figure 7.11: galvanostatic charge/discharge voltage profiles of the electrodes in the initial cycles at C/10: SnO_2/C45 (a) and commercial SnO_2 + C45 (b).

The results show that the specific capacity of the electrodes upon cycling is sensitive to the structure and synergies between SnO_2 and C45. During the 1st lithiation most of the processes are irreversible and only a small percentage of the initial capacity is recovered in the following de-lithiation. This behaviour, presented in the charge/discharge profiles of both samples, is also due to a SEI layer formation typically occurring during the first cycles around 1 V vs Li$^+$/Li^0. At C/10, the commercial SnO_2 + C45 anode displays low charge capacities

ranging from 815 to 741 mAh g^{-1} (Figure 7.11 b). A strong change in the voltage profile is observed from the 1st to the 2nd cycle since the flat plateau at 0.9 V vs. Li^0/Li$^+$ disappears at the 2nd cycle. This is consistent with CV results and mostly suggests incomplete Li$_2$O conversion from the 1st cycle in addition to a consistent SEI layer formation. On the contrary, in the same experimental conditions, SnO$_2$/C45 composite electrode (Figure 7.11 a) exhibited higher charge capacities ranging from 1486 to 1409 mA h g^{-1}. Since the observed capacities are totally ascribable to the SnO$_2$ particles, these values are very close to the theoretical one (1494 mA h g^{-1}) that includes both the alloying and conversion processes.

As expected, SnO$_2$/C45 showed improved reversibility of the electrochemical reaction ascribable to the synergic effect between SnO$_2$ and C45. However, the significant improvements are more observable through long cycling tests (Figure 7.12).

At higher current density (1C = 1.48 A g^{-1} of SnO$_2$, corresponding to 0.31 mA cm^{-2}) the electrode prepared by mixing commercial SnO$_2$ and C45 suffered severe capacity fading (Figure 7.12 b). In this case, lithiation of SnO$_2$ delivers 792 mAh g^{-1}, which decreases to 255 mA h g^{-1} after 100 cycles with ~ 67 % loss. At the 400th cycle the specific capacity is 50 mAh g^{-1}, which means no SnO$_2$ is electrochemically active. In contrast, the SnO$_2$/C45 anode (Figure 7.12 a) exhibited almost steady-state and reversible capacity through long cycling operation. In particular, in the first 100 cycles the coulombic efficiency is almost 98.8 % while the specific capacity is ~ 750 mAh g^{-1} (relative to pure SnO$_2$ particles). Also, the capacity retention is good, with only 11.1 % loss from 10th to 100th cycles, and a discharge capacity still stable at 616 mAh g^{-1} until ~ 400th cycle (560 mAh g^{-1} and CE of 99.8 %).

Lastly, after 1000 cycles the specific capacity is almost 300 mAh g^{-1} with coulombic efficiency of 99.9 %, and 670 mAh g^{-1} when the current returns to 0.148 A g^{-1}, which demonstrate the good stability of SnO$_2$/C45 composite.
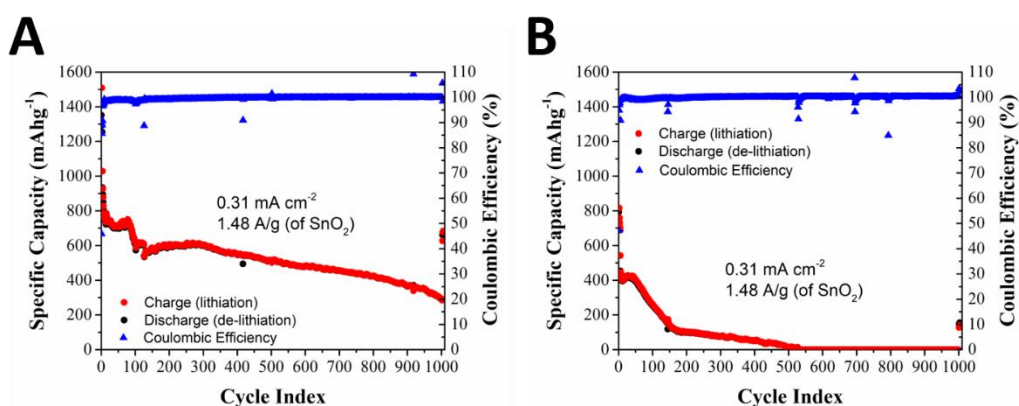
Figure 7.12 : galvanostatic charge/discharge profiles of: SnO$_2$/C45 (a) and commercial SnO$_2$ + C45 (b).

To better elucidate the differences of composite SnO_2/C45 and simple mixed commercial SnO_2 + C45 dQ/dV curves were obtained from the capacity of de-lithiation in the range of 0.01 - 2.00 V at 1C, at different cycles (Figure 7.13).

Starting from the dQ/dV curve of 5th cycle, the differential capacity (dQ/dV) curves of SnO_2/C45 (Figure 7.13 a), shows that the peaks due to de-alloying process are not as sharp as in commercial SnO_2 + C45 (Figure 7.13 b). The curves corresponding to the 10th and 5th cycle almost overlap without showing any shrinkage of the peaks, indicating very good cyclability of SnO_2/C45. No shift to higher potentials is seen for the peaks related to the de-alloying process, which results in less polarization of the electrode upon cycling. The dQ/dV curves still reveal the high activity of the reversed conversion in the initial cycles due to the large intensity of the peak at 1.3 V, which still accounts 29.6 % of the charge integral intensity at the 100th cycle.

On the contrary, at the 5th cycle, no obvious peak is visible in the potential range of 1.0 - 2.0 V for commercial SnO_2 + C45 (Figure 7.13 b) suggesting that the activity of the conversion reaction declined dramatically at the very first cycles. While only three sharp peaks attributable to de-alloying process ($Li_xSn{\rightarrow}Sn$) are observable in the range of 0.5 - 0.7 V. These peaks decrease in intensity and shift to higher potentials as the number of cycles increases. This result has an explanation in the coarsening/agglomeration of Sn and Li_xSn phases in the Li_2O matrix, which affects the reaction kinetics and increase the polarization of the de-alloying process. Such lithiation-induced Sn coarsening has been observed in pure SnO_2 film electrodes [256] and is explained as the gradual diffusion of Sn from one Sn/Li_2O zone to the others nearby, due to the tendency of nanosized Sn grains to reduce their surface/interface energy in the lithiated SnO_2.

The evolution of the peaks in dQ/dV *vs.* V curves suggests the possibility for the conversion of SnO_2 to Sn(0) to proceed through different intermediate species instead of separated Sn and Li_2O. Unfortunately, the intermediate reaction steps are mostly overlapped, confirming the difficulty to discriminate the various contributions. The good dispersion of SnO_2 nanoparticles on C45 and the chemical interaction among Sn, O and C, observed by XPS analysis, can reasonably affect the reversible conversion reaction and most of the re-formed SnO_x phases could result from the reaction of Sn with neighbouring oxygen and not from direct decomposition of Li_2O [257], which results in a stable material system where most of the initial capacity is retained after prolonged cycling at reasonably high C-rates.
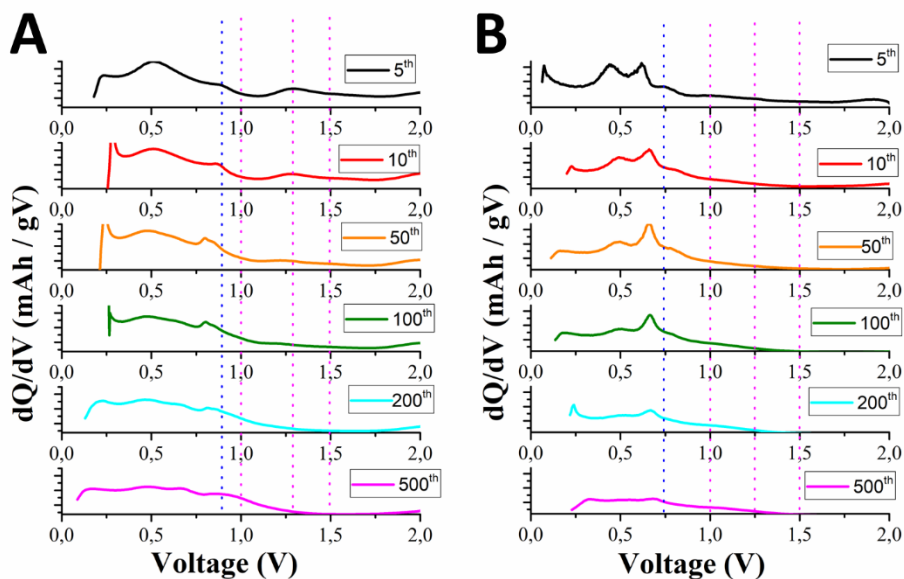
Figure 7.13: derivative curves dQ/dV vs. cell voltage and specific capacity vs. cell voltage of: SnO_2/C45 (a) and commercial SnO_2 + C45 (b)

The rate performance of SnO_2/C45 was also evaluated (Figure 7.14, Table 7.2). The specific capacities of SnO_2/C45 are 570, 430, 375, 315 mAh g^{-1} at 0.2, 1.1, 2.2, and 4.4 mA cm^{-2} respectively (Figure 7.14 a). When the current density reverts to 0.2 mA cm^{-2} after 85 cycles, the specific capacity is still 520 mAh g^{-1} equivalent to 89.7 % of the initial value, confirming the stable electrochemical behaviour at high current regimes. For comparison the reversible capacity of pristine C45 electrode, subjected to the same current density, was determined independently (Figure 7.14 b).
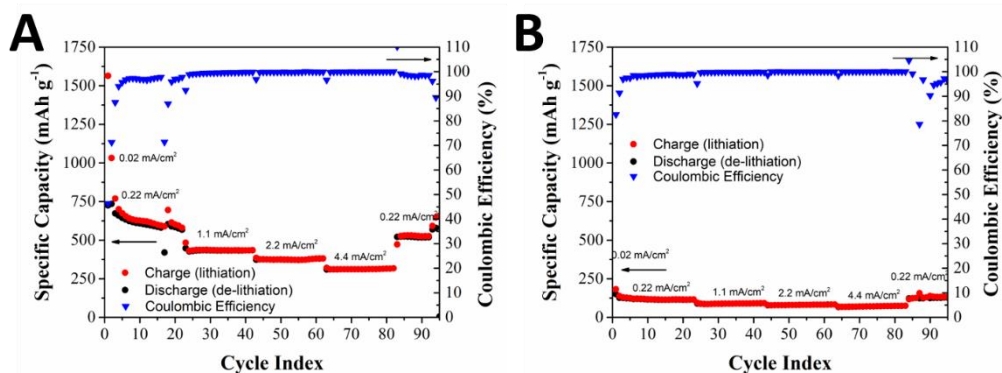
Figure 7.14 cycling performance of SnO_2/C45 (a) and pure C45 (b) galvanostatically tested at different current regimes.

As reported in Table 7.2, at the same current regime the pure C45 electrode delivered a consistently lower specific capacity, confirming the high contribution of SnO_2 to the electrochemical performances of the sample.

Table 7.2: specific capacity comparison at different current regimes of SnO_2/C45 and pure C45 electrodes.

Current/electrode area (mA cm^{-2})	Specific capacity (mAh g^{-1})	
	C45	SnO_2/C45
0.02	150	730
0.2	120	570
1.1	90	430
2.2	80	375
4.4	70	315

Post cycling FESEM analysis was carried out to evaluate the morphology of SnO_2/C45 material after 1000 galvanostatic charge/discharge cycles (Figure 7.15 b) in comparison with the pristine material (Figure 7.15 a). After cycling, the electrode shows particles ascribable to tin species, which confirm that C45 provides sufficient anchoring to SnO_2 nanoparticles. After long cycling the average particle size is around 10 nm suggesting that, although particle agglomeration occurred as a consequence of lithiation and de-lithiation reactions, the material still retains its original morphology, which reflects the ability of the anode to mitigate any large morphological change.
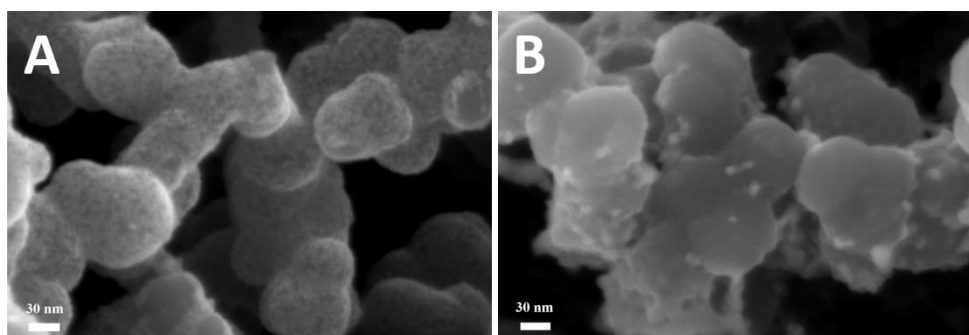
Figure 7.15: FESEM micrographs of pristine SnO_2/C45 electrode (a) and SnO_2/C45 electrode cycled for 1000 cycles (b).

The better performances of the SnO_2/C45 composite can be explained by the chemical bond between SnO_2 and carbon which affects the reversibility of the conversion reaction and facilitates the reaction of Sn and other oxygenated species (like Li_2O) to reform SnO_2 as previously reported by Cheng et al. [250].

Moreover a blended amorphous structure like a solid-solution of three element Sn, O and Li, such as $Li_xSnO_{1.45}$ was identified as responsible of the high capacity retention of a SnO_2 nanodots/Ketijen Black (KjB) electrode [246]. The proposed new species were found to be confined within the structure of carbon and partially inhibited the irreversible Li_2O formation by the maintenance of Sn-Li and Sn−O bonds, providing reversible reaction mechanisms.

In conclusion, a fast and inexpensive method was used to synthesize tin dioxide material with average size 5.0 nm SnO_2 nanoparticles finely dispersed across the surface of commercial carbon black.

The as obtained composite materials presented a morphology with enough space among SnO_2 nanoparticles able to accommodate the large volume expansion of tin during the alloying process. The remarkable stability of the composite was also confirmed by the presence of tin particles after 1000 cycles. Moreover, the peculiar nanostructure of the composite offers a specific capacity of 560 mAh g^{-1} for more than 400 cycles with a CE of 99.8 %.

Considering the fast and inexpensive method used to prepare SnO_2/C45, these results, in terms of reversible capacities and long cycling stability, are competitive among others obtained for SnO_2-based materials synthetized by hydrothermal, sonochemical, solvothermal, *etc*. methods. All these considerations make the synthetic route reported in this chapter a suitable and interesting approach for large scale production.

Chapter 8

8 SnO$_2$/C$_3$N$_4$ anode for high rate Li-ion battery

As mentioned in Chapter 6, SnO$_2$ is a low-cost raw material (roughly 20 dollars per kilograms) [258], thus such benefit is lost if complicated and costly synthesis are adopted for its preparation. For instance, the synthesis of nano-structured SnO$_2$ [259][260] is usually unsuitable for mass production because particles dimensions and structure are difficult to be controlled on large scale [261]. Moreover, high tap density of electrodes is a requirement that usually nanostructured active materials do not satisfy. On one hand, nano-engineering enhances physicochemical properties of materials, on the other long lasting and expensive procedures are often needed.

Simultaneously, wrapping or covering SnO$_2$ with conductive light carbon matrices such as graphene, result in increasing conductivity and releasing strain energy [262]. Unfortunately, the synthesis of hybrid material is expensive or not suitable for large-scale production.

Taking into account these considerations in the present section I propose a cheaper and alternative tin-oxide hybrid compound with carbon nitride as valid substitute of traditional carbonaceous wrapping agents.

Graphitic carbon nitride (g-C$_3$N$_4$), has recently become an attractive material in many energy-related fields. In particular, g-C$_3$N$_4$ has been used to design new SnO$_2$ composite materials for photo-catalysis [263][264] and gas sensing [265] applications.

DFT calculations suggest that a single-layer Li$_2$C$_3$N$_4$ can be directly used as anode [266] for Li-ion battery delivering a theoretical specific capacity of about 534 mAh g^{-1} which is almost twice than that of LiC$_6$ (372 mAh g^{-1}). However experimental studies demonstrate that g-C$_3$N$_4$ alone is practically unsuitable as alternative anode for LiBs, having a real reversible capacity of about 38 mAh g^{-1} [267]. While SnO$_2$/g-C$_3$N$_4$ hybrid materials cover a wide range of applications, only few studies report their use as anodes [268][269][270] in Li-ion batteries.

In this chapter, I show that $SnO_2@C_3N_4$ can be easily obtained by fast solid-state reaction, which is feasible for upscaling active material production [271]. The adopted strategy to produce $SnO_2@C_3N_4$ is inspired by the approach of Cao *et al.* [265] for gas sensing and here proposed for the first time for LIBs applications. Synergies between the components allow to achieve better electrochemical performances particularly at high rates, which render such material appealing for industrial anode development.

Part of the results described in this chapter were previously published [271].

8.1.1 Synthesis

Graphitic carbon nitride (g-C_3N_4) is synthesized by thermal condensation of urea (CH_4N_2O). Urea was placed in a semi-closed alumina crucible, subsequently inserted in a tubular furnace and heated at 550°C for 4 hours at 3°C/min in argon atmosphere. The as obtained graphitic carbon nitride powder was mixed with Tin (IV) chloride pentahydrate ($SnCl_4 \cdot 5H_2O$, 99.0%) and polyethylene glycol 400 (PEG-400) in a mortar. NaOH was added to the mixture and grounded for 30 minutes to obtain tin oxide. During the grinding process a huge releases of water vapor and heat was observed. The resulting product was firstly separated by centrifuge and washed several times with distilled water and absolute ethanol and then dried at 60 °C overnight. As comparison, pure SnO_2 was synthesized by the same procedure without the addition of g-C_3N_4.
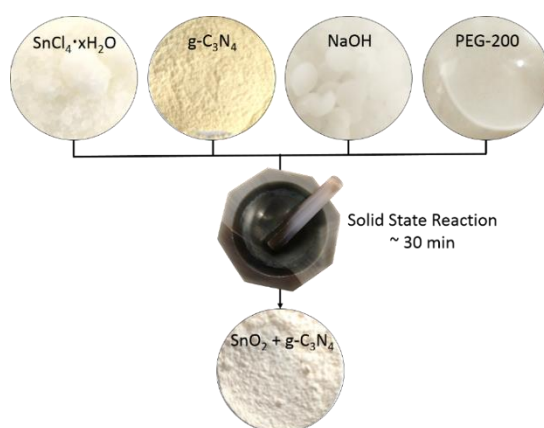
Figure 8.1: solid-state synthesis scheme of
$SnO_2@C_3N_4$

8.1.2 Structural and morphological characterization

XRD patterns of bare SnO_2, g-C_3N_4 and $SnO_2@C_3N_4$ are shown in Figure 8.2. For g-C_3N_4, the diffraction peak at 27.0° is assigned to the (002) reflection of graphitic-like aromatic structure and the weaker peak at 13.9° corresponds to the in-plane structural packing of tri-s-triazine units, (JCPDS No. 87-1526) [272][273][274]. The diffraction peaks of SnO_2 (back line) can be indexed to tetragonal rutile (JCPDS No. 41-1445) where peaks at 26.3°, 33.9°, 51.7° and 65.9° correspond to (110), (101), (211) and (301) planes, respectively. The XRD pattern of $SnO_2@C_3N_4$ (blu line) mainly exhibits the diffraction peaks of tetragonal SnO_2 because of the higher amount of tin dioxide in the sample. However, it is impossible to discern the peak of g-C_3N_4 at 27.6° from the peak of SnO_2 at 26.6°. The absence of additional peaks in $SnO_2@C_3N_4$ confirms that the material is entirely composed of carbon nitride and tin dioxide [264]. The average crystallite size of the composite material is about of 7.0 ± 0.5 nm determined according to Scherrer equation.
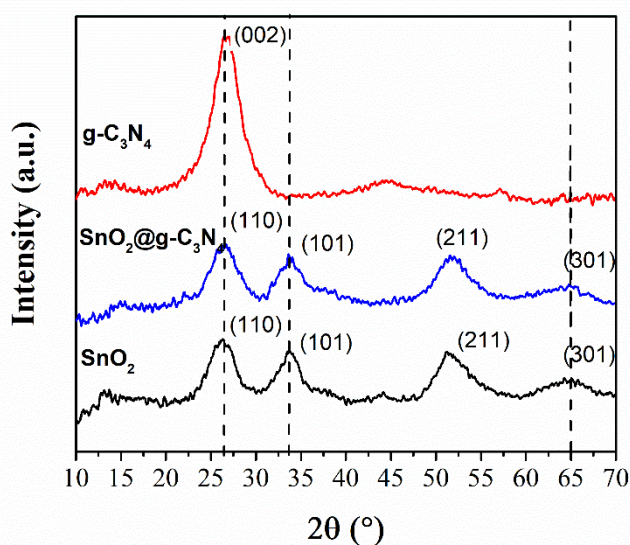
Figure 8.2: XRD patterns of g-C_3N_4, SnO_2 and $SnO_2@C_3N_4$.

As reported in Figure 8.3 the experimental amount of g-C_3N_4 in $SnO_2@C_3N_4$ hybrid material was defined by thermogravimetric analysis (TGA). The TGA analysis was also performed on bare SnO_2 and pure g-C_3N_4, at the same condition, for comparison.

Observing the weight of pure g-C_3N_4, it is almost constant at temperature below 450 °C, indicating its good thermal stability. For this reason, the weight amount of g-C_3N_4 in $SnO_2@C_3N_4$ was determined between 500 °C and 550 °C (at which decomposition of carbon nitride occurs) and it was attested ~ 8.04 wt %. It

is worth noting that in $SnO_2@C_3N_4$ hybrid sample, the g-C_3N_4 shows lower thermal stability due to its catalytic oxidation directly driven by SnO_2 [275][276].

Both bare SnO_2 and $SnO_2@C_3N_4$ samples show an initial weight loss under 100 °C which is attributable to the loss of absorbed water for all the samples. The final content of SnO_2 in the hybrid compound was attested around 77.3 wt.%, as observable from the residual weight after heating the sample over 700 °C.
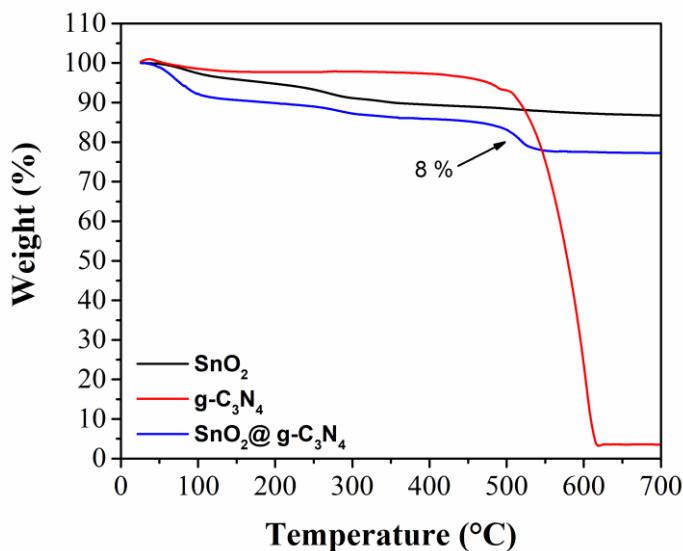
Figure 8.3: TGA curve comparison of g-C_3N_4, SnO_2, $SnO_2@C_3N_4$.

Nitrogen adsorption-desorption isotherms of g-C_3N_4, SnO_2 and $SnO_2@C_3N_4$ were measured at 77 K with the aim of calculating and comparing the specific surface areas (SSA) of the samples. The specific surface area of g-C_3N_4 mainly depends on the precursors and synthesis conditions. Urea is considered a favorable precursor to obtain high surface area carbon nitride, with sheets of small thickness. Thermal condensation likely happens at temperatures of 450 - 600 °C, which is good to improve the interconnectivity and electron delocalization of the aromatic sheets [277].

As observable in Table 8.1, the specific surface area of SnO_2 and $SnO_2@C_3N_4$ are 211.1 m² g⁻¹ and 262.5 m² g⁻¹ respectively, suggesting a synergic effect rather than a bare mixing of the two components.

Table 8.1: specific surface area (SSA) of of g-C_3N_4, SnO_2, $SnO_2@C_3N_4$.

Sample	SSA (BET) (m² g⁻¹)
g-C₃N₄	115.0
SnO₂	211.1
SnO₂@ g-C₃N₄	262.5

The slight increase of SSA from SnO_2 to $SnO_2@C_3N_4$, means larger contact areas between the electrode and electrolyte which improve the electrochemical reaction kinetics.

As expected, g-C_3N_4 is mesoporous (Figure 8.4) and displays hysteresis loops of isotherms that indicate the presence of aggregates of plate-like particles giving rise to slit-shaped pores [278]. The pore distribution of pure SnO_2 shows an average diameter lower than 50 Å, which is increased to 70 Å with the presence of g-C_3N_4 in the compound. The average pore size is about 2 nm for $SnO_2@C_3N_4$ according to the NLDFT method.
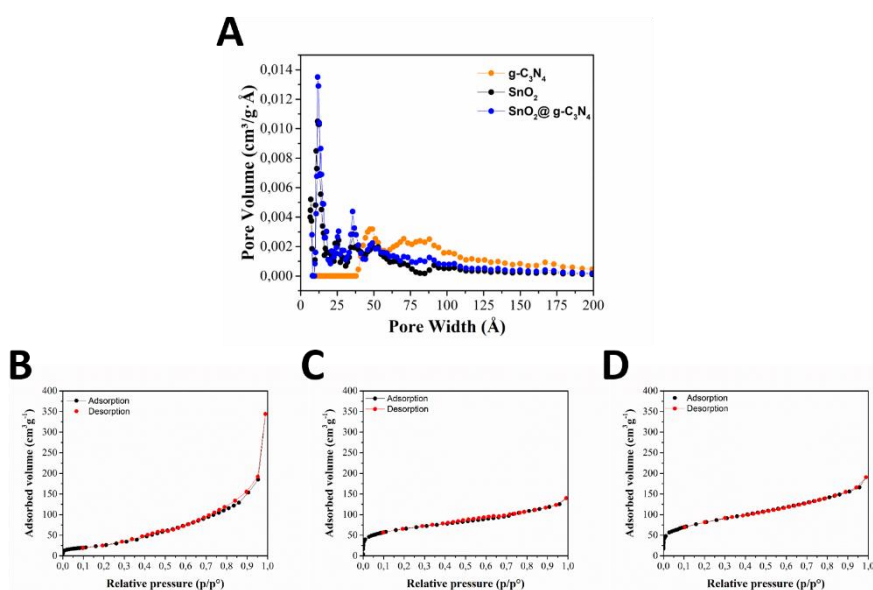
Figure 8.4: pore size distribution comparison of g-C_3N_4, SnO_2 and $SnO_2@C_3N_4$ (a), N_2 adsorption-desorption isotherms for: g-C_3N_4 (b), SnO_2 (c) and $SnO_2@C_3N_4$ (d).

The FT-IR analysis (Figure 8.5) substantially shows two sets of vibration peaks in the $SnO_2@C_3N_4$ spectrum. More in detail the vibration peaks at 485 cm^{-1} and 653 cm^{-1} are assigned to symmetric and anti-symmetric stretching of SnO_2 [275]. While the peak at 810 cm^{-1} corresponds to bending vibration of triazine units in g-C_3N_4 [279] and from 1240 to 1638 cm^{-1} to the stretching vibration of C–N heterocycles (C-N at 1240 cm^{-1}, 1314 cm^{-1}, 1418 cm^{-1}, C=N at 1638 cm^{-1}) [267]. The broad peaks in the range of 3000 - 3700 cm^{-1} are mainly stretching modes of O-H from adsorbed H_2O, or to N-H stretching modes of residual amino groups [198].
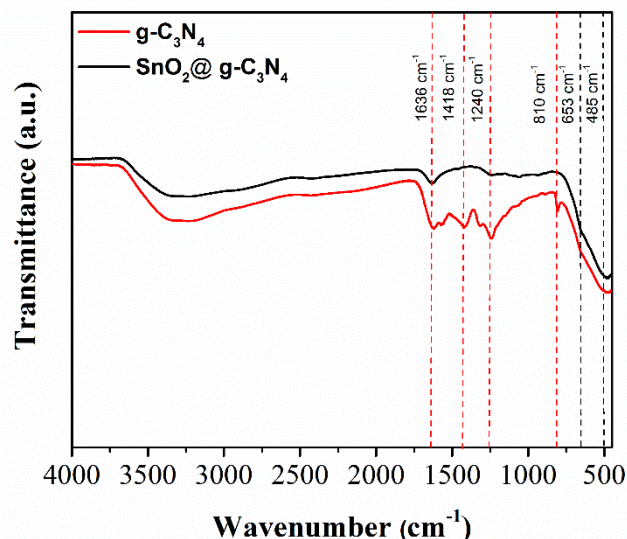
Figure 8.5: FT-IR spectra of g-C_3N_4 and $SnO_2@C_3N_4$

The XPS survey spectra reported in Figure 8.6, shows that the atomic % of C, N, Sn, O, Cl elements in $SnO_2@C_3N_4$ are 14.3 %, 11.2 %, 31.1 %, 41.2 % and 2.2 %, respectively. Cl is an impurity due to the use of $SnCl_4 \cdot 5H_2O$ in the synthesis. Analyzing the high resolution XPS spectra for Sn3d, the splitting between $Sn3d_{5/2}$ and $Sn3d_{3/2}$ of 8.41 eV, is consistent to Sn^{4+} [280]. As previously mentioned, the two components of $SnO_2@C_3N_4$ are not barely mixed, as indicated by the clear changes in electronic states. For SnO_2 and $SnO_2@C_3N_4$, the slight shift of the Sn3d spectra is indicative of interactions between g-C_3N_4 and SnO_2 [281]. The high resolution O1s spectra has no significant shift in the characteristic binding energy. However, the O1s spectra of SnO_2 (Figure 8.6 c) is resolved into three signals: the first at 531.10 eV is typical for oxygen bonded to tin atoms, the second at around 532 eV is due to C=O, the third at 532.8 eV is due to O-H. The first two peaks show shifts when SnO_2 grows over g-C_3N_4, which indicate an interaction between the two components, as previously discussed for Sn3d. In Figure 8.6 (e), the status of carbon C1s in $SnO_2@C_3N_4$ include the main peak at 284.71 eV, which is assigned to C-C and C=C (graphitic carbon), along with combination of C-N groups centered at 285.75 eV [282] and the sp^2-hybridized carbon N–C=N (288.06 eV). The peak at 289.43 eV is mainly assigned to CO groups originating from surface carbon that interacts with O_2 and/or CO_2 from the air [251]. N1s spectrum of $SnO_2@C_3N_4$ (Figure 8.6 f) confirmed the presence of sp^2-hybridized aromatic N bonded to C atom (398.23 eV) and ternary N bonded to C atom in the form of N–$(C)_3$ (399.33 eV). The peak at 400.9 eV is ascribed to the N–H structure, while the peak at 404 eV is attributable to the π-π* excitation.

It is important to note that the intimate interaction that is noted by XPS analysis of the hybrid compound would benefit the charge transfer between SnO_2 and g-C_3N_4.

154
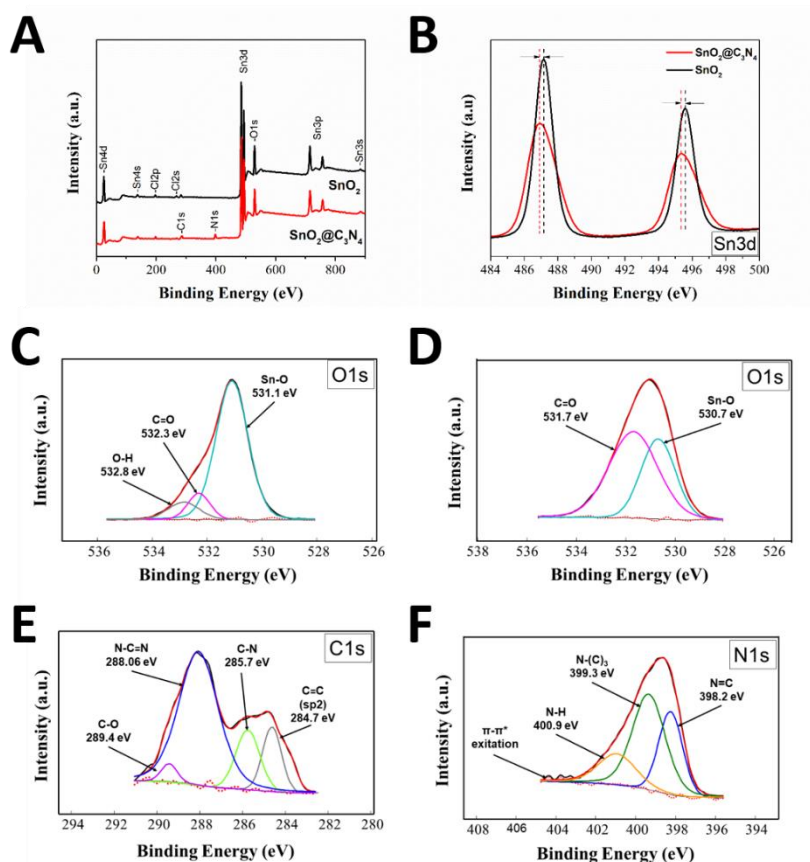
Figure 8.6: XPS survey spectra of SnO$_2$ and SnO$_2$@C$_3$N$_4$ (a), Sn3d high resolution XPS spectra of SnO$_2$ and SnO$_2$@C$_3$N$_4$ (b); O1s high resolution spectra of SnO$_2$ (c) and SnO$_2$@C$_3$N$_4$ (d); C1s high resolution spectra (e) and N1s high resolution spectra (f) of SnO$_2$@C$_3$N$_4$.

FESEM investigation of g-C$_3$N$_4$, SnO$_2$, and SnO$_2$@C$_3$N$_4$ are depicted in Figure 8.7. The micrograph of g-C$_3$N$_4$ (Figure 8.7 a) shows thin wrapped sheets, forming hollow structures. As visible in Figure 8.7 (b), pure SnO$_2$ is composed of clusters of large dimensions, due to the strong tendency of SnO$_2$ particles to agglomerate during the solid-state synthesis. In SnO$_2$@C$_3$N$_4$ sample (Figure 8.7 c), the wrapped and hollow structure of carbon nitride is covered by SnO$_2$ particles, resulting in a porous and wrinkled material. The surface of SnO$_2$@C$_3$N$_4$ material is smooth and SnO$_2$ particles are homogenously distributed on g-C$_3$N$_4$. This demonstrates that g-C$_3$N$_4$ [283] prevents aggregation of SnO$_2$ particles during the solid-state synthesis.
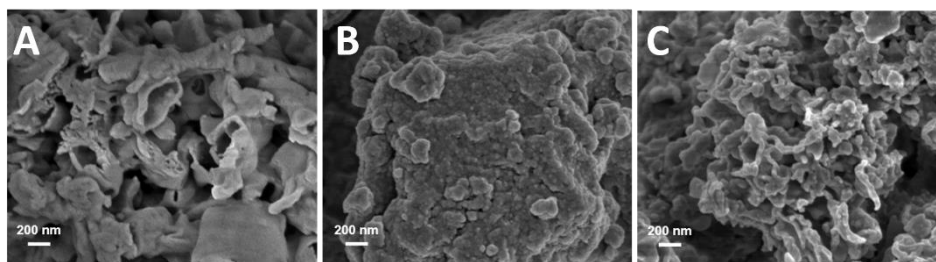
Figure 8.7: FESEM images of g-C$_3$N$_4$ (a), SnO$_2$ (b) and SnO$_2$@C$_3$N$_4$ (c).

Figure 8.8 and Table 8.2 compare the EDS analysis of pure SnO$_2$ and SnO$_2$@C$_3$N$_4$. Three different areas have been analyzed that are representative of the sample. Nitrogen was detected only in the hybrid compound, confirming the presence of carbon nitride in the sample. The weight % of Sn, O, C and N is almost the same in all the selected areas, which proves the homogeneous distribution of SnO$_2$@C$_3$N$_4$ sample.
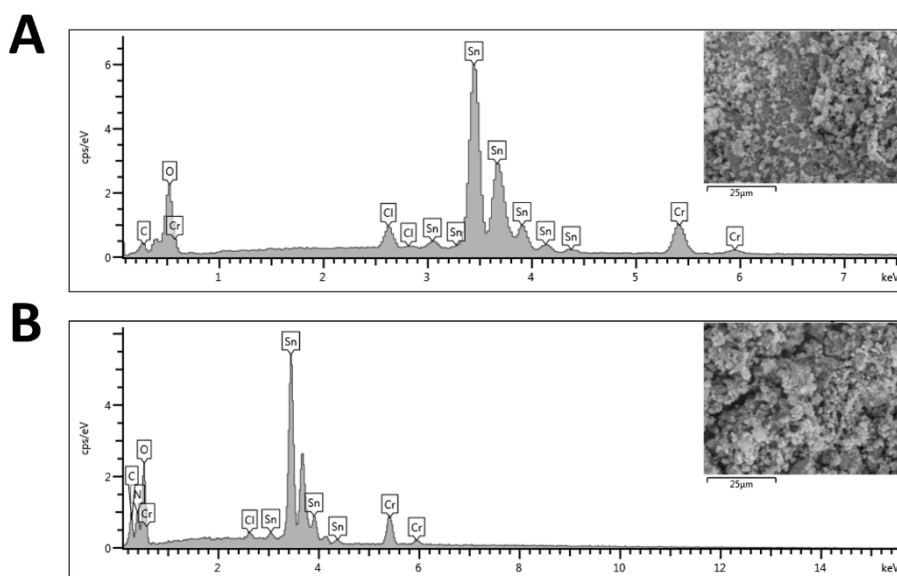
Figure 8.8: EDS analysis of pure SnO$_2$ (a) and SnO$_2$@C$_3$N$_4$ (b).

Table 8.2: EDS element analysis of SnO$_2$ and SnO$_2$@C$_3$N$_4$.

Element	SnO$_2$		SnO$_2$@g-C$_3$N$_4$	
	Wt%	Atomic %	Wt%	Atomic %
C	2.88	4.10	5.97	16.51
N	-	-	4.31	10.21
O	24.89	61.65	26.62	55.26
Cl	2.14	0.94	0.54	0.50
Sn	70.08	33.31	62.57	17.51
Total:	100.00	100.00	100.00	100.00

8.1.3 Electrochemical characterization

The working electrodes were prepared by solvent tape casting procedure. N-methyl-2-pyrrolidone (NMP, Aldrich) slurries of active material mixed with acetylene black (Shawiningan Black AB50, Chevron Corp., USA) and polyvinyledenfluoride as binder (Arkema Kynar 761) in the weight ratio of 70:20:10 was prepared. The as obtained slurries were deposited on a copper foil current collector (Goodfellow, 0.0125 mm thickness) by doctor blade technique (200 μm thickness), with an automatic film applicator (Sheen 1133N, 50 nm s^{-1} speed). After evaporating the solvent in air, discs of 0.8 cm^2 and 1.8 cm^2 were punched, vacuum dried at 150°C (Büchi glass oven B585) for 4h, then transferred into an Ar filled glove box (MBraun Labstar, with H$_2$O and O$_2$ contents < 1ppm) for cell assembling. The electrode active material loading, corresponding to 1.3 mg cm^{-2}, was calculated considering only SnO$_2$ amount.

The electrochemical behavior of pure SnO$_2$ and SnO$_2$@C$_3$N$_4$ was tested via cyclic voltammetry (CV) and by galvanostatic discharge/charge cycles vs. Li^0/Li$^+$.

The electrodes were assembled either in T-cells (for CV) or in coin cells 2032 (for GC). Two lithium disks (Chemetall Foote Corporation) were used as counter and reference electrodes while the separator was a 0.63 mm thick glass-wool Whatmann (GF/A) impregnated with electrolyte solution of 1.0 M LiPF$_6$ in 1:1 v/v mix of Ethylene Carbonate (EC) and Diethyl Carbonate (DEC) + 1.0 % Vinyl Carbonate (VC) (battery grade, Solvionic). The electrochemical performances of the prepared cells were investigated by means of galvanostatic discharge-charge cycling (GC) protocol using an Arbin BT-2000 battery tester at room temperature. Galvanostatic discharge-charge were carried out in the potential range of 0.01 - 2.0 V vs. Li^0/Li$^+$ at different C-rates (assuming the theoretical capacity of SnO$_2$ of 782 mAh g^{-1}). For cyclic voltammetry (CV), the electrode potential was reversibly scanned between 0.01 and 3.0 V vs. Li^0/Li$^+$ at 0.50 mV s^{-1}.

As deeply discussed in the previous chapters the lithiation reaction of tin oxide is a two-step process. In the first step, a conversion reaction occurs in which inactive Li$_2$O is uniformly formed around the active Sn. The concomitant formation of Li$_2$O and solid electrolyte interphase (SEI) layer in the first cycles usually results in a large irreversible specific capacity loss [274].

On the contrary, the second step is reversible, but unfortunately, upon cycling, the active Sn tends to aggregate, and cracking/pulverizing of active material usually occurs as a consequence of the volume changes of the alloying/dealloying process.

Figure 8.9 shows the CV profiles of SnO$_2$@C$_3$N$_4$. In the 1st cycle, the cathodic peak at 0.95 V vs. Li^0/Li$^+$ is attributed to the irreversible reduction of SnO$_2$ to metallic Sn and Li$_2$O. In this same cycle, other two processes are occurring simultaneously: the formation of solid electrolyte interphase (SEI) and a

partial electrolyte decomposition. The other peaks in the region between 0.01 - 0.7 V vs. Li^0/Li^+ are due to the multiple phase transitions from $Li_{4.4}Sn$ alloy [265].

The corresponding oxidation peak at 0.55 V and the subsequent peaks in the region between 1.25 V and 1.75 V are attributed to the dealloying process and the re-oxidation of Sn to SnO_2 [284].

The oxidation peak in the range of around 1.25 V - 1.75 V weakens after 10 consecutive galvanostatic discharge/charge cycles at 1C = 0.78 A g^{-1} (Figure 8.9 c) suggesting that the reaction is mainly irreversible, which is expected for micrometric sized SnO_2 [284]. The CV curve, also shows a new peak at 0.86 V vs. Li^0/Li^+ in the anodic region, which corresponds to de-lithiation processes of different Li-Sn compounds [285][286]. The subsequent cycles remain almost unchanged and representative of the electrode processes.
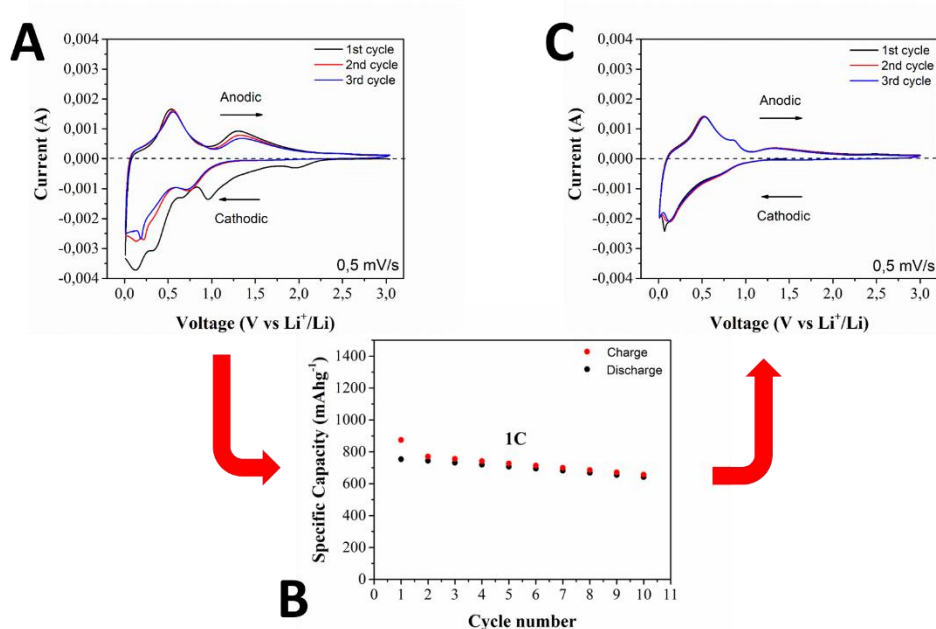
Figure 8.9: cyclic voltammetry profile over the potential range of 3.0-0.01 V vs Li/Li$^+$ at 0.5 mV s^{-1} for fresh electrode (a), 10 galvanostatic discharge/charge cycles at 0.78 A g^{-1} (b), and cyclic voltammetry profile after 10 galvanostatic cycles (c).

The cycling performances of the cells were investigated by galvanostatic charge/discharge cycling in the voltage range from 0.01 to 2.0 V at 0.078 A g^{-1} for the first ten cycles and at 0.78 A g^{-1} until the 100th cycle.

Figure 8.10 compares the first three galvanostatic cycles of SnO_2 and $SnO_2@C_3N_4$ electrodes at low current regime (0.1C = 0.078 A g^{-1}). No relevant differences are observed in the behavior of SnO_2 and $SnO_2@C_3N_4$ electrodes at these low current rates. Both the electrodes are affected by an initial capacity loss, of about 42 % for SnO_2 and 52 % for $SnO_2@C_3N_4$ and a Coulombic efficiency of about 56 and 44 % respectively. It is worth noting that in both cases, these results are in line with several SnO_2/C composites reported in literature [287]. However,

after the initial lithiation process, the two samples show comparable discharge capacity (~ 1000 mAh g^{-1}) and good reaction reversibility in the following two cycles. Observing the first discharge curve the different behavior can be explained by the integration of mesoporous g-C$_3$N$_4$, resulting in a porous composite that allows easier access of the electrolyte. Therefore, the contacting area between the electrolyte increased in the SnO$_2$@C$_3$N$_4$ composite and consequently the specific capacity results higher [288]. It is important to underline that the amount of g-C$_3$N$_4$ in the hybrid compound is only 8.04 wt.% and the contribution of carbon nitride to the specific capacity is not relevant. In fact, the g-C$_3$N$_4$ can show an initial high lithium uptake capacity [289] but in few cycles the material becomes unstable with lithiation, resulting in a low specific capacity of 30 mAh g^{-1}. Thus, g-C$_3$N$_4$ can only contribute with large irreversible capacity at the first cycle with practical achievable capacity less than 38 mAh g^{-1} [267]. Such inactivity is mainly due to the irreversible Li interaction with C$_3$N species of heptazine. The limited Li uptake has also been addressed by Miller *et al.* [290] to the low electrical conductivity of the individual g-C$_3$N$_4$ particles.
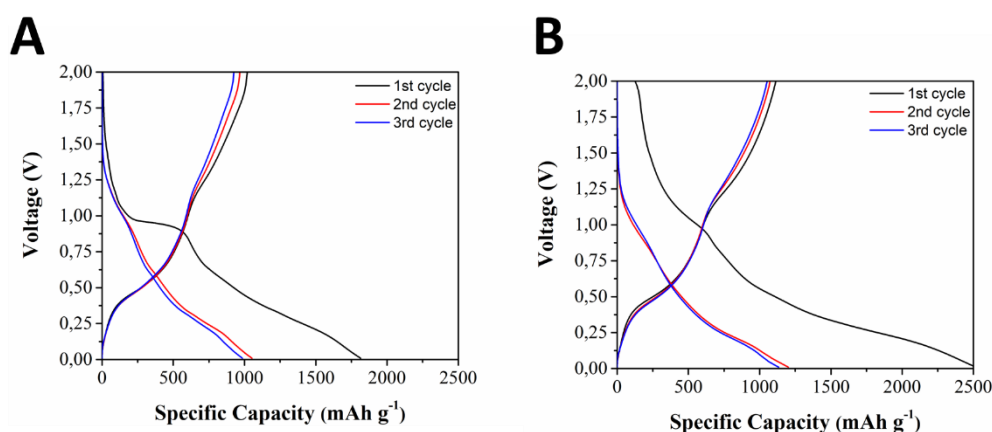
Figure 8.10: first three cycles galvanostatic profiles at 0.078 A g^{-1} for bare SnO$_2$ electrode (a) and SnO$_2$@C$_3$N$_4$ electrode (b).

As possible to observe in Figure 8.11, considering more cycles at higher current range (0.78 A g^{-1}) the specific capacity of SnO$_2$ is attested around 240 mAh g^{-1} while SnO$_2$@C$_3$N$_4$ still delivers 500 mAh g^{-1} after 50 cycles. More in detail the bare SnO$_2$ electrode (Figure 8.11 a) shows severe capacity degradation up to 120 mAh g^{-1} after 100 cycles, with capacity retention of about 13 %. This behavior is typically related to the alloying reaction that results in large volume expansion inducing surface cracking of the electrode that causes losses in the electrical contact between the active material and carbon black particles. On the contrary, after 100 cycles the specific capacity of SnO$_2$@C$_3$N$_4$ is 470 mAh g^{-1} and the capacity retention is 57 % (Figure 8.11 b).

The differential capacity profiles (dQ/dV vs. voltage) of SnO$_2$@C$_3$N$_4$ and SnO$_2$ are shown respectively in Figure 8.11 c and d. The range of potential between 0.01 and 0.7 V vs. Li^0/Li$^+$ refers to the lithiation steps related to the

formation of Li_xSn alloys [270]. For the $SnO_2@C_3N_4$ (Figure 8.11 d) the intensities corresponding to the Li_xSn peak at 0.19 V (cathodic region) slowly decreased. While in the anodic region, the peaks appearing at around the 40th cycle (at 0.49, 0.60, 0.78 and 0.85 V) are attributed to subsequent regeneration of $Li_{3.5}Sn$, $Li_{2.33}Sn$, LiSn, and Sn, from de-lithiation of $Li_{4.4}Sn$. For bare SnO_2 electrode (Figure 8.11 c), all the peak intensities of both alloying and conversion reactions rapidly decrease, which suggests that the process is dramatically hampered [291].
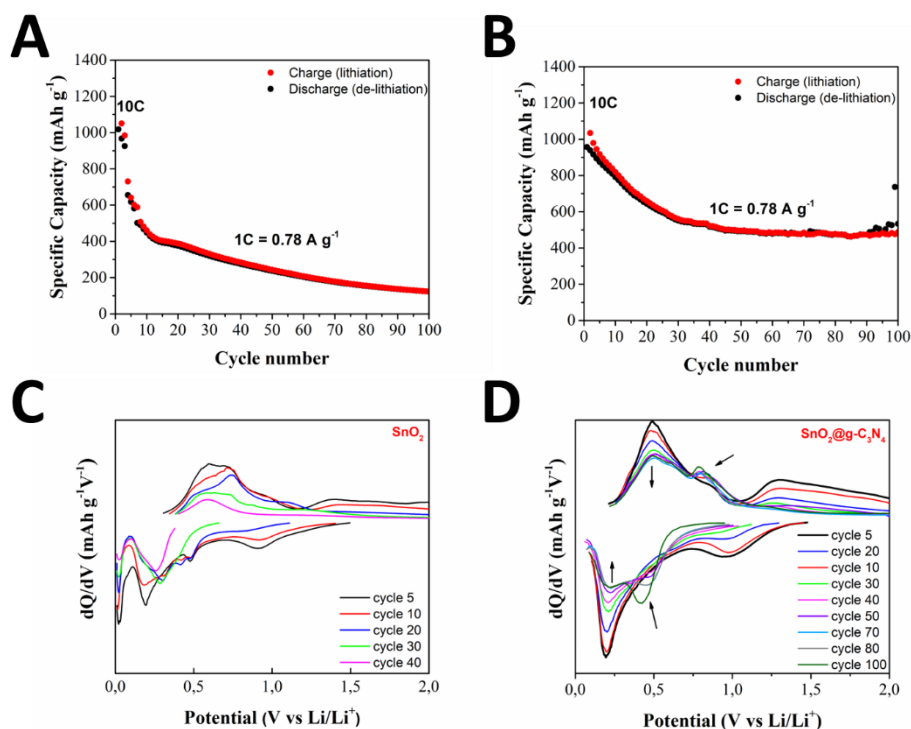
Figure 8.11: galvanostatic cycles at 0.78 A g^{-1} over the potential range of 2.0-0.01 V vs Li/Li$^+$ of SnO_2 (a) and $SnO_2@C_3N_4$ (b). Differential capacity profiles (dQ/dV *vs.* voltage) of SnO_2 (c) and $SnO_2@C_3N_4$ (d).

As previously discussed, the layered morphology of g-C_3N_4 increases cathode wettability [292] and prevent agglomeration of SnO_2 particles that results in larger density of active sites. Thus, $SnO_2@C_3N_4$ electrode benefits large advantages over pure SnO_2 when the cell operates at high current regimes, as discussed below.

Figure 8.12 shows the cycling performance of $SnO_2@C_3N_4$ at higher and different current regimes. At 0.16 A g^{-1} the initial discharge capacity of 995 mAh g^{-1} is decreased to 934 mAh g^{-1} after 3 cycles. While at higher C-rate, as 3.9 A g^{-1}, the $SnO_2@C_3N_4$ delivered a high capacity of 431 mAh g^{-1}, which slowly decreased to 329 mAh g^{-1} after 10 cycles. When the C-rate was reduced back to 0.16 A g^{-1}, the electrode recovered a considerable amount of capacity (798 mAh g^{-1}), with capacity retention of 85.4 %. These results corroborate the idea that the structure of the electrode remains stable even under cycling at high rates of 16 A g^{-1}, resulting in an improved rate capability of the cell.
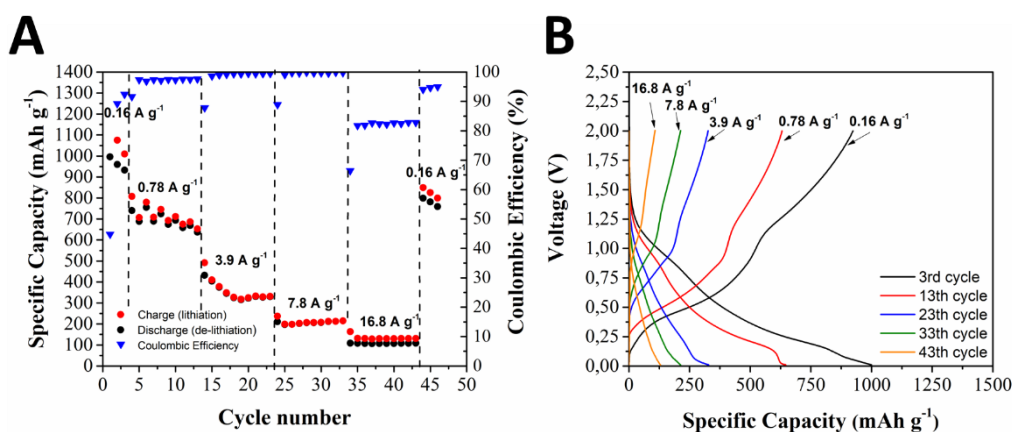
Figure 8.12: galvanostatic cycling performance (a) and galvanostatic profiles (b) of SnO$_2$@C$_3$N$_4$ at high and different current regimes.

In general, the more stable Li ion storage of SnO$_2$@C$_3$N$_4$ is explained by the ability of the material to preserve its original architecture during cycling. In this case the mesoporous g-C$_3$N$_4$ acts as a buffer for the volume changes during the alloying reaction that helps to retain the capacity upon cycling. To confirm this hypothesis the cells were disassembled after cycling and the electrodes were examined by FESEM as shown in Figure 8.13.

The SnO$_2$@C$_3$N$_4$ electrode maintains a good adhesion with the current collector without the formation of relevant cracks after 100 cycles (Figure 8.13 a).

While evident cracks and fractures are well visible on the surface of pure SnO$_2$ electrode after cycling (Figure 8.13 b).

Thus, g-C$_3$N$_4$ inhibits the coarsening of SnO$_2$ particles during synthesis and helps to maintain the integrity of anode material after repeated cycling.
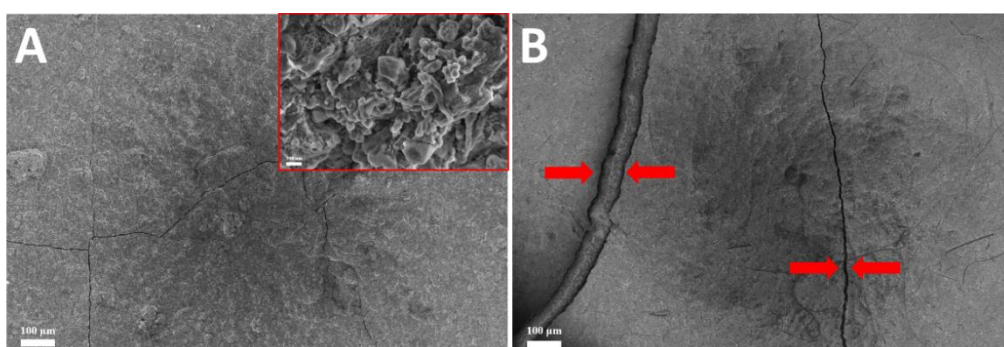
Figure 8.13: FESEM images of SnO$_2$@C$_3$N$_4$ (a) and SnO$_2$ (b) electrodes after galvanostatic cycles at 0.78 A g^{-1} over the potential range of 2.0-0.01 V vs Li/Li$^+$.

In conclusion, the adopted solid-state reaction gives a uniform product, which remains almost unchanged after cycling at high C-rates. The introduction, during the synthesis of a small amount of g-C$_3$N$_4$ demonstrates to prevent coarsening of SnO$_2$ particles, and remarkably improve the electrolyte transport during cell cycling. From electrochemical point of view, the mutual interaction between the

g-C_3N_4 and SnO_2 is beneficial for charge transfer, for this reason the electrodes display high specific capacities of about 1000 mAh g^{-1} at 0.16 A g^{-1} and retain almost 50 % of the initial specific capacity at the very high rates of 3.9 A g^{-1}.

If compared to other synthesis approach (e.g. Hydrothermal, solvothermal *etc*.), the adopted strategy is simpler, cheaper and convenient, because it involves lower amounts of solvent and the addition of more expensive additives (like rGO) is unnecessary. Furthermore, it's important to underline that in many cases, high specific capacities are achieved with an optimized SnO_2 content which is lower than 50 wt.%. This inevitably means a large amount of "inert material" in the electrode which results in low tap density during electrode manufacture. In our case g-C_3N_4 is only 8% of the total weight, and only contribute as support, to immobilize SnO_2 particles and prevent excessive particle growth during the solid-state synthesis.

9 Conclusions and perspectives

This dissertation has been focused on the synthesis of novel cathode and anode materials and their in-depth characterization for the application in Li-ion and post Li-ion batteries.

It is worth noting that, in order to increase the energy of a battery, two possible solutions can be adopted. The first option is related to the increment of operating voltage, adopting the so-called high voltage materials. In this case a higher energy can be achieved but, at the same time, a consistent reduction of the cell safety is also observed, due to the traditional liquid electrolyte instability at high voltage. The second possibility, investigated in the present work, is related to the utilization of materials with higher specific capacity.

In this work we focused the attention on both high capacity cathode and high capacity anode materials. More in detail, sulphur-based cathode and tin oxide anode materials were investigated.

In the first part of the present dissertation the lithium-sulphur system was selected as promising post-lithium ion technology, for high energy application. Besides the well-known advantages, Li-S systems suffers from some issues, related to the multistep reaction process. In addition to low electronic conductivity of sulphur and Li_2S, and the expansion volume due to the solid-liquid transition during the conversion reaction with lithium, this system is deeply affected by shuttle phenomenon. The so-called "shuttle effect" is due to the long-chain polysulfides, which are formed during the first part of the reaction pathway and can migrate from the cathode to the anode side where they directly interact with metallic lithium by parasitic reaction originating a fast capacity fading of the system.

To limit the shuttle effect a double-layer approach, based on carbon nitride, was investigated in chapter 5. The double-layer approach was chosen in order to not insert directly the carbon nitride inside the slurry composition of the cathode, ensuring a good dispersion of carbon nitride on the electrode surface. This way carbon nitride can directly interact with the lithium polysulfides and, at the same time, the interaction between sulphur and carbon black is guaranteed. Carbon nitride was chosen because it is a non-toxic, cheap and stable material, but in particular because, according to DFT calculation, it can directly interact with long chain polysulfides by electrostatic interaction. Starting from these considerations carbon nitride was synthetized from different precursors, with the aim of evaluating the polysulfides trapping ability in relation with morphology and surface chemistry of different carbon nitride materials. Carbon nitride was synthetized by a simple thermal condensation route, simply inserting the precursors in a tubular oven. For the electrochemical characterization, a standard

sulphur cathode, simply mixed with Ketjen black, was selected. In this way melt infusion, or other more complex synthesis route, were avoided and the role of carbon nitride-based double-layer was isolated. According to structural, morphological and electrochemical results, carbon nitride synthetized from urea presented better performances in comparison to carbon nitride obtained from dicyandiamide and melamine. Anyway, all the double-layer electrodes showed better results than single-layer electrode, presenting a specific capacity of 750 mAh g^{-1} instead of 345 mAh g^{-1}.

Starting from these first conclusions, carbon nitride was synthetized from urea at different temperatures in order to discriminate the morphological influence to surface chemistry role in the polysulfides trapping action. Carbon nitride synthetized at different temperatures showed different specific surface area and different surface functionalities. In particular, the samples obtained at 450, 550 and 650 °C showed a different amount of pyridinic nitrogen, which directly interacts with polysulfides. In conclusion, carbon nitride obtained from urea at 550 °C results the best candidate to be used as trapping agent in the double-layer sulphur cathode. Moreover, the active role of carbon nitride and the real influence of double-layer approach was investigated by different electrochemical measurements, such as GITT and EIS. Lastly, the double-layer was optimized in order to reduce the polarization effect due to a thick second layer. The amount of carbon nitride was also modulated with the aim to identify an optimal sulphur/carbon nitride ratio. In this case, two formulations with 0.86 mg cm^{-2} and 1.46 mg cm^{-2} as sulphur loading were investigated. Both the double-layer electrodes, containing the same amount of carbon nitride, showed better results than corresponding single-layer cathodes. In particular, the electrode containing a lower amount of sulphur and a higher S/g-C$_3$N$_4$ ratio demonstrates long cycling performances, for more than 500 cycles, as well as better electrochemical performances at higher C-rates.

In conclusion, the double-layer approach, with the addition of carbon nitride obtained from urea at 550 °C, as additive for polysulfides trapping, resulted a valid strategy to increase the electrochemical performances of sulphur-based cathodes. Last but not least, the adopted strategy resulted versatile for future optimizations and for future industrial scale-up.

Concerning high capacity anode materials, in this dissertation different strategies to obtain hybrid compound based on tin dioxide were evaluated.

Tin dioxide was chosen because, together with silicon, it is the most promising anode material, able to provide high specific capacity. In fact, tin dioxide, considering the two-step reaction mechanism (conversion and alloying) with lithium ion, is able to provide a theoretical specific capacity of 1495 mAh g^{-1}, which is more than three times higher if compared to the specific capacity of graphite. Unfortunately, tin oxide has some intrinsic drawbacks: it has a low electronic conductivity and during the alloying process it is subjected to a huge volumetric expansion. These issues mean low cycling stability of tin oxide-based anode.

In this work two different strategies were presented in order to limit the rapid capacity fading of tin oxide anode, increasing the reversibility of the conversion reaction and at the same time containing the huge volume expansion.

The first strategy reported was a simple wet impregnation synthesis, where tin oxide was directly grown on the surface of a commercial carbon black (C45). In this way the final hybrid compound, containing 30 wt.% of SnO_2 showed a specific capacity higher than 600 mAh g^{-1} for 100 cycles and it remain around 500 mAh g^{-1} for more than 500 cycles, with a coulombic efficiency of about 99.9 %. Moreover, the cells with SnO_2@C45 anode was still active to lithiation after 1000 cycles. The electrochemical results were correlated to a good distribution of small tin oxide nanoparticles (average size of 5 nm) directly anchored to C45 surface.

The second strategy adopted g-C_3N_4 (already used for Li-S) as high surface support for tin dioxide growth. In this case, a simple solid-state synthesis was selected, and the tin oxide precursors were directly mixed with an already formed carbon nitride. The final hybrid compound showed a final amount of SnO_2 of about 90 wt.% and a huge specific surface area able to contain the volume expansion of tin oxide particles during the alloying process. The SnO_2@C_3N_4 compound showed good electrochemical results, presenting a specific capacity of about 500 mAh g^{-1} for 100 cycles at 1C, and interesting results at higher current regimes.

Both the synthesis strategies used to prepare the tin oxide-based materials were chosen for their simplicity considering a possible future scale-up of the process. At the same time, precursors and chemicals were selected taking into account cost and availability. Post-synthesis treatments were also avoided in order to simplify the process for future optimization and scale-up.

10 References

[1]   B. Bednar-Friedl *et al.*, 'Transport', in *Springer Climate*, 2015, pp. 279–300.

[2]   D. Larcher and J.-M. Tarascon, 'Towards greener and more sustainable batteries for electrical energy storage', *Nat. Chem.*, vol. 7, no. 1, pp. 19–29, 2015.

[3]   G. Berckmans, M. Messagie, J. Smekens, N. Omar, L. Vanhaverbeke, and J. Van Mierlo, 'Cost projection of state of the art lithium-ion batteries for electric vehicles up to 2030', *Energies*, vol. 10, no. 9, 2017.

[4]   G. E. Blomgren, 'The Development and Future of Lithium Ion Batteries', *J. Electrochem. Soc.*, vol. 164, no. 1, pp. A5019–A5025, 2017.

[5]   G. Benveniste, H. Rallo, L. Canals Casals, A. Merino, and B. Amante, 'Comparison of the state of Lithium-Sulphur and lithium-ion batteries applied to electromobility', *J. Environ. Manage.*, vol. 226, no. July, pp. 1–12, 2018.

[6]   N. Zhao, C. Li, and X. Guo, 'Review of Methods for Improving the Cyclic Stability of Li–Air Batteries by Controlling Cathode Reactions', *Energy Technol.*, vol. 2, no. 4, pp. 317–324, 2014.

[7]   N. Nitta, F. Wu, J. T. Lee, and G. Yushin, 'Li-ion battery materials: Present and future', *Materials Today*, vol. 18, no. 5. Elsevier Ltd., pp. 252–264, 2015.

[8]   M. Winter and R. J. Brodd, 'What are batteries, fuel cells, and supercapacitors?', *Chem. Rev.*, vol. 104, no. 10, pp. 4245–4269, 2004.

[9]   B. Scrosati, 'History of lithium batteries', *J. Solid State Electrochem.*, vol. 15, no. 7–8, pp. 1623–1630, 2011.

[10]   J. M. Tarascon and M. Armand, 'Issues and challenges facing rechargeable lithium batteries', *Nature*, vol. 414, no. 6861. pp. 359–367, 2001.

[11]   J. F., M. Hasan, S. Patil, D. P., and T. Clancy, 'Energy Storage: Battery Materials and Architectures at the Nanoscale', *ICT - Energy - Concepts Towar. Zero - Power Inf. Commun. Technol.*, 2014.

[12]   F. Schipper and D. Aurbach, 'A brief review: Past, present and future of lithium ion batteries', *Russ. J. Electrochem.*, vol. 52, no. 12, pp. 1095–1121, 2016.

[13]   D. E. Demirocak, S. S. Srinivasan, and E. K. Stefanakos, 'A review on nanocomposite materials for rechargeable Li-ion batteries', *Appl. Sci.*, vol.

7, no. 7, pp. 1–26, 2017.

[14] T. Nagaura and K. Tozawa, *Progress in Batteries and Solar Cells*, vol. 9. United States: Cleveland, OH (United States); JEC Press Inc., 1990.

[15] S. Basu, C. Zeller, P. J. Flanders, C. D. Fuerst, W. D. Johnson, and J. E. Fischer, 'Synthesis and properties of lithium-graphite intercalation compounds', *Mater. Sci. Eng.*, vol. 38, no. 3, pp. 275–283, 1979.

[16] J. B. Goodenough and K. Mizuchima, 'Electrochemical cell with new fast ion conductors', 1981.

[17] D. Linden and T. B. Reddy, 'Handbook of batteries', *Choice Rev. Online*, vol. 33, no. 04, pp. 33-2144-33–2144, 1995.

[18] K. Xu, 'Nonaqueous liquid electrolytes for lithium-based rechargeable batteries', *Chem. Rev.*, vol. 104, no. 10, pp. 4303–4417, Oct. 2004.

[19] B. Lestriez, 'Comptes Rendus Chimie Functions of polymers in composite electrodes of lithium ion batteries', *Comptes rendus - Chim.*, vol. 13, no. 11, pp. 1341–1350, 2010.

[20] M. Hu, X. Pang, and Z. Zhou, 'Recent progress in high-voltage lithium ion batteries', *J. Power Sources*, vol. 237, pp. 229–242, 2013.

[21] C. Julien and A. Mauger, *Lithium Batteries*. .

[22] S. J. An, J. Li, C. Daniel, D. Mohanty, S. Nagpure, and D. L. Wood, 'The state of understanding of the lithium-ion-battery graphite solid electrolyte interphase (SEI) and its relationship to formation cycling', *Carbon N. Y.*, vol. 105, pp. 52–76, 2016.

[23] V. A. Agubra and J. W. Fergus, 'The formation and stability of the solid electrolyte interface on the graphite anode', *J. Power Sources*, vol. 268, pp. 153–162, 2014.

[24] Y. Tang, Y. Zhang, W. Li, B. Ma, and X. Chen, 'Rational material design for ultrafast rechargeable lithium-ion batteries', *Chem. Soc. Rev.*, vol. 44, no. 17, pp. 5926–5940, 2015.

[25] M. Winter and J. O. Besenhard, 'Electrochemical lithiation of tin and tin-based intermetallics and composites', *Electrochim. Acta*, vol. 45, no. 1, pp. 31–50, 1999.

[26] M. Wachtler, J. O. Besenhard, and M. Winter, 'Tin and tin-based intermetallics as new anode materials for lithium-ion cells', *J. Power Sources*, vol. 94, no. 2, pp. 189–193, 2001.

[27] R. A. Huggins and W. D. Nix, 'Decrepitation model for capacity loss during cycling of alloys in rechargeable electrochemical systems', *Ionics (Kiel).*, vol. 6, no. 1, pp. 57–63, 2000.

[28] A. Casimir, H. Zhang, O. Ogoke, J. C. Amine, J. Lu, and G. Wu, 'Silicon-based anodes for lithium-ion batteries: Effectiveness of materials synthesis and electrode preparation', *Nano Energy*, vol. 27, pp. 359–376, 2016.

[29] M. N. Obrovac and V. L. Chevrier, 'Alloy Negative Electrodes for Li-Ion Batteries', 2014.

[30] T. Ohzuku, 'Zero-Strain Insertion Material of Li[Li[sub 1⁄3]Ti[sub 5⁄3]]O[sub 4] for Rechargeable Lithium Cells', *J. Electrochem. Soc.*, vol. 142, no. 5, p. 1431, 1995.

[31] M. Minella *et al.*, 'Anodic Materials for Lithium-ion Batteries: TiO2-rGO Composites for High Power Applications', *Electrochim. Acta*, vol. 230, pp. 132–140, 2017.

[32] S. Goriparti, E. Miele, F. De Angelis, E. Di Fabrizio, R. Proietti Zaccaria, and C. Capiglia, 'Review on recent progress of nanostructured anode materials for Li-ion batteries', *J. Power Sources*, vol. 257, pp. 421–443,

2014.

[33] M. Li and J. Lu, 'Cobalt in lithium-ion batteries', *Science (80-.).*, vol. 367, no. 6481, pp. 979 LP – 980, Feb. 2020.

[34] B. K. Sovacool, A. Hook, M. Martiskainen, A. Brock, and B. Turnheim, 'The decarbonisation divide: Contextualizing landscapes of low-carbon exploitation and toxicity in Africa', *Glob. Environ. Chang.*, vol. 60, p. 102028, 2020.

[35] T. Ohzuku and Y. Makimura, 'Layered Lithium Insertion Material of LiNi1/2Mn1/2O2 : A Possible Alternative to LiCoO2 for Advanced Lithium-Ion Batteries', *Chem. Lett.*, vol. 30, no. 8, pp. 744–745, Aug. 2001.

[36] M. M. Thackeray, W. I. F. David, P. G. Bruce, and J. B. Goodenough, 'Lithium insertion into manganese spinels', *Mater. Res. Bull.*, vol. 18, no. 4, pp. 461–472, 1983.

[37] R. Chen and M. S. Whittingham, 'Cathodic Behavior of Alkali Manganese Oxides from Permanganate', *J. Electrochem. Soc.*, vol. 144, no. 4, pp. L64–L67, 1997.

[38] F. Capitaine, P. Gravereau, and C. Delmas, 'A new variety of LiMnO2 with a layered structure', *Solid State Ionics*, vol. 89, no. 3–4, pp. 197–202, 1996.

[39] H. Yang, G. V Zhuang, and P. N. Ross, 'Thermal stability of LiPF6 salt and Li-ion battery electrolytes containing LiPF6', *J. Power Sources*, vol. 161, no. 1, pp. 573–579, 2006.

[40] Z. Liu, A. Yu, and J. Y. Lee, 'Synthesis and characterization of LiNi1−x−yCoxMnyO2 as the cathode materials of secondary lithium batteries', *J. Power Sources*, vol. 81–82, pp. 416–419, 1999.

[41] X. Xiao, Z. Liu, L. Baggetto, G. M. Veith, K. L. More, and R. R. Unocic, 'Unraveling manganese dissolution/deposition mechanisms on the negative electrode in lithium ion batteries', *Phys. Chem. Chem. Phys.*, vol. 16, no. 22, pp. 10398–10402, 2014.

[42] N. P. W. Pieczonka *et al.*, 'Understanding Transition-Metal Dissolution Behavior in LiNi0.5Mn1.5O4 High-Voltage Spinel for Lithium Ion Batteries', *J. Phys. Chem. C*, vol. 117, no. 31, pp. 15947–15957, Aug. 2013.

[43] V. G. Pron, D. Versaci, J. Amici, C. Francia, M. Santarelli, and S. Bodoardo, 'Electrochemical Characterization and Solid Electrolyte Interface Modeling of LiNi 0.5 Mn 1.5 O 4 -Graphite Cells', *J. Electrochem. Soc.*, vol. 166, no. 10, pp. A2255–A2263, Jun. 2019.

[44] C. Masquelier and L. Croguennec, 'Polyanionic (Phosphates, Silicates, Sulfates) Frameworks as Electrode Materials for Rechargeable Li (or Na) Batteries', *Chem. Rev.*, vol. 113, no. 8, pp. 6552–6591, Aug. 2013.

[45] F. Di Lupo, G. Meligrana, C. Gerbaldi, S. Bodoardo, and N. Penazzi, 'Surfactant-assisted mild solvothermal synthesis of nanostructured LiFePO4/C cathodes evidencing ultrafast rate capability', *Electrochim. Acta*, vol. 156, pp. 188–198, 2015.

[46] J. Haber, M. Witko, and R. Tokarz, 'Vanadium pentoxide I. Structures and properties', *Appl. Catal. A Gen.*, vol. 157, no. 1–2, pp. 3–22, 1997.

[47] N. Bahlawane and D. Lenoble, 'Vanadium oxide compounds: Structure, properties, and growth from the gas phase', *Chem. Vap. Depos.*, vol. 20, no. 7–9, pp. 299–311, 2014.

[48] A. M. Cao, J. S. Hu, H. P. Liang, and L. J. Wan, 'Self-assembled vanadium pentoxide (V2O5) hollow microspheres from nanorods and their

application in lithium-ion batteries', *Angew. Chemie - Int. Ed.*, vol. 44, no. 28, pp. 4391–4395, 2005.

[49] J. Huang *et al.*, 'V2O5 self-assembled nanosheets as high stable cathodes for Lithium-ion batteries', *Electrochim. Acta*, vol. 191, pp. 158–164, 2016.

[50] Z. Zou *et al.*, 'V6O13nanosheets synthesized from ethanol-aqueous solutions as high energy cathode material for lithium-ion batteries', *Electrochim. Acta*, vol. 135, pp. 175–180, 2014.

[51] X. X. Zhang, K. K. Wang, X. Wei, and J. J. Chen, 'Carbon-Coated V2O5 Nanocrystals as High Performance Cathode Material for Lithium Ion Batteries', *Chem. Mater.*, pp. 1–6, 2005.

[52] C. Delmas, J. M. Cocciantelli, and J. P. Doumerc, 'The LixV2O5 system : An overview of the structure modifications induced by the lithium intercalation', *Solid State Ionics*, vol. 69, no. 3–4, pp. 257–264, 1994.

[53] H. Song, C. Zhang, Y. Liu, C. Liu, X. Nan, and G. Cao, 'Facile synthesis of mesoporous V2O5 nanosheets with superior rate capability and excellent cycling stability for lithium ion batteries', *J. Power Sources*, vol. 294, pp. 1–7, 2015.

[54] Q. An *et al.*, 'Supercritically exfoliated ultrathin vanadium pentoxide nanosheets with high rate capability for lithium batteries', *Phys. Chem. Chem. Phys.*, vol. 15, no. 39, p. 16828, 2013.

[55] Y. Zhang *et al.*, 'V2O5 Nanowire Composite Paper as a High-Performance Lithium-Ion Battery Cathode', *ACS Omega*, vol. 2, no. 3, pp. 793–799, 2017.

[56] Y. Li *et al.*, 'Leaf-like V2O5 nanosheets fabricated by a facile green approach as high energy cathode material for lithium-ion batteries', *Adv. Energy Mater.*, vol. 3, no. 9, pp. 1171–1175, 2013.

[57] A. Pan *et al.*, 'Facile synthesized nanorod structured vanadium pentoxide for high-rate lithium batteries', *J. Mater. Chem.*, vol. 20, no. 41, p. 9193, 2010.

[58] L. Mai, X. Xu, L. Xu, C. Han, and Y. Luo, 'Vanadium oxide nanowires for Li-ion batteries', *J. Mater. Res.*, vol. 26, no. 17, pp. 2175–2185, 2011.

[59] Y. Wang, K. Takahashi, H. Shang, and G. Cao, 'Synthesis and Electrochemical Properties of Vanadium Pentoxide Nanotube Arrays', *J. Phys. Chem. B*, vol. 109, no. 8, pp. 3085–3088, 2005.

[60] S. Liang *et al.*, 'Template-free synthesis of ultra-large V2O5nanosheets with exceptional small thickness for high-performance lithium-ion batteries', *Nano Energy*, vol. 13, pp. 58–66, 2015.

[61] L. Z. and X. W. (David) Lou An Qiang Pan, Hao Bin Wu, 'Uniform V2O5 nanosheet-assembled hollow microflowers with excellent lithium storage properties', *Energy Environ. Sci.*, pp. 1476–1479, 2013.

[62] S. B. Chikkannanavar, D. M. Bernardi, and L. Liu, 'A review of blended cathode materials for use in Li-ion batteries', *Journal of Power Sources*, vol. 248. Elsevier B.V, pp. 91–100, 2014.

[63] D. Bresser, D. Buchholz, A. Moretti, A. Varzi, and S. Passerini, 'Alternative binders for sustainable electrochemical energy storage-the transition to aqueous electrode processing and bio-derived polymers', *Energy Environ. Sci.*, vol. 11, no. 11, pp. 3096–3127, 2018.

[64] D. L. Wood, J. Li, and C. Daniel, 'Prospects for reducing the processing cost of lithium ion batteries', *J. Power Sources*, vol. 275, pp. 234–242, 2015.

[65] T. S. Poet, C. R. Kirman, M. Bader, C. van Thriel, M. L. Gargas, and P. M.

Hinderliter, 'Quantitative Risk Analysis for N-Methyl Pyrrolidone Using Physiologically Based Pharmacokinetic and Benchmark Dose Modeling', *Toxicol. Sci.*, vol. 113, no. 2, pp. 468–482, Feb. 2010.

[66] D. L. Wood, J. D. Quass, J. Li, S. Ahmed, D. Ventola, and C. Daniel, 'Technical and economic analysis of solvent-based lithium-ion electrode drying with water and NMP', *Dry. Technol.*, vol. 36, no. 2, pp. 234–244, Jan. 2018.

[67] M. Valvo, A. Liivat, H. Eriksson, C.-W. Tai, and K. Edström, 'Iron-Based Electrodes Meet Water-Based Preparation, Fluorine-Free Electrolyte and Binder: A Chance for More Sustainable Lithium-Ion Batteries?', *ChemSusChem*, vol. 10, no. 11, pp. 2431–2448, Jun. 2017.

[68] D. Versaci *et al.*, 'New eco-friendly low-cost binders for Li-ion anodes', *J. Solid State Electrochem.*, vol. 21, no. 12, pp. 3429–3435, 2017.

[69] H. Buqa, M. Holzapfel, F. Krumeich, C. Veit, and P. Novák, 'Study of styrene butadiene rubber and sodium methyl cellulose as binder for negative electrodes in lithium-ion batteries', *J. Power Sources*, vol. 161, no. 1, pp. 617–622, 2006.

[70] J. Drofenik *et al.*, 'Cellulose as a binding material in graphitic anodes for Li ion batteries: a performance and degradation study', *Electrochim. Acta*, vol. 48, no. 7, pp. 883–889, 2003.

[71] S. F. Lux, F. Schappacher, A. Balducci, S. Passerini, and M. Winter, 'Low Cost, Environmentally Benign Binders for Lithium-Ion Batteries', *J. Electrochem. Soc.*, vol. 157, no. 3, p. A320, 2010.

[72] B. Lestriez, S. Bahri, I. Sandu, L. Roué, and D. Guyomard, 'On the binding mechanism of CMC in Si negative electrodes for Li-ion batteries', *Electrochem. commun.*, vol. 9, no. 12, pp. 2801–2806, 2007.

[73] F. M. Courtel, S. Niketic, D. Duguay, Y. Abu-Lebdeh, and I. J. Davidson, 'Water-soluble binders for MCMB carbon anodes for lithium-ion batteries', *J. Power Sources*, vol. 196, no. 4, pp. 2128–2134, 2011.

[74] W.-R. Liu, M.-H. Yang, H.-C. Wu, S. M. Chiao, and N.-L. Wu, 'Enhanced Cycle Life of Si Anode for Li-Ion Batteries by Using Modified Elastomeric Binder', *Electrochem. Solid-State Lett.*, vol. 8, no. 2, p. A100, 2005.

[75] R. Dominko *et al.*, 'Understanding the Role of Gelatin as a Pretreating Agent for Use in Li-Ion Batteries', *J. Electrochem. Soc.*, vol. 151, no. 7, p. A1058, 2004.

[76] I. Kovalenko *et al.*, 'A Major Constituent of Brown Algae for Use in High-Capacity Li-Ion Batteries', *Science (80-.).*, vol. 334, no. 6052, pp. 75 LP – 79, Oct. 2011.

[77] L. Chai, Q. Qu, L. Zhang, M. Shen, L. Zhang, and H. Zheng, 'Chitosan, a new and environmental benign electrode binder for use with graphite anode in lithium-ion batteries', *Electrochim. Acta*, vol. 105, pp. 378–383, 2013.

[78] N. Cuesta, A. Ramos, I. Cameán, C. Antuña, and A. B. García, 'Hydrocolloids as binders for graphite anodes of lithium-ion batteries', *Electrochim. Acta*, vol. 155, pp. 140–147, 2015.

[79] A. Magasinski *et al.*, 'Toward Efficient Binders for Li-Ion Battery Si-Based Anodes: Polyacrylic Acid', *ACS Appl. Mater. Interfaces*, vol. 2, no. 11, pp. 3004–3010, Nov. 2010.

[80] S. Komaba, K. Shimomura, N. Yabuuchi, T. Ozeki, H. Yui, and K. Konno, 'Study on Polymer Binders for High-Capacity SiO Negative Electrode of Li-Ion Batteries', *J. Phys. Chem. C*, vol. 115, no. 27, pp. 13487–13495, Jul. 2011.

[81] Z. Zhang *et al.*, 'Cycle performance improvement of LiFePO4 cathode with polyacrylic acid as binder', *Electrochim. Acta*, vol. 80, pp. 440–444, 2012.

[82] S. Komaba *et al.*, 'Functional binders for reversible lithium intercalation into graphite in propylene carbonate and ionic liquid media', *J. Power Sources*, vol. 195, no. 18, pp. 6069–6074, 2010.

[83] S. S. Zhang, K. Xu, and T. R. Jow, 'Evaluation on a water-based binder for the graphite anode of Li-ion batteries', *J. Power Sources*, vol. 138, no. 1, pp. 226–231, 2004.

[84] K. Xu, S. Zhang, J. L. Allen, and T. R. Jow, 'Nonflammable Electrolytes for Li-Ion Batteries Based on a Fluorinated Phosphate', *J. Electrochem. Soc.*, vol. 149, no. 8, p. A1079, 2002.

[85] K. Xu, S. Zhang, T. R. Jow, W. Xu, and C. A. Angell, 'LiBOB as Salt for Lithium-Ion Batteries:A Possible Solution for High Temperature Operation', *Electrochem. Solid-State Lett.*, vol. 5, no. 1, p. A26, 2002.

[86] K. Xu, 'Tailoring Electrolyte Composition for LiBOB', *J. Electrochem. Soc.*, vol. 155, no. 10, p. A733, 2008.

[87] A. M. Andersson, M. Herstedt, A. G. Bishop, and K. Edström, 'The influence of lithium salt on the interfacial reactions controlling the thermal stability of graphite anodes', *Electrochim. Acta*, vol. 47, no. 12, pp. 1885–1898, 2002.

[88] J. Neumann, S. Steudte, C.-W. Cho, J. Thöming, and S. Stolte, 'Biodegradability of 27 pyrrolidinium, morpholinium, piperidinium, imidazolium and pyridinium ionic liquid cations under aerobic conditions', *Green Chem.*, vol. 16, no. 4, pp. 2174–2184, 2014.

[89] S. S. Zhang and T. R. Jow, 'Aluminum corrosion in electrolyte of Li-ion battery', *J. Power Sources*, vol. 109, no. 2, pp. 458–464, 2002.

[90] J. B. Goodenough, 'General Concepts', *Lithium Ion Batteries*. pp. 1–25, 12-Jun-1998.

[91] P. Jankowski, W. Wieczorek, and P. Johansson, 'SEI-forming electrolyte additives for lithium-ion batteries: development and benchmarking of computational approaches', *J. Mol. Model.*, vol. 23, no. 1, p. 6, Jan. 2017.

[92] A. M. Haregewoin, A. S. Wotango, and B.-J. Hwang, 'Electrolyte additives for lithium ion battery electrodes: progress and perspectives', *Energy Environ. Sci.*, vol. 9, no. 6, pp. 1955–1988, 2016.

[93] N. Kumar and D. J. Siegel, 'Interface-Induced Renormalization of Electrolyte Energy Levels in Magnesium Batteries', *J. Phys. Chem. Lett.*, vol. 7, no. 5, pp. 874–881, Mar. 2016.

[94] H. Zhang, M.-Y. Zhou, C.-E. Lin, and B.-K. Zhu, 'Progress in polymeric separators for lithium ion batteries', *RSC Adv.*, vol. 5, no. 109, pp. 89848–89860, 2015.

[95] P. Arora and Z. (John) Zhang, 'Battery Separators', *Chem. Rev.*, vol. 104, no. 10, pp. 4419–4462, Oct. 2004.

[96] H. Lee, M. Yanilmaz, O. Toprakci, K. Fu, and X. Zhang, 'A review of recent developments in membrane separators for rechargeable lithium-ion batteries', *Energy Environ. Sci.*, vol. 7, no. 12, pp. 3857–3886, 2014.

[97] A. A. Review and A. Fotouhi, 'Lithium-Sulfur Battery Technology Readiness', 2017.

[98] M. Hagen, D. Hanselmann, K. Ahlbrecht, R. Maça, D. Gerber, and J. Tübke, 'Lithium-Sulfur Cells: The Gap between the State-of-the-Art and the Requirements for High Energy Battery Cells', *Adv. Energy Mater.*, vol. 5, no. 16, 2015.

[99] H. Danuta, U. Juliusz, D. Herbert, and J. Ulam, 'Electric dry cells and storage batteries', *US Pat*, vol. 3043896, 1962.

[100] R. D. Rauh, 'A Lithium/Dissolved Sulfur Battery with an Organic Electrolyte', *J. Electrochem. Soc.*, vol. 126, no. 4, p. 523, 1979.

[101] A. Rosenman, E. Markevich, G. Salitra, D. Aurbach, A. Garsuch, and F. F. Chesneau, 'Review on Li-Sulfur Battery Systems: An Integral Perspective', *Advanced Energy Materials*, vol. 5, no. 16. pp. 1–21, 2015.

[102] G. Li, S. Wang, Y. Zhang, M. Li, Z. Chen, and J. Lu, 'Revisiting the Role of Polysulfides in Lithium–Sulfur Batteries', *Advanced Materials*, vol. 30, no. 22. pp. 1–19, 2018.

[103] S. Evers and L. F. Nazar, 'New approaches for high energy density lithium-sulfur battery cathodes', *Acc. Chem. Res.*, vol. 46, no. 5, pp. 1135–1143, 2013.

[104] L. Borchardt, M. Oschatz, and S. Kaskel, 'Carbon Materials for Lithium Sulfur Batteries - Ten Critical Questions', *Chem. - A Eur. J.*, vol. 22, no. 22, pp. 7324–7351, 2016.

[105] A. Manthiram, Y. Fu, S.-H. Chung, C. Zu, and Y.-S. Su, 'Rechargeable Lithium–Sulfur Batteries', *Chem. Rev.*, vol. 114, no. 23, pp. 11751–11787, Dec. 2014.

[106] R. Xu, J. Lu, and K. Amine, 'Progress in Mechanistic Understanding and Characterization Techniques of Li-S Batteries', *Advanced Energy Materials*, vol. 5, no. 16. pp. 1–22, 2015.

[107] Y. V Mikhaylik and J. R. Akridge, 'Polysulfide Shuttle Study in the Li/S Battery System', *J. Electrochem. Soc.*, vol. 151, no. 11, p. A1969, 2004.

[108] M. Wild *et al.*, 'Lithium sulfur batteries, a mechanistic review', *Energy and Environmental Science*, vol. 8, no. 12. Royal Society of Chemistry, pp. 3477–3494, 2015.

[109] K. Propp *et al.*, 'Multi-temperature state-dependent equivalent circuit discharge model for lithium-sulfur batteries', *J. Power Sources*, vol. 328, pp. 289–299, 2016.

[110] D. Lei *et al.*, 'Progress and Perspective of Solid-State Lithium–Sulfur Batteries', *Adv. Funct. Mater.*, vol. 28, no. 38, pp. 1–27, 2018.

[111] T. Li *et al.*, 'A Comprehensive Understanding of Lithium–Sulfur Battery Technology', *Advanced Functional Materials*, vol. 29, no. 32. pp. 1–56, 2019.

[112] W. Xu *et al.*, 'Lithium metal anodes for rechargeable batteries', *Energy Environ. Sci.*, vol. 7, no. 2, pp. 513–537, 2014.

[113] X. Ji, K. T. Lee, and L. F. Nazar, 'A highly ordered nanostructured carbon–sulphur cathode for lithium–sulphur batteries', *Nat. Mater.*, vol. 8, no. 6, pp. 500–506, 2009.

[114] R. Younesi, G. M. Veith, P. Johansson, K. Edström, and T. Vegge, 'Lithium salts for advanced lithium batteries: Li–metal, Li–O2, and Li–S', *Energy Environ. Sci.*, vol. 8, no. 7, pp. 1905–1922, 2015.

[115] E. Peled, 'Lithium-Sulfur Battery: Evaluation of Dioxolane-Based Electrolytes', *J. Electrochem. Soc.*, vol. 136, no. 6, p. 1621, 1989.

[116] N. Angulakshmi and A. M. Stephan, 'Efficient electrolytes for lithium-sulfur batteries', *Frontiers in Energy Research*, vol. 3, no. MAY. pp. 1–8, 2015.

[117] S. Y. Li, W. P. Wang, H. Duan, and Y. G. Guo, 'Recent progress on confinement of polysulfides through physical and chemical methods', *Journal of Energy Chemistry*, vol. 27, no. 6. Elsevier B.V. and Science

Press, pp. 1555–1565, 2018.

[118] J. Zheng *et al.*, 'Lewis Acid–Base Interactions between Polysulfides and Metal Organic Framework in Lithium Sulfur Batteries', *Nano Lett.*, vol. 14, no. 5, pp. 2345–2352, May 2014.

[119] X. Hong, R. Wang, Y. Liu, J. Fu, J. Liang, and S. Dou, 'Recent advances in chemical adsorption and catalytic conversion materials for Li–S batteries', *Journal of Energy Chemistry*, vol. 42. Elsevier B.V. and Science Press, pp. 144–168, 2020.

[120] Y. C. Jeong, J. H. Kim, S. Nam, C. R. Park, and S. J. Yang, 'Rational Design of Nanostructured Functional Interlayer/Separator for Advanced Li–S Batteries', *Advanced Functional Materials*, vol. 28, no. 38. pp. 1–32, 2018.

[121] Y.-S. Su and A. Manthiram, 'Lithium–sulphur batteries with a microporous carbon paper as a bifunctional interlayer', *Nat. Commun.*, vol. 3, no. 1, p. 1166, 2012.

[122] L. Fan, M. Li, X. Li, W. Xiao, Z. Chen, and J. Lu, 'Interlayer Material Selection for Lithium-Sulfur Batteries', *Joule*, vol. 3, no. 2. Elsevier Inc., pp. 361–386, 2019.

[123] J. Q. Huang, Q. Zhang, and F. Wei, 'Multi-functional separator/interlayer system for high-stable lithium-sulfur batteries: Progress and prospects', *Energy Storage Materials*, vol. 1. Elsevier, pp. 127–145, 2015.

[124] Z. Xiao *et al.*, 'A lightweight TiO2/Graphene interlayer, applied as a highly effective polysulfide absorbent for fast, long-life lithium-sulfur batteries', *Adv. Mater.*, vol. 27, no. 18, pp. 2891–2898, 2015.

[125] J. Fang *et al.*, 'Improved performance of sulfur cathode by an easy and scale-up coating strategy', *J. Power Sources*, vol. 297, pp. 265–270, 2015.

[126] Y. Fan *et al.*, 'Functionalized Boron Nitride Nanosheets/Graphene Interlayer for Fast and Long-Life Lithium–Sulfur Batteries', *Adv. Energy Mater.*, vol. 7, no. 13, pp. 1–6, 2017.

[127] W. Sun *et al.*, 'A simply effective double-coating cathode with MnO2 nanosheets/graphene as functionalized interlayer for high performance lithium-sulfur batteries', *Electrochim. Acta*, vol. 207, pp. 198–206, 2016.

[128] L. Qu *et al.*, 'Enhanced Cycling Performance for Lithium–Sulfur Batteries by a Laminated 2D g-C 3 N 4 /Graphene Cathode Interlayer', *ChemSusChem*, vol. 12, no. 1, pp. 213–223, 2019.

[129] J. LIEBIG, 'Analyse der Harnsäure', *Ann. der Pharm.*, vol. 10, no. 1, pp. 47–48, Jan. 1834.

[130] J. Liu, H. Wang, and M. Antonietti, 'Graphitic carbon nitride "reloaded": Emerging applications beyond (photo)catalysis', *Chemical Society Reviews*, vol. 45, no. 8. Royal Society of Chemistry, pp. 2308–2326, 2016.

[131] E. C. Franklin, 'THE AMMONO CARBONIC ACIDS', *J. Am. Chem. Soc.*, vol. 44, no. 3, pp. 486–509, Mar. 1922.

[132] 'Recently Added'. [Online]. Available: https://www.mendeley.com/library/. [Accessed: 15-Apr-2020].

[133] X. Wang *et al.*, 'A metal-free polymeric photocatalyst for hydrogen production from water under visible light', *Nat. Mater.*, vol. 8, no. 1, pp. 76–80, 2009.

[134] J. Wen, J. Xie, X. Chen, and X. Li, 'A review on g-C 3 N 4 -based photocatalysts', *Appl. Surf. Sci.*, vol. 391, pp. 72–123, 2017.

[135] A. Thomas *et al.*, 'Graphitic carbon nitride materials: Variation of structure and morphology and their use as metal-free catalysts', *J. Mater. Chem.*,

vol. 18, no. 41, pp. 4893–4908, 2008.

[136] Y. Wang, X. Wang, and M. Antonietti, 'Polymeric graphitic carbon nitride as a heterogeneous organocatalyst: From photochemistry to multipurpose catalysis to sustainable chemistry', *Angew. Chemie - Int. Ed.*, vol. 51, no. 1, pp. 68–89, 2012.

[137] E. G. Gillan, 'Synthesis of Nitrogen-Rich Carbon Nitride Networks from an Energetic Molecular Azide Precursor', *Chem. Mater.*, vol. 12, no. 12, pp. 3906–3912, Dec. 2000.

[138] Y. Zhang, A. Thomas, M. Antonietti, and X. Wang, 'Activation of Carbon Nitride Solids by Protonation: Morphology Changes, Enhanced Ionic Conductivity, and Photoconduction Experiments', *J. Am. Chem. Soc.*, vol. 131, no. 1, pp. 50–51, Jan. 2009.

[139] J. Zhu, P. Xiao, H. Li, and S. A. C. Carabineiro, 'Graphitic carbon nitride: Synthesis, properties, and applications in catalysis', *ACS Applied Materials and Interfaces*, vol. 6, no. 19. pp. 16449–16465, 08-Oct-2014.

[140] A. Thomas *et al.*, 'Graphitic carbon nitride materials: variation of structure and morphology and their use as metal-free catalysts', *J. Mater. Chem.*, vol. 18, no. 41, pp. 4893–4908, 2008.

[141] Y. pei Sun, W. Ha, J. Chen, H. yang Qi, and Y. ping Shi, 'Advances and applications of graphitic carbon nitride as sorbent in analytical chemistry for sample pretreatment: A review', *TrAC - Trends in Analytical Chemistry*, vol. 84. Elsevier B.V., pp. 12–21, 2016.

[142] L. Jiang *et al.*, 'Doping of graphitic carbon nitride for photocatalysis: A reveiw', *Appl. Catal. B Environ.*, vol. 217, pp. 388–406, 2017.

[143] Y. Zhang, T. Mori, J. Ye, and M. Antonietti, 'Phosphorus-Doped Carbon Nitride Solid: Enhanced Electrical Conductivity and Photocurrent Generation', *J. Am. Chem. Soc.*, vol. 132, no. 18, pp. 6294–6295, May 2010.

[144] S. Hu *et al.*, 'A simple and efficient method to prepare a phosphorus modified g-C3N4 visible light photocatalyst', *RSC Adv.*, vol. 4, no. 41, pp. 21657–21663, 2014.

[145] J. Ran, T. Y. Ma, G. Gao, X.-W. Du, and S. Z. Qiao, 'Porous P-doped graphitic carbon nitride nanosheets for synergistically enhanced visible-light photocatalytic H2 production', *Energy Environ. Sci.*, vol. 8, no. 12, pp. 3708–3717, 2015.

[146] Y.-P. Zhu, T.-Z. Ren, and Z.-Y. Yuan, 'Mesoporous Phosphorus-Doped g-C3N4 Nanostructured Flowers with Superior Photocatalytic Hydrogen Evolution Performance', *ACS Appl. Mater. Interfaces*, vol. 7, no. 30, pp. 16850–16856, Aug. 2015.

[147] D.-H. Lan, H.-T. Wang, L. Chen, C.-T. Au, and S.-F. Yin, 'Phosphorous-modified bulk graphitic carbon nitride: Facile preparation and application as an acid-base bifunctional and efficient catalyst for CO2 cycloaddition with epoxides', *Carbon N. Y.*, vol. 100, pp. 81–89, 2016.

[148] B. Chai, J. Yan, C. Wang, Z. Ren, and Y. Zhu, 'Enhanced visible light photocatalytic degradation of Rhodamine B over phosphorus doped graphitic carbon nitride', *Appl. Surf. Sci.*, vol. 391, pp. 376–383, 2017.

[149] S. Guo *et al.*, 'Phosphorus-Doped Carbon Nitride Tubes with a Layered Micro-nanostructure for Enhanced Visible-Light Photocatalytic Hydrogen Evolution', *Angew. Chemie Int. Ed.*, vol. 55, no. 5, pp. 1830–1834, Jan. 2016.

[150] G. Liu *et al.*, 'Unique Electronic Structure Induced High Photoreactivity of

Sulfur-Doped Graphitic C3N4', *J. Am. Chem. Soc.*, vol. 132, no. 33, pp. 11642–11648, Aug. 2010.

[151] J. Hong, X. Xia, Y. Wang, and R. Xu, 'Mesoporous carbon nitride with in situ sulfur doping for enhanced photocatalytic hydrogen evolution from water under visible light', *J. Mater. Chem.*, vol. 22, no. 30, pp. 15006–15012, 2012.

[152] S. C. Yan, Z. S. Li, and Z. G. Zou, 'Photodegradation of Rhodamine B and Methyl Orange over Boron-Doped g-C3N4 under Visible Light Irradiation', *Langmuir*, vol. 26, no. 6, pp. 3894–3901, Mar. 2010.

[153] Y. Wang, Y. Di, M. Antonietti, H. Li, X. Chen, and X. Wang, 'Excellent Visible-Light Photocatalysis of Fluorinated Polymeric Carbon Nitride Solids', *Chem. Mater.*, vol. 22, no. 18, pp. 5119–5121, Sep. 2010.

[154] H.-M. Zhao, C.-M. Di, L. Wang, Y. Chun, and Q.-H. Xu, 'Synthesis of mesoporous graphitic C3N4 using cross-linked bimodal mesoporous SBA-15 as a hard template', *Microporous Mesoporous Mater.*, vol. 208, pp. 98–104, 2015.

[155] Y. Wang, X. Wang, M. Antonietti, and Y. Zhang, 'Facile one-pot synthesis of nanoporous carbon nitride solids by using soft templates', *ChemSusChem*, vol. 3, no. 4, pp. 435–439, 2010.

[156] W. Shen, L. Ren, H. Zhou, S. Zhang, and W. Fan, 'Facile one-pot synthesis of bimodal mesoporous carbon nitride and its function as a lipase immobilization support', *J. Mater. Chem.*, vol. 21, no. 11, pp. 3890–3894, 2011.

[157] H. Yan, 'Soft-templating synthesis of mesoporous graphitic carbon nitride with enhanced photocatalytic H2 evolution under visible light', *Chem. Commun.*, vol. 48, no. 28, pp. 3430–3432, 2012.

[158] Z. Lin and X. Wang, 'Ionic Liquid Promoted Synthesis of Conjugated Carbon Nitride Photocatalysts from Urea', *ChemSusChem*, vol. 7, no. 6, pp. 1547–1550, Jun. 2014.

[159] X. Dong and F. Cheng, 'Recent development in exfoliated two-dimensional g-C3N4 nanosheets for photocatalytic applications', *J. Mater. Chem. A*, vol. 3, no. 47, pp. 23642–23652, 2015.

[160] Y. Yin *et al.*, 'Facile synthesis of few-layer-thick carbon nitride nanosheets by liquid ammonia-assisted lithiation method and their photocatalytic redox properties', *RSC Adv.*, vol. 4, no. 62, pp. 32690–32697, 2014.

[161] P. Niu, L. Zhang, G. Liu, and H.-M. Cheng, 'Graphene-Like Carbon Nitride Nanosheets for Improved Photocatalytic Activities', *Adv. Funct. Mater.*, vol. 22, no. 22, pp. 4763–4770, Nov. 2012.

[162] X. Lu, K. Xu, P. Chen, K. Jia, S. Liu, and C. Wu, 'Facile one step method realizing scalable production of g-C3N4 nanosheets and study of their photocatalytic H2 evolution activity', *J. Mater. Chem. A*, vol. 2, no. 44, pp. 18924–18928, 2014.

[163] Y. Gong, M. Li, and Y. Wang, 'Carbon Nitride in Energy Conversion and Storage: Recent Advances and Future Prospects', *ChemSusChem*, vol. 8, no. 6. pp. 931–946, 2015.

[164] J. Liang *et al.*, 'Kinetically Enhanced Electrochemical Redox of Polysulfides on Polymeric Carbon Nitrides for Improved Lithium-Sulfur Batteries', *ACS Appl. Mater. Interfaces*, vol. 8, no. 38, pp. 25193–25201, Sep. 2016.

[165] Q. Pang and L. F. Nazar, 'Long-Life and High-Areal-Capacity Li–S Batteries Enabled by a Light-Weight Polar Host with Intrinsic Polysulfide

Adsorption', *ACS Nano*, vol. 10, no. 4, pp. 4111–4118, Apr. 2016.

[166] Y. Zheng, H. Li, H. Yuan, H. Fan, W. Li, and J. Zhang, 'Understanding the anchoring effect of Graphene, BN, C 2 N and C 3 N 4 monolayers for lithium−polysulfides in Li−S batteries', *Appl. Surf. Sci.*, vol. 434, pp. 596–603, 2018.

[167] C.-Y. Fan *et al.*, 'The Effective Design of a Polysulfide-Trapped Separator at the Molecular Level for High Energy Density Li–S Batteries', *ACS Appl. Mater. Interfaces*, vol. 8, no. 25, pp. 16108–16115, Jun. 2016.

[168] K. Liao *et al.*, 'Stabilization of polysulfides via lithium bonds for Li-S batteries', *J. Mater. Chem. A*, vol. 4, no. 15, pp. 5406–5409, 2016.

[169] J. Wutthiprom, N. Phattharasupakun, J. Khuntilo, T. Maihom, J. Limtrakul, and M. Sawangphruk, 'Collaborative design of Li-S batteries using 3D N-doped graphene aerogel as a sulfur host and graphitic carbon nitride paper as an interlayer', *Sustain. Energy Fuels*, vol. 1, no. 8, pp. 1759–1765, 2017.

[170] J. Liu *et al.*, 'A Graphene-like Oxygenated Carbon Nitride Material for Improved Cycle-Life Lithium/Sulfur Batteries', *Nano Lett.*, vol. 15, no. 8, pp. 5137–5142, Aug. 2015.

[171] Z. Meng, Y. Xie, T. Cai, Z. Sun, K. Jiang, and W. Q. Han, 'Graphene-like g-C3N4 nanosheets/sulfur as cathode for lithium-sulfur battery', *Electrochim. Acta*, vol. 210, pp. 829–836, 2016.

[172] Z. Li, Y. Du, K. Zhu, A. Meng, and Q. Li, 'Porous g-C 3 N 4 with high pyridine N/sulfur composites as the cathode for high performance lithium-sulfur battery', *Mater. Lett.*, vol. 213, pp. 338–341, 2018.

[173] S. Yao *et al.*, 'Synthesis of graphitic carbon nitride at different thermal-pyrolysis temperature of urea and it application in lithium – sulfur batteries', *J. Mater. Sci. Mater. Electron.*, vol. 0, no. 0, p. 0, 2018.

[174] M. Wang *et al.*, 'Catalyzing polysulfide conversion by g-C3N4 in a graphene network for long-life lithium-sulfur batteries', *Nano Res.*, vol. 11, no. 6, pp. 3480–3489, 2018.

[175] J. Ma *et al.*, 'A 2D/2D graphitic carbon nitride/N-doped graphene hybrid as an effective polysulfide mediator in lithium-sulfur batteries', *Mater. Chem. Front.*, vol. 3, no. 9, pp. 1807–1815, 2019.

[176] Z. Deng, Q. Wang, P. Song, Y. Chen, X. Xia, and H. Liu, 'Hierarchical porous g-C3N4/reduced graphene oxide architecture as light-weight sulfur host material for high-performance lithium-sulfur batteries', *Ionics (Kiel).*, vol. 25, no. 11, pp. 5361–5371, 2019.

[177] X. Guo, X. Liu, H. Yu, Y. Lu, Q. Liu, and Z. Li, 'Designable Hierarchical Cathode for a High-Efficiency Polysulfide Trapper Toward High-Performance Lithium–Sulfur Batteries', *J. Electron. Mater.*, vol. 48, no. 1, pp. 551–559, 2019.

[178] S. Majumder, M. Shao, Y. Deng, and G. Chen, 'Ultrathin sheets of MoS 2 / g-C 3 N 4 composite as a good hosting material of sulfur for lithium – sulfur batteries', *J. Power Sources*, vol. 431, no. May, pp. 93–104, 2019.

[179] H. Dunya *et al.*, 'A new graphitic carbon nitride-coated dual Core – Shell sulfur cathode for highly stable lithium – sulfur cells', *Mater. Chem. Phys.*, vol. 246, no. February, p. 122842, 2020.

[180] R. Jiang, M. Jiang, Z. Huang, J. Wang, Y. Kuang, and C. Fu, 'Constructing light-weight polar boron-doped carbon nitride nanosheets with increased active sites and conductivity for high performance lithium-sulfur batteries', *Int. J. Hydrogen Energy*, vol. 45, no. 29, pp. 14940–14952, May 2020.

[181] Y. Huangfu *et al.*, 'Facile fabrication of permselective g-C3N4 separator

for improved lithium-sulfur batteries', *Electrochim. Acta*, vol. 272, pp. 60–67, 2018.

[182] V. Do, Deepika, M. S. Kim, M. S. Kim, K. R. Lee, and W. Il Cho, 'Carbon Nitride Phosphorus as an Effective Lithium Polysulfide Adsorbent for Lithium–Sulfur Batteries', *ACS Appl. Mater. Interfaces*, vol. 11, no. 12, pp. 11431–11441, Mar. 2019.

[183] M. Chen *et al.*, 'Kinetically elevated redox conversion of polysulfides of lithium-sulfur battery using a separator modified with transition metals coordinated g-C3N4 with carbon-conjugated', *Chem. Eng. J.*, vol. 385, no. October 2019, p. 123905, 2020.

[184] Z. Wu *et al.*, 'Freestanding graphitic carbon nitride-based carbon nanotubes hybrid membrane as electrode for lithium/polysulfides batteries', *Int. J. Energy Res.*, vol. 44, no. 4, pp. 3110–3121, 2020.

[185] F. Zhao *et al.*, 'Handheld spraying of g-C3N4 nanosheets on cathode for high-performance lithium-sulfur batteries', *Ionics (Kiel).*, vol. 25, no. 7, pp. 3099–3106, 2019.

[186] C. Xiong, Y. X. Ren, H. R. Jiang, M. C. Wu, and T. S. Zhao, 'Artificial Bifunctional Protective layer Composed of Carbon Nitride Nanosheets for High Performance Lithium–Sulfur Batteries', *J. Energy Storage*, vol. 26, no. October, 2019.

[187] Z. Jia *et al.*, 'Trithiocyanuric acid derived g–C3N4 for anchoring the polysulfide in Li–S batteries application', *J. Energy Chem.*, vol. 43, pp. 71–77, 2020.

[188] W. Zhang, Q. Zhang, F. Dong, and Z. Zhao, 'The multiple effects of precursors on the properties of polymeric carbon nitride', *Int. J. Photoenergy*, vol. 2013, 2013.

[189] H. Y. Xu, L. C. Wu, H. Zhao, L. G. Jin, and S. Y. Qi, 'Synergic Effect between Adsorption and Photocatalysis of Metal-Free g-C3N4 Derived from Different Precursors', *PLoS One*, vol. 10, no. 11, pp. 1–20, 2015.

[190] M. Ismael, Y. Wu, D. H. Taffa, P. Bottke, and M. Wark, 'Graphitic carbon nitride synthesized by simple pyrolysis: Role of precursor in photocatalytic hydrogen production', *New J. Chem.*, vol. 43, no. 18, pp. 6909–6920, 2019.

[191] H. Dong, X. Guo, C. Yang, and Z. Ouyang, 'Synthesis of g-C3N4 by different precursors under burning explosion effect and its photocatalytic degradation for tylosin', *Appl. Catal. B Environ.*, vol. 230, no. January, pp. 65–76, 2018.

[192] T. S. Miller, A. B. Jorge, T. M. Suter, A. Sella, F. Corà, and P. F. McMillan, 'Carbon nitrides: Synthesis and characterization of a new class of functional materials', *Phys. Chem. Chem. Phys.*, vol. 19, no. 24, pp. 15613–15638, 2017.

[193] M. Thommes *et al.*, 'Physisorption of gases, with special reference to the evaluation of surface area and pore size distribution (IUPAC Technical Report)', *Pure Appl. Chem.*, vol. 87, no. 9–10, pp. 1051–1069, 2015.

[194] D. S. Wu *et al.*, 'Quantitative investigation of polysulfide adsorption capability of candidate materials for Li-S batteries', *Energy Storage Mater.*, vol. 13, no. February, pp. 241–246, 2018.

[195] E. T. Kim *et al.*, 'Conformal Polymeric Multilayer Coatings on Sulfur Cathodes via the Layer-by-Layer Deposition for High Capacity Retention in Li-S Batteries', *ACS Macro Lett.*, vol. 5, no. 4, pp. 471–475, 2016.

[196] P. Spinelli, C. Francia, E. P. Ambrosio, and M. Lucariello, 'Semi-empirical evaluation of PEMFC electro-catalytic activity', *J. Power Sources*, vol.

178, no. 2, pp. 517–524, 2008.

[197] Q. Pang, C. Y. Kwok, D. Kundu, X. Liang, and L. F. Nazar, 'Lightweight Metallic MgB 2 Mediates Polysulfide Redox and Promises High-Energy-Density Lithium-Sulfur Batteries', *Joule*, vol. 3, no. 1, pp. 136–148, 2019.

[198] I. Papailias, T. Giannakopoulou, N. Todorova, D. Demotikali, T. Vaimakis, and C. Trapalis, 'Effect of processing temperature on structure and photocatalytic properties of g-C 3 N 4', *Appl. Surf. Sci.*, vol. 358, pp. 278–286, 2015.

[199] F. Dong, Y. Li, Z. Wang, and W. K. Ho, 'Enhanced visible light photocatalytic activity and oxidation ability of porous graphene-like g-C 3 N 4 nanosheets via thermal exfoliation', in *Applied Surface Science*, 2015, vol. 358, pp. 393–403.

[200] P. Wu, J. Wang, J. Zhao, L. Guo, and F. E. Osterloh, 'Structure defects in g-C3N4 limit visible light driven hydrogen evolution and photovoltage', *J. Mater. Chem. A*, vol. 2, no. 47, pp. 20338–20344, 2014.

[201] X. Fan, Z. Xing, Z. Shu, L. Zhang, L. Wang, and J. Shi, 'Improved photocatalytic activity of g-C3N4 derived from cyanamide-urea solution', *RSC Adv.*, vol. 5, no. 11, pp. 8323–8328, 2015.

[202] L. T. Mai Oanh *et al.*, 'Influence of annealing temperature on physical properties and photocatalytic ability of g-C 3 N 4 nanosheets synthesized through urea polymerization in Ar atmosphere', *Phys. B Condens. Matter*, vol. 532, no. May 2017, pp. 48–53, 2018.

[203] B. Choudhury, K. K. Paul, D. Sanyal, A. Hazarika, and P. K. Giri, 'Evolution of Nitrogen-Related Defects in Graphitic Carbon Nitride Nanosheets Probed by Positron Annihilation and Photoluminescence Spectroscopy', *J. Phys. Chem. C*, vol. 122, no. 16, pp. 9209–9219, Apr. 2018.

[204] J. Liu, T. Zhang, Z. Wang, G. Dawson, and W. Chen, 'Simple pyrolysis of urea into graphitic carbon nitride with recyclable adsorption and photocatalytic activity', *J. Mater. Chem.*, vol. 21, no. 38, pp. 14398–14401, 2011.

[205] J. W. Dibden *et al.*, 'Quantitative Galvanostatic Intermittent Titration Technique for the Analysis of a Model System with Applications in Lithium−Sulfur Batteries', *J. Power Sources*, vol. 5, no. 3, pp. 289–299, 2014.

[206] M. R. Busche, P. Adelhelm, H. Sommer, H. Schneider, K. Leitner, and J. Janek, 'Systematical electrochemical study on the parasitic shuttle-effect in lithium-sulfur-cells at different temperatures and different rates', *J. Power Sources*, vol. 259, pp. 289–299, 2014.

[207] M. J. Lacey, K. Edström, and D. Brandell, 'Visualising the problems with balancing lithium-sulfur batteries by "mapping" internal resistance', *Chem. Commun.*, vol. 51, no. 92, pp. 16502–16505, 2015.

[208] M. J. Lacey, 'Influence of the Electrolyte on the Internal Resistance of Lithium−Sulfur Batteries Studied with an Intermittent Current Interruption Method', *ChemElectroChem*, vol. 4, no. 8, pp. 1997–2004, 2017.

[209] M. Hagen *et al.*, 'Sulfur Cathodes with Carbon Current Collector for Li-S cells', *J. Electrochem. Soc.*, vol. 160, no. 6, pp. A996–A1002, Apr. 2013.

[210] N. A. Cañas, K. Hirose, B. Pascucci, N. Wagner, K. A. Friedrich, and R. Hiesgen, 'Investigations of lithium-sulfur batteries using electrochemical impedance spectroscopy', *Electrochim. Acta*, vol. 97, pp. 42–51, 2013.

[211] Z. Deng, Z. Zhang, Y. Lai, J. Liu, J. Li, and Y. Liu, 'Electrochemical

Impedance Spectroscopy Study of a Lithium/Sulfur Battery: Modeling and Analysis of Capacity Fading', *J. Electrochem. Soc.*, vol. 160, no. 4, pp. A553–A558, 2013.

[212] S. Drvarič Talian, J. Moškon, R. Dominko, and M. Gaberšček, 'Reactivity and Diffusivity of Li Polysulfides: A Fundamental Study Using Impedance Spectroscopy', *ACS Appl. Mater. Interfaces*, vol. 9, no. 35, pp. 29760–29770, Sep. 2017.

[213] S. Drvarič Talian, J. Moškon, R. Dominko, and M. Gaberšček, 'Impedance response of porous carbon cathodes in polysulfide redox system', *Electrochim. Acta*, vol. 302, pp. 169–179, 2019.

[214] Y. Idota, T. Kubota, and A. Matsufuji, 'Tin-Based Amorphous Oxide : A High-Capacity Lithium-Ion – Storage Material', vol. 31, no. May, pp. 1395–1398, 1997.

[215] M. Zhang, T. Wang, and G. Cao, 'Promises and challenges of tin-based compounds as anode materials for lithium-ion batteries', *Int. Mater. Rev.*, vol. 60, no. 6, pp. 330–352, 2015.

[216] I. A. Courtney, 'Electrochemical and In Situ X-Ray Diffraction Studies of the Reaction of Lithium with Tin Oxide Composites', *J. Electrochem. Soc.*, vol. 144, no. 6, p. 2045, 1997.

[217] M. V Reddy, T. T. Linh, D. T. Hien, and B. V. R. Chowdari, 'SnO2 Based Materials and Their Energy Storage Studies', *ACS Sustain. Chem. Eng.*, vol. 4, no. 12, pp. 6268–6276, Dec. 2016.

[218] R. Hu *et al.*, 'Dramatically enhanced reversibility of Li2O in SnO2-based electrodes: the effect of nanostructure on high initial reversible capacity', *Energy Environ. Sci.*, vol. 9, no. 2, pp. 595–603, 2016.

[219] K. Ui, S. Kawamura, and N. Kumagai, 'Fabrication of binder-free SnO2 nanoparticle electrode for lithium secondary batteries by electrophoretic deposition method', *Electrochim. Acta*, vol. 76, pp. 383–388, 2012.

[220] S. Böhme, B. Philippe, K. Edström, and L. Nyholm, 'Photoelectron Spectroscopic Evidence for Overlapping Redox Reactions for SnO2 Electrodes in Lithium-Ion Batteries', *J. Phys. Chem. C*, vol. 121, no. 9, pp. 4924–4936, Mar. 2017.

[221] Y. Cheng, A. Nie, L. Y. Gan, Q. Zhang, and U. Schwingenschlögl, 'A global view of the phase transitions of SnO2 in rechargeable batteries based on results of high throuput calculations', *J. Mater. Chem. A*, vol. 3, no. 38, pp. 19483–19489, 2015.

[222] G. Ferraresi, C. Villevieille, I. Czekaj, M. Horisberger, P. Novák, and M. El Kazzi, 'SnO 2 Model Electrode Cycled in Li-Ion Battery Reveals the Formation of Li 2 SnO 3 and Li 8 SnO 6 Phases through Conversion Reactions', *ACS Appl. Mater. Interfaces*, vol. 10, no. 10, pp. 8712–8720, Mar. 2018.

[223] C. Kim, M. Noh, M. Choi, J. Cho, and B. Park, 'Critical Size of a Nano SnO2 Electrode for Li-Secondary Battery', *Chem. Mater.*, vol. 17, no. 12, pp. 3297–3301, Jun. 2005.

[224] F. Zoller, D. Böhm, T. Bein, and D. Fattakhova-Rohlfing, 'Tin Oxide Based Nanomaterials and Their Application as Anodes in Lithium-Ion Batteries and Beyond', *ChemSusChem*, vol. 12, no. 18. pp. 4140–4159, 2019.

[225] W. Yao, S. Wu, L. Zhan, and Y. Wang, 'Two-dimensional porous carbon-coated sandwich-like mesoporous SnO2/graphene/mesoporous SnO2 nanosheets towards high-rate and long cycle life lithium-ion batteries',

Chem. Eng. J., vol. 361, pp. 329–341, 2019.

[226] M. Liu *et al.*, 'Nano-SnO2/Carbon Nanotube Hairball Composite as a High-Capacity Anode Material for Lithium Ion Batteries', *ACS Sustain. Chem. Eng.*, vol. 7, no. 4, pp. 4195–4203, Feb. 2019.

[227] X. Zhou, L. Yu, and X. W. (David) Lou, 'Nanowire-templated formation of SnO2/carbon nanotubes with enhanced lithium storage properties', *Nanoscale*, vol. 8, no. 15, pp. 8384–8389, 2016.

[228] P.-Y. Chang and R. Doong, 'Microwave-assisted synthesis of SnO2/mesoporous carbon core-satellite microspheres as anode material for high-rate lithium ion batteries', *J. Alloys Compd.*, vol. 775, pp. 214–224, 2019.

[229] J. S. Chen and X. W. (David) Lou, 'SnO2-Based Nanomaterials: Synthesis and Application in Lithium-Ion Batteries', *Small*, vol. 9, no. 11, pp. 1877–1893, Jun. 2013.

[230] D. Song *et al.*, 'Ultra-small SnO2 nanoparticles decorated on three-dimensional nitrogen-doped graphene aerogel for high-performance bind-free anode material', *Appl. Surf. Sci.*, vol. 478, pp. 290–298, 2019.

[231] H. Li *et al.*, 'Dual-carbon confined SnO2 as ultralong-life anode for Li-ion batteries', *Ceram. Int.*, vol. 45, no. 6, pp. 7830–7838, 2019.

[232] L. Sun *et al.*, 'Sn-SnO2 hybrid nanoclusters embedded in carbon nanotubes with enhanced electrochemical performance for advanced lithium ion batteries', *J. Power Sources*, vol. 415, pp. 126–135, 2019.

[233] X. Han, R. Li, S. Qiu, X. Zhang, Q. Zhang, and Y. Yang, 'Sonochemistry-enabled uniform coupling of SnO2 nanocrystals with graphene sheets as anode materials for lithium-ion batteries', *RSC Adv.*, vol. 9, no. 11, pp. 5942–5947, 2019.

[234] M. E. Spahr, D. Goers, A. Leone, S. Stallone, and E. Grivei, 'Development of carbon conductive additives for advanced lithium ion batteries', *J. Power Sources*, vol. 196, no. 7, pp. 3404–3413, 2011.

[235] A. Barroso-Bogeat, M. Alexandre-Franco, C. Fernández-González, and V. Gómez-Serrano, 'Preparation of activated carbon-metal oxide hybrid catalysts: textural characterization', *Fuel Process. Technol.*, vol. 126, pp. 95–103, 2014.

[236] D. Versaci *et al.*, 'Ultrasmall SnO 2 directly grown on commercial C45 carbon as lithium-ion battery anodes for long cycling performance', *Electrochim. Acta*, no. xxxx, p. 137489, 2020.

[237] A. Barroso-Bogeat, M. Alexandre-Franco, C. Fernández-González, A. Macías-García, and V. Gómez-Serrano, 'Preparation of Activated Carbon-SnO2, TiO2, and WO3 Catalysts. Study by FT-IR Spectroscopy', *Ind. Eng. Chem. Res.*, vol. 55, no. 18, pp. 5200–5206, May 2016.

[238] W.-Q. Han and A. Zettl, 'Coating Single-Walled Carbon Nanotubes with Tin Oxide', *Nano Lett.*, vol. 3, no. 5, pp. 681–683, May 2003.

[239] H.-T. Fang *et al.*, 'Synthesis of Tin (II or IV) Oxide Coated Multiwall Carbon Nanotubes with Controlled Morphology', *J. Phys. Chem. C*, vol. 112, no. 15, pp. 5790–5794, Apr. 2008.

[240] C. A. Ibarguen, A. Mosquera, R. Parra, M. S. Castro, and J. E. Rodríguez-Páez, 'Synthesis of SnO2 nanoparticles through the controlled precipitation route', *Mater. Chem. Phys.*, vol. 101, no. 2, pp. 433–440, 2007.

[241] J. Przyłuski, M. Kasprzak, and J. Bieliński, 'Investigations of SnCl2-sensitizing solutions for electroless plating', *Surf. Coatings Technol.*, vol. 31, no. 3, pp. 203–211, 1987.

[242] K. Ke, Y. Yamazaki, and K. Waki, 'A simple method to controllably coat crystalline SnO2 nanoparticles on multiwalled carbon nanotubes.', *J. Nanosci. Nanotechnol.*, vol. 9, no. 1, pp. 366–370, Jan. 2009.

[243] M. . Al-Khatib *et al.*, 'The effect of impregnation of activated carbon with SnCl2.2H2O on its porosity, surface composition and CO gas adsorption', *Carbon N. Y.*, vol. 40, no. 11, pp. 1929–1936, 2002.

[244] M. A. Montes-Morán, J. A. Menéndez, E. Fuente, and D. Suárez, 'Contribution of the Basal Planes to Carbon Basicity: An Ab Initio Study of the H3O+−π Interaction in Cluster Models', *J. Phys. Chem. B*, vol. 102, no. 29, pp. 5595–5601, Jul. 1998.

[245] T. Jiang and M. S. Whittingham, 'A Comparative Study of Carbon Anodes Produced by Ball Milling for Lithium-Ion Batteries', 2017.

[246] K. Kisu *et al.*, 'The origin of anomalous large reversible capacity for SnO2 conversion reaction', *J. Mater. Chem. A*, vol. 2, no. 32, pp. 13058–13068, 2014.

[247] P. Mars and D. W. van Krevelen, 'Oxidations carried out by means of vanadium oxide catalysts', *Chem. Eng. Sci.*, vol. 3, pp. 41–59, 1954.

[248] M. Dimitrov, T. Tsoncheva, S. Shao, and R. Köhn, 'Novel preparation of nanosized mesoporous SnO2 powders: Physicochemical and catalytic properties', *Appl. Catal. B Environ.*, vol. 94, no. 1, pp. 158–165, 2010.

[249] L. Ren, Y. Yao, K. Wang, S. Li, K. Zhu, and J. Liu, 'Novel one-step in situ growth of SnO2 quantum dots on reduced graphene oxide and its application for lithium ion batteries', *J. Solid State Chem.*, vol. 273, pp. 128–131, 2019.

[250] Y. Cheng *et al.*, 'Adjusting the Chemical Bonding of SnO2@CNT Composite for Enhanced Conversion Reaction Kinetics', *Small*, vol. 13, no. 31, p. 1700656, Aug. 2017.

[251] Y. Yang, X.-A. Yang, D. Leng, S.-B. Wang, and W.-B. Zhang, 'Fabrication of g-C3N4/SnS2/SnO2 nanocomposites for promoting photocatalytic reduction of aqueous Cr(VI) under visible light', *Chem. Eng. J.*, vol. 335, pp. 491–500, 2018.

[252] Y. Hong *et al.*, 'Nitrogen-doped carbon coated SnO2 nanoparticles embedded in a hierarchical porous carbon framework for high-performance lithium-ion battery anodes', *J. Power Sources*, vol. 428, pp. 44–52, 2019.

[253] Y. Lee, M. R. Jo, K. Song, K. M. Nam, J. T. Park, and Y.-M. Kang, 'Hollow Sn–SnO2 Nanocrystal/Graphite Composites and Their Lithium Storage Properties', *ACS Appl. Mater. Interfaces*, vol. 4, no. 7, pp. 3459–3464, Jul. 2012.

[254] A. Sivashanmugam, T. P. Kumar, N. G. Renganathan, S. Gopukumar, M. Wohlfahrt-Mehrens, and J. Garche, 'Electrochemical behavior of Sn/SnO2 mixtures for use as anode in lithium rechargeable batteries', *J. Power Sources*, vol. 144, no. 1, pp. 197–203, 2005.

[255] J. G. Kim, S. H. Nam, S. H. Lee, S. M. Choi, and W. B. Kim, 'SnO2 Nanorod-Planted Graphite: An Effective Nanostructure Configuration for Reversible Lithium Ion Storage', *ACS Appl. Mater. Interfaces*, vol. 3, no. 3, pp. 828–835, Mar. 2011.

[256] R. Hu *et al.*, 'Unveiling critical size of coarsened Sn nanograins for achieving high round-trip efficiency of reversible conversion reaction in lithiated SnO2 nanocrystals', *Nano Energy*, vol. 45, pp. 255–265, 2018.

[257] S.-Y. Lee *et al.*, 'Unveiling origin of additional capacity of SnO2 anode in lithium-ion batteries by realistic ex situ TEM analysis', *Nano Energy*, vol.

19, pp. 234–245, 2016.

[258] S. M. Hwang *et al.*, 'A case study on fibrous porous SnO2 anode for robust, high-capacity lithium-ion batteries', *Nano Energy*, vol. 10, pp. 53–62, 2014.

[259] L. Ding *et al.*, 'Ultrasmall SnO2 Nanocrystals: Hot-bubbling Synthesis, Encapsulation in Carbon Layers and Applications in High Capacity Li-Ion Storage', *Sci. Rep.*, vol. 4, no. 1, p. 4647, 2014.

[260] J. S. Cho and Y. C. Kang, 'Nanofibers Comprising Yolk–Shell Sn@void@SnO/SnO2 and Hollow SnO/SnO2 and SnO2 Nanospheres via the Kirkendall Diffusion Effect and Their Electrochemical Properties', *Small*, vol. 11, no. 36, pp. 4673–4681, Sep. 2015.

[261] P. G. Bruce, B. Scrosati, and J.-M. Tarascon, 'Nanomaterials for Rechargeable Lithium Batteries', *Angew. Chemie Int. Ed.*, vol. 47, no. 16, pp. 2930–2946, Apr. 2008.

[262] Y. Zhao, X. Li, B. Yan, D. Li, S. Lawes, and X. Sun, 'Significant impact of 2D graphene nanosheets on large volume change tin-based anodes in lithium-ion batteries: A review', *J. Power Sources*, vol. 274, pp. 869–884, 2015.

[263] L. Yang *et al.*, 'Sb doped SnO2-decorated porous g-C3N4 nanosheet heterostructures with enhanced photocatalytic activities under visible light irradiation', *Appl. Catal. B Environ.*, vol. 221, pp. 670–680, 2018.

[264] D. Masih, Y. Ma, and S. Rohani, 'Graphitic C3N4 based noble-metal-free photocatalyst systems: A review', *Appl. Catal. B Environ.*, vol. 206, pp. 556–588, 2017.

[265] J. Cao, C. Qin, Y. Wang, H. Zhang, G. Sun, and Z. Zhang, 'Solid-state method synthesis of SnO2-decorated g-C3N4 nanocomposites with enhanced gas-sensing property to ethanol', *Materials (Basel).*, vol. 10, no. 6, 2017.

[266] M. Wu, Q. Wang, Q. Sun, and P. Jena, 'Functionalized Graphitic Carbon Nitride for Efficient Energy Storage', *J. Phys. Chem. C*, vol. 117, no. 12, pp. 6055–6059, Mar. 2013.

[267] G. M. Veith *et al.*, 'Electrochemical and Solid-State Lithiation of Graphitic C3N4', *Chem. Mater.*, vol. 25, no. 3, pp. 503–508, Feb. 2013.

[268] V. Vo *et al.*, 'SnO 2 nanosheets/g-C 3 N 4 composite with improved lithium storage capabilities', *Chem. Phys. Lett.*, vol. 674, pp. 42–47, Apr. 2017.

[269] Y. Wang *et al.*, 'Erratum to "Critical influence of carbon nitride self-assembly coating on the electrochemical performance of SnO2-TiO2 nanocomposite anode material for lithium ion battery" [Int. J. Electrochem. Sci., 11 ,(2016), 2461-2472]', *Int. J. Electrochem. Sci.*, vol. 11, no. 4, p. 3260, 2016.

[270] H. H. Tran *et al.*, 'SnO2 nanosheets/graphite oxide/g-C3N4 composite as enhanced performance anode material for lithium ion batteries', *Chem. Phys. Lett.*, vol. 715, pp. 284–292, 2019.

[271] D. Versaci, J. Amici, C. Francia, and S. Bodoardo, 'Simple approach using g-C3N4 to enable SnO2 anode high rate performance for Li ion battery', *Solid State Ionics*, vol. 346, p. 115210, 2020.

[272] F. Dong *et al.*, 'In Situ Construction of g-C3N4/g-C3N4 Metal-Free Heterojunction for Enhanced Visible-Light Photocatalysis', *ACS Appl. Mater. Interfaces*, vol. 5, no. 21, pp. 11392–11401, Nov. 2013.

[273] S. C. Yan, Z. S. Li, and Z. G. Zou, 'Photodegradation Performance of g-

C3N4 Fabricated by Directly Heating Melamine', *Langmuir*, vol. 25, no. 17, pp. 10397–10401, Sep. 2009.

[274] H.-B. Fang, Y. Luo, Y.-Z. Zheng, W. Ma, and X. Tao, 'Facile Large-Scale Synthesis of Urea-Derived Porous Graphitic Carbon Nitride with Extraordinary Visible-Light Spectrum Photodegradation', *Ind. Eng. Chem. Res.*, vol. 55, no. 16, pp. 4506–4514, Apr. 2016.

[275] H. Shen, X. Zhao, L. Duan, R. Liu, and H. Li, 'Enhanced visible light photocatalytic activity in SnO2@g-C3N4 core-shell structures', *Mater. Sci. Eng. B*, vol. 218, pp. 23–30, 2017.

[276] K. Li *et al.*, 'In-Situ-Reduced Synthesis of Ti3+ Self-Doped TiO2/g-C3N4 Heterojunctions with High Photocatalytic Performance under LED Light Irradiation', *ACS Appl. Mater. Interfaces*, vol. 7, no. 17, pp. 9023–9030, May 2015.

[277] S. Cao, J. Low, J. Yu, and M. Jaroniec, 'Polymeric Photocatalysts Based on Graphitic Carbon Nitride', *Adv. Mater.*, vol. 27, no. 13, pp. 2150–2176, Apr. 2015.

[278] P. Praus, L. Svoboda, R. Dvorský, and M. Reli, 'Nanocomposites of SnO2 and g-C3N4: Preparation, characterization and photocatalysis under visible LED irradiation', *Ceram. Int.*, vol. 44, no. 4, pp. 3837–3846, 2018.

[279] Y. Zang, L. Li, X. Li, R. Lin, and G. Li, 'Synergistic collaboration of g-C3N4/SnO2 composites for enhanced visible-light photocatalytic activity', *Chem. Eng. J.*, vol. 246, pp. 277–286, 2014.

[280] M. A. Stranick and A. Moskwa, 'SnO2 by XPS', *Surf. Sci. Spectra*, vol. 2, no. 1, pp. 50–54, Jan. 1993.

[281] Q. Xue *et al.*, 'Hydrothermal synthesis of blue-fluorescent monolayer BN and BCNO quantum dots for bio-imaging probes', *RSC Adv.*, vol. 6, no. 82, pp. 79090–79094, 2016.

[282] X. Zhou, L.-J. Wan, and Y.-G. Guo, 'Binding SnO2 Nanocrystals in Nitrogen-Doped Graphene Sheets as Anode Materials for Lithium-Ion Batteries', *Adv. Mater.*, vol. 25, no. 15, pp. 2152–2157, Apr. 2013.

[283] Y. Wang *et al.*, 'Critical influence of carbon nitride self-assembly coating on the electrochemical performance of SnO2-TiO2 nanocomposite anode material for lithium ion battery', *Int J Electrochem Sci*, vol. 11, pp. 2461–2472, 2015.

[284] Y.-J. Kim, H. Lee, and H.-J. Sohn, 'Lithia formation mechanism in tin oxide anodes for lithium–ion rechargeable batteries', *Electrochem. commun.*, vol. 11, no. 11, pp. 2125–2128, 2009.

[285] J. Wang, H. Zhao, X. Liu, J. Wang, and C. Wang, 'Electrochemical properties of SnO2/carbon composite materials as anode material for lithium-ion batteries', *Electrochim. Acta*, vol. 56, no. 18, pp. 6441–6447, 2011.

[286] R. Demir-Cakan, Y.-S. Hu, M. Antonietti, J. Maier, and M.-M. Titirici, 'Facile One-Pot Synthesis of Mesoporous SnO2 Microspheres via Nanoparticles Assembly and Lithium Storage Properties', *Chem. Mater.*, vol. 20, no. 4, pp. 1227–1229, Feb. 2008.

[287] Y. Deng, C. Fang, and G. Chen, 'The developments of SnO2/graphene nanocomposites as anode materials for high performance lithium ion batteries: A review', *J. Power Sources*, vol. 304, pp. 81–101, 2016.

[288] Y. Hou, J. Li, Z. Wen, S. Cui, C. Yuan, and J. Chen, 'N-doped graphene/porous g-C3N4 nanosheets supported layered-MoS2 hybrid as robust anode materials for lithium-ion batteries', *Nano Energy*, vol. 8, pp.

157–164, 2014.

[289] M. Hankel, D. Ye, L. Wang, and D. J. Searles, 'Lithium and Sodium Storage on Graphitic Carbon Nitride', *J. Phys. Chem. C*, vol. 119, no. 38, pp. 21921–21927, Sep. 2015.

[290] T. S. Miller *et al.*, 'The Use of Graphitic Carbon Nitride Based Composite Anodes for Lithium-Ion Battery Applications', *Electroanalysis*, vol. 27, no. 11, pp. 2614–2619, Nov. 2015.

[291] J. H. Um *et al.*, '3D interconnected SnO2-coated Cu foam as a high-performance anode for lithium-ion battery applications', *RSC Adv.*, vol. 4, no. 101, pp. 58059–58063, 2014.

[292] C. M Subramaniyam *et al.*, '2D Layered Graphitic Carbon Nitride Sandwiched with Reduced Graphene Oxide as Nanoarchitectured Anode for Highly Stable Lithium-ion Battery', *Electrochim. Acta*, vol. 237, pp. 69–77, 2017.

11 Appendix A

List of abbreviations

AC – Activated carbon
AMAC – Methyl acrylate copolymer latex
AMMA – Acrylonitile methyl metacrylate
BET – Brunauer-emmett-teller theory
C – Carbon
C45 – C-NERGY super C45
CE – Coulombic efficiency
CG/CG – Galvanostatic charge/discharge cycling
CMC – Carboxymethyl cellulose
CN – Carbon nitride
CNT/MWCNT – Carbon nanotube/multiwalled carbon nanotube
CPE – Constant phase element
CV – Cyclic voltammetry
DCDA – Dicyandiamide
DFT – Density functional theory
DL – Double-layer
DMC – Dimethyl carbonate
DME – Dimethoxyethane
DMF – Dimethylformamide
DOC – Depth of charge
DOD – Depth of discharge
DOL – Dioxolane
E – Energy
EC – Ethylene carbonate
EDS – Energy dispersive X-ray spectroscopy
EIS – Electrochemical impedance spectroscopy
EMC – Ethyl methyl carbonate
EV – Electric vehicle
FE-SEM – Field emission scanning electron microscopy
FT-IR – Fourier-transform infrared spectroscopy
GHG – Greenhouse gas
GITT – Galvanostatic intermittent titration technique
GO/rGO – Graphene oxide/reduced graphene oxide
GPE – Gel polymer electrolyte
HOMO – highest occupied molecular orbital
ICE – Internal combustion engine
ILs – Ionic liquids
JCPDS - Joint Committee on Powder Diffraction Standards

KjB – Ketjenblack EC-300j

LFP – lithium iron phosphate

LIB/Li-ion – lithium ion battery

LiBOB – Lithium bis(oxalato)borate

LiPSs/PSs – Lithium polysulfides

Li-S – Lithium-sulphur battery

LiTFSI – Lithium bis(trifluoromethanesulfonyl)imide

LNMO – Lithium nickel manganese oxide

LSV – Linear sweep voltammetry

LTO – Lithium Titanate

LUMO – lower un-occupied molecular orbital

MLM – Melamine

MO – Metal oxide

MOF – Metal organic framework

MXene – 2D transition metal carbides/nitrides

NCA – Lithium cobalt aluminum oxide

NMC – Lithium nickel manganese cobalt oxide

NMP – N-methyl-2-pyrrolidone

OCV – open circuit voltage

P – Power

PA – Paris Agreement

PAA – Polyacrylic acid

PAN – polyacrylonitrile

PANI – Polyaniline

PE – Polyethylene

PEO – Polyethylene glycol

PF – polyolefin

PHEV – Plug-in hybrid electric vehicle

PMA – Poly(methyl acrylate)

PMMA – Poly(methyl metacrylate)

PP – Polypropylene

PSD – Pore size distribution

PVA – Polyvinyl alcohol

PVdF – Poly(vinylidene fluoride)

PVdF/HFP - Poly(vinylidene fluoride co-hexafluoropropylene)

Q – Capacity

Rct – Charge-transfer resistance

Rel – Electrolyte resistance

S – Sulphur

SDA – Structure directing agent

SEI – Solid electrolyte interphase

SHE – Standard hydrogen electrode

SL – Single-layer

SSA – Specific surface area

SSE – Solid-state electrolyte

SOC – State of Charge
SOD – State of Discharge
STD – Standard
TEM – Transmission electron microscopy
TGA -Thermogravimetric analysis
U – Urea
VOC – volatile organic compound
XPS – X-ray photoelectron spectroscopy
XRD – X-ray powder diffraction

12 Appendix B

List of publications

"Synthesis and characterization of LNMO cathode materials for lithium-ion batteries"
G. Ganas, G. Kastrinaki, D. Zarvalis, G. Karagiannakis, A. G. Konstandopoulos, D. Versaci, S. Bodoardo, Materials Today: Proceedings 5, 14, 2018, 27416-27424.
(DOI:10.1016/j.matpr.2018.09.059)

"UV-cured methacrylate based polymer composite electrolyte for metallic lithium batteries."
J. Amici, S. Romanin, M. Alidoost, D. Versaci, C. Francia, F. Smeacetto, S. Bodoardo, Journal of Electroanalytical Chemistry 837, 2019, 103-107.
(DOI: 10.1016/j.jelechem.2019.02.027)

"Electrochemical characterization and Solid Electrolyte Interface modeling of $LiNi_{0.5}Mn_{1.5}O_4$-Graphite Cells"
V. Giai Pron, D. Versaci, J. Amici, C. Francia, M. Santarelli, S. Bodoardo, Journal of the Electrochemical Society, 166(10) (2019) A2255-A2263.
(DOI: 10.1149/2.0941910jes)

"Simple Approach Using g-C_3N_4 to Enable SnO_2 Anode High Rate Performance for Li-Ion Battery"
D. Versaci, J. Amici, C. Francia, S. Bodoardo, Solid State Ionics 346 (2020) 115210.
(DOI: 10.1016/j.ssi.2019.115210)

"Chitosan and its char as fillers in cement-base composites: A case study"
R. Nisticò, L. Lavagna, D. Versaci, P. Ivanchenko, P. Benzi, Boletin de la Sociedad Espanola de Ceramica y Vidrio 59(5) (2020)186-192
(DOI: 10.1016/j.bsecv.2019.10.002)

"Ultrasmall SnO_2 directly grown on commercial C45 carbon as lithium-ion battery anodes for long cycling performance"
D. Versaci, A. Costanzo, S.M. Ronchetti, B. Onida, J. Amici, C. Francia, S. Bodoardo, Electrochimica Acta (2021) 137489.
(DOI: 10.1016/j.electacta.2020.137489)

"Synthesis and characterization of montmorillonite/polyaniline composites and its usage to modify a commercial separator"

M.L. Para, D. Versaci, J, Amici, M. F. Caballero, M. V. Cozzarin, C. Francia, S. Bodoardo, M. Gamba, Journal of Electroanalytical Chemistry 880 (2021) 114876.
(DOI: 10.1016/j.jelechem.2020.114876)

"Lithium polysulfides immobilization exploiting formate-ion doped polyaniline wrapped carbon for Long cycle life sulfur cathodes via conventional electrode processing"
U. Zubair, D. Versaci, M. Umer, J. Amici, C. Francia, S. Bodoardo, Materials Today Communications 26 (2021) 101970.
(DOI: 10.1016/j.mtcomm.2020.101970)

"Tragacanth gum as green binder for sustainable water-processable electrochemical capacitor"
A. Scalia, P. Zaccagnini, M. Armandi, G. Latini, D. Versaci, V. Lanzio, A. Varzi, S. Passerini, A. Lamberti, CHEMSUSCHEM 14 (2021) 356-362.
(DOI: 10.1002/cssc.202001754)

Patent

"High power and high energy self-switching electrochemical storage device"
S. Bodoardo, U. Zubair, M. Serrapede, J. Amici, P. Zaccagnini, D. Versaci, C. Francia, C. F. Pirri, A. Lamberti
International Application No.: PCT/IB2019/053525
Also published as: EP2019726159, IT201800005943

13 Appendix C

List of oral/poster presentation

Poster: "Facile synthesis of SnO_2/g-C_3N_4 hybrid compound for anode application"
D. Versaci, S. Bodoardo, A. Marchisio, J. Amici, C. Francia, N. Penazzi, GEI 2018 (Giornate dell'elettrochimica italiana 2018), Jenuary 21-25, Sestriere.

Poster: "SnO_2 anode materials for high capacity Li-ion cells"
D. Versaci, S. Vankova, N. Penazzi, S. Bodoardo, G. A. Ganas, G. Kastrinaki, D. Zarvalis, A.G. Konstandopoulos, TRA 2018 (Transport Research Arena 2018), April 16-19, Vienna.

Oral presentation: " Simply double layer approach for enhancing Li-S battery performances"
D. Versaci, M. Cozzarin, J. Amici, M. E. Zoloff Michoff, C. Francia, A. Visintin, E. P. M. Leiva, S. Bodoardo, GEI 2019 (Giornate dell'elettrochimica italiana 2019), September 8-12, Padova.

Poster: " Facile Synthesis of SnO_2/Carbon anode material for high performance Li-ion battery"
D. Versaci, A. Costanzo, J. Amici, M. Cozzarin, S.M. Ronchetti, B. Onida C. Francia, S. Bodoardo,, GEI 2019 (Giornate dell'elettrochimica italiana 2019), September 8-12, Padova.

Poster: "SnO_2/Carbon anode material for high performance Li-ion battery"
D. Versaci, A. Costanzo, J. Amici, M. Cozzarin, S.M. Ronchetti, B. Onida C. Francia, S. Bodoardo, LIBD 2019 (Lithium Ion Battery Discussion 2019), September 15-20, Arcachon.

Poster: "Carbon nitride based double layer approach for enhancing Li-S battery performances"
D. Versaci, M. Cozzarin, J. Amici, M. E. Zoloff Michoff, C. Francia, A. Visintin, E. P. M. Leiva, S. Bodoardo, IWLIME (7th International workshop on lithium, industrial minerals and energy 2020), November 9-11, online.